



Supercritical Fluids and Their Application to the
Recycling of High-Performance Carbon Fibre
Reinforced Composite Materials

By
Luke Omar Dandy

A Thesis Submitted to the University of
Birmingham for the Award of the Degree
Doctor of Philosophy

April 2015

UNIVERSITY OF
BIRMINGHAM

University of Birmingham Research Archive

e-theses repository

This unpublished thesis/dissertation is copyright of the author and/or third parties. The intellectual property rights of the author or third parties in respect of this work are as defined by The Copyright Designs and Patents Act 1988 or as modified by any successor legislation.

Any use made of information contained in this thesis/dissertation must be in accordance with that legislation and must be properly acknowledged. Further distribution or reproduction in any format is prohibited without the permission of the copyright holder.

ABSTRACT

The decomposition of high-performance thermoplastic and thermoset polymers is carried out by using supercritical fluids, in conjunction with a caesium carbonate catalyst (Cs_2CO_3). Polyetheretherketone (PEEK) and its carbon fibre filled composite are used as the high-performance thermoplastic, owing to its strong chemical resistance and excellent thermal and chemical stability. 2,2-Bis[4-(glycidyl)oxy]propane (BADGE) is cross-linked with 4,4'-diaminodiphenyl sulfone (DDS) to produce a high-performance thermoset resin used to investigate the decomposition of the polymer matrices used in the manufacture of carbon fibre reinforced polymers (CFRP's). It is determined that the complete decomposition of the BADGE based thermoset resin is possible at 573 K when using a catalyst concentration ($[\text{Cs}_2\text{CO}_3]$) of 10 mg ml^{-1} in 100 % ethanol or propanol and a reaction time of 30 minutes, with a percentage degradation of 90 % being achieved after 45 minutes. The decomposition of PEEK at 623 K, 7 K above its melt temperature, is possible within 30 minutes when using a supercritical fluid mixture of ethanol and water ($[\text{EtOH}] = 20 \text{ \%v}$) and a Cs_2CO_3 concentration of 10 mg ml^{-1} . Decomposition of PEEK in 100 % ethanol was not observed, indicating that the decomposition reaction is hydrolysis. Conversely, the decomposition of the BADGE based thermoset resin was essentially impeded by the presence of water and is therefore one of solvolysis. Both decomposition reactions were found to be 1st order with respect to $[\text{Cs}_2\text{CO}_3]$.

Tensile testing of carbon fibre bundles, made possible by a method developed as part of this research to determine the number of fibres within a bundle, showed little reduction in the tensile strength of recycled fibres. X-Ray Photoelectron Spectroscopy demonstrated that,

depending on the reaction conditions, the sizing may be removed from carbon fibres during thermochemical processing, an important insight for recycling processes for CFRP's.

To my partner in life,

Erica Newman-Berry,

Love always

ACKNOWLEDGMENTS

This thesis represents my last 10 years of education, starting in 2005 and being concluded in 2015. This thesis, as is always the case, is the culmination of the research, development, concepts and ideas of the author. This significant milestone in my life however, is much more than solely the dedication and perseverance of myself and is the result of an excellent support network, family, friends, colleagues and supervisor. The support of my academic supervisor, Dr Gary Leeke, has been nothing short of exemplary and has much to do with the success of this project, for which I am most grateful. I would also like to thank the EPSRC for funding.

I would like to personally thank my mother and father for their continued support over the last decade that I have been at university. I am particularly grateful to my brother Levi Dandy BEng(Hons) MEd for inspiring me to go into Chemical Engineering in 2005, without whom this may not have happened. I wish to thank my brother Lewis, my sister Rochelle, my uncles Peter, Paul and Tony for their support over the years. I am especially grateful to my uncle Danny for supplying me with the computer that I used to run experiments leading to my first publication. I am fortunate to have great friends who have supported me throughout this project.

It is my belief that there are more than 100 people that have, in some way, contributed to the success of this project. I sincerely appreciate all of your efforts, it means a great deal to me, did not go unnoticed and will not be forgotten.

Peer – Reviewed Publications

- i. Counting Carbon Fibres by Electrical Resistance Measurement

*Composites Part A: Applied Science and Manufacturing, Impact Factor = 3.012,
Published*

doi:10.1016/j.compositesa.2014.10.015

- ii. Accelerated Degradation of Polyetheretherketone (PEEK) Composite Materials for Recycling Applications

Polymer Degradation and Stability, Impact Factor = 2.633, Published

doi:10.1016/j.polymdegradstab.2014.12.012

- iii. Catalytic Decomposition of Thermoset Polymers for Recycling Applications

Journal of Polymers and the Environment, Under Review

- iv. Supercritical Fluid Induced Swelling of Thermoset Epoxy Resin

Journal of Polymers and the Environment, Under Review

- v. Degradation of a Model Epoxy Resin by Solvolysis Routes

Polymer Degradation and Stability, Impact Factor = 2.633, Published

doi:10.1016/j.polymdegradstab.2015.04.016

- vi. The Current Status of Recycling Composite Materials: review of technologies, reuse applications and economic and life cycle assessment

Progress in Materials Science, Impact Factor = 25.870, Published

doi:10.1016/j.pmatsci.2015.01.004

Conferences and Conference Proceedings

- i. Determination of Carbon Fibre Bundle Sizes by Electrochemical Impedance Spectroscopy

16th European Conference on Composite Materials, Seville, Spain, 2014

- ii. A step change in the recycling of composite materials

4th International Conference on Industrial and Hazardous Waste Management, Chania, Crete, Greece, 2014

- iii. A step change in the recycling of composite materials

4th International Carbon Composites Conference, Arcachon, France, 2014

- iv. The Recycling of Carbon Fibre Reinforced Polymers

SET for Britain, House of Commons, London, UK, 2015

- v. Future directions in the recycling of composite materials

20th International Conference on Composite Materials, Copenhagen, Denmark, 2015

Contents

| | |
|--|----|
| List of Figures | 13 |
| List of Tables | 25 |
| List of Abbreviations | 27 |
| Nomenclature | 29 |
| Chapter 1. Introduction | 31 |
| Chapter 2. Literature Review | 35 |
| 2.1. Supercritical Fluids | 35 |
| 2.2. High-Performance Thermoplastic Polymers | 38 |
| 2.3. High-Performance Thermoset Polymers | 44 |
| 2.4. Fibre Reinforcement | 51 |
| 2.5. Carbon Fibre Reinforced Polymers | 55 |
| 2.5.1. Manufacturing CFRP's | 55 |
| 2.5.2. Damage Detection in CFRP's | 61 |
| 2.5.3. Recycling CFRP's | 64 |
| 2.6. Summary of Literature Review Findings | 73 |
| Chapter 3. Experimental Methodology | 75 |
| 3.1. Materials Investigated | 75 |
| 3.2. Reaction Vessels | 77 |
| 3.3. Reaction Conditions | 82 |
| 3.3.1. Supercritical Carbon Dioxide Processing of Polyetheretherketone | 82 |

| | |
|--|-----|
| 3.3.2. Recycling of Polyetheretherketone Composite Materials..... | 88 |
| 3.3.3. Decomposition and Recycling of Polyepoxide Thermoset Resin..... | 95 |
| 3.3.4. Processing and Characterisation of Carbon Fibre | 103 |
| 3.3.5. Recycling of Carbon Fibre Reinforced Polyepoxide Composite Materials | 108 |
| 3.4. Analytical Techniques | 109 |
| 3.4.1. Confirmation of PEEK Amorphicity | 109 |
| 3.4.2. Analysis of Supercritical Carbon Dioxide Processed PEEK..... | 114 |
| 3.4.3. Analysis of Polymer Decomposition Products..... | 121 |
| 3.4.4. Analysis of Carbon Fibre | 131 |
| 3.4.5. Analysis of Carbon Fibre Reinforced Polymeric Materials | 150 |
| Chapter 4. Results Part A: Processing and Recycling of Polyetheretherketone..... | 152 |
| 4.1. Supercritical Carbon Dioxide Processing of Polyetheretherketone | 152 |
| 4.1.1. Confirmation of Amorphicity | 152 |
| 4.1.2. Effects of scCO ₂ Processing on the Polymer Transitions | 161 |
| 4.1.3. High-Pressure Differential Scanning Calorimetry | 168 |
| 4.1.4. Carbon Dioxide Containment with PEEK | 172 |
| 4.2. Decomposition and Recycling of Polyetheretherketone Composite Materials | 179 |
| 4.2.1. Ethanol and Water Co-solvent System | 179 |
| 4.2.2. Propanol and Water Co-solvent System..... | 199 |
| 4.2.3. Acetone and Water Co-solvent System..... | 207 |

| | |
|--|-----|
| 4.2.4. Comparative Study of Ethanol, Propanol and Acetone Co-solvent Reaction Systems | 210 |
| Chapter 5. Results Part B: Decomposition and Recycling of Polyepoxide Thermoset Resin | 216 |
| 5.1. Solvolysis of Epoxy Resin in Supercritical Alcohols..... | 216 |
| 5.1.1. Water and Ethanol Co-solvent Decomposition Reactions | 217 |
| 5.1.2. Water and Propanol Co-solvent Decomposition Reactions | 227 |
| 5.1.3. Water and Butanol Co-solvent Decomposition Reactions | 234 |
| 5.1.4. Comparative Study between Ethanol and Propanol Systems | 238 |
| 5.2. Supercritical Fluid Induced Swelling of Epoxy Resin..... | 243 |
| Supercritical Ethanol | 244 |
| Supercritical Propanol..... | 248 |
| Chapter 6. Results Part C: Characterisation and Recycling of Carbon Fibre..... | 256 |
| 6.1. Tensile Properties of Recycled Carbon Fibres | 256 |
| 6.2. Effects of Recycling on Carbon Fibre Sizing | 262 |
| Chapter 7. Results Part D: Recycling of Carbon Fibre Reinforced Composite Materials..... | 270 |
| Chapter 8. Conclusions – The Processing and Recycling of High Performance Materials for use in Aerospace and Related Industries..... | 275 |
| List of References..... | 281 |
| Appendices..... | 301 |
| Appendix 1. High-Pressure Reactor Volume Calculation (CO ₂) | 301 |
| Appendix 2. Fibre diameter variability with respect to length..... | 306 |

| | |
|--|-----|
| Appendix 3. X-Ray Photoelectron Spectroscopy Data..... | 306 |
| Appendix 4. Impedance of fibre bundles..... | 311 |
| Appendix 5. Reactor Schematic Diagrams..... | 312 |

LIST OF FIGURES

| | |
|---|-----|
| Figure 1: Phase diagram for water, showing the triple and critical points, equilibrium data obtained from National Institute of Standards and Technology (NIST) and [1]. Solid lines represent phase transitions | 36 |
| Figure 2: Structure of poly(oxy-1,4-phenyleneoxy-1,4-phenylenelecarbonyl-1,4-phenylene) PEEK | 75 |
| Figure 3: Left; 2,2-Bis[4-(glycidyoxy)phenyl]propane (DER 332, BADGE), Right; 4,4'-diaminodiphenyl sulfone (DDS) | 76 |
| Figure 4: Low-Temperature Reactor (LTR) system showing a; complete setup, b; sapphire viewing windows..... | 79 |
| Figure 5: High-Temperature Reactor (HTR), 100 ml nominal volume, a; Side profile showing identification markings (Hastelloy), b; top-view showing internal volume (Hastelloy), c; complete setup (stainless-steel)..... | 81 |
| Figure 6: High-Temperature Reactors showing the discolouration at the end-of-life of the reactor, Hastelloy (left), stainless-steel (right) | 82 |
| Figure 7: D.E.R. 332 DDS Polyepoxide curing cycle, all dynamic segment rates = 1 K min ⁻¹ ... | 98 |
| Figure 8: Bespoke carbon fibre alignment tool, stainless steel, approximately 120 mm in length | 107 |
| Figure 9: DSC method 1; Determination of percentage crystallinity (%X _c)..... | 112 |
| Figure 10: HPDSC Method 1, analysis of PEEK melting process under CO ₂ pressure environment | 115 |
| Figure 11: HPDSC Method 2, single dynamic segment with a slow heating rate to investigate the impact of CO ₂ on T _g , T _c and T _m | 116 |
| Figure 12: HPDSC Method 3, minimal heating rate for maximum thermal equilibrium..... | 117 |

Figure 13: HPDSC Method 4, dynamic measurement of polymer transition temperatures. 118

Figure 14: HPDSC Method 5, rapid heating through all polymeric transitions T_g , T_c and T_m 119

Figure 15: TGA Method 1, post $scCO_2$ processing analysis of PEEK121

Figure 16: DSC Method 2 used for the analysis of recovered epoxy resin samples. $dT / dt = 10 \text{ K min}^{-1}$ 122

Figure 17: TGA Method 2 used for the analysis of thermoset and thermoplastic polymers and their associated composite materials. $dT / dt = 10 \text{ K min}^{-1}$123

Figure 18: GC-MS Method 1 used for the separation and subsequent identification of polymer decomposition products. Column = ZB5-MS, $dT / dt = 20 \text{ K min}^{-1}$, $Q_{He} = 1 \text{ ml min}^{-1}$, $V_{INJ} = 1 \mu\text{l}$ 126

Figure 19: GC-MS Method 2 used for the separation and subsequent identification of polymer decomposition products. $dT / dt = 13.25 \text{ K min}^{-1}$, $Q_{He} = 1 \text{ ml min}^{-1}$, $V_{INJ} = 1 \mu\text{l}$ 127

Figure 20: HPLC Method 1 for the separation of polymer decomposition products. $Q = 1 \text{ ml min}^{-1}$, $T_{COL} = 308 \text{ K}$, $P = 15 \text{ MPa}$, $V_{INJ} = 10 \mu\text{l}$128

Figure 21: HPLC Calibration curve for phenol concentrations [PhOH] given in Table 19. $\lambda = 254 \text{ nm}$, HPLC Method 1, $R^2 = 0.998$131

Figure 22: EIS Schematic Diagram, working electrode (WE), counter electrode (CE), reference electrode (RE).....134

Figure 23: EIS Equivalent circuit, system impedance (R_s), carbon fibre impedance (R_1)136

Figure 24: Single carbon fibre with 25 □m Molybdenum
.....136

Figure 25: SEM Micrograph of the single carbon fibre, 150 mm in length (full length not shown), subsequently used in Electrical Impedance Measurements137

Figure 26: Impedance as a function of length for single carbon fibres139

| | |
|--|-----|
| Figure 27: SEM micrograph of a single carbon fibre used for EIM, 150 mm in length (full length not shown)..... | 141 |
| Figure 28: SEM micrograph of a single carbon fibre used for EIM, 120 mm in length (full length not shown)..... | 142 |
| Figure 29: Impedance as a function of the number of fibres within a carbon fibre bundle, 85 mm in length..... | 143 |
| Figure 30: Bespoke carbon fibre alignment tool, manufactured by University of Birmingham, showing aligned fibre bundle set in Araldite Rapid resin..... | 149 |
| Figure 31: DSC thermogram for PEEK150PF as received, 7.0 mg, DSC Method 1, endothermic-up..... | 153 |
| Figure 32: DSC thermogram for PEEK150PF generated by quenching from melt phase, 11.2 mg, DSC Method 1, endothermic-up..... | 154 |
| Figure 33: FT-IR Absorbance spectrum for PEEK150PF as received, full range not shown, A = 1307 cm ⁻¹ , B = 1280 cm ⁻¹ | 156 |
| Figure 34: FT-IR Absorbance spectrum for PEEK150PF post quenching, full range not shown, A = 1307 cm ⁻¹ , B = 1280 cm ⁻¹ | 157 |
| Figure 35: WAXS Spectrum for PEEK150PF as received, 50 µm powder..... | 160 |
| Figure 36: WAXS Spectrum for PEEK150PF post quenching from melt phase..... | 161 |
| Figure 37: Main effects plot for influence of CO ₂ processing pressure on glass transition temperature (T _g), T = 413 - 453 K, t _r = 10 - 30 min..... | 162 |
| Figure 38: Cube plot for the effects of scCO ₂ processing on the glass transition temperature (T _g) of PEEK150PF observed by DSC. DOE conditions; T = 413 – 453 K, P = 5 – 15 MPa, t _r = 10 – 30 min, centre-point T = 433 K, P = 10 MPa, t _r = 20 min..... | 163 |

| | |
|--|-----|
| Figure 39: Cube plot showing the percentage crystallisation observed by DSC for PEEK processed with scCO ₂ . DOE conditions; T = 413 – 453 K, P = 5 – 15 MPa, t _r = 10 – 30 min, centre-point T = 433 K, P = 10 MPa, t _r = 20 min | 165 |
| Figure 40: DSC thermograms for PEEK 150PF samples processed from amorphous state using scCO ₂ , T = 453 K. DSC Method 1 | 167 |
| Figure 41: HPDSC thermogram for amorphous PEEK in-situ measurement, P _{iCO2} = 3.0 MPa, HPDSC method 5..... | 170 |
| Figure 42: HPDSC thermogram for amorphous PEEK in-situ measurement, P _{iCO2} = 3.5 MPa, HPDSC method 1..... | 171 |
| Figure 43: Mass loss observed by TGA as a function of Lag Time for PEEK processed with scCO ₂ , P = 20.0 MPa, T = 413 K, t = 30 min | 173 |
| Figure 44: TGA thermogram for PEEK450PF processed in scCO ₂ showing the furnace temperature and 1 st order differential of mass loss (DTG), P = 20.0 MPa, T = 413 K, t = 30 min. TGA Method 1..... | 175 |
| Figure 45: 3D FT-IR spectrum for analysis of TGA exhaust gasses from PEEK450PF processed in scCO ₂ , lag time = 60 min, (Processing conditions; P = 20.0 MPa, T = 413 K, t = 30 min)... | 177 |
| Figure 46: 3D FT-IR spectrum for analysis of TGA exhaust gasses from PEEK450PF processed in scCO ₂ , lag time = 180 min, (Processing conditions; P = 20.0 MPa, T = 413 K, t = 30 min). | 177 |
| Figure 47: Phenol concentration [PhOH] with respect to ethanol concentration [EtOH], 623 K, 30 min, 10 mg ml ⁻¹ Cs ₂ CO ₃ , P = 15.8 – 25.5 MPa. Determined by HPLC..... | 180 |
| Figure 48: Optical Microscopy image of PEEK, Victrex 150CA30, post processing in sch ₂ O, 648 K, 25 min, 30 MPa, showing the macro-porous structure..... | 181 |
| Figure 49: SEM Micrographs of post processed PEEK 150CA30, 30 min, 623 K, 10 mg ml ⁻¹ Cs ₂ CO ₃ , a) [EtOH] = 20 %v, 16.7 MPa, b) [EtOH] = 100 %, 23.9 MPa..... | 181 |

| | |
|--|-----|
| Figure 50: Effect of caesium carbonate concentration [Cs_2CO_3] on the production of phenol [PhOH] by the decomposition of PEEK. 20 %v ethanol, 80 %v water, 30 min, 623.15 K, 16.8 ± 0.2 MPa. Determined by HPLC..... | 183 |
| Figure 51: FT-IR of PEEK 150CA30 post processing, 30 min, 623.15 K, 20 %v ethanol, 80 %v water, 16.8 ± 0.2 MPa, without Cs_2CO_3 ; Peak 1 = 1305 cm^{-1} , Peak 2 = 1280 cm^{-1} | 184 |
| Figure 52: FT-IR of PEEK 150CA30 post processing, 30 min, 623.15 K, 20 %v ethanol, 80 %v water, 16.8 ± 0.2 MPa, $10 \text{ mg ml}^{-1} \text{ Cs}_2\text{CO}_3$ | 184 |
| Figure 53: DSC thermogram for PEEK 150CA30 processed for 30 minutes using 20 %v ethanol, 80 %v water, 16.8 ± 0.2 MPa, 1 - $6 \text{ mg ml}^{-1} \text{ Cs}_2\text{CO}_3$ | 186 |
| Figure 54: Phenol concentration [PhOH] with respect to reaction time, 623.15 K, [EtOH] = 20 %v, [H_2O] = 80 %v, 16.8 ± 0.2 MPa, $10 \text{ mg ml}^{-1} \text{ Cs}_2\text{CO}_3$, 10 mg ml^{-1} PEEK. Determined by HPLC | 187 |
| Figure 55: Decomposition of PEEK150CA30 and separation of the carbon fibres with increasing reaction time. 20 %v ethanol, 80 %v water, 16.8 ± 0.2 MPa, 623.15 K, 10 mg ml^{-1} , a) 0 min, b) 30 min, c) 60 min, d) 120 min..... | 189 |
| Figure 56: Fibres reclaimed from PEEK150CA30 using 20 %v ethanol, 80 %v water, 16.8 ± 0.2 MPa, 623.15 K, 10 mg ml^{-1} , a) 0 min, b) 30 min, c) 60 min, d) 120 min | 190 |
| Figure 57: Energy Dispersive X-Ray Spectrometry of solids deposits using 20 %v ethanol, 80 %v water, 16.8 ± 0.2 MPa, 623.15 K, 10 mg ml^{-1} , a) 0 min, b) 60 min..... | 191 |
| Figure 58: Effect of reaction time on observed mass loss by Thermogravimetric Analysis. 623 K, $10 \text{ mg ml}^{-1} \text{ Cs}_2\text{CO}_3$, [EtOH] = 20 %v, [H_2O] = 80 %v..... | 193 |
| Figure 59: Differential Scanning Calorimetry of PEEK 150CA30 and processed samples, 0 - 120 min, 623 K, $10 \text{ mg ml}^{-1} \text{ Cs}_2\text{CO}_3$, [EtOH] = 20 %v, [H_2O] = 80 %v, 16.8 ± 0.2 MPa | 196 |

| | |
|---|-----|
| Figure 60: Main decomposition products from the decomposition of poly(oxy-1,4-phenyleneoxy-1,4-phenylenelecarbonyl-1,4-phenylene), solid arrows = major product formation, dashed arrows = minor product formation..... | 197 |
| Figure 61: Phenol concentration [PhOH] with respect to propanol concentration [PrOH], 623 K, $t_r = 30$ min, $10 \text{ mg ml}^{-1} \text{ Cs}_2\text{CO}_3$, $P = 15.8 - 20.5 \text{ MPa}$. Determined by HPLC..... | 199 |
| Figure 62: Pressure as a function of temperature for propanol and water co-solvent system, $T = 623 \text{ K}$, $[\text{Cs}_2\text{CO}_3] = 10 \text{ mg ml}^{-1}$, $t_r = 30$ min, solvent loading = 50 %v..... | 200 |
| Figure 63: Effect of caesium carbonate concentration $[\text{Cs}_2\text{CO}_3]$ on the production of phenol [PhOH] by the decomposition of PEEK. $[\text{PrOH}] = 20 \text{ %v}$, $[\text{H}_2\text{O}] = 80 \text{ %v}$, $t_r = 30$ min, 623.15 K , $16.4 \pm 0.4 \text{ MPa}$. Determined by HPLC..... | 202 |
| Figure 64: DSC thermograms for PEEK 150CA30 processed for 30 minutes using $[\text{PrOH}] = 20 \text{ %v}$, $[\text{H}_2\text{O}] = 80 \text{ %v}$, $16.4 \pm 0.4 \text{ MPa}$, $1 - 8 \text{ mg ml}^{-1} \text{ Cs}_2\text{CO}_3$ | 203 |
| Figure 65: Phenol concentration [PhOH] with respect to reaction time, 623 K , $[\text{PrOH}] = 20 \text{ %v}$, $[\text{H}_2\text{O}] = 80 \text{ %v}$, $16.4 \pm 0.2 \text{ MPa}$, $10 \text{ mg ml}^{-1} \text{ Cs}_2\text{CO}_3$, $10 \text{ mg ml}^{-1} \text{ PEEK}$. Determined by HPLC..... | 204 |
| Figure 66: Thermogravimetric analysis of recovered solids according to reaction time, $t_r = 0 - 120$ min, $[\text{PrOH}] = 20 \text{ %v}$, $[\text{H}_2\text{O}] = 80 \text{ %v}$, $[\text{Cs}_2\text{CO}_3] = 10 \text{ mg ml}^{-1}$, $T = 623 \text{ K}$, $P = 16.4 \pm 0.2 \text{ MPa}$ | 205 |
| Figure 67: Thermogravimetric analysis of recovered solids according to reaction time, showing rate of mass change (DTG) as observed by TGA, $t_r = 0 - 120$ min, $[\text{PrOH}] = 20 \text{ %v}$, $[\text{H}_2\text{O}] = 80 \text{ %v}$, $[\text{Cs}_2\text{CO}_3] = 10 \text{ mg ml}^{-1}$, $T = 623 \text{ K}$, $P = 16.4 \pm 0.2 \text{ MPa}$ | 206 |
| Figure 68: Phenol concentration [PhOH] as a function of acetone concentration [DMK], $t_r = 30$ min, $T = 623 \text{ K}$, $[\text{Cs}_2\text{CO}_3] = 10 \text{ mg ml}^{-1}$, $P = 15.7 - 16.2 \text{ MPa}$. Determined by HPLC..... | 208 |

| | |
|--|-----|
| Figure 69: Pressure as a function of temperature for acetone (DMK) and water co-solvent system, $T = 623 \text{ K}$, $[\text{Cs}_2\text{CO}_3] = 10 \text{ mg ml}^{-1}$, $t_r = 30 \text{ min}$, $[\text{DMK}] = 10 - 50 \text{ \%v}$, $[\text{H}_2\text{O}] = 90 - 50 \text{ \%v}$, solvent loading = 50 %v | 209 |
| Figure 70: Comparative study of phenol concentration $[\text{PhOH}]$ as a function of co-solvent concentration [co-solvent], $T = 623 \text{ K}$, $t_r = 30 \text{ min}$, solvent loading = 50 %v, $[\text{Cs}_2\text{CO}_3] = 10 \text{ mg ml}^{-1}$, $[\text{PEEK}] = 10 \text{ mg ml}^{-1}$, ethanol (EtOH), propanol (PrOH) and acetone (DMK)..... | 211 |
| Figure 71: Comparative study of phenol concentration $[\text{PhOH}]$ as a function of caesium carbonate concentration $[\text{Cs}_2\text{CO}_3]$, $T = 623 \text{ K}$, $t_r = 30 \text{ min}$, $[\text{PEEK}] = 10 \text{ mg ml}^{-1}$, ethanol (EtOH), propanol (PrOH) | 212 |
| Figure 72: Phenol concentration $[\text{PhOH}]$ as a function of reaction time for ethanol (EtOH) and propanol (PrOH) co-solvents, $T = 623 \text{ K}$, $[\text{Cs}_2\text{CO}_3] = 10 \text{ mg ml}^{-1}$ | 213 |
| Figure 73: Thermogravimetric analysis compilation of recovered solids showing mass loss and rate of mass change (DTG) observed by TGA, $T = 623 \text{ K}$, $[\text{Cs}_2\text{CO}_3] = 10 \text{ mg ml}^{-1}$, $t_r = 0 - 120 \text{ min}$, ethanol concentration $[\text{EtOH}] = 20 \text{ \%v}$, propanol concentration $[\text{PrOH}] = 20 \text{ \%v}$, $[\text{H}_2\text{O}] = 80 \text{ \%v}$ | 214 |
| Figure 74: Virgin BADGE / DDS epoxy resin showing a) within mould, b) after de-moulding | 217 |
| Figure 75: Effect of ethanol concentration $[\text{EtOH}]$, $t = 30 \text{ min}$, $T = 573 \text{ K}$, $[\text{Cs}_2\text{CO}_3] = 10 \text{ mg ml}^{-1}$, $[\text{Resin}] = 33.3 \text{ mg} \pm \text{ml}^{-1}$ | 218 |
| Figure 76: Production of phenol with respect to the ethanol concentration $[\text{EtOH}]$, $t = 30 \text{ min}$, $T = 573 \text{ K}$, $10 \text{ mg ml}^{-1} \text{ Cs}_2\text{CO}_3$, $[\text{Resin}] 33.3 \text{ mg} \pm \text{ml}^{-1}$ | 218 |
| Figure 77: Reactor internal pressure as a function of temperature for ethanol concentrations $[\text{EtOH}] = 0, 10, 20, 35, 50, 65, 80$ and 100 \%v ; $[\text{Cs}_2\text{CO}_3] = 10 \text{ mg ml}^{-1}$ | 219 |

Figure 78: Percentage mass loss with respect to the caesium carbonate concentration
 $[\text{Cs}_2\text{CO}_3]$, $T = 573 \text{ K}$, $t = 30 \text{ min}$, $[\text{Resin}] = 32 \pm 3 \text{ mg ml}^{-1}$, $P = 15.0 \pm 0.4 \text{ MPa}$, $R^2 = 0.995$221

Figure 79: Phenol concentration $[\text{PhOH}]$ with respect to caesium carbonate concentration
 $[\text{Cs}_2\text{CO}_3]$, $T = 573 \text{ K}$, $t = 30 \text{ min}$, $[\text{Resin}] = 32 \pm 3 \text{ mg ml}^{-1}$, $P = 15.0 \pm 0.4 \text{ MPa}$, $R^2 = 0.968$221

Figure 80: Percentage mass loss with respect to reaction time, $[\text{EtOH}] = 100 \%$, $T = 573 \text{ K}$,
 $[\text{Cs}_2\text{CO}_3] = 10 \text{ mg ml}^{-1}$, $[\text{Resin}] = 35 \pm 5 \text{ mg ml}^{-1}$, $P = 14.7 \pm 0.3 \text{ MPa}$, $R^2 = 0.990$223

Figure 81: Phenol concentration $[\text{PhOH}]$ with respect to reaction time, $[\text{EtOH}] = 100 \%$, $T =$
 576 K , $[\text{Cs}_2\text{CO}_3] = 10 \text{ mg ml}^{-1}$, $[\text{Resin}] = 35 \pm 5 \text{ mg ml}^{-1}$, $P = 14.7 \pm 0.3 \text{ MPa}$, $R^2 = 0.963$223

Figure 82: Reactor residual pressure at 313 K as a function of reaction time for $[\text{EtOH}] = 100$
 $\%$, $T = 576 \text{ K}$, $[\text{Cs}_2\text{CO}_3] = 10 \text{ mg ml}^{-1}$, $[\text{Resin}] = 35 \pm 5 \text{ mg ml}^{-1}$, $P = 14.7 \pm 0.3 \text{ MPa}$, $R^2 = 0.9661$
.....224

Figure 83: Production of phenol as a function of percentage mass loss of epoxy resin. $T = 573$
 K , $t = 0 - 60 \text{ min}$, $[\text{EtOH}] = 100 \%$, $[\text{Resin}] 32 \pm 3 \text{ mg ml}^{-1}$, $[\text{Cs}_2\text{CO}_3] = 10 \text{ mg ml}^{-1}$, $P = 15.1 \pm 0.4$
 MPa , $R^2 = 0.982$226

Figure 84: Percentage mass loss with respect to propanol concentration $[\text{PrOH}]$, $T = 573 \text{ K}$, t
 $= 30 \text{ min}$, $[\text{Cs}_2\text{CO}_3] = 10 \text{ mg ml}^{-1}$, $[\text{Resin}] = 33 \pm 3 \text{ mg ml}^{-1}$, $R^2 = 0.975$227

Figure 85: Phenol concentration $[\text{PhOH}]$ with respect to propanol concentration $[\text{PrOH}]$, $T =$
 573 K , $t = 30 \text{ min}$, $[\text{Cs}_2\text{CO}_3] = 10 \text{ mg ml}^{-1}$, $[\text{Resin}] = 33 \pm 3 \text{ mg ml}^{-1}$, $R^2 = 0.970$ 228

Figure 86: Reactor internal pressure as a function of temperature for varying propanol
concentrations $[\text{PrOH}]$ 229

Figure 87: Percentage mass with respect to caesium carbonate concentration $[\text{Cs}_2\text{CO}_3]$, $T =$
 573 K , $t = 30 \text{ min}$, $[\text{Resin}] = 32 \pm 3 \text{ mg ml}^{-1}$, $P = 12.4 \pm 0.4 \text{ MPa}$, $R^2 = 0.985$230

Figure 88: Phenol concentration $[\text{PhOH}]$ with respect to caesium carbonate concentration
 $[\text{Cs}_2\text{CO}_3]$, $T = 573 \text{ K}$, $t = 30 \text{ min}$, $[\text{Resin}] = 32 \pm 3 \text{ mg ml}^{-1}$, $P = 12.4 \pm 0.4 \text{ MPa}$, $R^2 = 0.974$231

Figure 89: Percentage decomposition with respect to reaction time, $T = 573 \text{ K}$, $[\text{PrOH}] = 100 \%$, $[\text{Cs}_2\text{CO}_3] = 10 \text{ mg ml}^{-1}$, $[\text{Resin}] = 35 \pm 5 \text{ mg ml}^{-1}$, $P = 12.2 \pm 0.5 \text{ MPa}$, $R^2 = 0.984$232

Figure 90: Phenol concentration $[\text{PhOH}]$ with respect to reaction time, $T = 573 \text{ K}$, $[\text{PrOH}] = 100 \%$, $[\text{Cs}_2\text{CO}_3] = 10 \text{ mg ml}^{-1}$, $[\text{Resin}] = 35 \pm 5 \text{ mg ml}^{-1}$, $P = 12.2 \pm 0.5 \text{ MPa}$, $R^2 = 0.990$233

Figure 91: Mass loss as a function of butanol concentration $[\text{BuOH}]$, $T = 573 \text{ K}$, $t_r = 30 \text{ min}$, $[\text{Cs}_2\text{CO}_3] = 10 \text{ mg ml}^{-1}$234

Figure 92: Reactor internal pressure as a function of temperature for $[\text{BuOH}] = 0 - 100 \%$, $t_r = 30 \text{ min}$, $[\text{Cs}_2\text{CO}_3] = 10 \text{ mg ml}^{-1}$235

Figure 93: Average phenol concentration $[\text{PhOH}]$ as a function of butanol concentration $[\text{BuOH}]$, $T = 573 \text{ K}$, $t_r = 30 \text{ min}$, $[\text{Cs}_2\text{CO}_3] = 10 \text{ mg ml}^{-1}$ 236

Figure 94: Evolution of phenol with respect to % mass loss as a function of reaction time, $[\text{Resin}] = 35 \text{ mg ml}^{-1}$, $[\text{Cs}_2\text{CO}_3] = 10 \text{ mg ml}^{-1}$, $T = 573 \text{ K}$; a.) $[\text{EtOH}] = 100 \%$, $P_{\text{EtOH}} = 15.1 \pm 0.7 \text{ MPa}$; b.) $[\text{PrOH}] = 100\%$, $P_{\text{PrOH}} = 12.1 \pm 1.0 \text{ MPa}$ 239

Figure 95: Comparison of phenol concentration $[\text{PhOH}]$ with respect to percentage mass loss, $[\text{EtOH}] = 100 \%$, $[\text{PrOH}] = 100 \%$. $T = 573 \text{ K}$, $t = 0 - 60 \text{ min}$, $[\text{Cs}_2\text{CO}_3] = 0 - 10 \text{ mg ml}^{-1}$, $[\text{Resin}] = 35 \pm 5 \text{ mg ml}^{-1}$, $P_{\text{EtOH}} = 15.1 \pm 0.7 \text{ MPa}$, $P_{\text{PrOH}} = 12.1 \pm 1.0 \text{ MPa}$, $E_x = \text{time (min) in EtOH}$, $P_x = \text{time (min) in PrOH}$ 240

Figure 96: Comparison of percentage mass loss with respect to reaction time, $[\text{EtOH}] = 100 \%$ and $[\text{PrOH}] = 100 \%$. $T = 573 \text{ K}$, $[\text{Cs}_2\text{CO}_3] = 10 \text{ mg ml}^{-1}$, $[\text{Resin}] = 35 \pm 5 \text{ mg ml}^{-1}$, $P_{\text{EtOH}} = 15.1 \pm 0.7 \text{ MPa}$, $P_{\text{PrOH}} = 12.1 \pm 1.0 \text{ MPa}$241

Figure 97: GC-MS Chromatogram comparison of decomposition products. $T = 573 \text{ K}$, $t = 30 \text{ min}$, $[\text{Cs}_2\text{CO}_3] = 10 \text{ mg ml}^{-1}$; a.) $[\text{EtOH}] = 100 \%$, b.) $[\text{PrOH}] = 100 \%$. A = phenol, B = 4-(1-methylethyl)-phenol, C = p-isopropenylphenol, D = 2-(1-methylethyl)-phenol, E = 3-(1-methylethyl)-phenol.242

Figure 98: SEM Micrographs of virgin samples of cured epoxy resin showing; a.) top surface, Mag = 250x, WD = 10.2; b.) cross-section, Mag = 2500x, WD= 10.1.....244

Figure 99: SEM micrographs for decomposition in scEtOH as a function of reaction time. [EtOH] = 100 %, [Cs₂CO₃] = 10 mg ml⁻¹, T = 573 K; a.) t = 0 min, Mag = 85x, WD = 10.1; b.) t = 0 min, Mag 650x, WD = 10.1; c.) t = 10 min, Mag = 120x, WD 9.0; d.) t = 10 min, Mag 200x, WD = 9.0.....245

Figure 100: SEM micrographs for decomposition in scEtOH as a function of reaction time. [EtOH] = 100 %, [Cs₂CO₃] = 10 mg ml⁻¹, T = 573 K; a.) t = 30 min, Mag = 350x, WD = 9.0; b.) t = 30 min, Mag 250x, WD = 9.0; c.) t = 45 min, Mag = 90x, WD 9.0; d.) t = 45 min, Mag 350x, WD = 10.....246

Figure 101: SEM micrographs for decomposition in scPrOH as a function of reaction time. [PrOH] = 100 %, [Cs₂CO₃] = 10 mg ml⁻¹, T = 573 K; a.) t = 0 min, Mag = 80x, WD = 10.0; b.) t = 0 min, Mag 3500x, WD = 9.6; c.) t = 10 min, Mag = 200x, WD 8.1; d.) t = 10 min, Mag 250x, WD = 8.1.....249

Figure 102: EDX Analysis of solid deposits on the surface of epoxy resin post-processing..250

Figure 103: SEM micrographs for decomposition in scPrOH as a function of reaction time. [PrOH] = 100 %, [Cs₂CO₃] = 10 mg ml⁻¹, T = 573 K; a.) t = 30 min, Mag = 250x, WD = 8.4; b.) t = 30 min, Mag 800x, WD = 8.4; c.) t = 45 min, Mag = 85x, WD 10.2; d.) t = 45 min, Mag 500x, WD = 10.2.....251

Figure 104: SEM micrographs of swelling derived fissure evolution. [PrOH] = 100 %, [Cs₂CO₃] = 10 mg ml⁻¹, T = 573 K; a.) t = 0 min, Mag = 12,000x, WD = 9.6; b.) t = 10 min, Mag 2,000x, WD = 8.1; c.) t = 30 min, Mag = 3,500x, WD 8.4; d.) t = 45 min, Mag 2,000x, WD = 10.4.....253

| | |
|---|-----|
| Figure 105: Comparison between tensile strength of single fibres and the mean fibre within a bundle; T = 623 K, t_r = 30 min, [EtOH] = 80 %v, # Single fibre test = 40, # Fibre bundle test = 5 x 300..... | 257 |
| Figure 106: Effect of ethanol concentration [EtOH] on the mean tensile strength of carbon fibre (Toray T700S 50E); T = 623 K, t_r = 30 min..... | 259 |
| Figure 107: Effect of propanol concentration [PrOH] on the mean tensile strength of carbon fibre (Toray T700S 50E); T = 623 K, t_r = 30 min..... | 259 |
| Figure 108: Effect of acetone concentration [DMK] on the mean tensile strength of carbon fibre (Toray T700S 50E); T = 623 K, t_r = 30 min..... | 260 |
| Figure 109: Effect of Cs_2CO_3 catalyst on the tensile strength of carbon fibres. T = 623 K, t_r = 30 min; FL1: H_2O ; FL2 H_2O , $[\text{Cs}_2\text{CO}_3] = 10 \text{ mg ml}^{-1}$; FL3: [EtOH] = 80 %v; FL4: [EtOH] = 80 %v, $[\text{Cs}_2\text{CO}_3] = 10 \text{ mg ml}^{-1}$ | 261 |
| Figure 110: High-resolution XPS carbon spectrum of virgin carbon fibre, Toray T700S..... | 263 |
| Figure 111: High-resolution XPS oxygen spectrum of virgin carbon fibre, Toray T700S..... | 263 |
| Figure 112: High-resolution XPS nitrogen spectrum of virgin carbon fibre, Toray T700S..... | 264 |
| Figure 113: High-resolution XPS silicon spectrum of virgin carbon fibre, Toray T700S..... | 264 |
| Figure 114: Functional group distribution on the surface of virgin carbon fibre, determined by XPS..... | 266 |
| Figure 115: Functional group distribution on the surface of processed carbon fibres; T = 523 K, t_r = 30 min, [EtOH] = 80 %v, determined by XPS..... | 267 |
| Figure 116: Relative abundance of carbonyl functional groups post-processing, determined by XPS; PS1, T = 523 K; PS2, PS3, PS4, T = 573 K; PS5, T = 623 K..... | 268 |

Figure 117: TGA thermograph of Hexcel CFRP's used in the manufacture of wing spas, post processing (Sample CS3); $T = 573 \text{ K}$, $P = 15 \pm 0.2 \text{ MPa}$, $t_r = 60 \text{ min}$, $[\text{EtOH}] = 100 \%$, $[\text{Cs}_2\text{CO}_3] = 10 \text{ mg ml}^{-1}$, $[\text{comp}] = 67.5 \text{ mg ml}^{-1}$ 272

Figure 118: SEM micrographs of CFRP post processing (CS3); $T = 573 \text{ K}$, $t_r = 60 \text{ min}$, $P = 15.0 \pm 0.2 \text{ MPa}$, $[\text{EtOH}] = 100 \%$, $[\text{Cs}_2\text{CO}_3] = 10 \text{ mg ml}^{-1}$, $[\text{comp}] = 67.5 \text{ mg ml}^{-1}$ 273

LIST OF TABLES

| | |
|--|-----|
| Table 1: Designed experiment (DOE) for the investigation of scCO ₂ induced crystallisation of PEEK, LTR..... | 85 |
| Table 2: CO ₂ Containment experiment conditions, T = 413 K, P = 20.0 MPa, LTR | 88 |
| Table 3: Reaction schedule for the investigation of ethanol concentration [EtOH] on the decomposition of PEEK in H ₂ O / EtOH, [Cs ₂ CO ₃] = 10 mg ml ⁻¹ | 91 |
| Table 4: Reaction schedule for the investigation of caesium carbonate concentration [Cs ₂ CO ₃] on the decomposition of PEEK in H ₂ O / EtOH | 91 |
| Table 5: Reaction schedule for the investigation of effects of reaction time on the decomposition of PEEK in H ₂ O / EtOH | 92 |
| Table 6: Reaction schedule for the investigation of propanol concentration [PrOH] on the decomposition of PEEK in H ₂ O / PrOH, [Cs ₂ CO ₃] = 10 mg ml ⁻¹ | 93 |
| Table 7: Reaction schedule for the investigation of caesium carbonate concentration [Cs ₂ CO ₃] on the decomposition of PEEK in H ₂ O / PrOH..... | 93 |
| Table 8: Reaction schedule for the investigation of effects of reaction time on the decomposition of PEEK in H ₂ O / PrOH..... | 94 |
| Table 9: Reaction schedule for the investigation of acetone concentration [DMK] on the decomposition of PEEK | 94 |
| Table 10: Processing condition for determination of the effect of co-solvent concentration on BADGE based resin..... | 100 |
| Table 11: Processing conditions for the determination of the effects of Cs ₂ CO ₃ on BADGE based resin | 101 |
| Table 12: Processing conditions for the determination of the effects of reaction time on BADGE based resin..... | 102 |

| | |
|---|-----|
| Table 13: Reaction schedule for the investigation of carbon chain-length on the decomposition of thermoset epoxy resin..... | 103 |
| Table 14: Carbon fibre processing control sample generation | 105 |
| Table 15: Reaction schedule for the investigation of the effect of co-solvent [Co-solvent] concentration on the tensile strength of carbon fibres. $[Cs_2CO_3] = 0 \text{ mg ml}^{-1}$ | 106 |
| Table 16: Specific investigation of effects of $[Cs_2CO_3]$ in conjunction with co-solvents on the physical properties of carbon fibres | 107 |
| Table 17: Reaction schedule for initial investigation into the decomposition of commercially available carbon fibre reinforced polymers..... | 109 |
| Table 18: HPLC mobile phase compositions for the quantitative analysis of polymer decomposition products | 128 |
| Table 19: HPLC Standard concentrations used to prepare the required calibration curve .. | 130 |
| Table 20: Impedance as a function of frequency for a single carbon fibre 85 mm in length | 138 |
| Table 21: Comparison between carbon fibre diameter as calculated by EIM and measured by SEM for multiple carbon fibres | 140 |
| Table 22: Limit of Detection (LOD) for determination of number of fibres in a bundle by EIM | 148 |
| Table 23: EDX Analysis of solid deposits after 0 and 60 minute reactions (conditions as in figure 57)..... | 192 |
| Table 24: Phenol concentration [PhOH] in organic and aqueous fractions, produced by the decomposition of epoxy resin. $T = 573 \text{ K}$, $t_r = 30 \text{ min}$, $[Cs_2CO_3] = 10 \text{ mg ml}^{-1}$ | 237 |
| Table 25: XPS binding energy of specific functional groups | 265 |
| Table 26: Initial findings for the recycling of commercially available CFRP's..... | 271 |

LIST OF ABBREVIATIONS

| | |
|-----------------------|--|
| <i>AFP</i> | Automated Fibre Placement |
| <i>ATR</i> | Attenuated Total Reflectance |
| <i>ATL</i> | Automated Tape Laying |
| <i>BADGE</i> | 2,2-Bis[4-(glycidyloxy)phenyl]propane (also DER 332) |
| <i>BE</i> | Binding Energy |
| <i>BPA</i> | Bisphenol A |
| <i>CFRP</i> | Carbon Fibre Reinforced Polymer |
| <i>CM</i> | Compression Moulding |
| <i>CO₂</i> | Carbon dioxide |
| <i>DDS</i> | 4,4'-diaminodiphenyl sulfone |
| <i>DMK</i> | Dimethyl Ketone (Acetone) |
| <i>DOE</i> | Design of Experiments |
| <i>DP</i> | Dipole moment |
| <i>DTG</i> | Rate of percentage mass loss |
| <i>DSC</i> | Differential Scanning Calorimetry |
| <i>EC</i> | Equivalent Circuit (for use by EIS and EIM) |
| <i>EDX</i> | Energy Dispersive X-Ray Spectrometry |
| <i>EIM</i> | Electrical Impedance Measurement |
| <i>EIS</i> | Electrochemical Impedance Measurement |
| <i>EOL</i> | End-of-life material |
| <i>EtOH</i> | Ethanol |
| <i>eV</i> | Electron Volt |
| <i>EXHUME</i> | Efficient X-sector use of Heterogeneous Materials in Manufacturing |
| <i>FT-IR</i> | Fourier Transform Infra-Red Spectrometry |
| <i>FW</i> | Filament Winding |
| <i>GC</i> | Gas Chromatography |
| <i>GC-MS</i> | Gas Chromatography – Mass Spectrometry |
| <i>GFRP</i> | Glass Fibre Reinforced Polymer |

| | |
|-------------------------|--|
| <i>GRAS</i> | Generally Recognised as Safe |
| <i>HPLC</i> | High-Performance Liquid Chromatography |
| <i>HTL</i> | Heated Transfer Line for use in TGA-FTIR |
| <i>HTR</i> | High Temperature Reactor |
| <i>Lag Time</i> | Time between reaction cessation and analysis |
| <i>LCA</i> | Life Cycle Analysis |
| <i>LOD</i> | Limit of Detection |
| <i>LTR</i> | Low Temperature Reactor |
| <i>PAN</i> | Poly(acrylonitrile) |
| <i>PCB</i> | Printed Circuit Board |
| <i>PDI</i> | Polydispersity Index |
| <i>PEEK</i> | poly(oxy-1,4-phenyleneoxy-1,4-phenylenelecarbonyl-1,4-phenylene) |
| <i>PrOH</i> | Propanol |
| <i>PVA</i> | Poly(ethanol) also called polyvinyl alcohol |
| <i>RIM</i> | Resin Infusion Moulding |
| <i>RTM</i> | Resin Transfer Moulding |
| <i>SEM</i> | Scanning Electron Microscopy |
| <i>SMC</i> | Sheet Moulding Compound |
| <i>scCO₂</i> | Supercritical carbon dioxide |
| <i>scH₂O</i> | Supercritical water |
| <i>Soak Time</i> | Time subjected to scCO ₂ |
| <i>TGA</i> | Thermogravimetric Analysis |
| <i>UTM</i> | Universal Testing Machine |
| <i>UV</i> | Ultra-Violet |
| <i>VARIM</i> | Vacuum Assisted Resin Infusion Moulding |
| <i>VARTM</i> | Vacuum Assisted Resin Transfer Moulding |
| <i>WAXS</i> | Wide Angle X-Ray Spectrometry |
| <i>XPS</i> | X-Ray Photoelectron Spectroscopy |

NOMENCLATURE

| | |
|----------------|---|
| A | Cross-sectional area (m^2) |
| A_C | Integral of crystallisation exotherm (mJ) |
| AC | Alternating current (V) |
| A_M | Integral of melting endotherm (mJ) |
| A_S | Cross-sectional area of a single carbon fibre (m^2) |
| A_T | Total cross-sectional area of a bundle of carbon fibres (m^2) |
| $[co-solvent]$ | Concentration of co-solvent (%v) |
| $[comp]$ | Concentration of composite ($mg\ ml^{-1}$) |
| $[Cs_2CO_3]$ | Concentration of caesium carbonate ($mg\ ml^{-1}$) |
| DC | Direct current (V) |
| EEW | Epoxide equivalent number |
| %dg | Percentage decomposition |
| F_{MAX} | Maximum tensile force applied to carbon fibres |
| Gy | Gray, unit of radiation received, equal to Sievert ($J\ kg^{-1}$) |
| H_{PA} | Height of peak 'A' |
| H_{PB} | Height of peak 'B' |
| I | Current (A) |
| K | Kelvin |
| L | Length of carbon fibre (m) |
| M_{Ef} | Final mass of epoxy resin (g) |
| M_{Ei} | Initial mass of epoxy resin (g) |
| M_N | Number average molecular mass ($g\ mol^{-1}$) |
| M_r | Relative molecular mass ($g\ mol^{-1}$) |
| M_W | Weight average molecular mass ($g\ mol^{-1}$) |
| M_X | Mass of substance 'X' (g) |
| P | Pressure (MPa) |
| ϕ | Phase angle between voltage and current ($^{\circ}$) |
| Q | Flow rate ($ml\ min^{-1}$) |

| | |
|----------------|---|
| R | Resistance (Ω) |
| ρ | Resistivity ($\Omega \text{ m}$) |
| $[R-OH]$ | Concentration of alcohol (%v) |
| $[Resin]$ | Concentration of epoxy resin (mg ml^{-1}) |
| $\bar{\sigma}$ | Mean tensile force per fibre (mN) |
| S | Conductivity (S) |
| T | Temperature (K) |
| t_r | Reaction time (min) |
| T_c | Crystallisation temperature (K) |
| T_{COL} | Column temperature |
| T_g | Glass transition temperature (K) |
| T_m | Melt temperature (K) |
| V | Amplitude of potential difference (V) |
| V_{INJ} | Injection volume (μl) |
| $\%X_C$ | Percentage crystallisation |
| Z' | Real impedance (Ω) |
| Z'' | Complex impedance (Ω) |
| Z_S | Impedance of a single fibre (Ω) |
| Z_T | Total impedance of a bundle of carbon fibres (Ω) |

CHAPTER 1. INTRODUCTION

Presented in this thesis are the findings of the fundamental research into the use of supercritical fluids in the recycling of high-performance carbon fibre reinforced thermoplastic and thermoset polymers. These materials exhibit exceptional physical properties and are increasingly used in aerospace and related industries in an attempt to reduce mass whilst retaining structural integrity. This research was conducted as part of the EPSRC funded Efficient X-sector use of Heterogeneous Materials in Manufacturing (EXHUME) project, a consortium comprising of University of Birmingham, University of Exeter, University of Manchester and Cranfield University. The EXHUME project considers the recycling of a wide range of composite materials, with partner institutions undertaking research areas towards a common objective. This research project is focused on the high-value, high-performance composites and has the following objective;

- To establish the conditions necessary to decompose and recycle carbon fibre reinforced polymers (CFRP's) in an environmentally sustainable and economic manner, whilst minimising the degradation of the physical properties of carbon fibres and extracting useful organic molecules from the degraded resins.

Ambitious in its approach, this objective is necessary given that the current disposal route of CFRP's is landfill, with no industrial recycling processes existing to date, and the manufacturing and use of CFRP's is ever increasing.

To address this objective, this thesis is structured in the following way.

Chapter 2 – Literature Review

This chapter provides a review of the recent literature pertaining to the manufacture, use and disposal of high-performance polymers and their composite materials. Owing to the advanced nature of this research literature sources are at times limited, especially prevalent where the topic is the subject of this research thesis.

Chapter 3 – Experimental Methodology

The preparation of thermoset polymers, reaction conditions and quality assurance methods are presented in this chapter. Many experimental techniques were used during this research, for which the experimental setup and analysis methods are also presented in this chapter.

Chapter 4 – Results Part A: Processing and Recycling of Polyetheretherketone

An investigation into the effects of supercritical fluids on PEEK is presented in this chapter, along with the results of the decomposition reactions carried out.

Chapter 5 – Results Part B: Decomposition and Recycling of Polyepoxide Thermoset Resins

The thermoset resin, prepared as part of this research, is subjected to a range of supercritical fluids. The results of the decomposition reactions are presented in this chapter.

Chapter 6 – Results Part C: Characterisation and Recycling of Carbon Fibre

Tensile testing is used in order to establish the effect of supercritical fluid processing on the physical properties of carbon fibres. Surface analysis is used to investigate whether supercritical fluid processing leads to removal of functional groups on the surface of carbon fibres, used to increase adhesion between the fibres and polymer matrix in CFRP's. The results of both investigations are provided in this chapter.

Chapter 7 – Results Part D: Recycling of Carbon Fibre Reinforced Composite Materials

The reaction conditions developed through Chapters 4 – 6 applied to a limited set of commercially available CFRP's is presented in this chapter, as well as an indication of the potential future direction of this research.

Chapter 8 – Conclusions

An overview of the main findings of this research is presented, highlighting the specific achievements of this research as well as specifying objectives that may be the subject of future research in this theme.

Significant portions of this research are published in peer-reviewed journals, notably Chapters 2, 4, 5 and 6. In addition, a methodology developed as part of this research has been presented at an international conference. A list of the peer-reviewed publications is provided prior to the contents page of this research thesis.

CHAPTER 2. LITERATURE REVIEW

This literature review will cover five principle areas of research; supercritical fluids and their application in a research context, high-performance thermoplastic polymers, high-performance thermoset polymers, carbon fibre properties and carbon fibre reinforced composite materials. A broad range of applications of high-performance polymers and composites will be presented in order to provide the context required.

2.1. SUPERCRITICAL FLUIDS

The physical properties of solvents and solutes are governed, in part, by their state and as such their ability to be applied in varying circumstances is also heavily dependent upon their state. The vast majority of elements and compounds exhibit solid, liquid and gaseous states according to their pressure and temperature. It is well known that under atmospheric pressure, 101.325 kPa, water exhibits the solid phase at 273 K, the liquid phase between 273 K – 373 K and the gaseous, or vapour, phase at temperatures above 373 K. Water may exhibit three states, solid, liquid and vapour, in equilibrium at its triple point of 273 K and 611.73 Pa [1] shown in Figure 1.

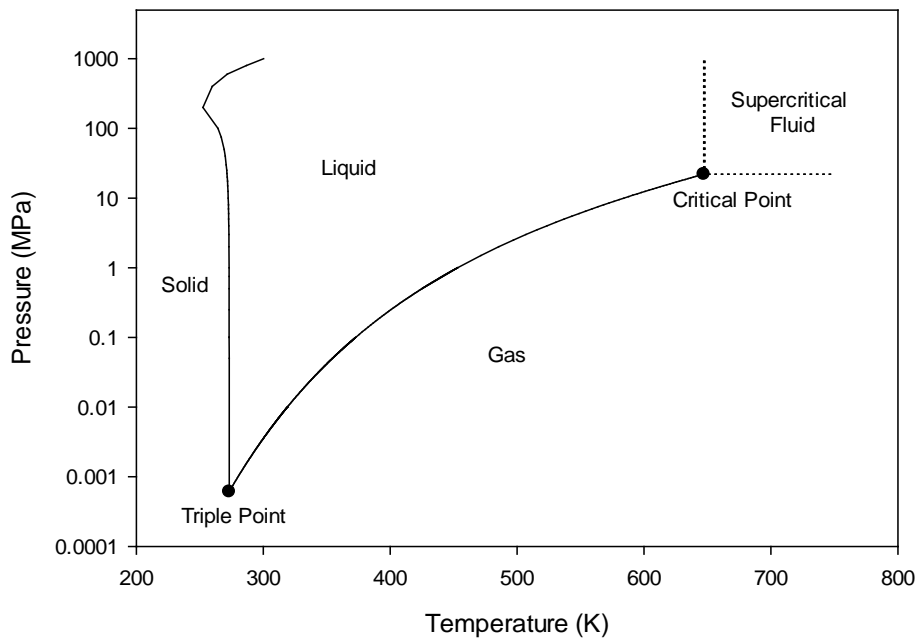


Figure 1: Phase diagram for water, showing the triple and critical points, equilibrium data obtained from National Institute of Standards and Technology (NIST) and [1]. Solid lines represent phase transitions

Manipulation of the state of water may be performed by pressure variation, allowing water to occupy either the solid, liquid or vapour phase both above and below the atmospheric boiling point. By increasing the pressure of water vapour it is possible to induce condensation and create the liquid phase, with additional application of pressure introducing the solid phase. Manipulation of the state of water is possible until the critical point of 647 K and 22.1 MPa [2] is attained, at which point the density of the liquid and vapour are identical, being 322 kg m^{-3} [1, 3]. Above the critical point no phase boundary exists between liquid and vapour and it is not possible to create a liquid phase irrespective of the pressure applied. Under such conditions water exists in a fourth state, known as the supercritical state, and exhibits gas-like and liquid-like properties simultaneously, as well as displaying a significant deviation from the properties often associated with water. The density of liquid water is $1,000 \text{ kg m}^{-3}$ at 277 K under atmospheric pressure and reduces

with increasing temperature until reaching the critical density of 322 kg m^{-3} , by comparison the density of gaseous water is 1 kg m^{-3} [4]. Supercritical water has a range of densities ($100 - 800 \text{ kg m}^{-3}$), viscosities ($0.05 - 0.1 \text{ } \mu\text{Pa s}$) and diffusivities ($0.01 - 0.1 \text{ mm}^2 \text{ s}^{-1}$), in each case the supercritical fluid values being between the values obtained for liquid and gaseous water [1, 3, 4]. These properties are tuneable by variation of the system pressure, an effect that is not exclusive to water and is the case for all supercritical fluids. All substances have a critical point, beyond which they exist only in the supercritical state and it is the control over properties in this state that allows supercritical fluids to be employed in a vast range of industrial and research fields. The critical points of different substances can vary greatly, for example; ethanol (EtOH) 516 K, 6.38 MPa [5], 2-propanol (PrOH) 508 K, 4.76 MPa [6], 1-butanol (BuOH) 560 K, 4.9 MPa [7] and carbon dioxide (CO_2) 304 K, 7.38 MPa [8], all have critical points significantly lower than that of water.

The relatively low critical temperature and pressure of CO_2 means that supercritical CO_2 (sc CO_2) finds application in a wide variety of processes such as polymer synthesis [9], polymer processing [10], drying [11-15] and extraction [16-20]. Research into polymer synthesis using CO_2 is active, owing to the environmental benefits associated with the use of CO_2 as opposed to organic solvents. A challenge to the routine polymer synthesis in CO_2 is the weak nature of CO_2 as a solvent, leading to low polymer solubility, although CO_2 compatible surfactants have been developed and are presented in the literature [21, 22]. For a range of polymer processing applications, such as manipulation of polymer transition temperatures [23] and the production of polymer foams [24, 25], sc CO_2 has been an ideal solvent due to the ease of separation post processing. Under atmospheric pressure and

ambient temperature CO₂ exists exclusively in the gaseous phase and consequently many polymer processes employing CO₂ simply vent to atmospheric conditions, liberating CO₂ as a gas. This is particularly useful for biomedical and food contact applications since it negates toxicological concerns associated with organic solvents, has a particularly high removal rate and residual CO₂ often poses very little risk. The effects of scCO₂ on high-performance thermoplastic polymers has also been an area of much interest [26, 27], owing largely to the environmental benefits of avoiding organic solvents.

2.2. HIGH-PERFORMANCE THERMOPLASTIC POLYMERS

Manufactured by Victrex[®], poly(ether ether ketone), (PEEK) is a poly(aryl ether ether ketone) and part of a class of high performance thermoplastic polymers, employed in a wide variety of demanding applications [28]. Other high-performance polymers of the same class include poly(ether ketone) (PEK) [29], poly(ether ketone ketone) (PEKK) [30], poly(ether ether ketone ketone) (PEEKK) [31] and poly(ether ketone ether ketone ketone) (PEKEKK) [32]. The physical properties of PEEK are discussed in detail in Chapter 3.1. This section focusses on the application of PEEK, its composites and derivatives, since PEEK is one subject of this research project.

Due to its chemical stability, biocompatibility and radiolucent properties, PEEK is increasingly used in orthopaedic surgery, finding particular application in spinal implant surgery since it has an elastic modulus similar to that of human bone [33-37]. Carbon fibre composites of PEEK are also biocompatible and, due to their enhanced wear resistance, may find application as components in femoral surgery [38]. It is essential to sterilise materials

prior to insertion in the human body to prevent infection and disease, a process that is usually carried out using steam treatment or gamma irradiation. Research has shown that the use of either sterilisation technique does not significantly alter the physical properties of PEEK, however, small changes at the polymer / carbon fibre interface are identified, most notably observed when steam sterilisation is used [39]. Although the physical properties of PEEK are conducive to use in the subcutaneous environment, research is underway into increasing the bioactivity thereby minimising the interfacial resistance between the surgical implant and the surrounding environment [40, 41]. Exploration into the range of applications of PEEK within the medical profession is ongoing, with research increasingly including the use of PEEK composite materials [28, 42-44]. Thermally sprayed PEEK may be used to create a polymeric coating, exhibiting substantial wear properties whilst maintaining the chemical and thermal properties associated with PEEK [45]. PEEK and PEEK composite coatings may also be produced using a printing process, with the coating demonstrating similar characteristics to thermally sprayed PEEK [46, 47].

Aside from the medical profession, PEEK is applied in the aerospace industry due to its relatively high glass transition temperature, high continuous use temperature, chemical resistance, tensile performance and low density [48]. These properties make PEEK an ideal material for components that are going to be in contact with, or immersed in, organic solvents such as fuels and lubricants [49]. Having a bulk density of $1,300 \text{ kg m}^{-3}$ (manufacturer's data), PEEK offers an opportunity to reduce the weight of a component when used in place of a conventional metal. Structural reinforcement of PEEK for industrial use is possible using carbon or Kevlar fibres, with increases in tribological performance

reported when composites incorporate fibres or silicon carbide (SiC) [47]. PEEK composites using modified nano-silica particles have been produced and show an increase in tensile strength of up to 50 % [50]. PEEK is effectively an electrical insulator and has a conductivity on the order of 10^{-14} S cm⁻¹ [51], and may therefore be alloyed and used to construct cable housing [52], maintaining much of the excellent mass characteristics associated with PEEK [53]. Efforts have been made to produce electrically conductive PEEK composites by using carbon nanotubes (CNT's) with varying levels of success [54]. Whilst in some cases the composite materials do show conductivity far greater than what is observed with PEEK alone, the conductivity is exclusively through connection of CNT's with the conductivity of the polymer remaining unchanged [55]. This is in contrast to the production of conducting polymers [56], which may in the future be used to create electrically conductive composite materials [57, 58]. The excellent physical properties described for PEEK naturally lend themselves to the automotive industry, for many of the same reasons as the aerospace industry [49].

Exploration is also ongoing into the development of functionalised PEEK and PEEK derivatives. These materials differ from the PEEK composite materials discussed, since they involve modification of the polymer's chemical structure, as opposed to the incorporation of reinforcing materials within the polymer matrix. In the case of composite materials, the polymeric transitions associated with PEEK remain largely unperturbed with enhancements to the physical properties being attributed to physical bonding between the polymer and reinforcement. Functionalised PEEK may behave very differently to PEEK, displaying very different polymeric transitions. The nitration of PEEK's phenyl rings produces PEEK-NO₂

which is soluble in dimethylformamide (DMF) as is the hydrated form PEEK-NH₂ [59, 60]. However, PEEK-NO₂ and PEEK-NH₂ have thermal stabilities of 623 K and 373 K, respectively [59]. Functionalisation of the ketone is also possible, an example is the production of PEEK-OH which may show a thermal stability similar to PEEK [59, 61]. However, it has also been demonstrated that the degree of hydroxylation of the carbonyl functional group is proportional to the exposure time, and further that higher degrees of hydroxylation leads to a decrease in the thermal stability [62]. Another approach to the functionalisation of PEEK is the production of co-polymers, incorporating the desired functional groups into the co-polymer and subsequently carrying out the polymerisation. Much research into the use of poly(ether sulfone) and poly(imide) has been conducted with the results often presenting a compromise between added functionality and the desired physical properties of PEEK [63-65]. Sulfonated PEEK (SPEEK) has been developed for specific challenges such as high performance membranes designed for hydrogen fuel cells (Proton Exchange Membranes) [66-68]. Significant improvements to the proton conductivity of SPEEK-PEM's is possible through doping, where samples doped with phosphotungstic acid show increases of up to 90 % when operating at 373 K [69]. The thermal stability of SPEEK is compromised compared to PEEK, typically being stable up to 523 K [66]. Control over the compromise of the polymer performance may be achieved by controlling the polymer composition, a parameter that is more easily defined for block co-polymers. An example of which is the 1,1-bi(4-hydroxyphenyl)-1-phenylethane / PEEK co-polymer and the 4,4'-difluorobenzophenone / PEEK co-polymer. In both cases increasing the proportion of the co-polymer increases the polymer's solubility in common solvents such as tetrahydrofuran (THF), chloroform (TCM), dichloromethane (DCM) and dimethyl sulfoxide (DMSO) [70]. The increased proportion of co-polymer also had the effect of removing the ability of the polymer to form

thermodynamically favourable alignment of the molecular chains, forming crystallites, and therefore the polymers produced are amorphous. The formation of crystallites, and therefore a semi-crystalline material, is extremely important for PEEK and has been studied extensively in the literature [71-75].

There is a dependence of PEEK's physical properties on the molecular weight, such as the increase in shear viscosity with increasing molecular weight [76]. However, manipulation of certain physical properties of polymers is possible, to some extent, without altering the chemical structure of the polymer, blending, creating co-polymers or composites [77]. This is done through polymer processing, during which only physical changes to the material take place post-polymerisation. The solubility of $scCO_2$ in polymers, both biodegradable and high-performance, has been an area of active research [27, 78]. Many industrially produced polymeric materials are low density foams. Research interests have often been centred around using $scCO_2$ to foam biodegradable polymers such as polycaprolactone (PCL) and polylacticacid (PLA) [79-82]. The targeting of specific applications such as regenerative bone support structures using PLA foamed with $scCO_2$ has also been explored [83]. The diffusion of $scCO_2$ into functionalised PEEK has been studied in the literature [26], this research has investigated the effects of supercritical fluids, including $scCO_2$, on the physical properties of un-modified PEEK. The processing parameters, such as temperature, CO_2 pressure, processing time and cooling rate are important when processing PEEK. Although the crystallisation of PEEK is rapid, a strong dependence upon the cooling rate exists [84]. The crystallisation of PEEK readily takes place upon reaching the thermodynamic crystallisation temperature of approximately 449 K, although it can be shown that there is an effect of the

sample's thermal history [85]. By using scCO₂, plasticisation of the polymer takes place by increasing the free volume between the molecular chains and facilitates crystallisation below the thermodynamic crystallisation temperature [23, 86]. Ordinarily, methyl substituted PEEK (MePEEK) does not crystallise, possibly as a consequence of the reduction in packing efficiency introduced by the methyl group. However, when processed with scCO₂ crystallisation is induced through a process of annealing leading to the formation of a semi-crystalline polymer [87]. Similar results are reported for tertiary-butyl substituted PEEK (t-b-PEEK) where it is apparent that greater CO₂ pressures are required to induce the crystallisation, potentially due to the increased size of the functional group in comparison to MePEEK [88]. Similarly to the polymeric foams created with PCL and PLA, efforts have been made to foam PEEK using scCO₂. Nanocellular foams have been reported for blends of PEEK and polyetherimide (PEI), however, it is notable that the foaming is constrained to the PEI within the blend and is not observed for PEEK [89].

The polymer processing conditions are important for controlling the final properties of the polymer, as stated previously. The processing conditions, in the extreme sense, may lead to degradation of the polymer matrix and thereby alter the polymer's chemical structure. An example of this is where flame spraying is used to create a PEEK coating. The temperatures required to sufficiently reduce the viscosity of the melt phase causes a reaction between the acetylene and PEEK, saturating the carbon atoms within the phenyl ring [90]. The radiation resistance of PEEK has been investigated, results showing that PEEK retains up to 60 % of its elongation at break with γ -ray doses up to 1 MGy [91]. It has been shown that PEEK's thermal history may influence the physical properties post processing, for example exposure

to water can destroy small crystallites which otherwise may have acted as nucleation sites for spherulitic growth [92]. Polymers age when in use, and may also age during storage depending on the polymer and its environment, and as such the polymer ageing process has been widely studied in the literature [93-96]. Ageing degrades the physical properties of polymers, as is the case for many materials, and PEEK is not an exception to this. However, since the ageing is a time dependent process, the degradation of physical properties is also a function of time. Consequently, in the literature the importance of both crystallinity and the orientation of the crystallites on the physical properties, factors that may be altered during the service life of a component, are reported [97, 98] with specific examples including the use of PEEK biomaterials. Many sources show that there is some degradation of PEEK's physical properties with time [99-101], however it is also reported that, where carbon fibre reinforced PEEK is used, the physical properties may remain unchanged and even surpass the fatigue performance of its metallic counterparts [102-104]. It is possible that PEEK, when exposed to high processing temperatures, undergoes irreversible changes to the polymer structure. An example of one such modification is the cross-linking by radical formation of the aryl rings to form a pseudo-dibenzofuran [105]. These modifications are not removed by melt processing and it is therefore necessary to consider the recycling options for PEEK.

2.3. HIGH-PERFORMANCE THERMOSET POLYMERS

Thermoset polymers differ from thermoplastics in that they contain cross-linking molecules between the polymer chains. These crosslinks significantly alter the polymer properties and are also responsible for the inability of thermoset polymers to be melt processed. Unlike

thermoplastics, thermosets have a decomposition temperature and do not enter the melt phase when heated. Examples of a thermoset polymers include polyesters, polyurethanes and polyepoxides [106]. Owing to their mechanical properties, thermoset polymers find application in a vast range of industries, including domestic appliances and consumer goods [107] as well as high-performance applications such as aerospace, automotive, energy and power generation industries. The context of this research is the high-performance applications and attention is devoted to 2,2-Bis[4-(glycidyloxy)phenyl]propane (BADGE). BADGE is a polyepoxide pre-polymer that may be cross-linked with amino compounds, such as 4,4'-diaminodiphenyl sulfone (DDS), at elevated temperatures to form a cross-linked (cured) resin that exhibits desirable physical and mechanical properties [108]. The properties of the cured resins are heavily dependent upon curing cycles and consequently the curing cycles have been widely studied in the literature [109-113]. Given that the cross-linking process reduces the mobility of the molecular chains, by forming bonds between them, it follows that the glass transition temperature of the cured resin is dependent upon the curing agent's ability to form such bonds, a process that is both time and temperature dependent [114]. The thermal history of both the pre-polymer and cured polymer also influence the glass transition temperature, although the effect is reported to be most prominent for the pre-polymer due to it having greater freedom of movement and therefore greater relaxation ability [115]. Research has shown that the thermal decomposition temperatures of cured BADGE based epoxy resins are dependent on the curing agent used [116], as is the percentage shrinking observed during the curing process [117]. The impact resistance of cured epoxy resins has been measured, research showing that enhancements are possible by the use of additives such as epoxy terminated hyper-branched polyester [118] and hyper-branched poly(ester amide) [119]. In addition to being

responsible for the mechanical properties exhibited by cured thermoset resins, the 3D cross-linked network also contributes to the chemical resistance of the material. Literature sources report the effects of the chemical structure on the chemical resistance of the cured product [120, 121]. The physical and chemical properties of thermoset polymers make them desirable for a wide range of applications, as stated previously. It is also these properties, especially in the case of chemical resistance, that creates a challenge for the recycling industry. Since thermoset polymers are largely insoluble in many environmentally sustainable organic solvents and cannot be melt processed, due to the presence of cross-links, it is necessary to consider alternative recycling processes. Similarly to PEEK, the focus of this research is on the deconstruction or decomposition of the polymer into smaller organic molecules that may find useful application, either within or external to the polymer industry.

BADGE based resins are used extensively in food contact applications and concern has been raised over the potential for bisphenol A (BPA) to migrate from within the polymer matrix and contaminate food [122-124]. Particularly important are applications where the resin is in direct contact with liquids, such as the lining of cans used for canned foodstuffs [125, 126]. Research into the toxicity and mutagenicity of BPA is ongoing in the literature [127-129], a common finding being that unreacted pre-polymer increases the possibility of exposure [130]. Migration is not unique to BPA and further studies have reported that derivatives of BPA have also been identified in foodstuffs, indicating that analysis of only BPA and its effects would be incomplete [131, 132]. Of the greatest concerns was the release of BPA and its derivatives from baby's bottles, which potentially could have a

negative impact on early development [133-135]. Effects of the storage conditions on the release of BPA have been investigated [136], with research showing that whilst the storage conditions are an influencing factor the service conditions are dominant, such as the use of surfactants or the ability of milk to perform aminolysis [137, 138]. Solvents extraction and leaching are not exclusive to BADGE based resins used in food contact applications and these effects are significant for high-performance applications. The uptake of water into thermoset resins has been studied [139-142], and in particular, it has been shown that for butane diol diglycidyl ether (BDDGE), water permeation reduces the glass transition temperature by up to 45 K and forms hydrogen bonds with hydroxyl functional groups [143]. The stresses induced by the ingress of water into a BADGE based epoxy resin, cured with DDS, have been studied by means of Photoelastic Stress Analysis (PSA) [144]. Where comparisons have been made it is evident that the degree of crosslinking, as well as the chemical composition of the cross-linking agent, contribute to the diffusivity of solutes through the polymer matrix.

For high-performance applications the physical properties, such as the toughness and tensile strength, are pivotal to use. These properties are affected by the effects discussed for food contact applications, exposure to solvents and surfactants, storage conditions, and the passage of time [145-147]. Additional factors are also present, such as loading, cyclical stressing and exposure to ultraviolet light (UV). Research presented in the literature has shown that wet ageing significantly reduces the critical stress factor after 48 h for a BADGE based epoxy resin, meaning that the material's ability to resist propagation of cracks is degraded [148]. It was demonstrated that the moisture content nearest to the defected

area was of greater influence than the moisture content throughout the sample. Further studies confirm the relationship between moisture ageing and significant reductions in the critical stress factor, for toughened epoxy blends the reduction was observed after 168 h [149]. Attempts have been made to model the uptake of moisture by a cured BADGE based epoxy resin, results showing that hydrolysis takes place with temperatures as low as 323 K [150]. Thermo-oxidative ageing of a cured BADGE based resin at 343 – 423 K, in the absence of an applied moisture content, shows that degradation of the polymer properties takes place by radical formation [151]. Radical formation through exposure to radiation is widely studied for many materials and is of interest to epoxy resins given their application in the nuclear industry. Radiochemical (γ -irradiation) ageing of amino cured BADGE based resins leads to a slight increase of water uptake, as well as a proportionally increased hyperoxide concentration [152], but does not lead to substantial degradation of the polymer properties and is less significant than thermal and hydrothermal ageing effects [153]. Conversely, radiochemical ageing of an amine cured tris-(hydroxyl phenyl)-methane based resin (Tactix), which could be considered a substituted or derivatised BADGE based resin, showed a considerable reduction in physical properties for comparable received doses [154]. It is noteworthy that the dose rates are dissimilar ($2 - 20 \text{ kGy h}^{-1}$ and 4 kGy h^{-1}) and comparisons are made based on the dose received by the samples. Whilst a kinetic model of the radiochemical ageing process is presented [155], the disparity between the BADGE and Tactix based resins is not reported and could be a result of the dose rate used, the pre-polymer structure or a combination of both. Resistance to electron radiation is less profound. Irradiation in inert atmospheres leads to radical formation and in the presence of oxygen leads to chain-scission and oxidation [156, 157]. As demonstrated, the properties of the cured resin are dependent on the cross-linking agent used and therefore it is expected

that the decomposition process may differ between literature sources. As well as the stresses induced by the ingress of water, or other solvents, into the polymer matrix, external stresses are applied to many epoxy resins during their in-service life particularly when used to form composite materials or coatings. Analysis of load-induced stresses on aged epoxy resin coating, applied to a metallic plate, by Electrochemical Impedance Spectroscopy (EIS) has been carried out, showing that the uptake of water is proportional to the degree of ageing and inversely proportional to the load applied [158].

The findings from studies on ageing may be applicable to the recycling process, depending on the recycling technology used. For example, diffusivity studies may be instrumental when considering solvolysis processes but may be less influential when pyrolysis is used. The decomposition of a BADGE based epoxy resin is a consideration for many high performance applications, such as the nuclear industry, and consequently the decomposition process has been studied and reported as one of hydrothermal oxidation, requiring 683 K and 24 MPa [159]. Experiments in sub-critical water (533 – 573 K, 3 MPa) have shown that the temperature and reaction time are of the most important factors [160], consistent with expectation considering kinetic and thermodynamic principles.

Specific applications require epoxy resins to exhibit fire resistance, often achieved by the use of halogenated compounds. The performance of fire resistance epoxy resins has therefore been a topic of interest and, since fire retardation is essentially the ability to resist thermal decompositions, it is incorporated into the general study of decomposition reactions [161]. Kinetic studies of the thermal decomposition of cured epoxy resins,

containing brominated flame retardants, are reported in the literature [162]. Combustion and decomposition mechanisms have been presented for high-performance cured epoxy resins using phosphorous based fire retardants, as opposed to halogenated compounds. Results suggest that retardation is provided through the production of a char layer, reducing the diffusivity of highly reactive species, effectively stifling the fuel source [163]. Qualitative investigations have shown that the oxidation state of phosphorous is a contributing factor in determining the composition of the char layer formed, meanwhile the composition of the cross-linking agent may contribute to resin's fire retardant properties [164]. The influence of the cross-linking agent has also been reported for halogenated flame retardant resins, with variations of up to 60 K in the decomposition temperature being recorded according to agent used [165]. The cross-linking agent may also affect the ability of the resin to release noxious compounds during pyrolysis and gasification processes, and as such material characterisation may be salient when evaluating recycling technologies [165, 166]. Aside from pyrolysis and gasification, thermal processing techniques for cured epoxy resins include solvolysis and hydrolysis. Research in this area has primarily focused on the recycling of printed circuit boards (PCB's), which have been mass produced on a global scale and often use brominated resins [167]. PCB's often contain high-purity metals, including precious metals, that would be useful to recover and recycle in addition to the organic constituents of the epoxy resin [168]. Hydrolysis using supercritical water (673 K, 25 MPa) has been carried out with the specific objective of recovering the metals and minimising the formation of char and tar-like polymer degradation products [169]. Debromination leads to the formation of hydrobromic acid in the aqueous phase with the major product of the organic phase being phenol [170]. With respect to high-performance applications there are some similarities between PEEK and epoxy resins, they are both used in the aerospace and

automotive industries. Moreover, common decomposition products exist, such as phenol. The decomposition of PEEK and moulding epoxy resin at 703 K in supercritical water containing a sodium carbonate (Na_2CO_3) catalyst has been studied, showing that in both cases phenol was both a common and major product [171].

Thermosetting polymers are utilised in many industries, as described previously. However, since the focus of this research is specifically high-performance materials, the focus of this literature review has been on polyepoxides. Similarly to PEEK, polyepoxides can be reinforced with fibres for load-bearing and structural applications. Indeed, the practice of producing polyepoxide based composite materials is more widely established and employed in comparison to PEEK, with the majority of literature pertaining to polyepoxides relating to composite materials. Therefore, it is vital to report on the research available in the literature associated with the development, production, application and recycling of composite materials. Commonly, fibres used to reinforce thermosetting polymers include glass [172, 173] and carbon [174, 175], with carbon fibres being both more expensive and durable than glass. Consequently, they are used for high-performance applications and are the subject of the next part of this literature review.

2.4. FIBRE REINFORCEMENT

Conventional reinforcement of polymer resins may be provided by a range of fibres constructed from various materials, such as glass, poly(aromatic aramid) and carbon. Research into the use of alternative fibres including basalt, hemp and flax is presented in the literature, namely as substitutes for glass fibres [176]. Hemp fibres have recently been

introduced into the automotive industry and are now utilised in the production of consumer vehicles by major vehicle manufacturers [177]. Glass fibres are widely used where thermal, electrical or chemical resistance is required from a composite material. In addition, these materials have a significantly increased strength to weight ratio in comparison to metals and have been the subject of interest in the aerospace and automotive industries [178-180]. Despite attempts to increase the strength and chemical resistance of glass fibres [181-183], the physical properties of carbon fibre are, for the majority of applications, superior [184, 185]. One significant difference between glass and carbon fibres is that carbon fibres readily conduct electricity whereas glass fibres are electrical insulators. Research into creating electrically conductive glass fibre reinforced composite materials by the addition of recycled carbon fibres has been carried out [186]. Whilst it is demonstrated to be possible, the electrical conductivity was exclusively reliant upon the carbon fibres and therefore the physical properties of the resulting composite material should be compared to that of a similar composite without the addition of carbon fibres. This would enable an understanding of the effect and viability of utilising recycled carbon fibres, in conjunction with glass fibres, for such applications. Given that glass fibres have been utilised within manufacturing for a greater period of time compared to carbon fibres, the majority of composite materials in circulation consist of glass fibres. Carbon fibres however, have superior mechanical properties and are used in high-performance applications where it would not be possible to employ glass fibres and a considerable strength-to-weight saving is required. Examples of aerospace applications include the Airbus A350, Boeing Dreamliner 787 [187, 188], McDonnell Douglas F/A 18 [189] and the Eurofighter Typhoon, the exterior of which consists of approximately 80 % carbon fibre reinforced polymers [190].

The majority of carbon fibres are produced from a poly(acrylonitrile) (PAN) precursor [191], which in turn is produced from propylene and ammonia. The bismuth catalysed ammonia and propylene reaction, patented by the Standard Oil of Ohio Company (SOHIO), produces acrylonitrile as the main product with useful by-products including acetonitrile [192]. The free radical polymerisation of acrylonitrile produces poly(acrylonitrile) [193] which may subsequently be used to form hollow fibres through a range of methods, such as electrospinning [194, 195] or gel-spinning [196]. Once formed, the PAN fibres are then oxidised before being carbonised at approximately 1,000 – 1500 K in an inert atmosphere [197], thereby forming fibres that are highly carbonaceous and low in impurities. The final stage of the carbon fibre production process heats the fibres to 1,773 – 3273 K in an inert atmosphere to allow for crystal realignment to take place, such that the fibre and crystal orientation are parallel [198]. The manufactured fibres are subsequently etched to increase the adhesion between the fibre and the polymer matrix when producing composite material, with research into etching techniques including plasma etching and electrochemical etching [199-201]. The adhesion between the polymer matrix and the carbon fibre is also heavily influenced by the presence, and type, of sizing used and is therefore wide studied in the literature [202-206]. The sizing also protects the carbon fibres during the filament winding process and it is therefore uncommon to obtain un-sized carbon fibres. The composition of the sizing used on industrially manufactured carbon fibres is usually unpublished and not available in the public domain, however, it is possible that during recycling processes the sizing could be removed. Therefore, its contribution to the adhesion of the carbon fibres is of importance to this research.

Life cycle analysis (LCA) has shown that the energy intensive production process for carbon fibres results in an embodied energy of 183 – 286 MJ kg⁻¹, significantly higher than that of glass fibres (13 – 32 MJ kg⁻¹) and flax fibres (6.5 MJ kg⁻¹) [207]. The high embodied energy coupled with superior mechanical properties of carbon fibres, compared to glass fibres, is reflected in the cost of the fibres. Within the United Kingdom carbon fibre composites account for 2 %v of the domestic market, yet they represent 40 % of the value as of 2012 [208]. The epoxy resins typically used in the manufacture of CFRP's have an embodied energy of 76 – 80 MJ kg⁻¹ [207]. Given the high mass fractions of fibres used [209], it is therefore evident that the vast majority of the embodied energy of the final product is attributed to the carbon fibres. The inverse situation exists with glass fibre reinforced polymers (GFRP's) where the embodied energy of the resin is typically 63 – 78 MJ kg⁻¹, up to several times that of the fibres [207]. Therefore, when considering recycling processes of CFRP's it is essential to consider the physical properties of the recycled fibres in conjunction with their proposed recycled application, without disregarding the decomposition products of the resin. Variation in manufacturing process parameters leads to the production of carbon fibres with specific attributes, and although the specific manufacturing process details are unpublished for commercial reasons, in general the tensile strength of virgin carbon fibres is in the region of 4.5 – 5.2 GPa [210, 211]. When considering recycling process for CFRP's the relationship between the tensile properties of virgin fibres and recycled fibres is paramount to understanding the effects of recycling, the destination application of the recycled fibres and in turn influences the LCA of composite materials. Since carbon fibres are not utilised alone and are incorporated into CFRP's, it is necessary to investigate the manufacturing, properties, applications and end-of-life (EOL) of CFRP's. Research pertaining

to the effects of recycling on the physical properties of the carbon fibres is given in Chapter 2.5.

2.5. CARBON FIBRE REINFORCED POLYMERS

2.5.1. Manufacturing CFRP's

Carbon fibres may be used to form tows, unidirectional tapes and weaves of various fibre alignments. The fibres may then be used to manufacture CFRP's by setting within a polymer matrix. Several process exist to create CFRP's including hand layup, open and compression moulding [212], resin transfer moulding (RTM) [213], vacuum assisted resin infusion moulding (VARIM) [214], vacuum assisted RTM (VARTM) [215], pultrusion [216], filament winding [217] and automated tape laying (ATL) [218]. Aside from the resin curing process described in Chapter 2.3, the fibre orientation, in conjunction with the CFRP production method, governs many of the final product properties. Combinations of resin selection, curing cycle, fibre volume fraction and orientation and manufacturing process are used to produce composite materials for specific applications. The design of recycling processes must consider the target application of the recycled fibres and therefore it is prudent to consider the specific attributes and requirements of the main production methods, since it is likely that such methods may be employed to produce composite materials from recycled fibres.

Hand Layup

The hand layup of carbon fibre may be used to produce aesthetic components for low performance applications. The process mimics that of the glass fibre layup process and typically uses out-of-autoclave resins that are cross-linked at, or near to, room temperature. The mould is coated with a layer of resin, onto which the first layer of carbon fibre is added. By applying a small amount of force to the carbon fibre the resin is pressed into the fabric from the mould. A second coating of resin is applied to the back of the fabric prior to adding the second layer of carbon fibre. The process is repeated until the required number of layers is achieved at which point the resin is allowed to crosslink.

Compression Moulding (CM)

Compression moulding offers advantages over hand layup processes with respect to the time taken per processed part. In compression moulding, carbon fibre that has been pre-impregnated with epoxy resin (pre-preg) may be stacked horizontally within a mould to form layers of a composite. The second half of the mould is then pressed, often using a hydraulic press, into the first half to complete the composite shape. The mould and press are heated during this process, causing the cross-linking of the curing agent to the polymer chains and thereby curing the resin. The cured composite is then removed from the mould and trimmed to remove excess resin. Complex composites mixing carbon fibre pre-preg and sheet moulding compound (SMC) to make a single material may be produced via this method [212].

Resin Transfer and Vacuum Assisted Resin Transfer Moulding (RTM and VARTM)

Similarly to compression moulding, RTM utilises a 2-part rigid mould to form the shape of the composite. However, RTM does not use carbon fibre pre-preg and uses dry, continuous or semi-continuous carbon fibre, commonly in a woven or stitched mat or tape. Layers of carbon fibre are laid into the lower mould to the desired depth at which point the mould is closed prior to the injection of the resin and associated cross-linking agent. The mould, containing the carbon fibre and resin, is subsequently heated to induce cross-linking according to the curing cycle of the specific resin used. Once cured, the mould is opened and the composite is removed and the process is repeated [219]. Attempts to produce CFRP's for high performance applications by RTM, without use of an autoclave, have been made with results showing similar mechanical performance to those produced in an autoclave [220]. The physical properties of the composite depend on the ability of the resin to permeate through the fibre matrix, essentially wetting the fibres in their entirety prior to curing the resin. The efficiency of this stage of the process can be improved by imposing a vacuum or partial vacuum, which is subsequently used to draw the resin through the mould and therefore through the fibres. In doing so, the transfer of resin through the fibre layers is increased and consequently it is possible to reduce the quantity of resin used and thereby minimise the product's mass. However, when using VARTM the maximum pressure differential possible is 0.1 MPa, lower than what is achievable by pumping the resin in RTM. However, VARTM may be used to selectively draw resin to particular parts of the mould that may be prone to low resin concentrations and consequently may reduce the potential for inhomogeneity [213, 215, 221].

Resin Infusion and Vacuum Assisted Resin Infusion Moulding (RIM and VARIM)

RIM has attributes of both RTM and hand layup processes in that an open mould is used to determine the geometry of the component, similarly to hand layup, and the resin is applied to the pre-formed component in a similar fashion to RTM. In RIM a release agent is applied to the open mould prior to fibre laying. Once the desired number of layers have been applied and the pre-form is complete a resin dispersion tool is applied to the top of the mould. The objective is to assist in the even distribution of the resin throughout the mould, minimising the probability of dry regions persisting which would adversely affect the physical properties of the component. A vacuum bag is fitted to the top of the open mould, attached to a vacuum sealing tape, and is subsequently evacuated. The resin is then drawn into the mould by the pressure differential and infuses through the fibre pre-form. The mould may then be placed into an autoclave to allow the resin to cure, after which a post curing cycle may also be used to produce the final component. Due to the accessibility provided by an open mould, complex geometries incorporating specific fibre orientations achieved by hand layup are possible. Consequently RIM may be used to produce high-performance CFRP's [214, 222, 223].

Filament Winding (FW)

Filament winding (FW) is an automated process that is often used to produce cylindrical and geometrically symmetrical, hollow structures such as pipes and aircraft structures. The process draws the fibres from a yarn through a resin bath and onto a rotating mandrel, where the fibres are wrapped around the axis of rotation. The mandrel may be heated during winding to assist in the resin distribution once the fibres are on the mandrel. As the

mandrel rotates it is necessary to continually move either the mandrel or the fibre feeding assembly horizontally such that fibres are laid over the entire surface of the mandrel. This process is carried out for a pre-determined period of time, which in turn governs the number of fibre layers at any given point on the mandrel. Once complete the mandrel, wound with fibre coated in resin, is placed in an oven and allowed to cure. After curing the component is removed from the mandrel to leave a hollow cylindrical tube of cured thermoset resin reinforced with continuous fibres [217, 224, 225]. Although cylindrical mandrels are typical, it is possible to use filament winding to produce components with a square-planar, conical, concave, convex, disc and other geometries having axial symmetry about which the rotation takes place [226-228].

Automated Fibre Placement and Automated Tape Laying (AFP and ATL)

Automated processes allow for the increased production throughput of CFRP's and, aside from filament winding, AFP and ATL are two of the most prominent automated processes. FW is essentially reliant upon the target component having symmetry along the rotational axis whereas this limitation does not apply to AFP and ATL. Consequently these techniques may be employed to produce CFRP's of many geometries.

Although the principle of operation is similar, subtle differences in the development of AFP and ATL leads to their deployment in differing duties. ATL utilises pre-preg uni-directional tape that is laid over the mould of the desired product. The pre-preg is heated as it is laid to ensure it is workable, while compacting rollers are used to reduce the space between tape layers and therefore reduce the voidage. Uni-directional tape is usually laid in one direction

across an entire layer of the mould with the second layer (or ply) being rotated through an angle, by rotating the laying head, of up to 90° . With the second layer laid over the first, the head is rotated again in preparation for laying the third layer, a process that is repeated until the desired number of layers is achieved [229-231]. Similarly to ATL, AFP uses pre-preg material however, AFP uses pre-preg carbon fibre tows. The width of a carbon fibre tow is dependent upon the number of fibres within the tow but, in general, is many times less than that of the unidirectional tape used in ATL. Consequently, it may take significantly greater amounts of time to lay fibres over the same area as ATL. The significant advantage of AFP over ATL is that due to the narrow nature of the tows, fibre placement over complex geometries is possible, therefore allowing for the automated production of complex components that may not be possible with ATL [232-234].

Due to the high precision, reproducibility and consistency of ATL and AFP, these techniques are used to produce high-performance components in the aerospace industry. However, the substantial capital investment required for equipment and tooling has prevented the widespread use of AFP and ATL in other areas of the composites manufacturing industry.

This overview of common manufacturing processes of CFRP's is used to provide the context of the composite recycling challenge. Assuming that recycled carbon fibres were readily available it is evident, from the processes presented herein, that manufacturing secondary CFRP's with recycled fibres requires adaptation of the manufacturing process, post recycling preparation of the fibres or a combination of both. Characterisation of the recycled fibres is paramount given that the structural reinforcement of CFRP's is directly linked to the fibre

properties and orientation and voidage of the polymer. Similarly, the use of recovered organic molecules requires quantitative analysis that is both robust and reliable. Within this context the conditions that may lead to the end-of-life of CFRP's, as well as techniques that may be used to measure the structural health (Structural Health Monitoring, SHM), will be presented.

2.5.2. Damage Detection in CFRP's

CFRP's are subjected to external forces when in use, especially in high-performance applications such as aerospace and automotive industries. Fatigue aside, CFRP's may be undergo impact with objects which may cause damage to the composite. Due to the complex structure of CFRP's it is possible for them to sustain damage, which may severely impede their use, whilst appearing to be visually intact. Therefore, research into methods of detection for impact and fatigue damage has been extensively conducted and is available in the literature. Finite element analysis has been used to identify concentrations of stress points of complex geometries and flat panels subjected to impact testing [235]. Impact resistance is a major concern in the aerospace industry, especially when considering load bearing components forming the exposed surface of aircraft and space probes. Impact may occur during manufacture, maintenance or during the service use of the component and as such a range of impact velocities are presented in the literature such as low velocity [236], high velocity (175 m s^{-1}) [237] and hyper velocity (up to $6,400 \text{ m s}^{-1}$) [238]. The effect of ice impact has also been a topic of research since this may be considered a normal scenario for

aviation components on the exterior of an airframe [239]. Attempts to increase the impact the impact resistance further for defence applications by using additional materials, such as Kevlar fibres or aluminium, has yielded limited success when considering the impact resistance per unit mass of composite [240]. The effect of the cross-sectional thickness of CFRP's on the impact resistance has also been presented in the literature, with results showing that the increased impact resistance is most pronounced when the projectile velocity is low [241-243].

Cracks introduced to the composite may propagate through the resin rich areas between the fibre layers, through the fibre layers or a combination of both. It has been suggested that the propagation of cracks through these regions is not identical and therefore research into strengthening the resin rich area between fibres has been carried out with limited success [244]. Given that carbon fibres readily conduct electricity it has been possible to utilise this property to obtain the diameter or number of fibres within a bundle by measuring the resistance [245]. Electrical conductivity of CFRP's is possible due to the carbon fibre content, the epoxy resin is essentially an electrical insulator, and therefore the resistance of the composite is a function of the layup process and fibre orientation [246]. It follows that for a single fibre, breakage leads to discontinuity and the resistance tends to infinity, for a bundles of fibres breakage of a proportion of the bundle leads to a proportional increase in resistance. This fundamental principle has been the subject of much research into damage detection and delamination of CFRP's [247-251], an area of great importance since physical damage and delamination of the bulk material may not be visible from the CFRP surface. Literature sources show that research in this area continues to

exploit the electrical properties of carbon fibre showing that, where impact damage exists, the corresponding increase in resistance and associated increase in temperature is detectable. Therefore, by using sensitive thermal equipment it is possible to identify damaged areas that are visually intact [252]. A similar approach using pulsed eddy currents has also been presented in the literature [253, 254]. Other research into the use of optical fibres laid between plies during the manufacturing process as a method of identifying impact locations is also presented [255], as well as the use of ultrasound [256, 257].

Effects of weathering on the physical properties of CFRP's are important and, for many applications, will dictate the service-life of the component [258]. Accelerated ageing, including exposure to moisture and UV, has been reported to decrease the flexural modulus [259]. Comparison of accelerated ageing of virgin epoxy resin and CFRP's under identical conditions have shown that the reduction in flexural modulus is greater in the case of the resin, highlighting the increased performance of CFRP's [260].

Whilst damage detection within CFRP's represents a challenge, a substantial difficulty is encountered when considering the remedial action. Thermoset polymers, by definition, are not melt processed and where a CFRP has sustained severe impact damage leading to fracture of the fibres, there is a requirement to seek restorative maintenance. For some components, particularly load bearing parts, it may not be possible to find a suitable remedial action and therefore the component must be replaced, leading to the formation of CFRP waste. Additional waste routes include manufacturing wastes and fatigue life components that must be replaced due to failure being catastrophic. The technologies

available for recycling CFRP's will be discussed, in conjunction with their specific attributes regarding the fibres and the polymer matrix.

2.5.3. Recycling CFRP's

The recycling technologies for CFRP's may be broadly categorised into three types, mechanical, thermal and chemical processes. Each type of process may be sub-divided into specific technologies, each having its attributes. However, to date examples of industrial scale processes are extremely limited due to the predominant disposal route for composite materials being landfill, usually based on economic concerns. This consensus is contrary to the EU Waste Management Hierarchy, where disposal to landfill is the least preferred option [261]. Legislation passed by the European Commission, enforceable as of 2015, aims to severely reduce the quantities of composite materials disposed of via landfill owing to the long lasting environmental impact associated with this route [262, 263]. An economic incentive usually encourages commercial entities to consider the recycling of materials and it is therefore expected that the recycling of CFRP's will be an area of significant growth in the near future. The objective of composite materials recycling is to separate the reinforcement fibres from the polymer matrix, characterise the fibres and the resin degradation products (if applicable) and then find a suitable application for the recycled material. The recycling of composites in general covers a vast range of materials and the recycling objectives vary according to the composite under consideration. For example, in GFRP's the reinforcement is relatively inexpensive and recovery of the resin is the prime objective whereas the inverse is true for CFRP's. An economically viable and environmentally sustainable recycling process for GFRP's may not be a suitable process for

CFRP's and hence the requirement for this research. GFRP's represent the vast majority of polymeric composite materials used to date, however, whilst being the minority with respect to annual production volumes, CFRPs represent a significant and growing proportion of the market according to value, attributable to the embodied energy and mechanical performance of carbon fibre [264]. This section focuses on the recycling of CFRP's, detailing recycling technologies and their characteristics.

Mechanical Recycling Process Technologies

It is necessary to distinguish between mechanical grinding as a recycling technology and cutting that is used to reduce the size of material. Commercial CFRP's are used to make large components, such as aerofoils, and it is not considered feasible to envisage a recycling technology that would handle a component of such size in its entirety. Therefore, size reduction is considered necessary irrespective of the recycling technology. Mechanical recycling, to date, consists of grinding of CFRP's to produce fine particulates that may be subsequently incorporated into new composite materials.

Comminution - Mechanical Grinding and Milling

Mechanical grinding or milling of CFRP's has been presented in the literature, although this methodology is typically reported for GFRP's owing to their greater abundance. The technique aims to reduce the size of material such that it may be incorporated into Sheet Moulding Compound (SMC) and thereby produce a recycled material. This may be done using impacting, cutting or stirred media mills followed by a classification step to separate particles according to their size. New SMC's may then be produced by inclusion of a

proportion of recycled, or reclaimed, material. Varying the proportion of recycled material into SMC's alters the final product's mechanical performance and therefore must be controlled [265]. It has been demonstrated that when recycled carbon fibre is used in place of virgin glass fibre as a filler in SMC's, the mechanical performance (such as the modulus of elasticity) of the recycled component may exceed that of the virgin component containing glass fibre [266]. This approach, whilst it does demonstrate the ability to use recycled carbon fibres to produce a material, does not necessarily represent an economically or environmentally sustainable option for end-of-life CFRP's. This is because the SMC's in question are typically made with glass fibres, having a substantially lower embodied energy and production cost, whereas the carbon fibre embodied energy, which was greater initially, now includes the energy associated with the recycling process. The use of recycled fibre SMC's in the automotive industry to produce body panels has been supported since the mid-1990's [267] and it is reported that mass reductions of up to 55 % are achievable when carbon fibre is used over other materials [268]. Attempts to devise economically viable processes for recycling GFRP have been presented, with this being the predominant method of recycling on an industrial scale [269]. The economic case for carbon fibres is different in that the particularly attractive properties of CFRP's are dependent upon the length, volume fraction and alignment of the carbon fibres. Thus, in order to produce high value products there is typically a requirement to recover carbon fibres as opposed to finely milled particles. Comminution has been successfully employed to produce low loading sports equipment from recycled CFRP's, by grinding the material into a fine powder prior to incorporation into a secondary CFRP [270].

The viability of applying this methodology to high-performance thermoplastics has been investigated using PEEK as an example [271]. Whilst PEEK has a high impact resistance and exceptional wear properties, especially when reinforced with carbon fibre, it is possible to produce $< 5\mu\text{m}$ particles with a narrow particle distribution when carried out at low temperatures [272]. In the case of PEEK an additional complication arises in that the cost of the polymer is many times that of the carbon fibres within it. Although PEEK is a thermoplastic, and therefore may be melt processed, conditions exist where melt processing is not a viable recycling option as discussed in Chapter 2.3. Many of those scenarios involve changes to the chemical structure of PEEK and therefore comminution, since it does not chemically alter the material, may not be a viable recycling route.

Comminution - High-Voltage Fragmentation

High-Voltage (HV) Fragmentation is a process utilised in the mining industry to separate minerals from ores, allowing for the efficient recovery of valuable components [273]. Rock samples to be fragmented are typically placed in a water bath and subjected to high voltage pulses of electricity, which may be $> 100\text{ kV}$, causing comminution of the rock and liberation of the desired mineral [274]. The geometry of the target influences the efficiency of the process, as does the target's ability to dissipate energy [275]. Although still in its infancy, research into this technology has been applied to the recycling of waste or end-of-life PCB's, which often contain polyepoxide resins as well as precious and valuable metals [276]. By extension, this technique has been directly applied to epoxy resins and has been demonstrated to efficiently fragment the polymer matrix [277]. Research into the

application of HV fragmentation to high-performance composite materials is ongoing, such as the fragmentation of PEEK composite materials [278].

Thermal Recycling Process Technologies

Contrary to mechanical recycling processes, thermal processes offer the opportunity to completely remove the polymer matrix from the fibres and as such isolated carbon fibres are attainable.

Pyrolysis – Fluidised and Fixed Bed Reactors

Pyrolysis is the process of thermally decomposing a material in an inert atmosphere, preventing the oxidation of the volatile products and producing pyrolysis oils and synthesis gasses. Depending upon the conditions and feedstock used, it is possible to produce synthesis gas, pyrolysis oil and combustible solid residue simultaneously. Indirect heating of the material is often carried out, although it is not necessarily the only option. Pyrolysis has been used extensively in biofuel from biomass research [279, 280]. The use of catalysts in pyrolysis reactions is commonplace [281-283], as is the use of both fixed bed [284, 285] and fluidised bed reactors [286, 287]. Fluidised bed pyrolysis has been applied to both GFRP's and CFRP's, however in the case of GFRP's the temperatures required to remove the polymer matrix are often sufficient to cause a collapse of the macro-porous structure of the fibres and subsequent loss of mechanical properties [288]. Similar temperatures are required to pyrolyse CFRP's (823 K) and GFRP's (723 K), however carbon fibres are less susceptible to temperature induced degradation and consequently the recovered fibres retain a greater proportion of their mechanical properties [261]. Pyrolysis provides an

encouraging route for the recycling of CFRP's because the polymer resins used to construct them typically have thermal decomposition temperatures below 873 K and carbon fibres are not oxidised at temperatures below 873 K even in the oxidative atmosphere of synthetic air [289]. Fluidised bed reactors typically have a uniform temperature distribution throughout the bed and therefore offer the ability to control the reaction temperature with some precision. In the case of CFRP pyrolysis however, the use of fluidised bed reactors removes the possibility of pyrolysis oils and favours the production of synthesis gasses. These are often oxidised and used to partially recover energy required to operate the process [261]. A comprehensive LCA is required to determine the viability and sustainability of this approach in comparison to recovering liquid organic products.

Pyrolysis – Microwave Induced

Microwave induced pyrolysis has been investigated as an alternative to fixed and fluidised bed reactors for the production of biofuels from biomass [290, 291]. The use of microwave pyrolysis with CFRP's is particularly interesting since many of the carbon allotropes are good absorbers of microwaves [292], which offers the ability to heat the composite material from within. Research into the application of this technology to the recovery of carbon fibres from CFRP's has shown that it is possible to recover relatively clean fibres that exhibit tensile properties greater than that achieved by fluidised bed pyrolysis, although it is noted that in all cases the tensile strength was reduced in comparison to virgin material (virgin = 4.09 GPa, microwave pyrolysis = 3.26 GPa, fluidised bed pyrolysis = 3.05 GPa) [293]. Topological changes to the carbon fibres as a result of microwave pyrolysis were identified.

It is possible that this is a fundamental consequence of exposing carbon to microwaves and is currently under research as a method of producing activated carbon [294-296].

Molten Salts

The use of molten potassium hydroxide (KOH) to decompose epoxy resins has been investigated, showing that the recovery of carbon fibres retaining up to 95 % of their original tensile strength is possible [297]. However, recovery of polymer decomposition products from the molten KOH was not investigated and therefore remains a challenge to the employment of this technique. It is not thought to be beyond reason to suggest that a solution may be sought, although LCA would be required to determine the environmental impact of the entire process.

Chemical Recycling Process Technologies

Dissolution

The use of nitric acid to dissolve an epoxy matrix has been investigated, with results showing that is both possible to dissolve the resin, extract the decomposed resin products and re-polymerise to synthesise a new resin [298]. This approach has also been applied to GFRP's, with results showing that the presence of glass fibres does not have an observable effect [299]. There are environmental concerns with the use of large quantities of concentrated nitric acid and, given that neutralisation is a pre-requisite to the extraction process, the use of nitric acid in this context is not considered sustainable. Incidentally, although this approach is not likely to be applied to CFRP's, research has demonstrated that

it is possible to use nitric acid to treat carbon fibres, with modification of the surface increasing bonding to both epoxy and polyurethane resins [300, 301].

Thermochemical Processes

Thermochemical processing, using sub-critical, near-critical and supercritical fluids allows chemicals that would not conventionally be considered capable of dissolving polymers to be applied. Information on supercritical fluids and their properties is provided in Chapter 2.1. Under supercritical conditions relatively benign solvents, such as water, may be used to decompose CFRP's when used with a catalyst [302]. The process of thermochemical degradation or decomposition of polymers is called solvolysis, although the name hydrolysis is given when water is the solvent. For BADGE based epoxy resins, and their associated composites, it is possible to partially decompose the polymer matrix (approximately 20 %) using water alone at 523 K, with the percentage decomposition rising with increasing temperature (> 60 % at 673 K) [303]. The efficiency of the decomposition may be increased by the addition of catalysts, such as potassium hydroxide (KOH), hydrogen peroxide (H₂O₂) and oxygen (O₂) [303, 304]. Phenol is a major product in the decomposition of BADGE based epoxy resins [171], and there is also evidence to suggest that there is a synergistic effect between phenol and some catalysts used in the decomposition reactions [302], leading to an auto accelerating reaction [305].

In attempts to reduce the temperature and pressure required for decomposition of the resin to take place, research into alternative supercritical fluids including methanol (scMeOH), ethanol (scEtOH) and propanol (scPrOH) have been reported. When using

scMeOH (543 K, 8 MPa, 90 min) it is reported that the cross-links responsible for producing the thermosetting resin may be selectively destroyed, allowing for recovery of clean fibres and a thermoplastic resin [306]. It is further reported that the recovered thermoplastic may be cross-linked to produce a secondary thermoset resin, although the physical properties of the secondary resin do not mimic that of the virgin material. It is reported that scPrOH is able to achieve approximately 80 % decomposition after 60 min at 593 K, with significant quantities of char being produced as an undesirable side-product [307]. The complete removal of char is not reported, although the quantity may be reduced by increasing the reaction time to 300 min. Control over the number, and nature, of the products was achieved by addition of KOH as a catalyst. The use of scEtOH produces similar results to that of scPrOH. This may be attributed to the similar dipole moments (DP) of EtOH and PrOH which is ultimately responsible for the solubility of the decomposition products in the solvent. The response of the EtOH system to a basic catalyst is also the same as the PrOH system. It is noted that the use of acetone (DMK) (DP = 2.881), having a greater dipole moment, outperforms the use of MeOH (DP = 1.700), EtOH (DP = 1.691) and PrOH (DP = 1.679), with respect to the percentage decomposition, with the most notable increase being observed when the temperature was 573 K [308]. The strength, and therefore quality, of carbon fibres recovered from thermochemical processing varies according to the fluid, reaction temperature, reaction time and catalyst used. However, it is typically reported that the residual tensile strength of the recovered fibres is greater than 90 % of the virgin material [210, 306, 308]. It has been reported that in some instances the recovered fibres had a tensile strength exceeding that of the virgin material [304].

A significant advantage of thermochemical processing, aside from the ability to recover carbon fibres free of resin that maintain much of their initial tensile properties, is the ability

to recover the polymer decomposition products. Thermochemical processing may be applied to thermoplastics, as well as thermosets as demonstrated. The use of carbonate based catalysts in the decomposition of both high-performance thermoplastics and high-performance thermosets has been reported [171], yielding phenol as a common major product.

2.6. SUMMARY OF LITERATURE REVIEW FINDINGS

Thermochemical processing, achieved by the use of supercritical fluids, represents an opportunity to recycle thermoset and thermoplastic materials and their composites. According to the specific reaction conditions used, it is possible to selectively decompose polymers and obtain reinforcing fibres free of resin which, if characterised, may potentially be used to produce secondary composite materials. It is evident that the choice of working fluid is crucial since it governs the minimum temperature and pressure (defined by the critical point), solubility of the reaction products and the solubility of the catalyst, should one be used. It has been demonstrated that mixtures of solvents will exhibit a critical point between that of the individual solvents and that the use of immiscible fluids may offer opportunities since all supercritical fluids are miscible in all proportions. The properties of recovered fibres, including surface conditions and the presence of sizing, must be established in order for the creation of a composite recycling industry. Research on surface treatment of carbon fibres has been presented, although the technology is not yet mature.

The ability of thermochemical processing to be applied to both thermoset and thermoplastic composite materials, in conjunction with the opportunity to potentially take advantage of

mixtures of relatively benign and environmentally sustainable solvents has led to hydrolysis and solvolysis being the methods of choice for this research project. The potential of these techniques to reduce the operating temperatures and pressure in the presence of a catalyst is thought to be unparalleled with the present technology.

CHAPTER 3. EXPERIMENTAL METHODOLOGY

3.1. MATERIALS INVESTIGATED

This research into the processing and recycling of high-performance materials includes both thermoplastic and thermoset polymers, as well as carbon fibre and Carbon Fibre Reinforced Polymers (CFRP's).

The class of thermoplastic polymers studied are poly(oxy-1,4-phenyleneoxy-1,4-phenylenelecarbonyl-1,4-phenylene) (PEEK), manufactured and supplied by Victrex Plc. In particular, PEEK150PF, PEEK450PF, PEEK150CA30 and PEEK450CA30. PEEK150PF and PEEK450PF are supplied as a semi-crystalline, fine powders, having melt viscosities of 130 Pa.s and 350 Pa.s at 673 K respectively. PEEK150CA30 and PEEK450CA30 are supplied as semi-crystalline pellets (diameter = 3.3 mm, length = 3.8 mm, approximately) containing 30 %v carbon fibre and have melt viscosities of 320 Pa.s and 675 Pa.s at 673 K respectively. The PEEK repeat unit is given in Figure 2.

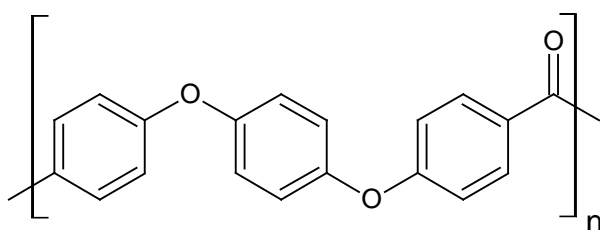


Figure 2: Structure of poly(oxy-1,4-phenyleneoxy-1,4-phenylenelecarbonyl-1,4-phenylene) PEEK

The thermoset polymer used is 2,2-Bis[4-(glycidyloxy)phenyl]propane (DER 332, BADGE, DGEBA) cross-linked with 4,4'-diaminodiphenyl sulfone (DDS), supplied by Sigma Aldrich.

The preparation of the cured resin is carried out as part of this research and is described in detail in Chapter 3.3.3. The structures of DER 332 and DDS are given in Figure 3.

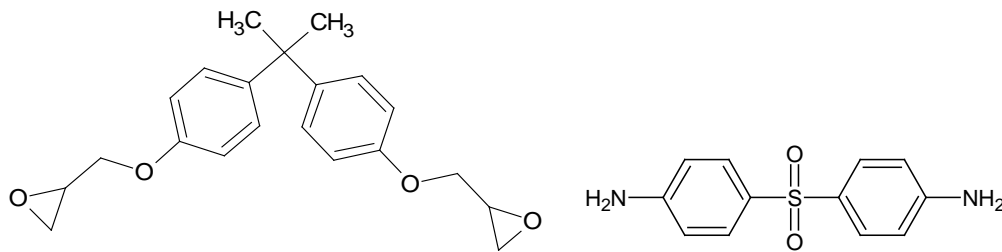


Figure 3: Left; 2,2-Bis[4-(glycidyloxy)phenyl]propane (DER 332, BADGE), Right; 4,4'-diaminodiphenyl sulfone (DDS)

Carbon fibre tow, T700S 50E, having a diameter of 7 μm was obtained from Toray Carbon Fibres America Inc. The analysis of virgin carbon fibres is provided in Chapter 3.3.4.

Carbon Fibre Reinforced Polymer samples were obtained from Hexcel, having a carbon fibre content of 53.8 %v. The average thickness of the plate is 6.23 mm, with a minimum thickness of 6.17 mm and a maximum thickness of 6.30 mm. Curing of the resin was carried out at 5.0 MPa. As this is a commercial composite material information about the composition of the resin, crosslinking agent and carbon fibres is not supplied. Since one objective of the project is the Efficient X-Sector use of Heterogeneous Materials in Manufacturing, an end-of-life CFRP bicycle wheel, supplied by Dolan Bikes, UK, was also used as part of this research. This material is also commercially produced and consequently information as to the resin composition, crosslinking agent, curing cycle and carbon fibre content was not available.

3.2. REACTION VESSELS

Two types of reaction vessel have been used in the research reported herein. The attributes of each reactor type and ancillary equipment will be discussed, paying particular attention to the differences between the two systems.

Low-Temperature Reactor System

The Low-Temperature Reactor (LTR), supplied by Parr Instrument Company (Moline, USA), was used to process PEEK samples with scCO₂. The LTR has a nominal volume of 25 ml and has minimum and maximum working temperatures of 263.15 K and 473.15 K respectively. The maximum working pressure of the reactor is 34.5 Mpa. The reactor lid was fitted with a bursting disc rated to 34.5 MPa. The stainless steel reactor is equipped with two sapphire viewing windows, front and rear. A Camtek DSP Colour Camera is used to observe the inside of the reactor from the front, illumination is provided by VWR VisiLight I-LED portable lights shone through the rear sapphire window. The video image is output to a monitor, no recording facility was available and imaging was used exclusively for qualitative purposes. Heating to the reactor is supplied by a Thermo Electron Corporation HAAKE B3 oil heater with a HAAKE DC 30 controller. The agitator cooling jacket is cooled by a PolyScience Chiller, maintained at 269 K. The reactor's internal pressure was monitored with an Ashcroft Duralife pressure gauge (accuracy, ± 1 %). The temperature was monitored by means of an RS Components type K thermocouple connected to an RS219-4602 Digitron 3900 display, in addition to the HAAKE DC 30 controller. Liquid CO₂ (purity, 99.99 %) was received from a liquid withdrawal CO₂ cylinder, supplied by BOC Ltd, to an HIP 62-6-10 manual piston pump.

The HIP pump has a maximum working pressure of 68.9 MPa and a stroke volume of 30 ml. The pump is cooled with the PolyScience chiller to maintain the liquid state of the CO₂ received from the CO₂ cylinder. The CO₂ volume is measured during the depressurisation stage using a Zeal DM3A volumetric meter (accuracy, ± 0.25 %). The LTR is shown in Figure 4.

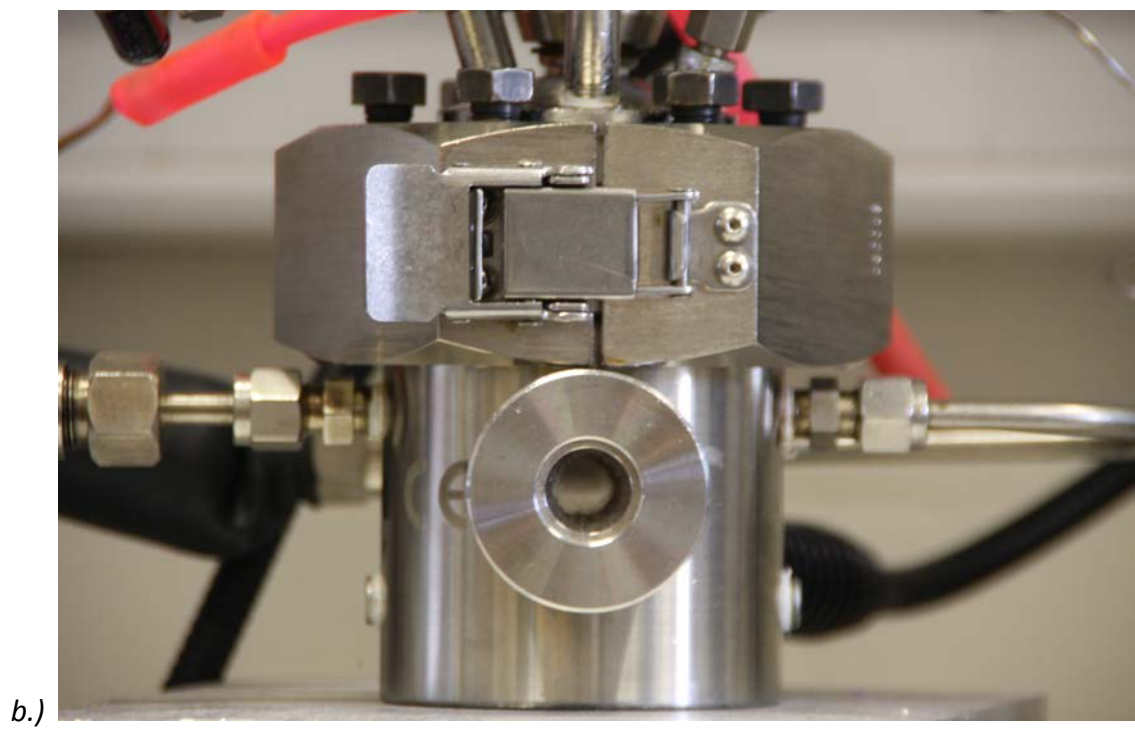
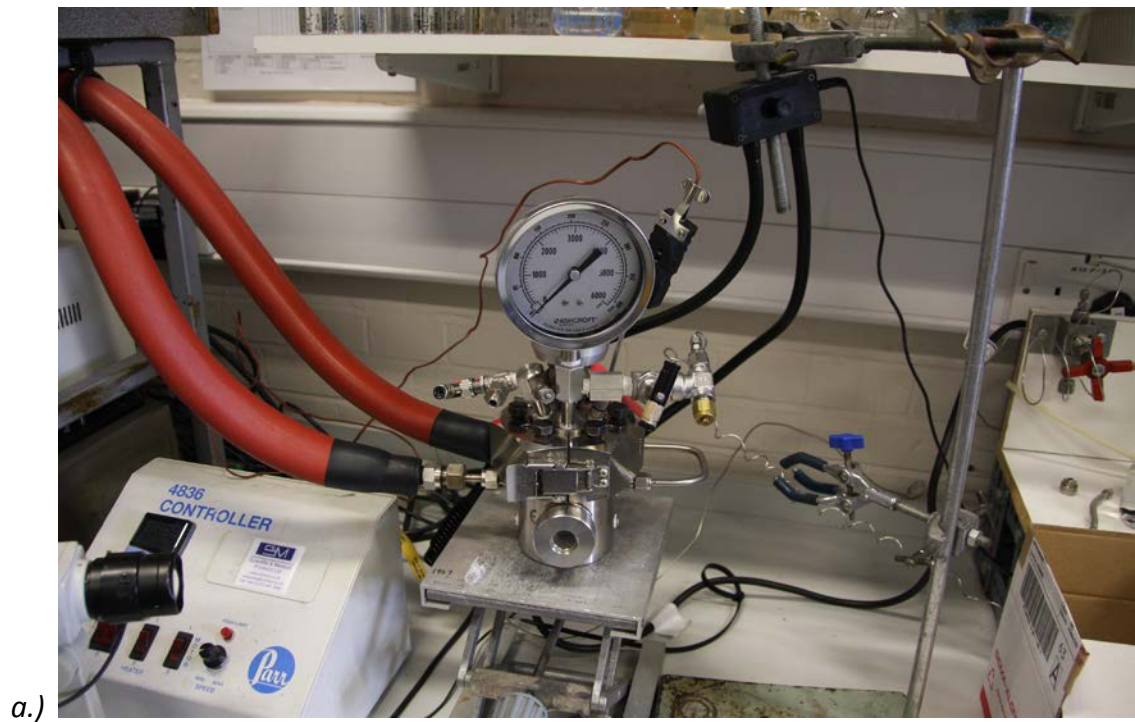


Figure 4: Low-Temperature Reactor (LTR) system showing a; complete setup, b; sapphire viewing windows

High-Temperature Reaction System

The High-Temperature Reactor (HTR), supplied by Parr Instruments Company (Moline, USA), comprises of a 100 ml (nominal volume) cylindrical vessel and lid assembly. Two such reactors were used, one constructed from stainless steel and one constructed from Hastelloy. With the exception of the material of construction both vessels were identical, with the Hastelloy vessel replacing the stainless steel vessel, and therefore will be described together. The vessels have minimum and maximum operating temperatures of 263 K and 773 K respectively and a maximum working pressure of 34.5 MPa. The vessel lid was fitted with a busting disc rated to 34.5 MPa. Where gasses were used, charging and discharging of the reactor was controlled through the use of Swagelok SS-3HNR4-G valves (Swagelok, USA). Where liquids were used as the sole working fluid, charging of the reactor was carried out prior to final assembly of the system. Swagelok valves provided a discharge capability at the end, and if necessary during, the reaction. In all cases solid samples were loaded into the reactor prior to assembly. Heating and control of the reactor temperature was supplied by a Parr Instruments Company 4848 Reactor Controller and Furnace, with a single type J thermocouple providing feedback to the controller. The reactor's internal pressure was measured by a pressure transducer with digital readout (Druck, UK) and an analogue pressure gauge (SPAN, USA) attached to the vessel lid. Cooling to the reactor's magnetic drive agitation system was provided by a peristaltic Watson-Marlow 302 pump (Watson-Marlow Pumps Group, UK) supplying coolant from a Polyscience Chiller (Polyscience, USA) maintained between 268 K and 273 K. The HTR's, both stainless-steel and Hastelloy, are shown in Figure 5 and Figure 6.

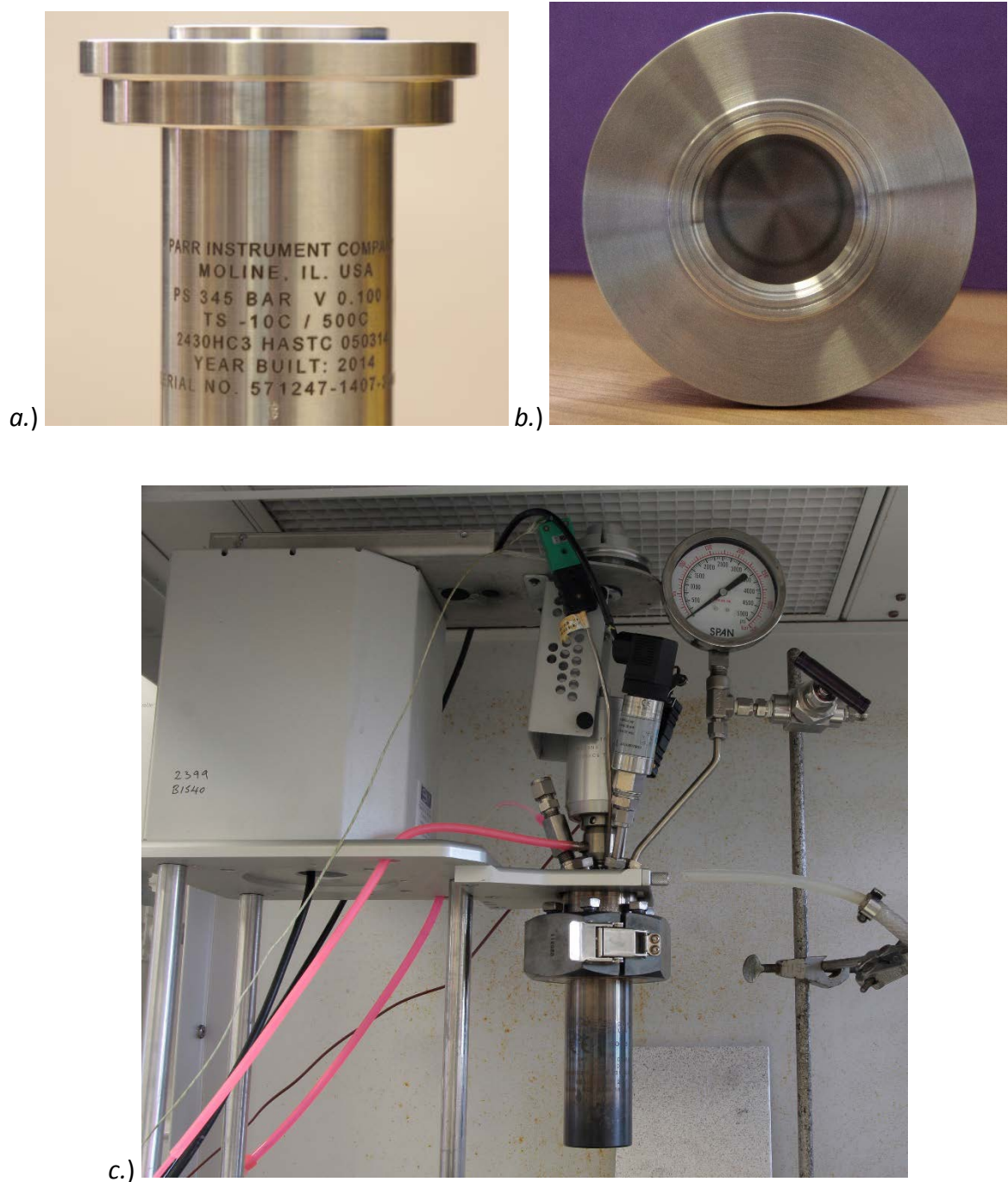


Figure 5: High-Temperature Reactor (HTR), 100 ml nominal volume, a; Side profile showing identification markings (Hastelloy), b; top-view showing internal volume (Hastelloy), c; complete setup (stainless-steel)



Figure 6: High-Temperature Reactors showing the discolouration at the end-of-life of the reactor, Hastelloy (left), stainless-steel (right)

The volume available for reaction was calculated via the method provided in Appendix 1. It was determined to be 115 ml when water is the reaction fluid and 130 ml when CO₂ is the fluid. These reaction volumes account for the ancillary fittings, valves and associated pipework (as shown in Figure 5), and differ due to the differing surface tensions of the fluids.

3.3. REACTION CONDITIONS

3.3.1. Supercritical Carbon Dioxide Processing of Polyetheretherketone

The polymer processing of polyetheretherketone (PEEK) using supercritical carbon dioxide (scCO₂) may be used to induce crystallisation and manipulate the glass transition temperature (T_g). In this context, polymer processing is used to describe the process by

which PEEK may undergo changes to the physical properties without altering the chemical structure. To identify the impact of using scCO₂ to process PEEK it is necessary to generate amorphous PEEK samples thereby ensuring the absence of crystalline regions.

Generation of Amorphous PEEK Samples

To generate amorphous PEEK 150PF and 450PF samples several milligrams of PEEK, obtained from Victrex Plc, were measured out into a pre weighed 40 μ l Aluminium Differential Scanning Calorimetry (DSC) pan, supplied by Mettler Toledo. The mass of the DSC pans was determined by using a Sartorius R160P Research balance (standard deviation, $\leq \pm 0.02$ mg). The DSC pan was then placed inside a ceramic bowl which was subsequently placed inside a Carbolite furnace. The furnace heating programme was designed to heat at 50 K min⁻¹ from ambient temperature to a final temperature of 673 K, the final temperature being maintained for 20 minutes to allow for thermal equilibration between the PEEK and furnace. At the end of this period the ceramic bowl, containing the DSC pan, was removed from the furnace. The DSC pan was immediately removed from the ceramic bowl and quenched into a beaker containing ice water. The cooling water supplied a cooling rate in excess of 10,000 K min⁻¹, preventing the arrangement of polymer chains into crystalline regions within the bulk polymer. The PEEK sample was subjected to the ice water for a minimum of 5 minutes before being removed and dried in a Fisons Drying Cabinet maintained at 313 K for 120 minutes. Since the mass of the DSC pan was taken prior to generation of the sample, the sample mass was determined by difference. The PEEK sample and the DSC pan were not separated at any point post melt processing.

Confirmation of Amorphicity

Having carried out the melt processing procedure it was necessary to confirm that the polymer sample was amorphous. Qualitatively this may initially be done by visual inspection using a microscope, since amorphous PEEK does not contain crystalline regions it is translucent whereas semi-crystalline PEEK is opaque. Quantitative analysis of the amorphicity of PEEK was carried out using the analytical techniques described in Chapter 3.4.1.

Polymer Processing of PEEK with Supercritical Carbon Dioxide

A Parr Instruments Company high-pressure bomb reactor (LTR) was used to process the amorphous PEEK samples with scCO₂. The amorphous PEEK samples, contained within their 40 µl aluminium DSC pans, were loaded into the LTR and the vessel was sealed. A liquid withdrawal CO₂ cylinder provided by BOC Ltd was used to supply liquid CO₂ at 5 MPa from the cylinder to a Jasco PU-1580-CO₂ delivery pump. The CO₂ delivery pump was used in conjunction with the reactor furnace to generate the conditions necessary. Once the required conditions were obtained Swagelock valves, SS-3NRM4 and SS-0VM2-A-BKB, were used to seal the reactor and maintain the internal pressure. Coolant maintained at 269 K was pumped, using a Watson-Marlow 302 Peristaltic Pump at 110 rpm, from a PolyScience Chiller to the agitator cooling jacket.

A design of experiments (DOE) approach was used to investigate the effects of supercritical carbon dioxide on the crystallinity of amorphous PEEK samples. The DOE used was a full

factorial design, comprising of 6 blocks, with 1 centre point per block, and triplicated corner points. The design is given in Table 1.

Table 1: Designed experiment (DOE) for the investigation of $scCO_2$ induced crystallisation of PEEK, LTR

| Standard Order | Run Order | Centre Point | Block | Temperature (K) | Pressure (MPa) | Soak Time (min) |
|----------------|-----------|--------------|-------|-----------------|----------------|-----------------|
| 3 | 1 | 1 | 1 | 453 | 5 | 30 |
| 1 | 2 | 1 | 1 | 413 | 5 | 10 |
| 5 | 3 | 0 | 1 | 433 | 10 | 20 |
| 2 | 4 | 1 | 1 | 453 | 15 | 10 |
| 4 | 5 | 1 | 1 | 413 | 15 | 30 |
| 8 | 6 | 1 | 2 | 413 | 5 | 30 |
| 7 | 7 | 1 | 2 | 413 | 15 | 10 |
| 9 | 8 | 1 | 2 | 453 | 15 | 30 |
| 10 | 9 | 0 | 2 | 433 | 10 | 20 |
| 6 | 10 | 1 | 2 | 453 | 5 | 10 |
| 29 | 11 | 1 | 6 | 453 | 15 | 30 |
| 28 | 12 | 1 | 6 | 413 | 5 | 30 |
| 27 | 13 | 1 | 6 | 413 | 15 | 10 |
| 26 | 14 | 1 | 6 | 453 | 5 | 10 |
| 30 | 15 | 0 | 6 | 433 | 10 | 20 |
| 25 | 16 | 0 | 5 | 433 | 10 | 20 |
| 24 | 17 | 1 | 5 | 413 | 15 | 30 |
| 22 | 18 | 1 | 5 | 453 | 15 | 10 |
| 23 | 19 | 1 | 5 | 453 | 5 | 30 |
| 21 | 20 | 1 | 5 | 413 | 5 | 10 |
| 12 | 21 | 1 | 3 | 453 | 15 | 10 |
| 15 | 22 | 0 | 3 | 433 | 10 | 20 |
| 11 | 23 | 1 | 3 | 413 | 5 | 10 |
| 14 | 24 | 1 | 3 | 413 | 15 | 30 |
| 13 | 25 | 1 | 3 | 453 | 5 | 30 |
| 20 | 26 | 0 | 4 | 433 | 10 | 20 |
| 19 | 27 | 1 | 4 | 453 | 15 | 30 |
| 18 | 28 | 1 | 4 | 413 | 5 | 30 |
| 17 | 29 | 1 | 4 | 413 | 15 | 10 |
| 16 | 30 | 1 | 4 | 453 | 5 | 10 |

The reactor was initially pressurised to 1 MPa with CO_2 , increasing the thermal conductivity between the vessel walls and the thermocouple, when compared to a non-pressurised vessel. This minimised the thermal overshoot observed during the heating stage. The

reactor was then simultaneously heated and pressurised to the conditions as stipulated by the designed experiment (Table 1). Once the desired conditions were attained, the pre-determined experiment time was allowed to elapse prior to cooling the reactor. The reactor was depressurised when the temperature reached 323 K. Analysis of the effects of scCO₂ processing of PEEK was carried out using DSC, FT-IR and TGA as detailed in Chapter 3.4.2. Heating and cooling processes were generally on the order of 30 minutes.

Supercritical Carbon Dioxide Induced Crystallisation

It is necessary to define 'supercritical CO₂ induced crystallisation' as opposed to spontaneous thermodynamic crystallisation. Supercritical CO₂ (scCO₂) induced crystallisation is defined as formation of crystalline regions within the PEEK matrix below the T_c, induced by the plasticisation effect attributed to scCO₂. To quantitatively assess this process there are two approaches available, the first is to process the polymer with scCO₂ and then carryout analysis by DSC (as discussed previously), the second method is to analyse an amorphous PEEK sample by means of High-Pressure DSC (HPDSC). HPDSC allows for the *in-situ* measurement of the crystallisation process and will highlight the effects of scCO₂. Post-processing DSC analysis in the absence of CO₂ provides detailed information about the effects of scCO₂ processing and separates the manipulation of the crystallisation temperature from the CO₂ induced crystallisation. A combination of both methods allows for a holistic approach and was used in this research.

HPDSC Processing of PEEK

Amorphous PEEK samples, typically having a mass of 10 mg, were subjected to scCO₂ and analysed *in-situ* by means of high-pressure DSC. A Mettler Toledo HPDSC827^e was used and has a maximum working pressure of 10 MPa. Amorphous samples contained within standard 40 µl aluminium DSC pans were placed inside the DSC with a second, empty, 40 µl Aluminium DSC pan used as a reference. The data were obtained directly from the Mettler Toledo STARe DSC software. Although this is polymer processing, since the analysis is performed *in-situ* the methods used are given as part of the analytical techniques in Chapter 3.4.2.

Carbon Dioxide Containment within the Polymer Matrix

PEEK samples were placed inside the LTR and the lid assembly was secured. The HAAKE temperature controller was activated and set to 413 K. Using the HIP pump the LTR was pressurised to 20.0 MPa, at which point the conditions were maintained for a period of 30 minutes. Once a period of 30 minutes under the processing conditions had elapsed the heating supply to the LTR was removed and the reactor allowed to cool to 323 K prior to depressurisation. A lag time, according to the experiment schedule given in Table 2, was allowed to elapse prior to analysis of the sample.

Table 2: CO₂ Containment experiment conditions, T = 413 K, P = 20.0 MPa, LTR

| Sample Type | Lag Time (min) |
|-------------|----------------|
| PEEK150PF | 0 |
| | 60 |
| | 120 |
| | 180 |
| | 240 |
| PEEK450PF | 0 |
| | 60 |
| | 120 |
| | 180 |
| | 240 |
| PEEK150CA30 | 0 |
| | 60 |
| | 120 |
| | 180 |
| | 240 |
| PEEK450CA30 | 0 |
| | 60 |
| | 120 |
| | 180 |
| | 240 |

A non-CO₂ processed sample of each grade of PEEK (150PF, 450PF, 150CA30 and 450CA30) was used as a control. The analysis of the scCO₂ processed samples was carried out by TGA as detailed in Chapter 3.4.2.

3.3.2. Recycling of Polyetheretherketone Composite Materials

PEEK, and its composites, are employed in many high-performance applications where resistance to temperature and chemical corrosion are essential, such as aerospace and automotive industries [309]. It is also possible to manufacture PEEK composite materials, filled or reinforced, with carbon fibre. In doing so, the recycling process is complicated as melt processing would destroy the fibre alignment that is responsible for the reinforcement

in composite materials. In addition, end-of-life PEEK may not retain the melt processing capability of the virgin material and may consequently require an alternative recycling process. This research focuses on the recycling of a PEEK composite, PEEK150CA30, filled with 30 %v carbon fibre.

In light of this, previous work, as detailed in Chapter 2.2. Literature Review, has investigated the decomposition of PEEK in supercritical water (scH₂O) in the presence of a sodium carbonate (Na₂CO₃) catalyst, with the polymer showing no decomposition at temperatures below 703 K [171]. The research presented herein was carried out using co-solvent systems comprising of alcohol and water, incorporating the use of a caesium carbonate catalyst (Cs₂CO₃). Unlike Na₂CO₃, Cs₂CO₃ is soluble in ethanol and propanol and, given that the carbonate functional group is responsible for the catalytic effect, substitution of Na₂CO₃ with Cs₂CO₃ facilitates the use of EtOH and PrOH as co-solvents. The use of co-solvents in combination with a catalyst is in an attempt to decompose PEEK close to its melting temperature of 616 K.

These reactions were carried in the HTR owing to the high temperatures required. A constant solvent loading rate of 50 %v was used for all PEEK decomposition reactions, irrespective of the solvent composition, in combination with a constant PEEK15CA30 loading of 10 mg ml⁻¹. Approximately 0.575g of PEEK150CA30 was accurately measured using a Sartorius Research R160P balance (Sartorius AG, Germany) and loaded into a stainless steel basket. The basket was attached to the agitator shaft, suspending the PEEK at the centreline of the reactor and therefore ensuring no contact with the reactor wall was made during the

reaction. The concentrations of water (H₂O), ethanol (EtOH), 2-propanol (PrOH), acetone (DMK) and Cs₂CO₃ are provided in Tables 3 through 9, according to the particular aspect under investigation. In general the approach was to determine the optimum co-solvent concentration, determine the effects of the catalyst concentration under the optimal co-solvent conditions and then investigate the effects of the reaction time using the optimal co-solvent and catalyst concentration. To that end, the alcohol concentration [R-OH] was varied from 0 – 100%v in at least 5 discrete intervals. The caesium carbonate concentration [Cs₂CO₃] was varied from 0 – 10 mg ml⁻¹ in 7 discrete intervals under the optimal solvent conditions. The study of each co-solvent system will be described. The HTR was cleaned using a Langford S1400 1 kW, 33 kHz ultrasonic bath (Langford Electronics, UK) for 30 minutes between each experiment.

Decomposition of PEEK using an H₂O and EtOH Co-solvent System

The reaction temperature was maintained at 623 K with constant Cs₂CO₃ and PEEK concentrations of 10 mg ml⁻¹. The reaction time was held at 30 min for all experiments. The reaction schedule is given in Table 3.

Table 3: Reaction schedule for the investigation of ethanol concentration [EtOH] on the decomposition of PEEK in H₂O / EtOH, [Cs₂CO₃] = 10 mg ml⁻¹

| Sample | [H ₂ O] (%v) | [EtOH] (%v) | M _{PEEK} (g) | P (MPa) | T (K) | t _r (min) |
|--------|----------------------------|----------------|--------------------------|------------|----------|-------------------------|
| 1 | 100 | 0 | 0.58 | 15.8 | 623 | 30 |
| 2 | 90 | 10 | 0.57 | 16.2 | | |
| 3 | 80 | 20 | 0.59 | 16.7 | | |
| 4 | 50 | 50 | 0.59 | 23.8 | | |
| 5 | 20 | 80 | 0.57 | 25.5 | | |
| 6 | 0 | 100 | 0.50 | 23.9 | | |

To investigate the effect of Cs₂CO₃ concentration with respect to the degradation of PEEK, the Cs₂CO₃ concentration was varied from 0 to 10 mg ml⁻¹ with the solvent loading rate being constant at 50 %v (57.5 ml). The co-solvent solution consisted of 80 %v H₂O and 20 %v EtOH. The concentration of PEEK [PEEK] was held constant at 10 mg ml⁻¹, the reaction temperature was 623 K and the reaction time was 30 minutes. The reaction schedule is presented in Table 4.

Table 4: Reaction schedule for the investigation of caesium carbonate concentration [Cs₂CO₃] on the decomposition of PEEK in H₂O / EtOH

| Sample | [Cs ₂ CO ₃] (mg ml ⁻¹) | M _{PEEK} (g) | T (K) | t _r (min) | P (MPa) |
|--------|--|--------------------------|----------|-------------------------|------------|
| 1 | 0.00 | 0.57 | 623 | 30 | 16.8 ± 0.2 |
| 2 | 0.94 | 0.58 | | | |
| 3 | 2.07 | 0.57 | | | |
| 4 | 4.21 | 0.57 | | | |
| 5 | 6.17 | 0.59 | | | |
| 6 | 8.14 | 0.57 | | | |
| 7 | 10.45 | 0.59 | | | |

The reaction time was varied from 0 - 120 minutes. The 0 minute experiment consisted exclusively of heating and cooling phases, with 0 minutes being spent at the reaction

temperature. Heating times were approximately 50 minutes, whereas cooling times were approximately 30 minutes. The Cs_2CO_3 and PEEK concentrations were maintained at 10 mg ml^{-1} for all experiments. The reaction mixture was a co-solvent comprising of 80 %v H_2O and 20 %v EtOH, the reaction temperature was 623 K. The reaction schedule is given in Table 5.

Table 5: Reaction schedule for the investigation of effects of reaction time on the decomposition of PEEK in H_2O / EtOH

| Sample | t_r (min) | M_{PEEK} (g) | T (K) | P (MPa) | $[\text{H}_2\text{O}]$ (%v) | $[\text{EtOH}]$ (%v) | $[\text{Cs}_2\text{CO}_3]$ (mg ml^{-1}) |
|--------|----------------|--------------------------|----------|----------------|--------------------------------|-------------------------|---|
| 1 | 0 | 0.57 | | | | | |
| 2 | 5 | 0.59 | | | | | |
| 3 | 10 | 0.59 | | | | | |
| 4 | 20 | 0.56 | 623 | 16.9 ± 0.3 | 80 | 20 | 10 |
| 5 | 30 | 0.59 | | | | | |
| 6 | 60 | 0.59 | | | | | |
| 7 | 120 | 0.57 | | | | | |

Decomposition of PEEK using an H_2O and PrOH Co-solvent System

The methodology for the investigation into the decomposition of PEEK using an H_2O / PrOH co-solvent system is identical to the methodology for the H_2O / EtOH system. The reaction schedules for the investigation of $[\text{Pr-OH}]$, $[\text{Cs}_2\text{CO}_3]$ and reaction time are given in Tables 6, 7 and 8 respectively.

Table 6: Reaction schedule for the investigation of propanol concentration [PrOH] on the decomposition of PEEK in H₂O / PrOH, [Cs₂CO₃] = 10 mg ml⁻¹

| Sample | [H ₂ O] (%v) | [PrOH] (%v) | M _{PEEK} (g) | P (MPa) | T (K) | t _r (min) |
|--------|----------------------------|----------------|--------------------------|------------|----------|-------------------------|
| 1 | 100 | 0 | 0.58 | 15.8 | 623 | 30 |
| 2 | 90 | 10 | 0.61 | 15.7 | | |
| 3 | 80 | 20 | 0.60 | 16.4 | | |
| 4 | 50 | 50 | 0.59 | 22.4 | | |
| 5 | 20 | 80 | 0.58 | 23.9 | | |
| 6 | 0 | 100 | 0.59 | 20.6 | | |

A mixture of 80 %v H₂O and 20 %v PrOH was selected as the solvent composition for the investigation of the effect of the catalyst concentration. The reaction schedule is provided in Table 7.

Table 7: Reaction schedule for the investigation of caesium carbonate concentration [Cs₂CO₃] on the decomposition of PEEK in H₂O / PrOH

| Sample | [Cs ₂ CO ₃] (mg ml ⁻¹) | M _{PEEK} (g) | T (K) | t _r (min) | P (MPa) |
|--------|--|--------------------------|----------|-------------------------|------------|
| 1 | 0.0 | 0.59 | 623 | 30 | 16.5 ± 0.3 |
| 2 | 1.0 | 0.58 | | | |
| 3 | 2.2 | 0.58 | | | |
| 4 | 4.3 | 0.58 | | | |
| 5 | 6.1 | 0.58 | | | |
| 6 | 8.0 | 0.58 | | | |
| 7 | 10.4 | 0.60 | | | |

The investigation into the effects of the reaction time was carried out by maintaining the co-solvent concentrations that were used to investigate the effect of the catalyst. The catalyst concentration and PEEK concentration were held constant at 10 mg ml⁻¹. The reaction schedule is given in Table 8.

Table 8: Reaction schedule for the investigation of effects of reaction time on the decomposition of PEEK in H₂O / PrOH

| Sample | t _r (min) | M _{PEEK} (g) | T (K) | P (MPa) | [H ₂ O] (%v) | [PrOH] (%v) | [Cs ₂ CO ₃] (mg ml ⁻¹) |
|--------|-------------------------|--------------------------|----------|------------|----------------------------|----------------|--|
| 1 | 0 | 0.57 | | | | | |
| 2 | 5 | 0.59 | | | | | |
| 3 | 10 | 0.59 | | | | | |
| 4 | 20 | 0.60 | 623 | 16.4 ± 0.2 | 80 | 20 | 10 |
| 5 | 30 | 0.60 | | | | | |
| 6 | 60 | 0.59 | | | | | |
| 7 | 120 | 0.62 | | | | | |

Decomposition of PEEK using an H₂O and DMK Co-solvent System

To investigate the effect of additional solvents that are Generally Recognised as Safe (GRAS), acetone was used as a co-solvent for a limited number of reactions. The limited number of experimental runs in this investigation is a result of a technical challenge that is discussed in Chapter 4.2.3. The reaction schedule is given in Table 9.

Table 9: Reaction schedule for the investigation of acetone concentration [DMK] on the decomposition of PEEK

| Sample | [H ₂ O] (%v) | [DMK] (%v) | M _{PEEK} (g) | P (MPa) | T (K) | t _r (min) |
|--------|----------------------------|---------------|--------------------------|------------|----------|-------------------------|
| 1 | 100 | 0 | 0.58 | 15.8 | | |
| 2 | 90 | 10 | 0.57 | 15.8 | 623 | 30 |
| 3 | 80 | 20 | 0.59 | 16.2 | | |
| 4 | 50 | 50 | 0.59 | 20.9 | | |

Analysis of the recovered aqueous / organic mixtures was carried out by High-Performance Liquid Chromatography (HPLC) and Gas Chromatography Mass Spectrometry (GC-MS). Analysis of the recovered solid material was carried out by Thermogravimetric Analysis (TGA), Fourier Transform Infra-Red Spectroscopy (FT-IR), Scanning Electron Microscopy (SEM), Energy Dispersive X-Ray Spectrometry (EDX), Differential Scanning Calorimetry (DSC)

and optical microscopy. A detailed explanation of the method of analysis for each technique is given in Chapter 3.4.3.

3.3.3. Decomposition and Recycling of Polyepoxide Thermoset Resin

A model polyepoxide resin, 2,2-bis[4-(glycidyloxy)phenyl]propane (DER 332, BADGE, DGEBA), was used to study the effects of a co-solvent system on the decomposition of a thermoset resin. By using this model resin, the objective was to transfer the knowledge gained to the study of composite materials. Carrying out this investigation in the absence of carbon fibres allows for the study of the decomposition reactions without the mass-transfer effects provided by the carbon fibres and prevents any potential interference of the carbon fibre sizing. Having previously discussed the application of co-solvents with respect to the decomposition of a high-performance thermoplastic composite materials (PEEK, see Chapter 3.3.2) water, ethanol and propanol were chosen as the initial solvents for this study. A fourth solvent, butanol, was also introduced to carryout a limited investigation into the effect of the carbon chain length on the decomposition reactions. The format of this investigation follows that of the PEEK decomposition reactions, starting with the effects of the co-solvent concentration [R-OH] followed by the effects of the catalyst concentration [Cs₂CO₃] before focussing on the effects of the reaction time (t_r). The investigation into the effect of the carbon chain length focussed only on the effect of [R-OH] and is therefore presented separately. The preparation of the BADGE based epoxy resin was identical for all reactions and will be presented prior to the decomposition reactions.

Preparation of BADGE Based Epoxy Resin

An aluminium mould was lined with a poly(ethanol) (PVA) release agent, designed to assist in the removal of the cured resin from the mould, and allowed to stand for approximately 30 minutes. Using a Sartorius Research R160P balance (Sartorius AG, Germany) (standard deviation, $\leq \pm 0.02$ mg) the DER 332 was measured into a glass beaker with the mass being accurately recorded. Using equation 1, the mass of DDS required was calculated and subsequently measured into a second beaker.

$$M_{DDS} = \frac{Mr_{DDS}}{N_S} \times \frac{M_{DER}}{EEW}$$

Equation 1: DER 332 + DDS reaction stoichiometry

Where; M_{DDS} = Mass of DDS required, Mr_{DDS} = Relative molecular mass of DDS, M_{DER} = Mass of DER 332 used, N_S = Number of substitution sites per DDS molecule, EEW = Epoxide equivalent number for DER 332

Therefore, to determine the mass of DDS required for the production of approximately 40 g of resin (cured mass) the following values are substituted into Equation 1;

$M_{r_{DDS}} = 248.3 \text{ g mol}^{-1}$, $M_{DER} = 30 \text{ g}$, $N_S = 4$, $EEW = 176$

$$M_{DDS} = \frac{248.3}{4} \times \frac{30}{176} = 11.279 \text{ g}$$

This calculation allows for a stoichiometric mixture of DER 332 and DDS. However, it is prudent to add the DDS in slight excess to ensure the absence of unreacted DER 332, the effects of which were discussed in Chapter 2.3. An excess of 5 % was used for all experiments.

Having obtained the required masses of DER 332 and DDS, the DER 332 was heated to 373 K using a Clifton Hotplate Stirrer (Nickel-Electro LTD, UK). A magnetic stirrer was used to distribute the heat throughout the sample, the temperature was monitored by means of a thermometer (Brannan, UK) (accuracy, $\pm 1 \text{ K}$ at 308 K). With the temperature of the DER 332 maintained between 373 and 393 K, the DDS was added to the beaker under stirring. After approximately 45 minutes the mixture was sufficiently mixed, indicated by transparency of the fluid. The viscous fluid was transferred to the aluminium mould (110 mm x 85 mm) and immediately placed in a pre-heated muffle furnace (Sanyo Gallenkamp Plc, UK) at 393 K to prevent cooling of the resin. The resin was then cured, starting with an initial heating rate of 1 K min^{-1} , according to the curing cycle shown in Figure 7.

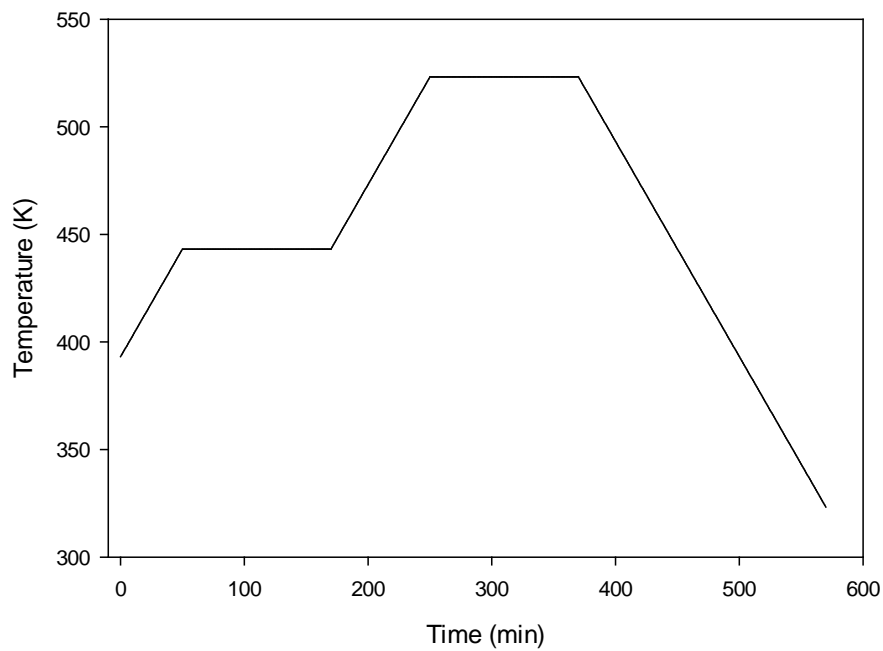


Figure 7: D.E.R. 332 DDS Polyepoxide curing cycle, all dynamic segment rates = 1 K min^{-1}

The cured polyepoxide resin was removed from the mould and its mass was recorded before being cut into sections for further processing.

Sample Quality Control

Analysis of the cured resin was carried out by means of optical microscopy, Differential Scanning Calorimetry, Fourier Transform Infra-Red Spectroscopy and Thermogravimetric Analysis. A detailed description of the analysis methods is provided in Chapter 3.4.3.

Decomposition Reactions for BADGE Based Epoxy Resin

Control Samples

Cured epoxy resin samples were subjected to reaction conditions comprising of water alone, at 573 K for 30 minutes in the High-Temperature Reactor (HTR) and used as a control. The reactor solvent loading was maintained at 50 %v, with the resin loading being $33 \pm 1 \text{ mg ml}^{-1}$. In all cases, epoxy resin samples were rectangular having an approximate length, width and depth of 40 mm, 10 mm and 5 mm respectively. Additional control samples were generated for each of the reaction conditions. In the investigation of the co-solvent concentration effects, the control consisted of water containing $10 \text{ mg ml}^{-1} \text{ Cs}_2\text{CO}_3$. When considering the Cs_2CO_3 concentration effects, the control sample consisted of the optimum alcohol concentration [R-OH] without the addition of Cs_2CO_3 .

Effect of Co-solvent Concentration

Decomposition reactions of epoxy resin samples were carried out in the HTR. A description of the HTR and associated equipment is provided in Chapter 3.2. The solvent loading was 50 %v for all reactions irrespective of the solvent composition and the experimental procedure was identical for all reactions, with the exception of varying compositions. The volumes of H_2O , PrOH and EtOH were measured out into a glass beaker using a burette (accuracy, $\pm 0.2 \text{ ml}$), prior to the addition of $10 \text{ mg ml}^{-1} \text{ Cs}_2\text{CO}_3$ according to the reaction schedule provided in Table 10.

Table 10: Processing condition for determination of the effect of co-solvent concentration on BADGE based resin

| Sample | T (K) | t _r (min) | Fluid | [R-OH] (%v) | [Cs ₂ CO ₃] (mg ml ⁻¹) | [Resin] (mg ml ⁻¹) |
|--------|----------|-------------------------|-------------------------|----------------|--|-----------------------------------|
| 1 | 573 | 30 | H ₂ O | 0 | 10 ± 0.4 | 33 ± 3 |
| 2 | | | EtOH/H ₂ O | 10 | | |
| 3 | | | EtOH/H ₂ O | 20 | | |
| 4 | | | EtOH/H ₂ O | 35 | | |
| 5 | | | EtOH/H ₂ O | 50 | | |
| 6 | | | EtOH/H ₂ O | 57.5 | | |
| 7 | | | EtOH/H ₂ O | 65 | | |
| 8 | | | EtOH/H ₂ O | 80 | | |
| 9 | | | EtOH | 100 | | |
| 10 | | | PrOH / H ₂ O | 10 | | |
| 11 | | | PrOH / H ₂ O | 20 | | |
| 12 | | | PrOH / H ₂ O | 50 | | |
| 13 | | | PrOH / H ₂ O | 80 | | |
| 14 | | | PrOH | 100 | | |

The contents of the beaker were then transferred to the reactor. With the epoxy resin samples contained within a stainless steel basket, suspended at the reactor centreline to ensure isolation from the reactor walls, the reactor was sealed. With the reactor sealed, and the coolant supply to the agitator cooling jacket activated, the furnace was switched on and the reactor was brought to the reaction temperature as specified in Table 10. Upon attaining the reaction temperature, the reaction time was allowed to elapse prior to removing the furnace from the reactor and cooling the reactor with compressed air. Typical heating and cooling times were 50 and 30 minutes respectively.

Effect of Caesium Carbonate Concentration

After investigating the effect of the co-solvent on the decomposition of the epoxy resin, the caesium carbonate concentration [Cs_2CO_3] was varied from 0 – 10 mg ml^{-1} in 100 % ethanol and 100 % propanol to study its effects on the decomposition process. The reaction conditions are presented in Table 11.

Table 11: Processing conditions for the determination of the effects of Cs_2CO_3 on BADGE based resin

| Sample | T (K) | t_r (min) | Fluid | [Cs_2CO_3] (mg ml^{-1}) | [Resin] (mg ml^{-1}) |
|--------|----------|----------------|-------|---|------------------------------------|
| 1 | 573 | 30 | EtOH | 0 | 32 ± 3 |
| 2 | | | EtOH | 1 | |
| 3 | | | EtOH | 2 | |
| 4 | | | EtOH | 4 | |
| 5 | | | EtOH | 6 | |
| 6 | | | EtOH | 8 | |
| 7 | | | EtOH | 10 | |
| 8 | | | PrOH | 0 | |
| 9 | | | PrOH | 1 | |
| 10 | | | PrOH | 2 | |
| 11 | | | PrOH | 4 | |
| 12 | | | PrOH | 6 | |
| 13 | | | PrOH | 8 | |
| 14 | | | PrOH | 10 | |

Effect of Reaction Time

The effect of the reaction time on the decomposition of the epoxy resin was investigated by varying the reaction time from 0 – 60 minutes. The processing conditions are given in Table 12.

Table 12: Processing conditions for the determination of the effects of reaction time on BADGE based resin

| Sample | T (K) | t _r (min) | Fluid | [Cs ₂ CO ₃] (mg ml ⁻¹) | [Resin] (mg ml ⁻¹) |
|--------|----------|-------------------------|-------|--|-----------------------------------|
| 1 | 573 | 0 | PrOH | 10 ± 0.1 | 35 ± 5 |
| 2 | | 5 | PrOH | | |
| 3 | | 10 | PrOH | | |
| 4 | | 20 | PrOH | | |
| 5 | | 30 | PrOH | | |
| 6 | | 45 | PrOH | | |
| 7 | | 60 | PrOH | | |
| 8 | | 0 | EtOH | | |
| 9 | | 5 | EtOH | | |
| 10 | | 10 | EtOH | | |
| 11 | | 20 | EtOH | | |
| 12 | | 30 | EtOH | | |
| 13 | | 45 | EtOH | | |
| 14 | | 60 | EtOH | | |

All samples were dried post reaction for 120 minutes in a drying oven maintained at 333 K, prior to having their mass recorded. The percentage decomposition was determined by difference, measuring the dry mass of the epoxy sample pre and post reaction. The percentage decomposition was ascertained by equation 2.

$$\%d_g = 100 - \left(\left(\frac{M_{Ei} - M_{Ef}}{M_{Ei}} \right) \times 100 \right)$$

Equation 2: % decomposition of epoxy resin

Where; %d_g = percentage decomposition, M_{Ei} = Initial mass of epoxy resin, M_{Ef} = Final mass of epoxy resin

Effect of Carbon Chain Length

Butanol (BuOH) was used to investigate the effect of the carbon chain length on the decomposition of a BADGE based epoxy resin. This was done to determine whether the differences between the ethanol and propanol reaction systems were attributable to the additional carbon atom possessed by propanol over ethanol. Only the effect of the butanol concentration was investigated. The reaction schedule for this investigation is provided in Table 13.

Table 13: Reaction schedule for the investigation of carbon chain-length on the decompositon of thermoset epoxy resin

| Sample | T (K) | t _r (min) | Fluid | [R-OH] (%v) | [Cs ₂ CO ₃] (mg ml ⁻¹) | [Resin] (mg ml ⁻¹) |
|--------|-------|----------------------|-------------------------|-------------|---|--------------------------------|
| 1 | 573 | 30 | H ₂ O | 0 | 10 ± 0.4 | 33 ± 3 |
| 2 | | | H ₂ O / BuOH | 10 | | |
| 3 | | | H ₂ O / BuOH | 20 | | |
| 4 | | | H ₂ O / BuOH | 50 | | |
| 5 | | | H ₂ O / BuOH | 80 | | |
| 6 | | | BuOH | 100 | | |

The reaction process was carried out in an identical way to the investigation into the effects of the ethanol and propanol concentrations, as detailed in the beginning of this chapter (Chapter 3.3.2). Whilst the investigation proceeds in the same way as the previous investigations, unlike the previous alcohols studied, water and butanol are immiscible and consequently form a bi-phasic mixture at room temperature. For this reason the study is presented separately, as is the case with the results of the study.

3.3.4. Processing and Characterisation of Carbon Fibre

The objective of the study was to investigate the effect of the process conditions used in the decomposition of PEEK and epoxy resins on the physical properties of carbon fibre. In the case of PEEK this was necessary as the carbon fibres contained within the PEEK pellets are short, having a length of several millimetres, and were beyond the limit of what can feasibly be subjected to tensile testing with the equipment available. Therefore, by processing carbon fibres under the same conditions it is possible to gain an understanding of how the said conditions affect the properties of the carbon fibres contained within the PEEK. Whilst this approach does not allow for the determination of the tensile strength of the carbon fibres within the PEEK pellets, it does allow the percentage deviation from the initial conditions to be made. By studying the effects of the processing conditions used to decompose the epoxy resin it is possible to investigate the impact of the processing conditions on the carbon fibres without the additional complications introduced by the resin decomposition products. In doing so, it is then possible to separate the effects of the co-solvents, the catalyst and the decomposition products in isolation. This leads to a more holistic understanding of the decomposition of carbon fibre reinforced composite materials and how the decomposition process affects the properties of the carbon fibres.

The processing of the carbon fibres was carried out in two stages. The initial stage investigated a range of co-solvent concentrations in the absence of Cs_2CO_3 . The second stage focused on the particular conditions that were used to decompose PEEK and epoxy resin, thereby incorporating the use of Cs_2CO_3 .

Carbon Fibre Sample Preparation for Supercritical Fluid Processing.

Bundles of carbon fibres, approximately 100 mm in length, were cut and loaded into the HTR. A full description of the HTR and ancillary equipment is provided in Chapter 3.2. A solvent loading of 50 %v was used for all experiments. To generate control samples, bundles of carbon fibre tow were cut into approximately 100 mm sections and subjected to processing with water, in the absence of a co-solvent or catalyst, as detailed in Table 14. With the reactor sealed, the furnace was switched on and allowed to reach the required set point. Once the set point was attained the reaction timer was started. Once the reaction time had elapsed the reactor was removed from the furnace and cooled using a water bath. The reaction time (t_r) is defined as the amount of time that the reactor spends at the set point and does not include the time taken to heat and cool the reactor. Heating and cooling times were typically 50 and 30 minutes respectively.

Table 14: Carbon fibre processing control sample generation

| Control Sample | T (K) | Solvent | t_r (min) | [Cs ₂ CO ₃] (mg ml ⁻¹) |
|----------------|-------|------------------|-------------|---|
| 1 | 523 | H ₂ O | 30 | 0 |
| 2 | 573 | | | |
| 3 | 623 | | | |

The carbon fibres were processed in an identical manner to the control samples, differing only in the concentration of the solvents and catalyst and reaction temperature. The solvent concentrations used, according to the designed Taguchi Experiment design, are provided in Table 15.

Table 15: Reaction schedule for the investigation of the effect of co-solvent [Co-solvent] concentration on the tensile strength of carbon fibres. $[Cs_2CO_3] = 0 \text{ mg ml}^{-1}$

| Sample | T (K) | Co-solvent | [co-solvent] (%v) | [H ₂ O] (%v) | t _r (min) |
|--------|----------|------------|----------------------|----------------------------|-------------------------|
| 1 | 623 | PrOH | 20 | 80 | 30 |
| 2 | | | 50 | 50 | |
| 3 | | | 80 | 20 | |
| 4 | | | 100 | 0 | |
| 5 | 623 | DMK | 20 | 80 | |
| 6 | | | 50 | 50 | |
| 7 | | | 80 | 20 | |
| 8 | | | 100 | 0 | |
| 9 | 623 | EtOH | 20 | 80 | |
| 10 | | | 50 | 50 | |
| 11 | | | 80 | 20 | |
| 12 | | | 100 | 0 | |
| 13 | 523 | PrOH | 20 | 80 | |
| 14 | | DMK | 50 | 50 | |
| 15 | | EtOH | 80 | 20 | |
| 16 | 573 | PrOH | 50 | 50 | |
| 17 | | DMK | 80 | 20 | |
| 18 | | EtOH | 20 | 80 | |
| 19 | 623 | PrOH | 80 | 20 | |
| 20 | | DMK | 20 | 80 | |
| 21 | | EtOH | 50 | 50 | |

Specific conditions investigated for their ability to decompose PEEK, epoxy resin, or both polymers are given in Table 16. In some respects this additional investigation is an extension of the Taguchi Experiment presented in Table 15. It was carried out separately to fully decouple the effects, or lack thereof, the catalyst has on the carbon fibre properties.

Table 16: Specific investigation of effects of $[Cs_2CO_3]$ in conjunction with co-solvents on the physical properties of carbon fibres

| Sample | Temperature (K) | Co-solvent | [R-OH] (%v) | [H ₂ O] (%v) | Time (min) | [Cs ₂ CO ₃] (mg ml ⁻¹) |
|--------|-----------------|------------|-------------|-------------------------|------------|---|
| 1 | 573 | - | - | 100 | 30 | 10 ± 0.5 |
| 2 | 573 | PrOH | 100 | 0 | | |
| 3 | 573 | EtOH | 100 | 0 | | |
| 4 | 623 | EtOH | 20 | 80 | | |

After cooling the HTR the carbon fibres were removed, placed onto aluminium foil and deposited into a drying cabinet (Fisons, UK) for 120 minutes at 333 K. After drying, the carbon fibres were removed from the drying oven and manually aligned into tows. The tows were then cut to 85 mm in length in preparation for counting. The number of fibres within each carbon fibre bundle was determined according to its electrical properties by using Electrochemical Impedance Spectroscopy (EIS) [245]. Having determined the number of fibres present in the bundle, the bundle was placed in a bespoke stainless steel carbon fibre alignment tool (see Figure 8) prior to having a small amount of Araldite Rapid resin (Huntsman Advanced Materials, USA) applied to either end. The resin was subsequently allowed to cure for 24 hours at room temperature.



Figure 8: Bespoke carbon fibre alignment tool, stainless steel, approximately 120 mm in length

Once the resin had cured, the carbon fibre bundles were loaded into to the Universal Testing Machine (UTM). The bundle of fibres were gripped at either end, with the grips in contact with the resin. A testing speed of 2 mm min^{-1} was used, the fibre bundles being tested to destruction. Since the number of fibres in the bundle was known, from EIS measurements, it was possible to determine both the average maximum tensile force and average work done per fibre. Knowledge of the number of fibres also facilitated in determination of the average tensile strength. Statistical analysis of the carbon fibre bundle properties was carried using Minitab® (Minitab Inc. USA).

Tensile Testing of Carbon Fibres

The tensile testing of single and bundles of carbon fibres is described in detail in Chapter 3.4.4. The method for accurately determining the number of carbon fibres in a given bundle was developed as part of this research. This method is also described in full in Chapter 3.4.4.

3.3.5. Recycling of Carbon Fibre Reinforced Polyepoxide Composite Materials

An initial investigation into the effects of the processing conditions used to decompose a model polyepoxide resin, see Chapter 3.1, was carried out. This research directs future research into the use of such conditions to decompose a range of thermoset and thermoplastic polymers and their associated composite materials. Since the intention was to assess the viability, similarities and differences between the model epoxy resin and a commercially available CFRP, the methodology of this initial investigation is identical to that carried out in Chapter 3.3.3. The reaction schedule for this limited investigation is given in Table 17.

Table 17: Reaction schedule for initial investigation into the decomposition of commercially available carbon fibre reinforced polymers

| Sample | T (K) | P (MPa) | t _r (min) | Solvent (%v) | [Cs ₂ CO ₃] (mg ml ⁻¹) | [comp] (mg ml ⁻¹) | Supplier |
|--------|----------|------------|-------------------------|-----------------|--|----------------------------------|-------------|
| 1 | 573 | 15.0 ± 0.2 | 60 | EtOH | 10 | 30.6 | Dolan Bikes |
| 2 | | | | | | 31.7 | Hexcel |
| 3 | | | | | | 67.5 | Hexcel |

Given that the precise composition and mass of epoxy resin used in the manufacture of the composite materials listed in Table 17 is not available, determination of the percentage decomposition is not trivial. However, two limiting cases exist; 1: if no decomposition of the polymer resin occurs as a result of supercritical processing, the mass loss according to TGA would be close to that of a virgin sample, and 2: if complete degradation of the polymer takes place during the supercritical processing, the mass loss according to TGA will be minimal. A detailed description of the analysis of CFRP's is provided in Chapter 3.4.3.

3.4. ANALYTICAL TECHNIQUES

3.4.1. Confirmation of PEEK Amorphicity

Differential Scanning Calorimetry

Amorphous samples were qualitatively identified by optical microscopy using a Prior Optical Microscope (Prior Scientific, UK). Amorphous PEEK, by definition, does not contain crystalline regions and consequently is translucent. Samples that did not meet this criteria were rejected and were not used in further experiments.

The heat of fusion (ΔH_f) for PEEK is 130 kJ kg^{-1} [85]. By using the heat of fusion the percentage crystallinity ($\%X_c$) may be determined by DSC. Analysis of the integral taken from the exotherm located at the crystallisation temperature (T_c) yields the change in enthalpy attributed to the formation of crystallites. For a sample of known mass, Equation 3 may be used to determine $\%X_c$.

$$\% X_c = \left(\frac{A_c}{M_s \times \Delta H_f} \right) \times 100$$

Equation 3: Percentage crystallinity determination for PEEK at T_c

Where: A_c = Integral value at T_c , M_s = Mass of sample, ΔH_f = Heat of fusion

Similarly, the integral obtained for the endothermic peak located at the melting temperature (T_m) may be used to calculate the percentage crystallinity. This is possible because the thermodynamic melting of a polymer is attributed to the destruction of polymer crystallites, producing an amorphous polymer melt. Thus, by substituting the

integral area of the exothermic peak (A_c) with the integral area for the endothermic peak (A_m) calculation of $\%X_c$ may be carried out by Equation 4.

$$\% X_c = \left(\frac{A_m}{M_s \times \Delta H_f} \right) \times 100$$

Equation 4: Percentage crystallinity determination for PEEK at T_m

Where: A_m = Integral value at T_m

Several samples were selected at random to undergo DSC analysis to verify the absence of crystallinity. In order to ascertain the absence of crystallinity by DSC it is necessary to heat the sample through the crystallisation temperature. It is therefore not possible to carry out polymer processing any sample that has previously been used to demonstrate the absence of crystallinity. DSC analysis was carried out using a Mettler Toledo HPDSC827^e. The DSC was calibrated using Indium, Zinc and Tin standards. Cooling was provided by a Julabo F12 chiller, maintained at 278 K, and integrated controller. The method used for determining the $\%X_c$ consisted of a single dynamic region from 298 K to 673 K using a heating rate of 10K min^{-1} as shown in Figure 9.

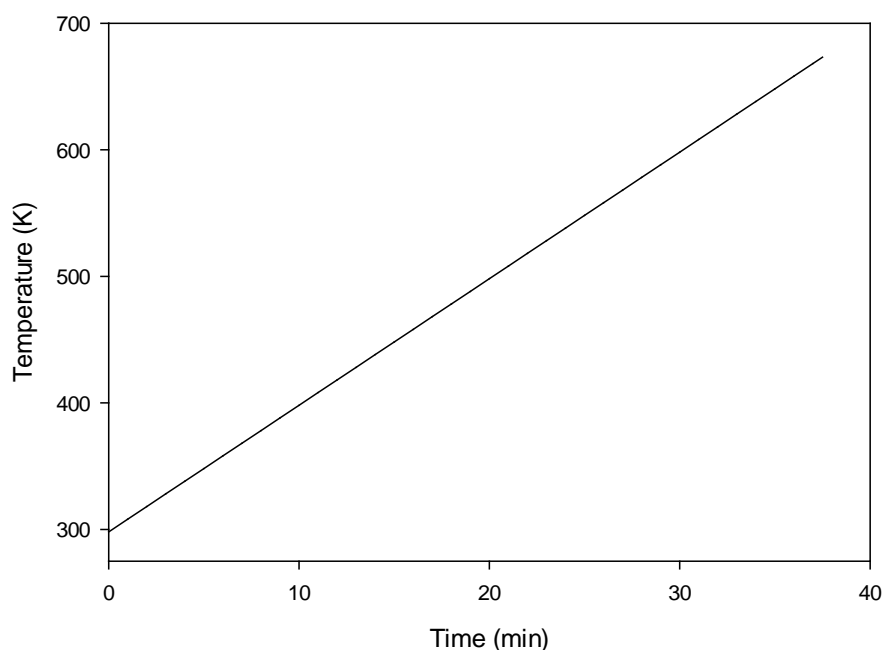


Figure 9: DSC method 1; Determination of percentage crystallinity (%X_c)

Fourier Transform Infra-Red Spectrometry

Fourier Transform Infra-Red (FT-IR) spectroscopy may be used to ascertain the percentage crystallinity of PEEK samples by analysis of the relative transmittance, or absorbance, of the sample at wavenumbers of 1305 cm^{-1} and 1280 cm^{-1} respectively [310]. A Jasco FT/IR-6300 spectrometer was used to obtain data with a resolution of 1 cm^{-1} over the range of 900 cm^{-1} to 4000 cm^{-1} with 300 accumulations, an aperture of 3.5 mm and a scanning rate of 2 mm sec^{-1} , without post accumulation data smoothing. Determination of crystallinity by FT-IR does not require the sample to be heated through the crystallisation temperature, and consequently, in theory it would be possible to analyse the samples by FT-IR prior to processing with supercritical fluids. However, due to the physical dimensions of the DSC pan severe distortion of the Aluminium pan takes place when mounted the Specac Attenuated Total Reflectance (ATR) Golden Gate accessory. Separation of the polymer sample from the

DSC pan negates this problem but also reduces the contact between the DSC pan and the polymer sample in the post supercritical fluid processing analysis. Therefore, samples analysed by FT-IR were not subsequently subjected to scCO₂ processing.

Wide Angle X-Ray Spectrometry

Wide Angle X-Ray Spectrometry (WAXS) may be used to determine the percentage crystallinity within a polymer sample by analysing the intensity of the peaks in contrast to that of the background. This technique was used as a qualitative method to further confirm the absence of crystallites in the sample. This information is combined with the data obtained by DSC and FT-IR to provide confirmation of the amorphous state of the polymer. Data were acquired using a Bruker D2 Phaser Diffractometer (Bruker, Germany) scanning over the range of $2\theta = 16 - 34^\circ$, with a potential, current and power of 30 kV, 10 mA and 300 W respectively using a cobalt source of wavelength 1.79026 Å. The sample was rotated at 15 rpm with the acquisition taking place using a Lynxeye[®] detector (Bruker, Germany).

Several grams of PEEK were loaded into the sample holder, prior to mounting the sample holder onto the stage. Where amorphous samples were used, the sample was loaded such that the flattest side faced the detector, thereby maximising the signal to noise ratio. Where PEEK powders were used, the sample holder was levelled prior to being loaded onto the sample stage. Since WAXS is a non-destructive technique and does not require the sample to be heated through any of the transition temperatures it was possible to use the samples analysed by WAXS in further experiments. WAXS was used exclusively to confirm the state

of the polymer samples prior to processing and was not used to perform post-processing analysis.

3.4.2. Analysis of Supercritical Carbon Dioxide Processed PEEK

Differential Scanning Calorimetry

Since the objective was to identify the effects of scCO₂ processing on the physical properties, in particular the polymeric transitions, of PEEK the same DSC method that was used to confirm their amorphicity was used to carryout the post scCO₂ processing analysis. The DSC method is described and presented in Chapter 3.4.1. (DSC Method 1).

High-Pressure Differential Scanning Calorimetry

Unlike conventional DSC, carrying out HPDSC with supercritical fluids is not trivial and requires consideration of the manner in which the fluid to be used will behave within the pressure chamber. The pressure chamber has a volume of approximately 150 cm³, part of which is occupied by the thermocouple, reference and sample pans. The thermocouple, by design, is the sole heat source within the pressure chamber and is designed to heat the sample and reference pans in a measured and precise way. The unintended side effect becomes apparent when considering the pressure chamber under a given pressure of CO₂. Under such circumstances, the thermocouple also heats the CO₂ within close proximity which leads to a reduction in the CO₂ density. Ultimately, the consequence is the introduction of turbulence within the system with the warmer, less dense CO₂ being

replaced with cooler more dense CO₂. Whilst DSC does not measure turbulence or density, turbulence introduces a fluid of a different temperature to the thermocouple, sample and reference pans. This process does not necessarily take place simultaneously to all components and the result is the introduction of noise to the measurement. This noise increases with increasing CO₂ pressure due to the increased density of the fluid. The noise also increases with increasing heating rate due to the reduced time allowed for the fluid and thermocouple to attain thermal equilibrium. Multiple methods were developed to mitigate this effect, with limited success, and are presented and discussed individually.

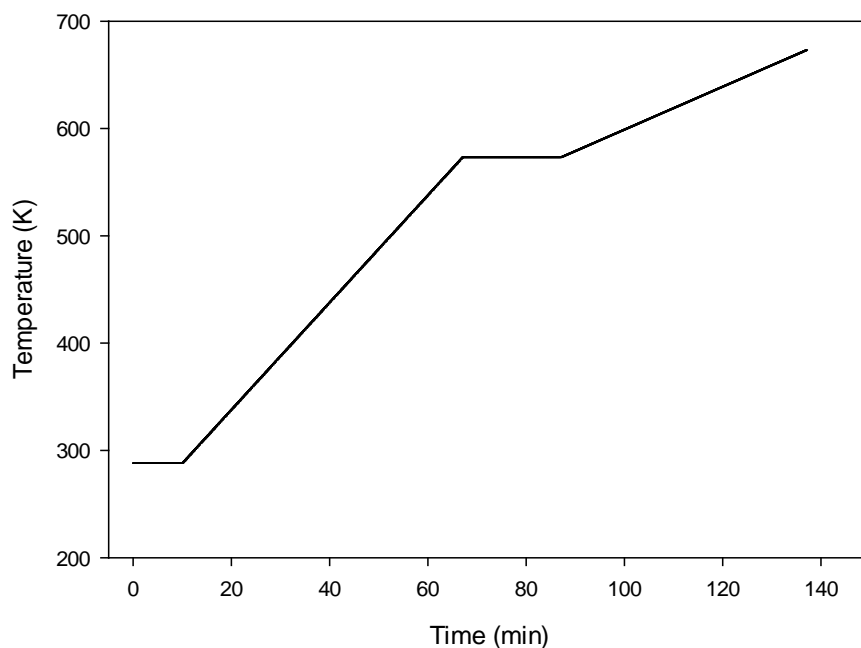


Figure 10: HPDSC Method 1, analysis of PEEK melting process under CO₂ pressure environment

HPDSC Method 1 is designed to allow a period of time to elapse, during which thermal equilibrium of the CO₂ and the thermocouple is taking place, prior to heating the sample

from 298 K to 573 K at 5 K min^{-1} . The sample is held isothermally at 573 K for 20 minutes before the sample is heated to 673 K at 2 K min^{-1} . By reducing the heating rate in the second dynamic segment the intention was to increase the thermal equilibrium between the CO_2 and the thermocouple, and therefore, reduce the experimental noise when carrying out analysis of the melting process of PEEK.

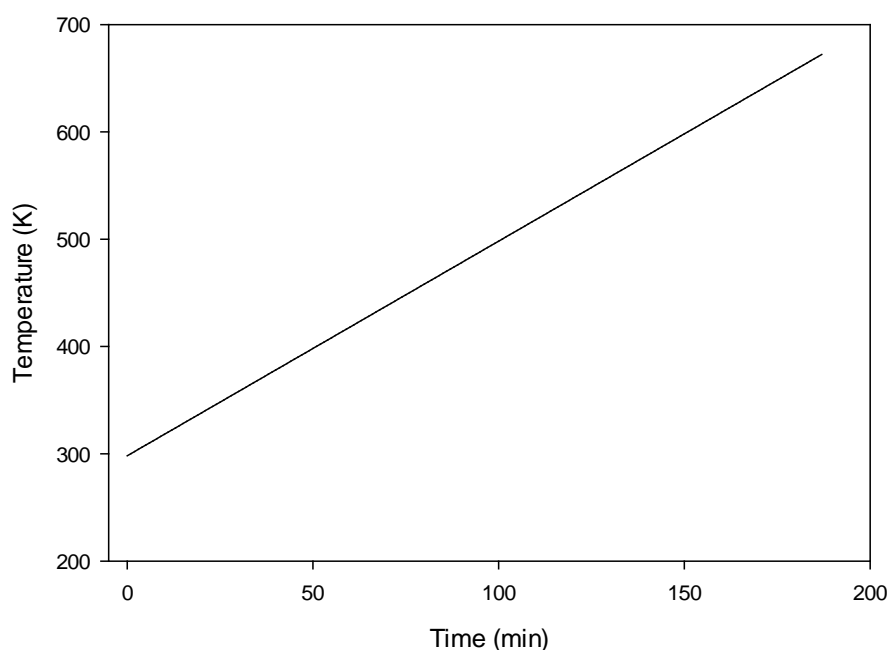


Figure 11: HPDSC Method 2, single dynamic segment with a slow heating rate to investigate the impact of CO_2 on T_g , T_c and T_m

HPDSC Method 2 consists of a single dynamic segment, heating from 298 K to 673 K at 2 K min^{-1} . The design intent was to reduce the experimental noise, introduced by the CO_2 , across all three polymer transitions to provide direct observation of the influence of CO_2 upon the T_c , T_g and T_m .

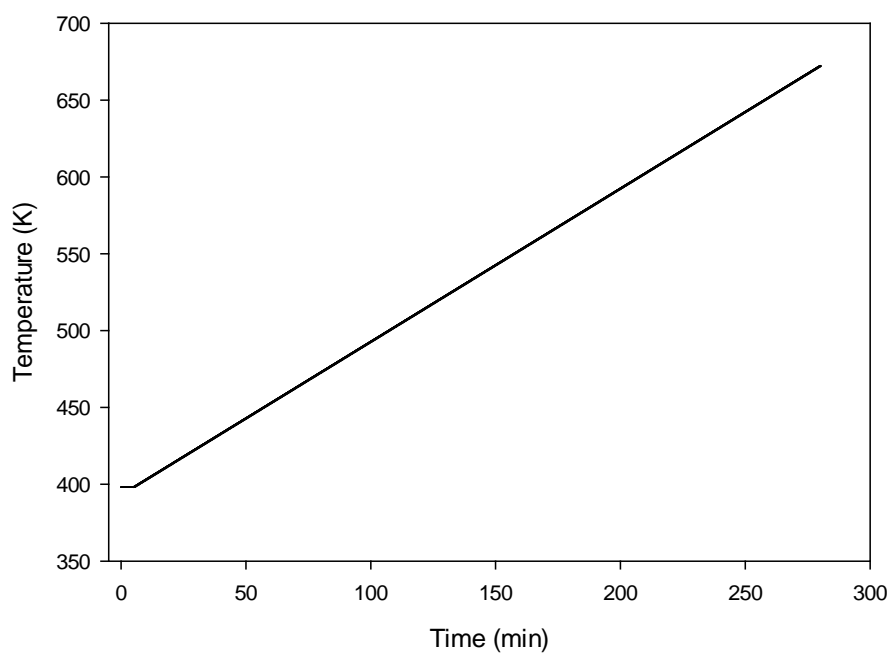


Figure 12: HPDSC Method 3, minimal heating rate for maximum thermal equilibrium

HPDSC Method 3 was designed to provide low-noise data across all polymeric transitions. Although it initially appears similar to HPDSC Method 2 (Figure 11) the starting temperature is 400 K, followed by a 5 min isothermal segment. The sample is then heated to 673 K at 1 K min^{-1} in an attempt to maximise the thermal equilibrium between the CO_2 and the thermocouple.

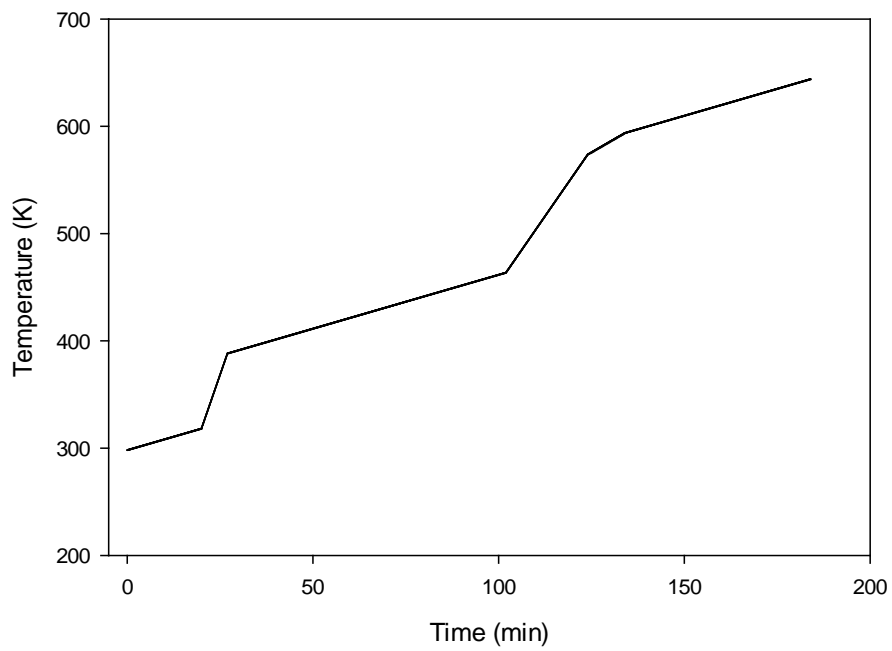


Figure 13: HPDSC Method 4, dynamic measurement of polymer transition temperatures

The design intention of HPDSC Method 4 (Figure 13) is similar to HPDSC Method 3, but is specifically designed to reduce the analysis time by more rapidly achieving the polymer transition temperatures than what is achievable with HPDSC Method 3.

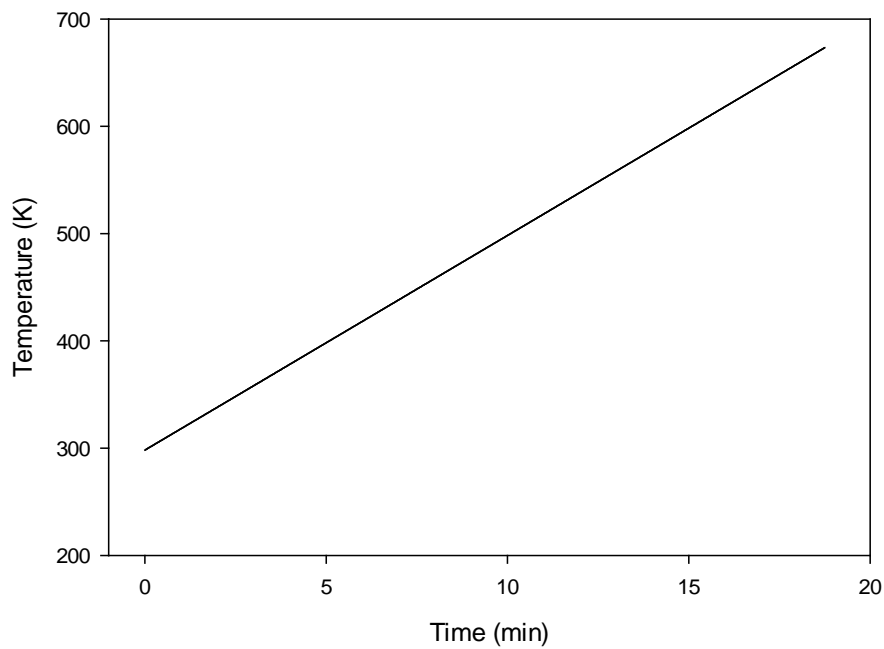


Figure 14: HPDSC Method 5, rapid heating through all polymeric transitions T_g , T_c and T_m

HPDSC Method 5 (Figure 14) consists of a single dynamic segment heating from 298 K to 673 K at 20 K min^{-1} . Contrary to HPDSC Methods 1 – 4, it is designed to minimise the thermal equilibrium between the thermocouple and the CO_2 . In doing so, it is likely that only the CO_2 adjacent to the sample and reference pans is close to the temperature of the sample. Having a relatively high heating rate it may be possible to alleviate, to some extent, the effects of CO_2 turbulence.

Fourier Transform Infra-Red Spectrometry

FT-IR Method 2

FT-IR spectrometry was used identify the functional groups associated with PEEK as well as to investigate the presence of CO_2 trapped within the polymer matrix. Each spectrum

consists of 32 accumulations over the range of 800 cm^{-1} – 4000 cm^{-1} with a resolution of 1 cm^{-1} , through a 3.2 mm aperture with a scan speed of 2 mm s^{-1} . The measurements were carried out at ambient conditions without the addition of external pressure. The samples were held in place by means of an Attenuated Total Reflectance accessory fitted to the FT-IR spectrometer as described in Chapter 3.4.1.

Thermogravimetric Analysis

Thermogravimetric Analysis (TGA) was used to investigate the temperature at which significant deviation from the original sample mass took place. This expedites the investigation into residual CO_2 trapped within the polymer matrix and may also be used to analyse the polymer transitions. The TGA method used is presented in Figure 15 (TGA Method 1).

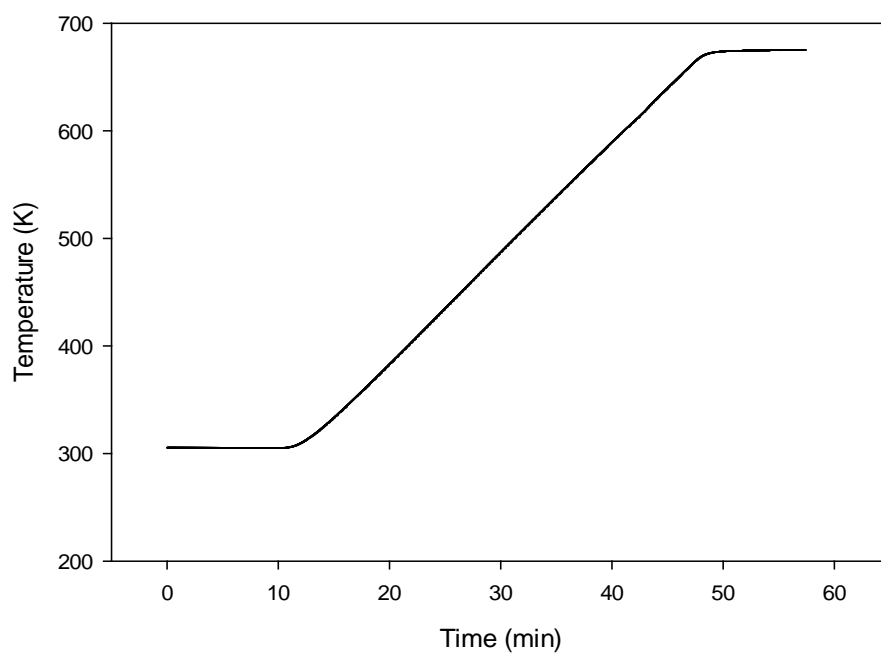


Figure 15: TGA Method 1, post $scCO_2$ processing analysis of PEEK

3.4.3. Analysis of Polymer Decomposition Products

Differential Scanning Calorimetry

The analysis of post-processing epoxy resin solid samples, where recovered, was carried out on a Mettler Toledo HPDSC 827^e using DSC Method 2 shown in Figure 16.

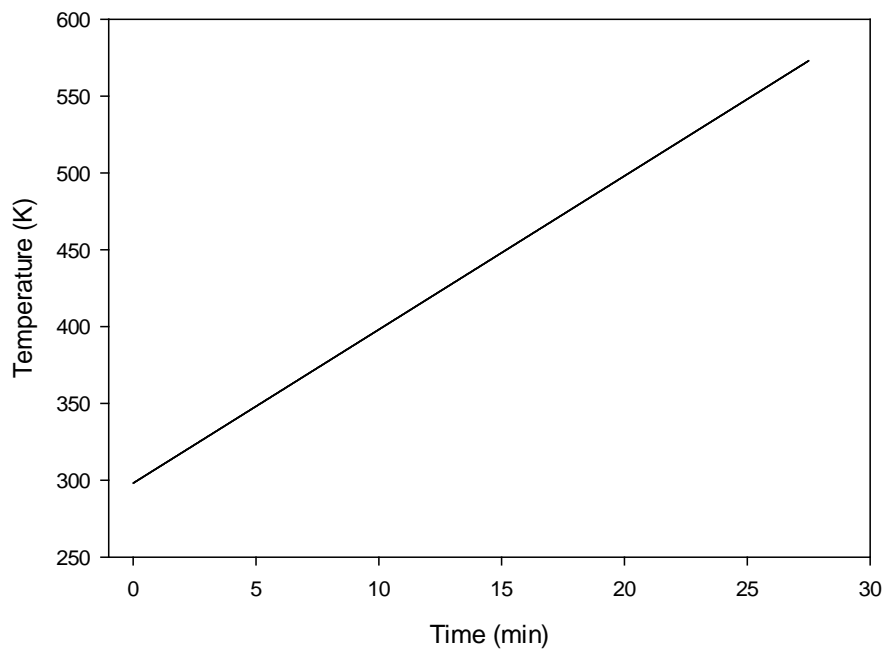


Figure 16: DSC Method 2 used for the analysis of recovered epoxy resin samples. $dT / dt = 10 \text{ K min}^{-1}$

The T_g of the cured BADGE based epoxy resin is a function of the cross-linking between the molecular chains. Therefore, by analysing the recovered solids by DSC the extent of the decomposition may be qualitatively evaluated. In addition, identification of decomposition products remaining within the polymer matrix may also be possible. DSC Method 2 was used for the analysis of all recovered solid samples of epoxy resin.

Fourier Transform Infra-Red Spectroscopy

FT-IR of thermoplastic, thermoset polymers and their associated composite materials was carried out using FT-IR Method 2, described previously in Chapter 3.4.2. The versatility of FT-IR Method 2 allows for the measurement of virgin material and post-processing solids, without modification.

Thermogravimetric Analysis

Thermogravimetric Analysis (TGA) was used to analyse solid samples, post-processing. Since the objective is to heat the sample through its decomposition temperature, a single method was developed to analyse both the thermoset and thermoplastic materials studied. TGA Method 2 is presented in Figure 17.

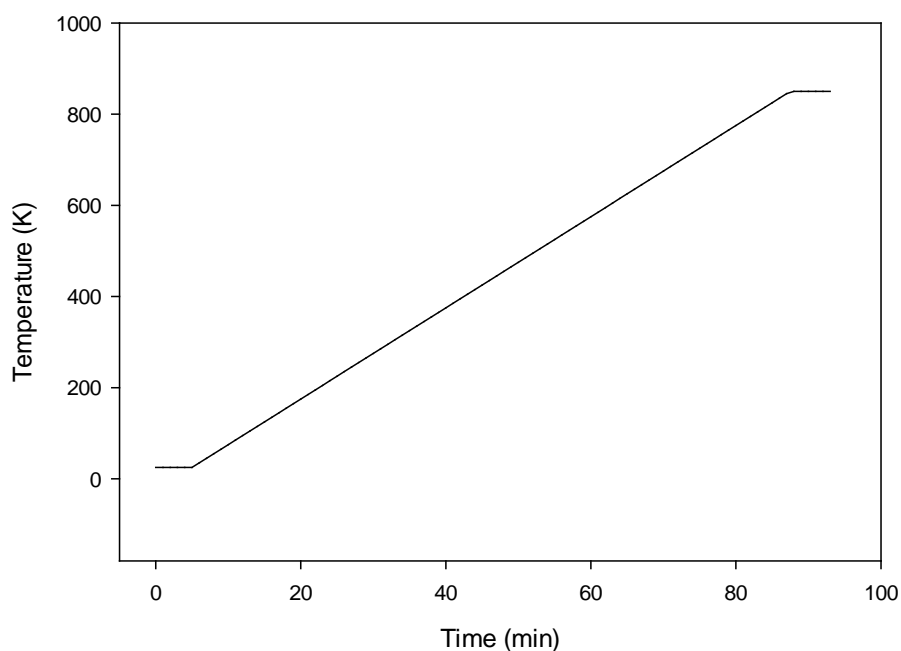


Figure 17: TGA Method 2 used for the analysis of thermoset and thermoplastic polymers and their associated composite materials. $dT / dt = 10 \text{ K min}^{-1}$

The isothermal segment at the beginning of the method is to allow all the necessary components to achieve thermal equilibrium prior to being heated from 298 K to 1123 K at 10 K min^{-1} . A second isothermal segment is employed at the end of the analysis to ensure that the decomposition is complete and once again the system is at thermal equilibrium.

Thermogravimetric Analysis – Fourier Transform Infra-Red Spectrometry

By analysing the exhaust gasses from the TGA it may be possible to identify, in part, the decomposition products produced at a given temperature. Unlike analysis of the scCO_2 processed samples, the polymer decomposition samples pass through their decomposition temperatures and as such may evolve condensable vapours. Transfer between the TGA and the FT-IR gas analysis cell requires the use of a Heated Transfer Line (HTL) to prevent the condensation of considerable proportions of the evolved vapours and gasses. As the TGA utilised TGA Method 2, presented previously, emphasis will be on the FT-IR parameters.

Three-dimensional FT-IR spectra were acquired over the range of $700\text{ cm}^{-1} - 4000\text{ cm}^{-1}$ with a resolution of 4 cm^{-1} . Individual spectra comprised of 32 accumulations, through a 7.1 mm aperture with a scan speed of 2 mm s^{-1} , were acquired for a period of 95 minutes to coincide with TGA Method 2. These parameters, with the exception of time, were also used to carryout a background spectrum prior to analysis of any samples. The flowrate through the HTL was approximately 200 ml min^{-1} , with the temperature of the HTL and gas analysis cell being 353 K.

Scanning Electron Microscopy and Energy Dispersive X-Ray Spectrometry

Samples were imaged using a Philips XL30 FEG ESEM Scanning Electron Microscope (Philips, Netherlands) with an amplitude of 20 kV. The working distance (WD) was adjusted according to the sample under analysis as was the magnification. Where necessary the samples were cut into sections, measuring approximately 15 mm^2 , and loaded onto standard SEM stubs that had been coated with an adhesive film. The samples were then

coated with gold using an Emscope SC 500 Sputter Coater (Quorum Technologies, UK) prior to being loaded into the SEM. When required Energy Dispersive X-Ray Spectrometry EDX analysis was carried out using an Inca X-Sight (Oxford Instruments, UK). Although the method of analysis is non-destructive with respect to the sample it was not possible to recover the samples analysed by SEM and SEM-EDX for further analysis due to the sample preparation process.

Gas Chromatography – Mass Spectrometry

Gas Chromatography – Mass Spectrometry (GC-MS) was used to perform separation and identification of decomposition products. A Waters Corporation GCT Premier GC-MS system (Waters Corporation, USA) was used in conjunction with necessary column to perform the required separation. The method is specific to the column type and therefore methods are presented according to the column used. In preparation for GC-MS, approximately 1.5 ml of reactor extract was filtered, to remove any suspended fines, and collected into standard GC vials. The initial method utilised a ZB5-MS column (Phenomenex, USA) and is shown in Figure 18.

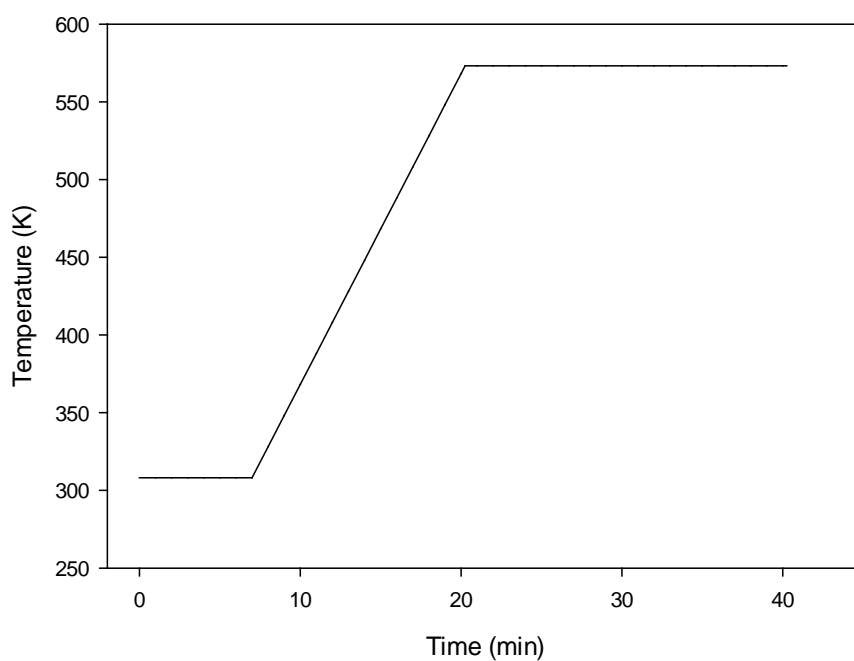


Figure 18: GC-MS Method 1 used for the separation and subsequent identification of polymer decomposition products. Column = ZB5-MS, $dT/dt = 20 \text{ K min}^{-1}$, $Q_{\text{He}} = 1 \text{ ml min}^{-1}$, $V_{\text{INJ}} = 1 \mu\text{l}$

With further development the column used for the identification of polymer decomposition products was changed to a Zebron ZB-WAX column (Zebron, Phenomenex USA). GC-MS Method 2 was used with the ZB-WAX column is presented in Figure 19.

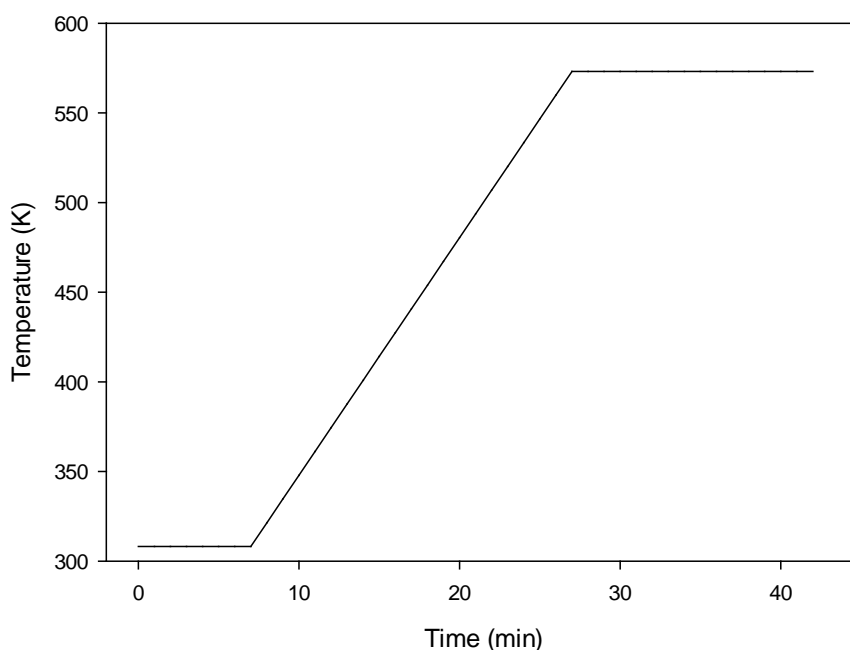


Figure 19: GC-MS Method 2 used for the separation and subsequent identification of polymer decomposition products. Column = HP5-MS, $dT/dt = 13.25 \text{ K min}^{-1}$, $Q_{\text{He}} = 1 \text{ ml min}^{-1}$, $V_{\text{INJ}} = 1 \mu\text{l}$

Identification of molecules was carried out by comparison of the fragmentation patterns of peaks from the GC-MS chromatogram against those of the National Institute of Standards and Technology (NIST, USA) library compiled within the MassLynx software (Water Corporation, USA). It is noted that comparison of fragmentation patterns is automated, returning suggested molecules for user selection.

High-Performance Liquid Chromatography

High-Performance Liquid Chromatography (HPLC) of the aqueous and organic fractions of the polymer decomposition products using a Shimadzu SCL-10A_{VP} system comprising of; SCL-10A_{VP} Controller, SIL-10AD_{VP} Auto-injector, LC-10AD_{VP} Pump, FCV-10AL_{VP} Solenoid controller, DGU-14A Degasser, CTO-10A_{VP} Column oven, SPD-10AV_{VP} UV-Vis Detector and

RF-10A_{XL} Fluorescence detector. The composition of the mobile phases used to carry out the separation of the polymer decomposition products across a Phenomenex Synergi Fusion RP C₁₈ column (Phenomenex, Country) are given in Table 18.

Table 18: HPLC mobile phase compositions for the quantitative analysis of polymer decomposition products

| Phase | [H ₂ O] (%v) | [MeCN] (%v) | [AcOH] (%v) |
|-------|----------------------------|----------------|----------------|
| A | 98.00 | 0.00 | 2.00 |
| B | 49.75 | 49.75 | 0.50 |
| C | 0.00 | 100.00 | 0.00 |
| D | 100.00 | 0.00 | 0.00 |

The isochoric method was used to perform the separation is shown in Figure 20.

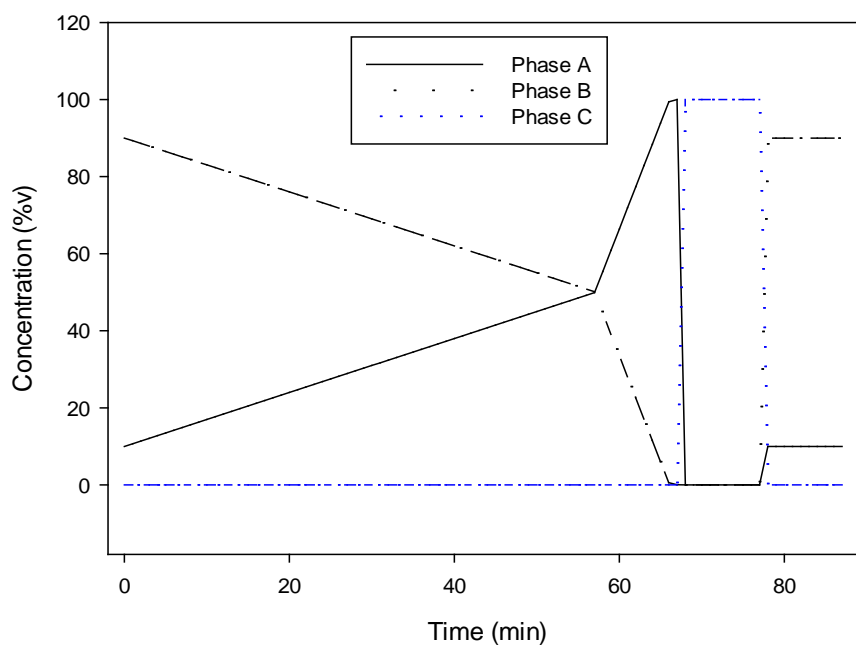


Figure 20: HPLC Method 1 for the separation of polymer decomposition products. $Q = 1 \text{ ml min}^{-1}$, $T_{\text{COL}} = 308 \text{ K}$, $P = 15 \text{ MPa}$, $V_{\text{INJ}} = 10 \text{ } \mu\text{l}$

The HPLC method shown in Figure 20 has been used previously by other authors in the analysis of phenol derivatives [311]. The concentrations of water [H₂O], acetonitrile [MeCN] and acetic acid [AcOH] used for each mobile phase is stated in Table 18. Notably, phases 'A' and 'B' are responsible for carrying out the separation of compounds across the column, phase 'C' is used to clean the column after each separation and phase 'D' is used for purging and rinsing the auto-injector and ancillary equipment. In preparation for HPLC, approximately 1.5 ml of each of the liquid phase decomposition product samples was filtered to remove any suspended solids, with the filtrate being collected into standard HPLC vials. The filtration was carried out using disposable pipettes and filter paper, with the funnel being washed between each filtration to prevent cross-contamination. Quantification of the phenol concentration [PhOH] was performed by producing a phenol standard. Phenol (C₆H₅OH) with a purity greater than 99 % was obtained from Sigma Aldrich and used to prepare 15 vials of known phenol concentrations as shown in Table 19.

Table 19: HPLC Standard concentrations used to prepare the required calibration curve

| Vial | [PhOH] (mg ml ⁻¹) |
|------|----------------------------------|
| 1 | 5.0000 |
| 2 | 3.5000 |
| 3 | 2.8000 |
| 4 | 2.5000 |
| 5 | 2.3300 |
| 6 | 2.0000 |
| 7 | 1.7500 |
| 8 | 1.5000 |
| 9 | 1.3125 |
| 10 | 0.8750 |
| 11 | 0.4375 |
| 12 | 0.2188 |
| 13 | 0.1094 |
| 14 | 0.0547 |
| 15 | 0.0091 |

HPLC analysis of the phenol standards given in Table 19, by means of a dual-channel UV-Vis detector set to 254 nm and 280 nm allows for the calibration curve presented in Figure 21 to be produced.

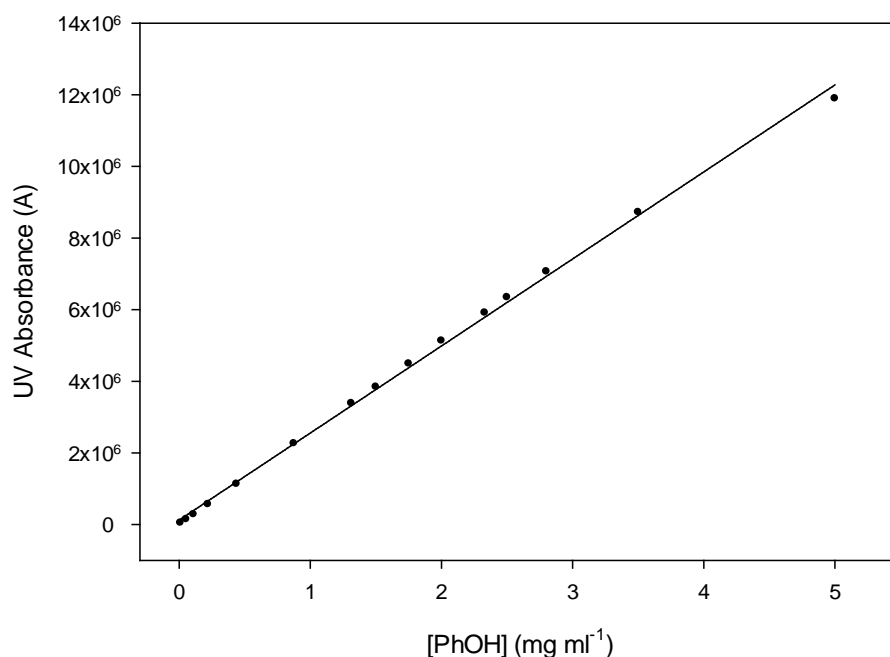


Figure 21: HPLC Calibration curve for phenol concentrations [PhOH] given in Table 19. $\lambda = 254 \text{ nm}$, HPLC Method 1, $R^2 = 0.998$

By using the calibration curve presented in Figure 21 it is then possible to carryout the quantitative HPLC analysis of polymer decomposition samples with respect to the phenol concentration [PhOH] $5 \text{ mg ml}^{-1} - 0.0091 \text{ mg ml}^{-1}$. Quantitative HPLC analysis of other decomposition products was not carried out.

3.4.4. Analysis of Carbon Fibre

Tensile Testing of Single Fibres by means of Universal Testing Machine

Individual carbon fibre were manually separated from a carbon fibre tow, T700s 50E (Toray Carbon Fibres Inc, USA). They were visually inspected by means of optical microscopy prior to being analysed by Electrochemical Impedance Spectroscopy (EIS). Since a single fibre has

a well-defined diameter and is electrically conductive it is possible to use the impedance, or resistance in the absence of a phase angle between the voltage and current, to determine the diameter of the fibre as long as the fibre length is known [245]. The methodology for this type of measurement is developed as part of this research and discussed extensively in the following section. At this point it is sufficient to acknowledge that single fibres may be readily identified by means of EIS measurement.

After confirming the presence of a single fibre, a small amount of Araldite Rapid epoxy resin (Huntsman Corporation, USA) was applied either end of the fibre to provide a gripping surface for the subsequent tensile test. The epoxy resin was allowed to cure for 24 hours prior to carrying out tensile testing. Tensile testing was carried out using a Zwick-Roell Z030 Universal Testing Machine (Zwick-Roell, Germany) with a testing speed of 2 mm min^{-1} and a data capture rate of 200 Hz. An Instron 100 N static load cell was used to measure the force applied to the fibre bundle. Tensile testing was also carried out using an Instron Micro Test 5848 (Instron, USA) using the same parameters.

Determination of the Number of Carbon Fibres within a Bundle

With respect to industrial applications, the testing of single carbon fibres must be conducted extensively to ensure that the fibres tested are representative of the bulk material. It is commonplace for a bundle of fibres to consist of several thousand fibres, and therefore testing of a representative number of single fibres presents a challenge. The tensile strength of a carbon fibre requires the knowledge of the cross-sectional area through which the force is transmitted, for a single cylindrical fibre calculation of this area is trivial. If the number of

fibres within a bundle of fibres is accurately known then the force applied to each fibre, on average, may be determined and thus yielding the average tensile strength per fibre. It may therefore be seen that determination of the number of carbon fibres in a bundle is essential for characterisation of the recycled material. A method was developed during the course of this research to accurately determine the number of carbon fibres present in a bundle. This will be presented prior to the explanation of the tensile testing of carbon fibre bundles.

Electrochemical Impedance Spectroscopy Sample preparation

Individual carbon fibres, T700S 50E having a diameter of 7 μm (manufacture's data) obtained from Toray Carbon Fibres America Inc., were separated from the bulk carbon fibre tow manually under a magnifier and confirmed as single fibres by means of optical microscopy and ImageJ imaging software. Molybdenum (Mo) wire, obtained from Advent RM having a diameter of 25 μm and purity of 99.95% (manufacturers data), was used as a reference. Individual carbon fibres were then measured and cut to the specified length prior to being crimped with aluminium foil at either end to provide a gripping surface and electrical contact.

Electrochemical Impedance Spectrometer Setup

A Solartron 1250 Frequency Response Analyser and 1286 Electrochemical Interface were used to scan individual carbon fibres through a range of frequencies from 1.5 kHz to 10 Hz, with an amplitude of 25 mV, 25 cycle integration and 0V DC potential. Data were recorded using Zplot and analysed using Zview software (Scribner Associates Inc.). A schematic representation of the 2-point experimental setup is provided in Figure 22.

After obtaining the impedance of an individual carbon fibre an additional carbon fibre was prepared and added to the Electrochemical Impedance Measurement (EIM) system. The impedance sweep was then carried out and repeated 9 times. This process was carried out on between 1 and 20 fibres. In a separate experiment the length of the carbon fibre was varied from 80, 120, 150, 200, 250 and 300 mm, using single fibres. The fibre length was measured using a steel rule with 1 mm graduation intervals. The frequency sweep conditions were preserved and each measurement was repeated 9 times.

Scanning Electron Microscopy (SEM)

Samples were imaged using a Philips XL30 FEG ESEM. Since carbon fibres are conductive gold sputtering was not necessary. Sections of individual carbon fibres were cut to approximately 15 mm and mounted directly onto adhesive stub mounts. Once mounted onto stubs, samples were loaded individually into the SEM and the sample chamber was evacuated. All images were taken with a working distance of 10.1 mm, an acceleration voltage of 20 kV and a magnification of 6500 times.

Validation of Electrochemical Impedance Spectroscopy Technique

The system impedance, including the aluminium crimps, was measured as 0.018 Ω . For low impedance measurements this value should be subtracted from the impedance measured. However, since the system impedance represents less than 0.01% of the impedance measured in all cases, it is deemed to be negligible and is consequently neglected. The equivalent circuit for the system is presented in Figure 23.



Figure 23: EIS Equivalent circuit, system impedance (R_s), carbon fibre impedance (R_1)

Analysis on Single Fibres

Figure 24 shows a single carbon fibre as observed by optical microscopy with a 25 μm Mo wire for scale. Bundles of fibres (from 2 to 20) were constructed by obtaining single fibres individually and compiling them. Since the fibres are obtained individually and added to the bundle, the number of fibres present in the bundle was always known.

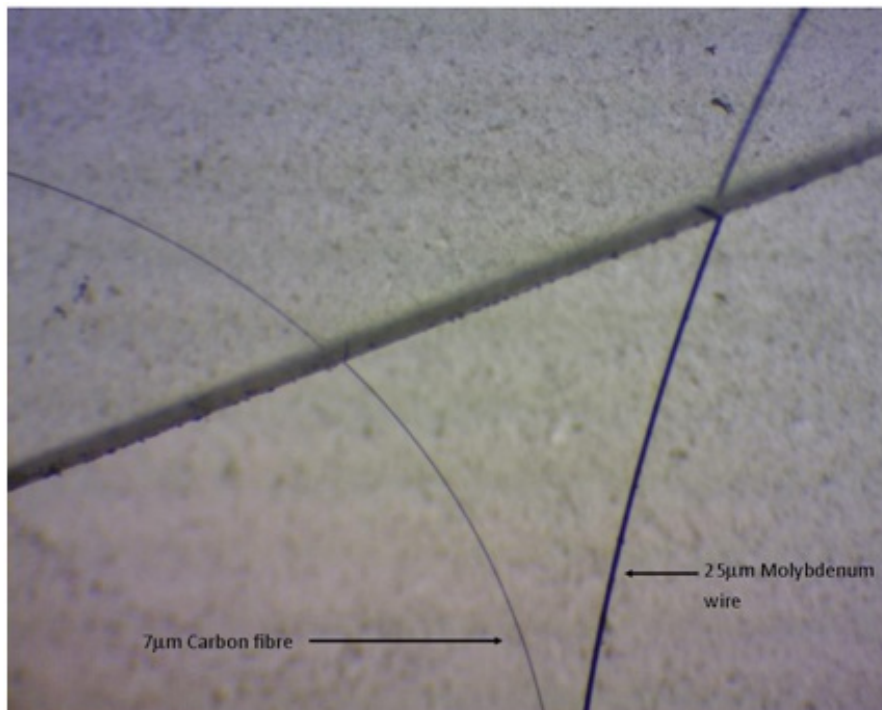


Figure 24: Single carbon fibre with 25

μm Molybdenum wire for scale (Optical Microscope)

The presence of single carbon fibres was also confirmed by SEM, see Figure 25. It was necessary to conduct the impedance measurements prior to the SEM since the fibres were not recoverable from the SEM stage. For this reason, single fibres were initially identified by optical microscopy.

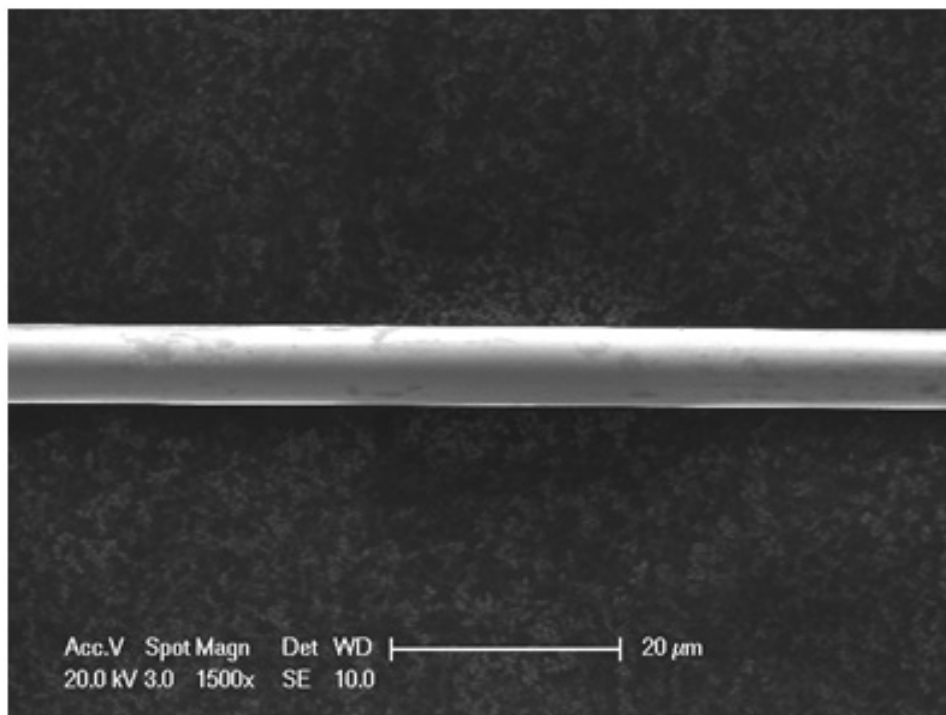


Figure 25: SEM Micrograph of the single carbon fibre, 150 mm in length (full length not shown), subsequently used in Electrical Impedance Measurements

The impedance data measured at 1.5 kHz and 10 Hz for a single 85 mm fibre (Toray T700S 50E) have been tabulated and are presented in Table 20. It is noted that the impedance value is independent of the frequency (since the fibres act as resistors), and consequently the impedance measured at any frequency throughout the sweep would be sufficient to calculate the fibre diameter.

Table 20: Impedance as a function of frequency for a single carbon fibre 85 mm in length

| Sweep Number | Z (Ω) (1.5kHz) | Z (Ω) (10Hz) |
|--------------|-------------------------|-----------------------|
| 1 | 42168 | 42557 |
| 2 | 43081 | 42889 |
| 3 | 43032 | 42086 |
| 4 | 42821 | 42626 |
| 5 | 42615 | 43140 |
| 6 | 43370 | 43393 |
| 7 | 43491 | 43407 |
| 8 | 43077 | 43039 |
| 9 | 42975 | 42932 |
| 10 | 42748 | 42703 |
| Mean | 42938 | 42877 |
| SD | 359 | 383 |

It is explicit from Equation 3 that the impedance will increase linearly with increasing length of fibre. In order to verify this single carbon fibres of varying lengths, 80, 85, 120, 150, 200, 250 and 300 mm, were prepared and their impedance measured. Figure 26 shows the linear increase in impedance observed with fibre length.

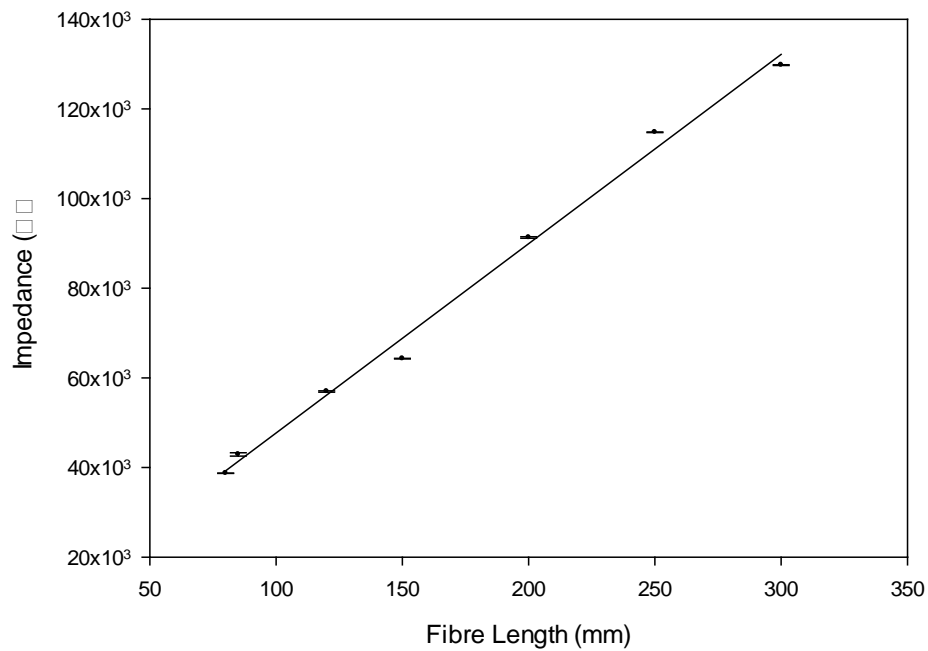


Figure 26: Impedance as a function of length for single carbon fibres

The presence of a single carbon fibre, observed by use of an optical microscope, was confirmed by SEM. The use of optical and scanning electron microscopy has been used to ratify the results obtained by EIM. By transposition of Equation 3, the cross-sectional area, and therefore the fibre diameter, may be elucidated. The single fibre diameters calculated from EIM and measured by SEM are presented in Table 21 for different fibre lengths.

Table 21: Comparison between carbon fibre diameter as calculated by EIM and measured by SEM for multiple carbon fibres

| Nominal Length (mm) | Diameter EIM (μm) | Diameter SEM (μm) | Difference (%) |
|---------------------|--------------------------------|--------------------------------|----------------|
| 80 | 6.49 | 6.52 | 0.46 |
| 85 | 6.35 | 6.46 | 1.70 |
| 120 | 6.55 | 6.72 | 2.53 |
| 150 | 6.89 | 6.85 | 0.58 |
| 200 | 6.68 | 6.22 | 7.40 |
| 250 | 6.66 | 6.48 | 2.78 |
| 300 | 6.86 | 6.55 | 4.73 |

Analysis of Table 21 shows that the EIM technique presented provides a ‘reasonably good’ fit with the manufacturer’s datasheet (7 μm) when applied to single fibres, especially when considering fibres with a length in excess of 150 mm. This increase in accuracy is thought to be attributed to the reduced percentage error in the length measurement which is done by hand. However, the small amount of error present in the length measurement is inconsequential for fibre bundles since all of the fibres are crimped at the same point and thus the length through which the current flows is essentially the same. Only the effect of the number of fibres therefore is observed.

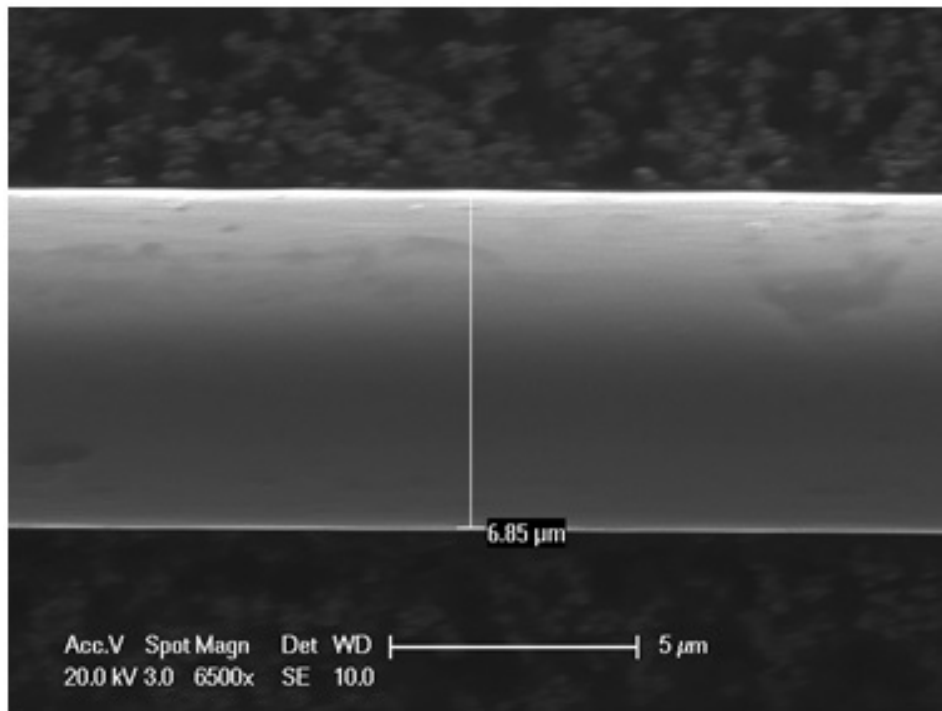


Figure 27: SEM micrograph of a single carbon fibre used for EIM, 150 mm in length (full length not shown)

The diameter of single carbon fibres was confirmed by means of SEM, see Figure 27. When measured by SEM the diameter of a 150 mm single fibre was found to be 6.85 µm, the diameter calculated by EIM was 6.89 µm. Furthermore, the diameter of the 120 mm carbon fibre determined by SEM was 6.72 µm, (see Figure 28), while the diameter calculated by EIM was 6.55 µm, again showing good agreement between the values. The variation in fibre diameter along the length of a fibre was investigated by means of SEM. Diameter measurements were taken at 5 arbitrarily selected points for 5 arbitrarily selected fibres. The standard deviation was less than 0.05 for any single fibre and 0.13 for the entire sample population. Full data are available in Appendix 2. The greatest variation observed within a fibre (0.09 µm) represents an error of less than 3%. Therefore, variation within a fibre is not thought to be a significant source of error.

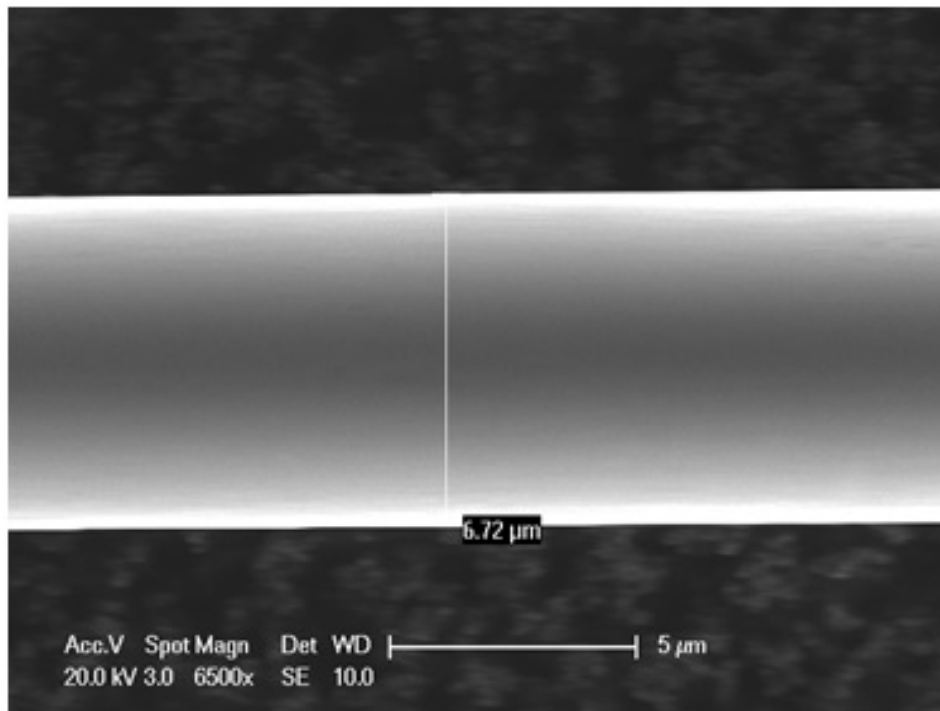


Figure 28: SEM micrograph of a single carbon fibre used for EIM, 120 mm in length (full length not shown)

It is therefore evident from both optical and Scanning Electron Microscopy that the electrical impedance measurement approach presented is sufficiently accurate, precise and sensitive to detect and measure the dimensions of individual carbon fibres.

The Approach for Fibre Bundles

The mean impedance of an 85 mm single carbon fibre was obtained to be $42.9 \text{ k}\Omega \pm 2 \%$, Table 20. The impedance value for each sweep at 1.5 kHz and 10 Hz was used to generate the average impedance for bundles containing 2 to 20 fibres that were again 85 mm in length. These data are collated in Figure 29.

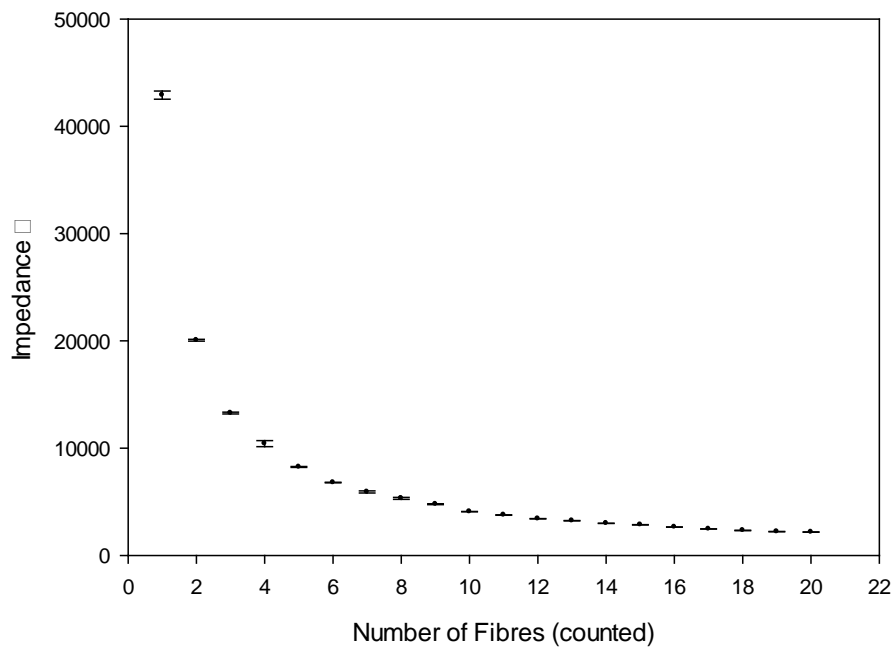


Figure 29: Impedance as a function of the number of fibres within a carbon fibre bundle, 85 mm in length

Since the phase angle (ϕ) between the voltage (V) and current (I) is approximately 0, and hence no frequency dependence of the impedance, single carbon fibres behave as resistors. The total impedance of the system may therefore be determined by Equation 4.

$$\frac{1}{Z_T} = \frac{1}{Z_1} + \frac{1}{Z_2} \dots \frac{1}{Z_n}$$

Equation 4: System total impedance, resistors in parallel

It follows from Equation 4 that for a constant fibre length the total impedance of the system is a function of the number of fibres. As the fibre length is known the number of fibres may be calculated by transposition of Equations 3 and 4. It also follows that for a given fibre

length, if the number of fibres is doubled the impedance is halved (see Figure 29). It is also explicit that the average impedance of a fibre in a bundle is independent of the number of fibres. For completeness this is shown in Appendix 4.

It has been possible to take a bundle of fibres, cut and crimped to a specified length, and calculate the number of fibres present by means of EIM. This in turn allows for the tensile testing of carbon fibre bundles and, as long as the bundle length is measured prior to the test, the number of fibres may be determined as shown by calculation 1 below. This is significant since it allows the tensile strength of the individual fibres within the bundle to be calculated, a step which is not possible without knowing the number of fibres present.

Calculation 1, determining the number of fibres in a bundle;

Since;

For bundles;
$$\rho = Z_T \frac{A_T}{l}, \quad \text{when } \phi = 0,$$

$$\frac{\rho l}{A_T} = Z_T$$

For single fibres;
$$\rho = Z_S \frac{A_S}{l}, \quad \text{when } \phi = 0,$$

$$\frac{\rho l}{A_S} = Z_S$$

Where: Z_T = Total impedance of bundle (Ω), Z_S = Impedance of single fibre (Ω), A_T = Total cross-sectional area of conduction through bundle (m^2), A_S = Cross-sectional area of single fibre (m^2), ρ = Resistivity (Ωm), l = Length of fibre (m)

Where A_T is the total cross-sectional area through which conduction takes place in a bundle, A_S is the cross-sectional area of a single fibre. Measuring the total impedance of a carbon fibre bundle allows the number of fibres present to be determined by the quotient A_T/A_S . For a carbon fibre bundle consisting of an unknown number of 85 mm fibres, the number of fibres present may be deduced in the following way:

By EIM,

$$Z_T = 2858.3 \Omega$$

$$Z_S = 42907.5 \Omega$$

$$\frac{Z_S}{Z_T} = \frac{\rho l A_T}{\rho l A_S} = \frac{A_T}{A_S} = \# \text{ fibres}$$

And therefore;

$$\frac{Z_S}{Z_T} = \frac{42907.5}{2858.3} = 15.01$$

Thus, it is determined that the bundle consists of 15 fibres which was verified by optical microscopy. This bundle of fibres may then be prepared for tensile testing and, as the number of fibres is known, the tensile strength of the fibres may be deduced.

Aside from the fibre length measurement, one source of error with this technique is that there could be instances when there are a small number of fibres not connected to an Al crimp. In such instances, the fibres that are not in contact with either the crimp or another fibre would not transmit the current, and therefore would not contribute to the impedance of the system. However, in a bundle of fibres should one end of a fibre become disconnected it is likely that the fibre will remain in contact with many of the other fibres by proximity alone. The majority of the fibre's length is subsequently available for conduction and the overall effect on the impedance measurement is small. This effect of touching carbon fibres providing an alternative current pathway has been identified previously in work by Irving et al [312]. This error is further reduced in large bundles, where a bundle may

commonly consist of several hundred fibres. In such instances the loss of a small proportion of a single fibre, or small number of fibres, becomes negligible on impedance and related measurements as shown by Equation 5.

$$\%Z_{inc} = \left(\frac{n_L}{n_I} \times 100 \right)$$

Equation 5: Effect of fibre loss on impedance of bundles

Where: $\%Z_{inc}$ = Percentage increase in impedance due to reduction in number of fibres, n_L = Number of fibres removed, assuming entire fibre length is non-conducting, n_I = Initial number of fibres within bundle

Limit of Detection

In principle, as long as the potential is applied to all the fibres the impedance of the system may be measured. This work demonstrates that the removal of a single fibre from a bundle of 20, amounting to a change of 5% in the bundle size, is easily detected (Figure 29). This technique readily detects changes as small as 5% in the bundle size. The limit of detection is concerned with the particular experimental setup. The largest bundle of 80 mm fibres that may be analysed is 215,000. Bundles in excess of this size would have an impedance within 10% of the system impedance (excluding carbon fibre), at which point the contribution of the Al crimps and associated cabling to the overall system impedance may not be negligible. The equivalent circuit shown in Figure 23 would no longer accurately model the system and a new equivalent circuit would need to be developed. Given that the impedance of a carbon

fibre is directly proportional its length, the limit of detection (LOD) is also a function of the fibre length. The LOD increases with increasing fibre length as shown in Table 22.

Table 22: Limit of Detection (LOD) for determination of number of fibres in a bundle by EIM

| Nominal Length (mm) | L.O.D. (# of fibres) |
|------------------------|-------------------------|
| 80 | 215,000 |
| 85 | 235,000 |
| 120 | 315,000 |
| 150 | 355,000 |
| 200 | 505,000 |
| 250 | 635,000 |
| 300 | 720,000 |

The work herein demonstrates that there is no frequency dependence when measuring the impedance of carbon fibres, and as such, carbon fibres behave as resistors. Consequently it would be possible to conduct this procedure using less sophisticated equipment, operating with Direct Current (DC) as opposed to Alternating Current (AC) as performed here. DC measurements of carbon fibres yield resistance, where the magnitude of the resistance is identical to the magnitude of the impedance since the phase angle is 0. The approach presented was necessary to demonstrate the applicability, reliability and validity of the method.

Tensile Testing of Multiple Carbon Fibres by means of Universal Testing Machine

After determining the number of carbon fibres present within a bundle, the bundle was placed in a bespoke carbon fibre alignment tool, Figure 30.



Figure 30: Bespoke carbon fibre alignment tool, manufactured by University of Birmingham, showing aligned fibre bundle set in Araldite Rapid resin

With the wells at either end of the tool liner with aluminium, a small amount of Araldite Rapid epoxy resin (Huntsman Corporation, USA) was applied to either end of the bundle to provide a gripping surface. The resin was allowed to cure for a period of 24 hours prior to the sample undergoing tensile testing. Tensile testing was carried out using a Zwick-Roell Z030 (Zwick-Roell, Germany) with a testing speed of 2 mm min^{-1} and a data capture rate of 200 Hz. An Instron 100 N static load cell was used to measure the force applied to the fibre bundle. Tensile testing was also carried out using an Instron Micro Test 5848 (Instron, USA) using the same parameters.

The cured epoxy resin applied to either end of the carbon fibre was used to grip and retain the fibre bundle within the Universal Testing Machine's (UTM) grips. Once secured, the jaws were separated to remove the majority of the slack from the fibres, thereby reducing the testing time. With the slack removed, the cross-head separation and tensile force zeroed, the test was initiated and allowed to proceed until the fibres fractured, identified by a sharp decline in the tensile force with respect to jaw displacement. When the tensile force tended towards 0, the test was halted and the data saved. The sample was subsequently removed

from the jaws and the cross-head distance returned to its initial position in preparation for the following sample.

Determination of the mean tensile force per fibre was possible since the number of fibres within the bundle was ascertained prior to the test, as detailed previously. Equation 6 gives the mean force per fibre.

$$\bar{\sigma} = \left(\frac{F_{MAX}}{A_T} \right)$$

Equation 6: Mean tensile strength of a carbon fibre

Where: $\bar{\sigma}$ = Mean tensile strength (N), F_{MAX} = Maximum tensile force applied (kg), A_T
= Total cross-sectional area through which force is applied (m²)

By using Equation 6 it is possible to compare bundles of carbon fibres processed using differing conditions as well as compare the data obtained from single fibre testing to the data obtained by testing carbon fibre bundles.

3.4.5. Analysis of Carbon Fibre Reinforced Polymeric Materials

The analysis of liquid fractions produced as a result of the decomposition of carbon fibre reinforced composite materials (CFRP's) was carried out by HPLC and GC-MS. Since the analysis was concerned with identifying the same products observed as a result of the BADGE based resin decomposition, HPLC Method 1 and GC-MS Method 2 were employed

(Figure 20 and Figure 19 respectively). Analysis of the recovered solids was carried out by TGA, utilising TGA Method 2 (Figure 17), as well as qualitative inspection by SEM, performed on a Philips XL30 FEG ESEM.

CHAPTER 4. RESULTS PART A: PROCESSING AND RECYCLING OF POLYETHERETHERKETONE

4.1. SUPERCRITICAL CARBON DIOXIDE PROCESSING OF POLYETHERETHERKETONE

Unfilled PEEK150PF was processed using supercritical carbon dioxide (scCO₂) according to the designed experiment shown in Chapter 3.3.1. The format of this results chapter follows that of the experimental methodology and will cover the effects of scCO₂ on the percentage crystallinity (%X_c), glass transition temperature (T_g), crystallisation temperature (T_c) and melting temperature (T_m) of the sample post processing. By understanding the behaviour of PEEK in subcritical and supercritical fluids, in particular the changes to the polymeric transitions, the intention is to focus on potential recycling and recovery techniques for end-of-life material. Supercritical conditions are readily available when CO₂ is used, having a critical temperature of 304.25 K and critical pressure of 7.38 MPa [313]. An overview of the properties of supercritical fluids is provided in Chapter 2.1.

4.1.1. Confirmation of Amorphicity

The polymer transition temperatures are important since they govern the behaviour of the material in each state. Amorphous PEEK samples were generated as described in Chapter 3.3.1. The DSC thermogram for PEEK 150PF as received is shown in Figure 31.

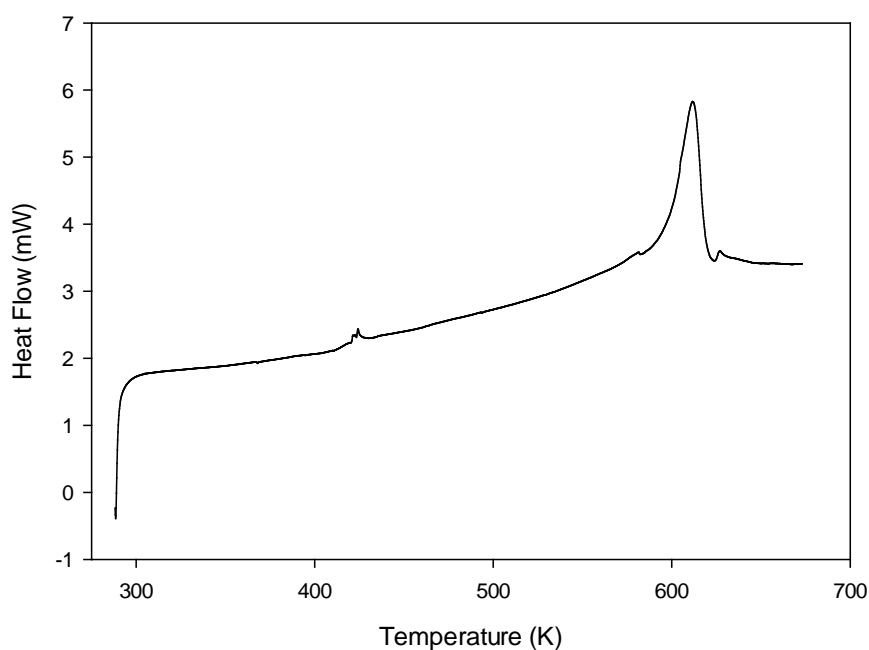


Figure 31: DSC thermogram for PEEK150PF as received, 7.0 mg, DSC Method 1, endothermic-up

Inspection of Figure 31 shows a glass transition at 416 K and the melt transition at 616 K, showing excellent adherence to the manufacturer's datasheet ($T_g = 416$ K, $T_m = 616$ K). Since the PEEK150PF is received in the semi-crystalline state no spontaneous thermodynamic crystallisation is observed by DSC for untreated samples. DSC analysis of PEEK150PF post quenching from the melt phase at 673 K should show an enhanced T_g , a prominent T_c as well as the prominent T_m shown in Figure 31. A DSC thermogram used for validation of the amorphous state is shown in Figure 32.

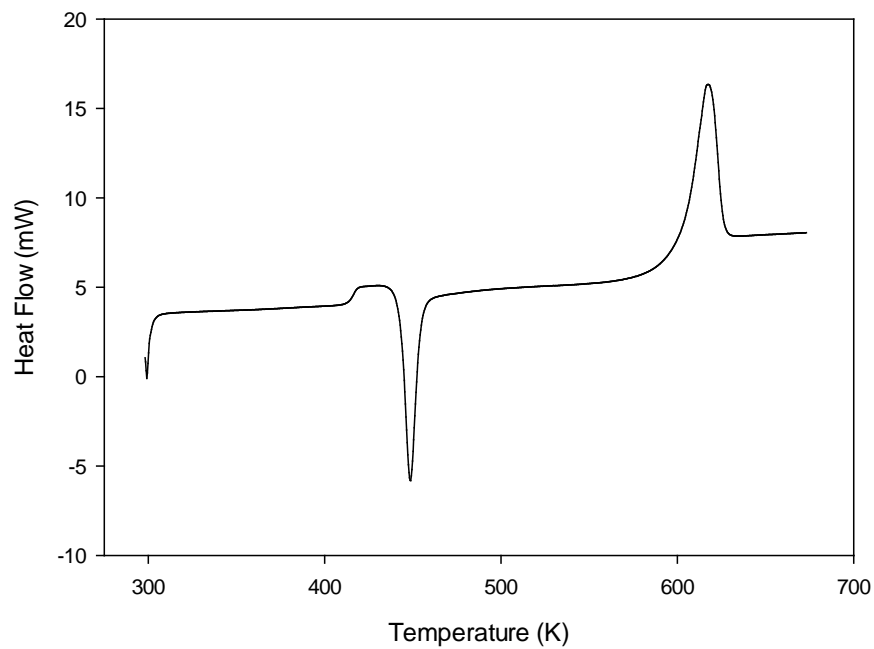


Figure 32: DSC thermogram for PEEK150PF generated by quenching from melt phase, 11.2 mg, DSC Method 1, endothermic-up

Figure 32 shows an enhanced T_g at 416 K followed by a strong exothermic peak at 449 K, attributed to the crystallisation from the amorphous state. The melting temperature of the amorphous sample is 616 K, unchanged from that of the as received sample. The percentage crystallinity is calculated using Calculation 2.

Calculation 2: Determination of percentage crystallinity of PEEK by DSC

From Chapter 3.4.1.

$$\% X_c = \left(\frac{A_c}{M_s \times \Delta H_f} \right) \times 100$$

Where: A_c = Integral value at T_c (J), M_s = Mass of sample (g), ΔH_f = Heat of fusion (J g^{-1})

Quenched PEEK150PF:

Integration of exotherm at T_c deduces; $A_c = 265.95 \text{ mJ}$, $M_s = 11.2 \text{ mg}$, $\Delta H_f = 130 \text{ J g}^{-1}$

Therefore;

$$\% X_c = \left(\frac{265.95 \times 10^{-3}}{11.2 \times 10^{-3} \times 130} \right) \times 100$$

At T_c $\% X_c = 18.27$

Integration of endotherm at T_m deduces; $A_m = 411.78 \text{ mJ}$, $M_s = 11.2 \text{ mg}$, $\Delta H_f = 130 \text{ J g}^{-1}$

Therefore;

$$\% X_c = \left(\frac{411.78 \times 10^{-3}}{11.2 \times 10^{-3} \times 130} \right) \times 100$$

At T_m $\% X_c = 28.29$

For PEEK 150PF samples as received, the percentage crystallinity may only be determined at the melting temperature due to the absence of an exothermic peak at T_c (see Figure 31).

The calculation is performed as shown in Calculation 2, the percentage crystallinity is

determined as 21.79 %. Further investigation into the amorphicity of the PEEK150PF samples was performed by FT-IR as described in Chapter 3.4.1. The FT-IR spectra for PEEK150PF as received and post quenching are shown in Figure 33 and Figure 34 respectively.

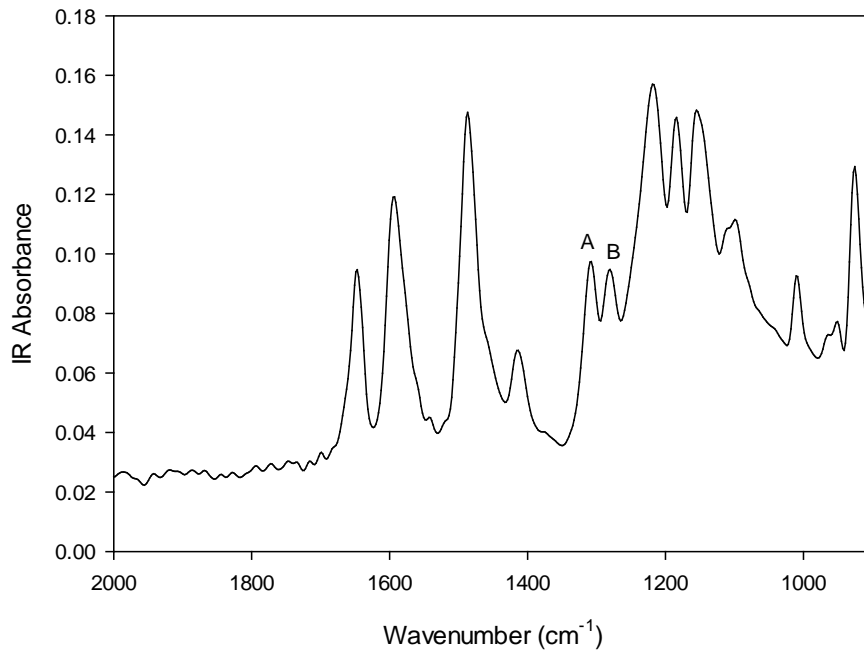


Figure 33: FT-IR Absorbance spectrum for PEEK150PF as received, full range not shown, A = 1307 cm⁻¹, B = 1280 cm⁻¹

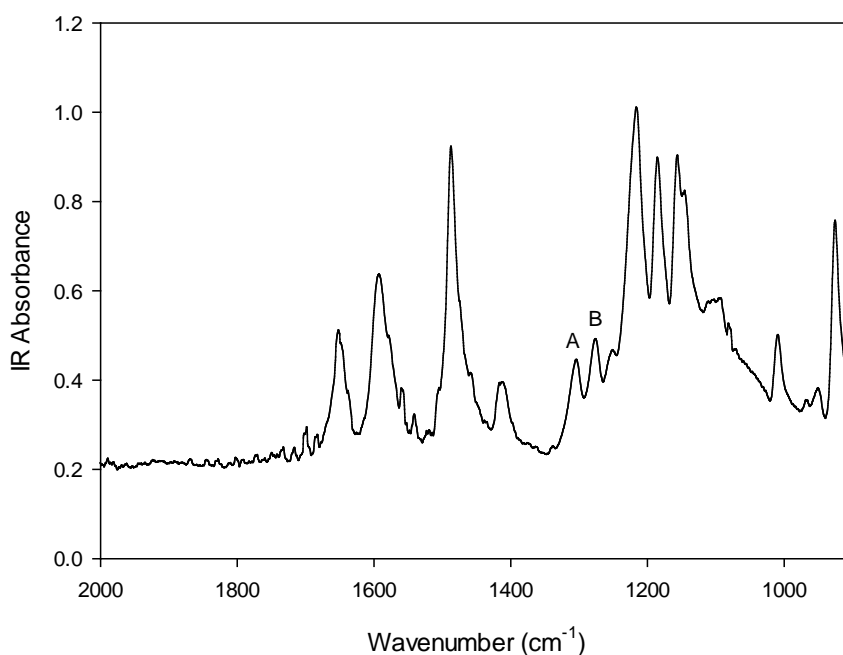


Figure 34: FT-IR Absorbance spectrum for PEEK150PF post quenching, full range not shown, A = 1307 cm^{-1} , B = 1280 cm^{-1}

Comparison of peaks labelled 'A' and 'B' in Figure 33 and Figure 34, where 'A' corresponds to 1307 cm^{-1} and 'B' corresponds to 1280 cm^{-1} , provides information about the crystallinity of the sample in a non-destructive manner as described in Chapter 3.4.1. This process would allow the sample to be used for further experiments, unlike determination by DSC where analysis causes the crystallisation of the polymer. However, analysis of the quenched samples by FT-IR severely deforms the DSC pan containing the sample and consequently samples analysed by this method were not used in subsequent analysis. Calculation of the percentage crystallinity by FT-IR is performed as detailed in Calculation 3.

Calculation 3: Determination of percentage crystallinity of PEEK by FT-IR

From Chapter 3.4.1;

$$\% X_C = \left(1 - \left(\frac{H_{PB}}{H_{PA}} \right) \right) \times 100$$

Where: $\%X_C$ = percentage crystallinity, H_{PA} = height of peak 'A', H_{PB} = height of peak 'B'

Measurement of peak height was conducted within Spectra Analysis software (Jasco Inc.);

PEEK150PF As received (Figure 33):

$$H_{PA} = 0.0221791, H_{PB} = 0.0172332$$

Therefore:

$$\% X_C = \left(1 - \left(\frac{0.0172332}{0.0221791} \right) \right) \times 100$$

$$\% X_C = 22.30$$

Quenched PEEK150PF (Figure 34):

$$H_{PA} = 0.131392, H_{PB} = 0.128402$$

Therefore:

$$\% X_C = \left(1 - \left(\frac{0.128402}{0.131392} \right) \right) \times 100$$

$$\% X_C = 2.28$$

The results obtained from analysis by FT-IR are in good agreement with those obtained by DSC. DSC analysis showed that PEEK150PF as received has a %X_C of 21.79 %, whereas FT-IR analysis showed that the %X_C was 22.30 %. The proximity of these measurements is deemed sufficient to confirm the presence polymer crystallites within the sample as received from Victrex Ltd. Analysis of the quenched sample by FT-IR shows that the sample was largely amorphous and had a %X_C of 2.28 %. This information, in conjunction with the DSC analysis where the spontaneous thermodynamic crystallisation taking place at T_c was determined as 18.27 %, means that immediately after T_c the %X_C could potentially be up to 20.55 %. Qualitative analysis by Wide Angle X-Ray Spectroscopy (WAXS) was also carried out, as detailed in Chapter 3.4.1. The WAXS spectrum for PEEK 150PF as received is given in Figure 35.

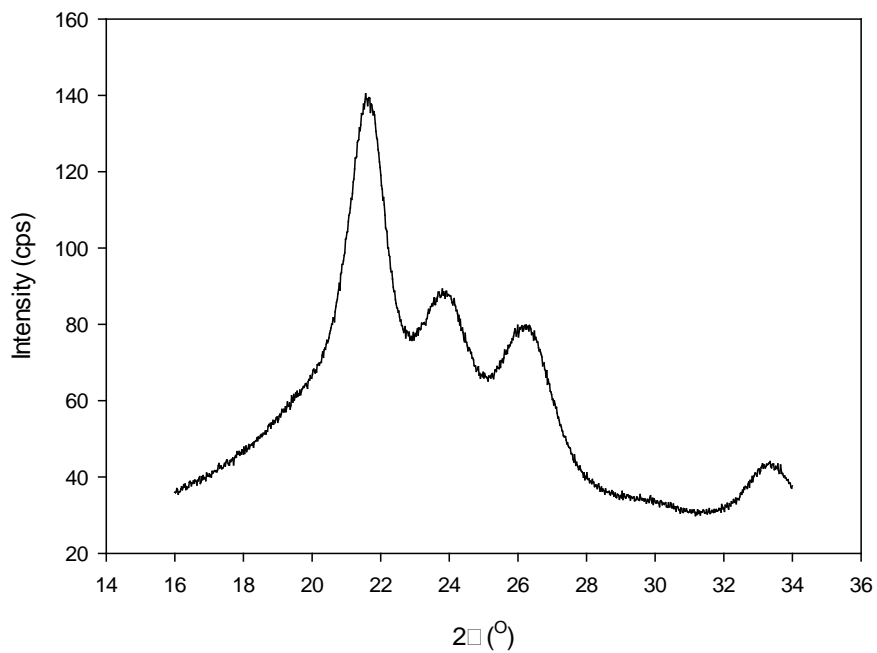


Figure 35: WAXS Spectrum for PEEK150PF as received, 50 μm powder

The scatter pattern of PEEK150PF as received consists of 4 well defined peaks created by the presence of crystallites within the bulk polymer [85]. In an amorphous sample crystallites do not exist and therefore the scatter pattern identified in Figure 35 would not be observed. The WAXS spectrum for a quenched PEEK150PF sample is presented in Figure 36.

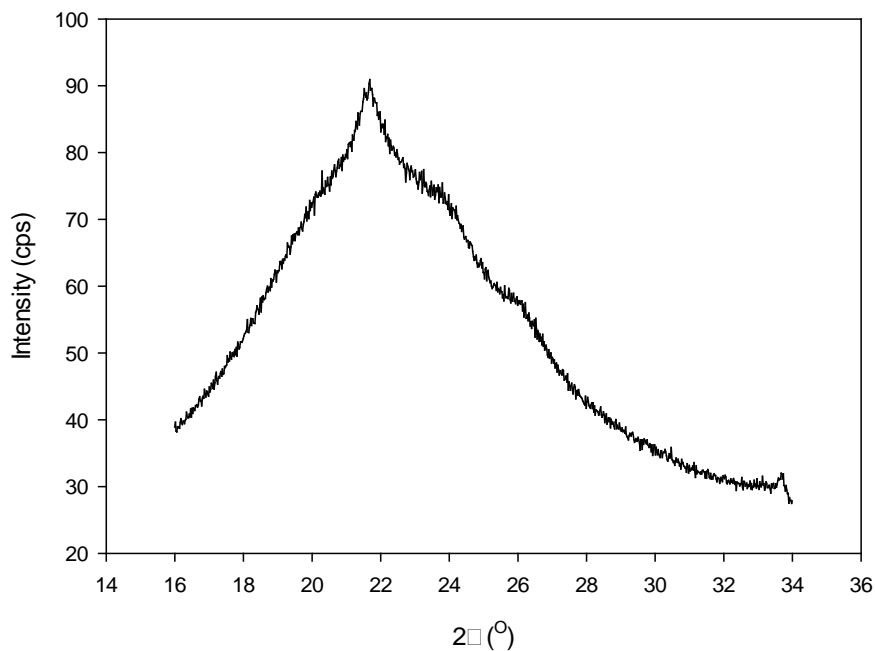


Figure 36: WAXS Spectrum for PEEK150PF post quenching from melt phase

Inspection of Figure 36 shows that the well-defined peaks, derived from the scattering by polymer crystallites, are not observed for quenched samples. Small deviations from the generally broad peak generated by the amorphous PEEK are identified. From these data it may be inferred that the sample is largely amorphous, and when combined with the information obtained by DSC and FT-IR, the samples are considered to not contain sufficient crystallinity to impede the investigation into the effects of scCO_2 processing carried out in this research. Having determined the amorphicity of the PEEK samples produced by quenching from the melt phase, attention is now directed towards investigating the effects of scCO_2 on the bulk polymer.

4.1.2. Effects of scCO_2 Processing on the Polymer Transitions

The designed experiment, given in the reaction schedule Chapter 3.3.1, was analysed using Minitab[®] 16 statistical analysis software. Figure 37 shows the effect of the CO₂ processing pressure on the glass transition temperature (T_g).

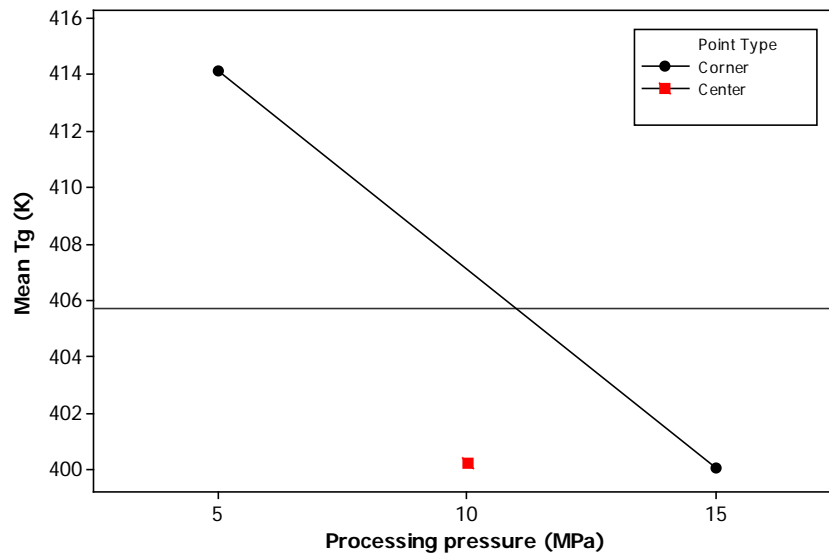


Figure 37: Main effects plot for influence of CO₂ processing pressure on glass transition temperature (T_g), $T = 413 - 453$ K, $t_r = 10 - 30$ min

Inspection of Figure 37 shows that the average glass transition temperature of PEEK decreases with increasing CO₂ pressure, within the range of 5 – 15 MPa, for processing temperatures of 413 – 453 K and processing times of up to 30 minutes. The T_g of PEEK as received is 416 K and therefore it may be seen from inspection of the reaction schedule, Chapter 3.3.1, that the majority of the processing conditions take place above the T_g . Processing above the T_g allows the permeation of the scCO₂ through the polymer matrix and facilitates the materialisation of the plasticisation effects of scCO₂. This plasticisation effect can also have an impact on the crystallisation of PEEK and is most evident when samples that are initially amorphous are used. The methodology for generating amorphous PEEK samples is provided in detail in Chapter 3.3.1, and the confirmation of their amorphicity is

presented in Chapter 4.1.1. A cube plot showing the effects of processing pressure, temperature and time on the T_g is provided in Figure 38.

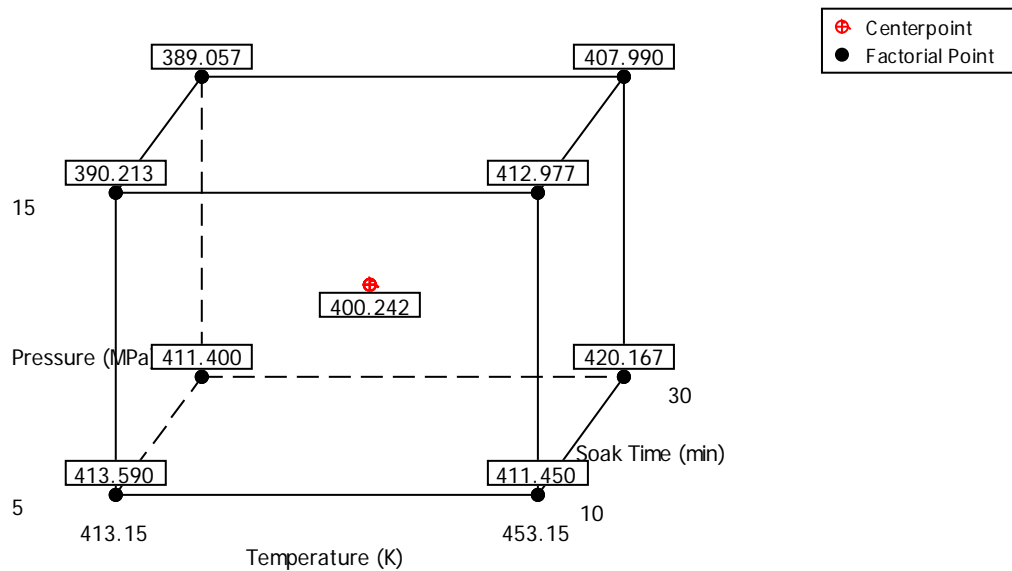


Figure 38: Cube plot for the effects of $scCO_2$ processing on the glass transition temperature (T_g) of PEEK150PF observed by DSC. DOE conditions; $T = 413 - 453$ K, $P = 5 - 15$ MPa, $t_r = 10 - 30$ min, centre-point $T = 433$ K, $P = 10$ MPa, $t_r = 20$ min

It is evident from Figure 38 that, with the exception of a processing time of 30 minutes at 453 K with a CO_2 pressure of 5 MPa, in all cases the T_g was reduced from 416 K observed with virgin material, an effect that is attributable to the presence of $scCO_2$. The greatest reductions were achieved when the CO_2 pressure was 15 MPa and was not dependent upon the processing time, with the T_g being approximately 390 K. Reductions in T_g were less substantial when the processing temperature was greater than T_c . When the molecular chains are randomly oriented, as opposed to being regularly ordered into well-defined crystal structures, there is a greater free volume through which the CO_2 may enter. This increases the potential of the CO_2 to plasticise the polymer and results in an increased

ability to manipulate the T_g compared to when semi-crystalline samples are used. Therefore, when processing samples at 453 K PEEK undergoes spontaneous thermodynamic crystallisation and is less susceptible to the effects of scCO₂ processing. Increasing the processing time above the crystallisation temperature promotes the crystallisation of the polymer and increases the tortuosity for the effusion of CO₂. For the plasticisation of the polymer to prevail it is then necessary to increase the processing pressure. In doing so, reductions in T_g of up to 9 K are observed in contrast to reductions of up to 26 K observed when PEEK is processed below T_c . In addition to manipulation of the glass transition temperature, the ability of scCO₂ to induce the crystallisation of PEEK below the spontaneous thermodynamic crystallisation temperature was investigated. A cube plot showing the percentage crystallisation observed by DSC with respect to the processing temperature, pressure and time is given in Figure 39.

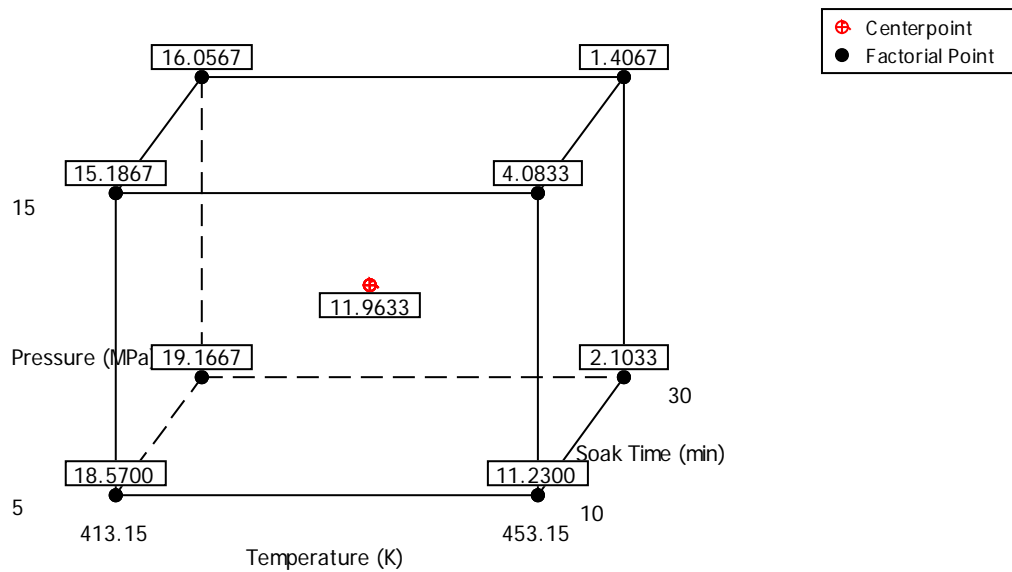


Figure 39: Cube plot showing the percentage crystallisation observed by DSC for PEEK processed with $scCO_2$. DOE conditions; $T = 413 - 453$ K, $P = 5 - 15$ MPa, $t_r = 10 - 30$ min, centre-point $T = 433$ K, $P = 10$ MPa, $t_r = 20$ min

It is important to state that Figure 39 shows the percentage crystallisation observed by DSC, post $scCO_2$ processing. The PEEK samples, being amorphous prior to processing, would typically show a $\%X_C$ of 18 % at T_c when analysed by DSC as detailed in Chapter 4.1.1. FT-IR analysis of quenched PEEK150PF samples showed that the samples generated could potentially have a $\%X_C$ of 2.3 % and therefore the maximum $\%X_C$ that could be observed would be 20.3 %. This would indicate that the polymer was 100 % amorphous post processing and the crystallisation process takes place exclusively within the DSC. Conversely, the minimum $\%X_C$ observable by DSC is 0 and relates to the maximum crystallisation possible taking place during the polymer processing. The crystallisation process is irreversible and therefore not observable during the DSC analysis. By using these

two boundary conditions it is then possible to use the data obtained from DSC analysis, presented in Figure 39, to determine the impact of scCO₂ on the crystallisation of PEEK.

It is observed that when the processing temperature is 413 K a high CO₂ pressure is required to induce crystallisation within the polymer, a %X_c 15.2 % is observed when the pressure is 15 MPa in comparison to 18.6 % when the CO₂ pressure is 5 MPa. At the centre-point, T = 433 K, P = 10 MPa and t_r = 20 min, a %X_c of 12 % is observed indicating the induction of approximately 6 %X_c as a result of scCO₂ processing. The expectation would be that by increasing the processing temperature beyond T_c the polymer would undergo crystallisation, as is the case in the absence of CO₂. However, this differs from the empirical observations and it is apparent that whilst scCO₂ can induce crystallisation, the induced crystallisation process takes place at a reduced rate compared to the spontaneous thermodynamic crystallisation process. Whilst not immediately intuitive, this is consistent with the scCO₂ plasticisation effect. With the CO₂ effusing between the polymer chains, increasing the free volume and facilitating the movement of the molecular chains, in order for crystallisation to take place there is a requirement to displace the CO₂ and allow the polymer chains to compact, forming crystals. This is likely to be a time dependent process and therefore the %X_c will be proportional to the soak time. Increasing the CO₂ pressure under such conditions exerts greater pressure on the bulk material, and may be responsible for forcing the molecular chains together more rapidly to form crystallites. The displacement of CO₂ must still take place and therefore %X_c is still directly proportional to time. This effect is demonstrated in Figure 39 where it can be seen that the %X_c observed by DSC reduces from 11.2 % to 2.1 % when the soak time is increase from 10 to 30 minutes.

It is evident that the crystallisation process induced by the use of scCO₂ differs from that of the spontaneous thermodynamic process, which in turn leads to the formation of differing crystal structures. The polymer melting process takes place by destroying the crystalline regions within the polymer and returning the material to a fully amorphous state. Therefore, it follows that if there are multiple types of crystals it may be possible to identify multiple melt transitions. Figure 40 provides a comparison of DSC thermograms for PEEK150PF samples processed under differing conditions.

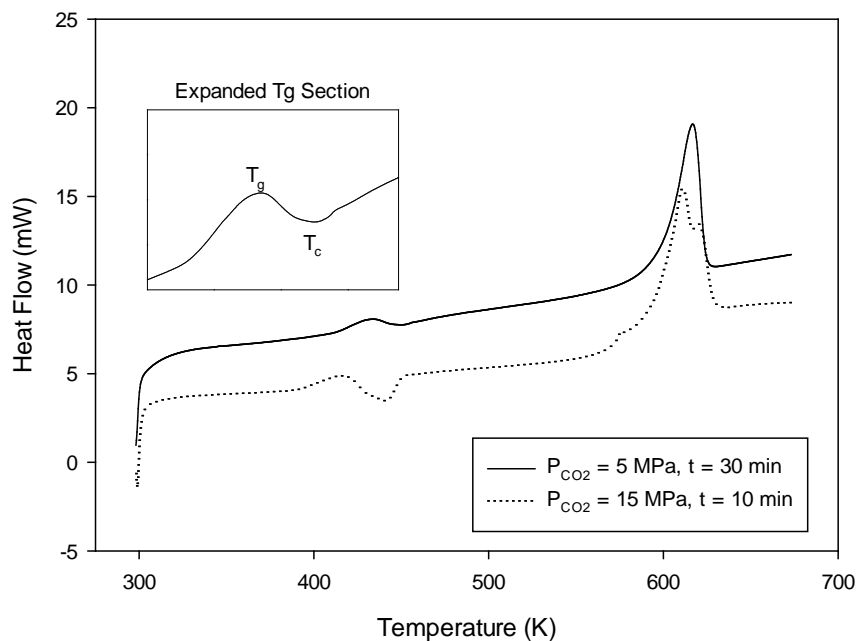


Figure 40: DSC thermograms for PEEK 150PF samples processed from amorphous state using scCO₂, T = 453 K. DSC Method 1

Inspection of Figure 40 reveals that when processed at 453 K for 30 minutes with a CO₂ pressure of 5 MPa, crystallisation of the polymer takes place and therefore only small amounts of crystallisation are observed when analysed by DSC. This is the also the

observation of Figure 39. It is further observed that a single endothermic peak, corresponding to the melting of the polymer is observed. By contrast, when processed at 453 K for 10 minutes with a CO₂ pressure of 15 MPa the spontaneous thermodynamic crystallisation process is observed by DSC, with the reduced integral (compare to amorphous material, Figure 32, Page 154) being a consequence of the induction of crystallisation by scCO₂. It is apparent that the crystallites within the polymer were formed by two dissimilar processes and inspection of the endotherm associated with the melting of the polymer reveals two distinct melt transitions. Analysis of the DSC thermograms identified that where the polymer was processed for extended time periods, allowing the thermodynamic crystallisation process to prevail, a single melt peak was observed and that in the case of the example presented in Figure 40, the melting temperature was 616 K in agreement with the virgin material. Conversely, with respect to the double melting peak presented in Figure 40, the lower transition takes place at 609 K and the upper transition takes place at 619 K. Thus, empirical findings suggest that the processing of PEEK with scCO₂ manipulates the glass transition temperature and induces crystallisation, which in turn may indirectly alter the melting process due to the formation of dissimilar crystallites.

4.1.3. High-Pressure Differential Scanning Calorimetry

The measurements presented so far are concerned with identifying the effects of scCO₂ on polymer matrix by analysing the material post processing. Identification of the effects of scCO₂ on the melting process are restricted to considering the formation of crystallites at, or near to, the crystallisation temperature. In carrying out such an investigation, it is not known whether CO₂ is present within the polymer upon reaching the melt temperature, and

therefore its impact cannot be assessed. To investigate such impacts it is necessary to subject the polymer to scCO₂ whilst conducting the DSC analysis. Attention is turned towards the use of High-Pressure DSC (HPDSC) to carry out this investigation.

Any manipulation of the crystallisation temperature of PEEK may be identified directly by carrying out HPDSC, where the observations may appear to differ from those previously presented. The apparent difference arises from the fact that the T_c observed in post processing analysis is the crystallisation process taking place in the absence of CO₂ but as a result of CO₂ processing. During CO₂ processing, crystallisation may have taken place and the temperature at which it took place is not necessarily the same as when the remaining crystallisation takes place in the absence of CO₂. By contrast, the crystallisation temperature observed by HPDSC is representative of the conditions to which the PEEK is subjected since the measurement is *in-situ*. Figure 41 shows an HPDSC thermogram for PEEK.

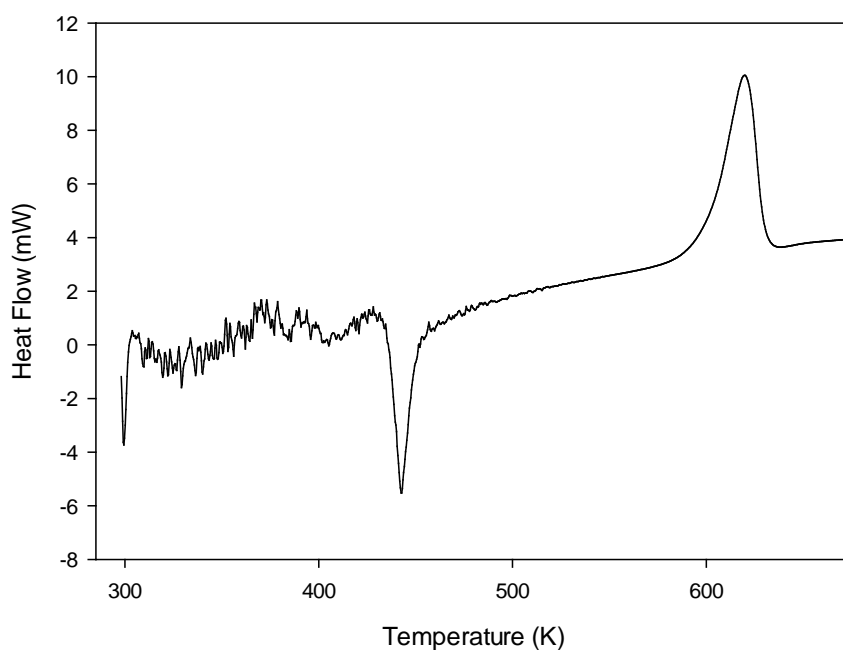


Figure 41: HPDSC thermogram for amorphous PEEK *in-situ* measurement, $P_{\text{CO}_2} = 3.0 \text{ MPa}$, HPDSC method 5

Figure 41 shows that the *in-situ* measurement of the effects of CO_2 on the polymer transitions is possible, with limited success, by means of HPDSC. The crystallisation and melting temperatures are prominent and easily identified. The glass transition temperature however is obscured by noise introduced by the use of CO_2 , as discussed in Chapter 3.4.2. The crystallisation temperature during the *in-situ* measurement was reduced from 449 K to 443 K, in accordance with the post processing analysis discussed previously. The melt temperature increased by 3 K, further indicating that the potential for high-pressure CO_2 to force the molecular chains together. Increasing the CO_2 pressure further significantly increases the noise as shown in Figure 42.

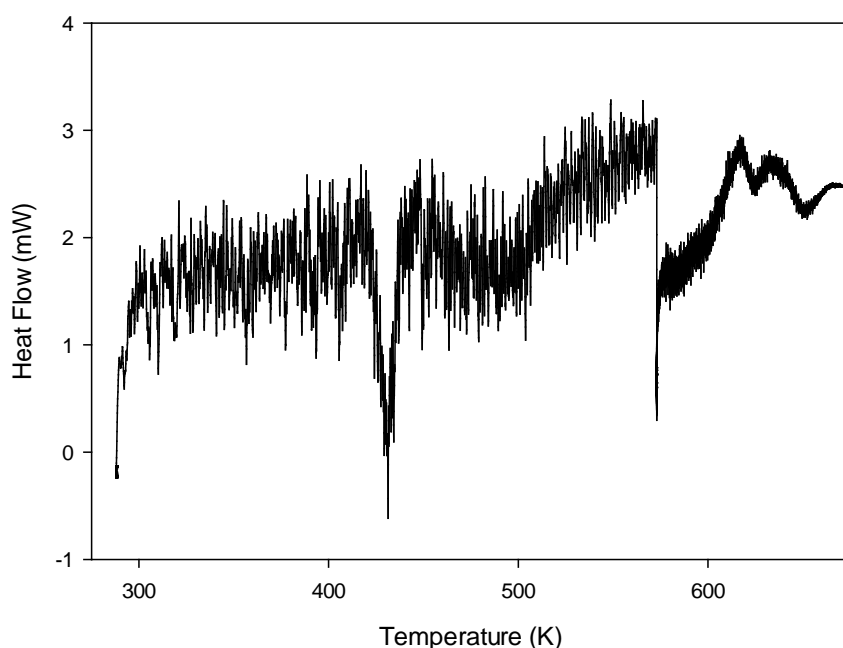


Figure 42: HPDSC thermogram for amorphous PEEK in-situ measurement, $P_{\text{CO}_2} = 3.5 \text{ MPa}$, HPDSC method 1

The increase in noise, as a result of the increased CO_2 pressure, is considerable as can be seen in Figure 42. The glass transition temperature is obscured by noise, however, the crystallisation and melting temperatures are visible. It can be seen that the crystallisation temperature is reduced to 431 K from 449 K observed with virgin material. It is therefore evident that the use of CO_2 with a pressure of 3.5 MPa is sufficient to reduce the crystallisation temperature to below that of the centre-point used in the designed experiment, Chapter 4.1.2. The melt transition consists of two peaks, indicating the presence of two crystal structures within the polymer, as previously discussed. The initial melt peak is at 617 K, in accordance with the virgin material, the second melt peak appearing at 633 K. This represents a considerable increase in the melt temperature of 16 K, with the increase being directly attributable to the increased CO_2 pressure.

Increasing the CO₂ pressure further leads to results that are illegible without the use of extensive smoothing and noise reduction. In processing the data in this way, much of the valuable information is destroyed or manipulated such that it no longer may be considered representative of the experiment. As such, the use of HPDSC was limited. The data obtained are in very good agreement with the results obtained from the designed experiment (Chapter 4.1.2) and are used to provide insight into the interactions taking place between the CO₂ and the polymer within the reactor.

4.1.4. Carbon Dioxide Containment with PEEK

Having studied the interaction between CO₂ and the polymer during polymer processing, it is prudent to investigate whether CO₂ is released from the polymer upon depressurisation or retained for a period of time. Retention of CO₂ within the polymer may influence the physical properties of the material, given that it has previously been established that the presence of CO₂ can manipulate the glass transition and crystallisation temperatures and indirectly influence the melting temperature. The methodology for this investigation is presented in Chapter 3.3.1. and essentially comprises of processing PEEK with scCO₂ and allowing for a period of time to elapse prior to analysis by TGA. A summary of the findings is presented in Figure 43.

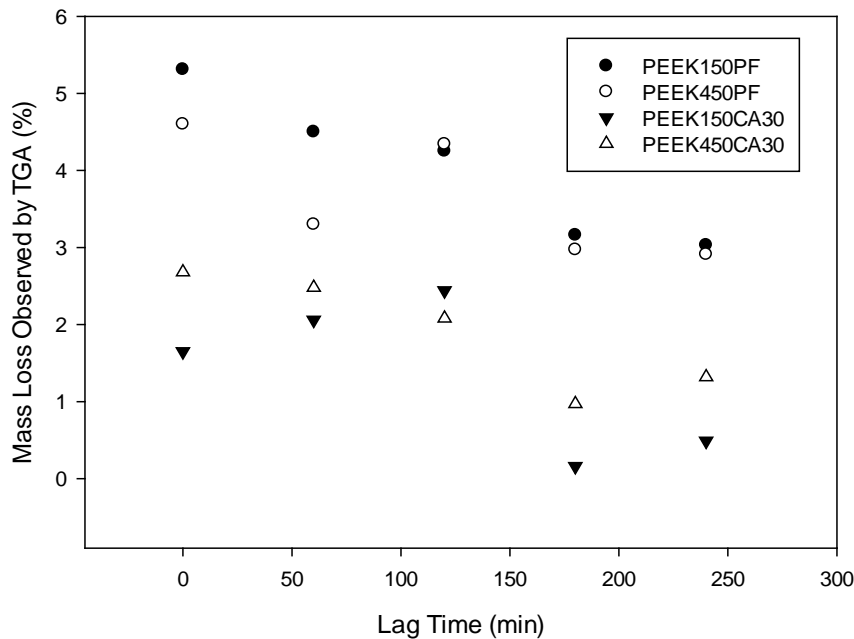


Figure 43: Mass loss observed by TGA as a function of Lag Time for PEEK processed with $scCO_2$, $P = 20.0 \text{ MPa}$, $T = 413 \text{ K}$, $t = 30 \text{ min}$

Figure 43 shows that in general, the mass loss observed by TGA is inversely proportional to the Lag Time, indicating that the CO_2 escapes from the polymer under ambient conditions. The control samples showed a mass loss of 0.25 % when analysed by TGA, thought to be attributable to experimental error. The responses of PEEK 150PF and 450PF are similar to each other, as are the responses from PEEK 150CA30 and 450CA30. It is evident that the carbon fibres contained within the PEEK 150CA30 and 450CA30 grades contribute to the release of CO_2 , and hence the mass loss observed by carbon fibre filled samples was lower than that of their unfilled counterparts. It is possible that in the case of carbon fibre filled PEEK samples that the uptake of CO_2 into the polymer matrix was lower than that of the unfilled PEEK, which in turn would result in a lower percentage mass loss observed by TGA. However, given that the sample is 30 %v carbon fibre, the majority of the sample consists of the polymer matrix and therefore 70 %v of the sample would be expected to behave in a

similar way to its unfilled counterpart. An alternative hypothesis is that the boundary between the carbon fibre and the PEEK provides small channels through which the CO₂ may travel preferentially, negating somewhat the more tortuous route through the polymer matrix. This hypothesis is supported by observation made from Figure 43 where it can be seen that the percentage mass loss is loosely linear for unfilled PEEK, whereas there is a step change after a lag time of 120 minutes for the carbon fibre filled grades. This step change is thought to be the result of two effusion rates of CO₂ from the sample. The primary route is via the channels formed by the presence of carbon fibres, the second route being via the polymer matrix. The offset in percentage mass loss between filled and unfilled PEEK, shown in Figure 43, results from the carbon fibre's inability to absorb CO₂. Therefore, for a given sample mass it is apparent that the carbon fibre filled sample will absorb, and therefore release, a lower mass of CO₂.

Since the PEEK samples were processed exclusively with CO₂ it is possible to infer that the mass loss observed by TGA is a result of the release of CO₂. To test this inference, the exhaust gas from the TGA was coupled to the FT-IR using a gas cyclone accessory as detailed in Chapter 3.4.3. The TGA thermogram for PEEK 450PF processed with scCO₂ are shown in Figure 44.

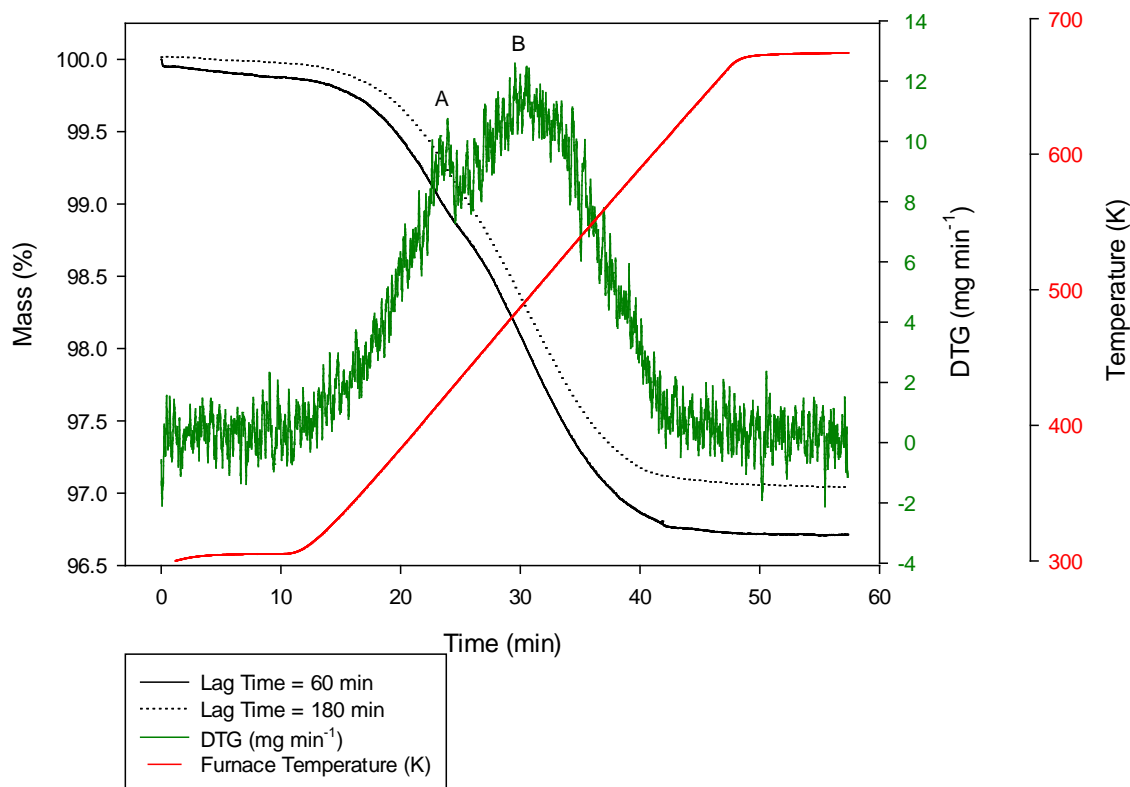


Figure 44: TGA thermogram for PEEK450PF processed in $scCO_2$ showing the furnace temperature and 1st order differential of mass loss (DTG), $P = 20.0 \text{ MPa}$, $T = 413 \text{ K}$, $t = 30 \text{ min}$. TGA Method 1

By inspection of Figure 44 it can be seen that the rate of mass loss is approximately constant for the samples analysed. The magnitude, however, differs according to the lag time as previously discussed. It is notable that the mass loss is not linear for the temperature range analysed and actually goes through two maxima, labelled 'A' and 'B'. The first maximum 'A' occurs at approximately 24.5 minutes, corresponding to a temperature of 417 K, with the second maximum 'B' occurring at 30.5 minutes, corresponding to a temperature of 489 K. Figure 44, point 'A' takes place within close proximity to the glass transition temperature of PEEK, 416 K, and it is likely that the increase in molecular motion present above the T_g is responsible for the increase in CO_2 release rate from the polymer. The rate of CO_2 release

from the sample then subsides prior to the attaining the crystallisation temperature. At T_C , with the re-ordering process of the molecular chains taking place forming crystallites throughout the sample, there is an increasing opportunity for CO_2 to migrate from within the bulk polymer to the surface and subsequently escape. This is manifested in the rate of mass loss increasing to a maximum point observed in Figure 44, point 'B'. There is an offset of 30 K, equivalent to a period of 3 minutes (considering a heating rate of 10 K min^{-1} was used), between the polymer reaching the crystallisation temperature and the maximum rate of CO_2 release being observed. After point 'B' the rate of mass loss declines rapidly, reaching essentially 0 prior to the polymer reaching its melting temperature of 616 K. Having determined the temperatures at which CO_2 is released most rapidly from the sample, expectation would be to observe the greatest intensity of absorbance by FT-IR due to CO_2 at a similar time should the TGA exhaust gasses be analysed on-line. Figure 45 and Figure 46 show the three dimensional FT-IR spectra of the TGA exhaust gasses for PEEK450PF analysed after 60 minute and 180 minute lag times respectively.

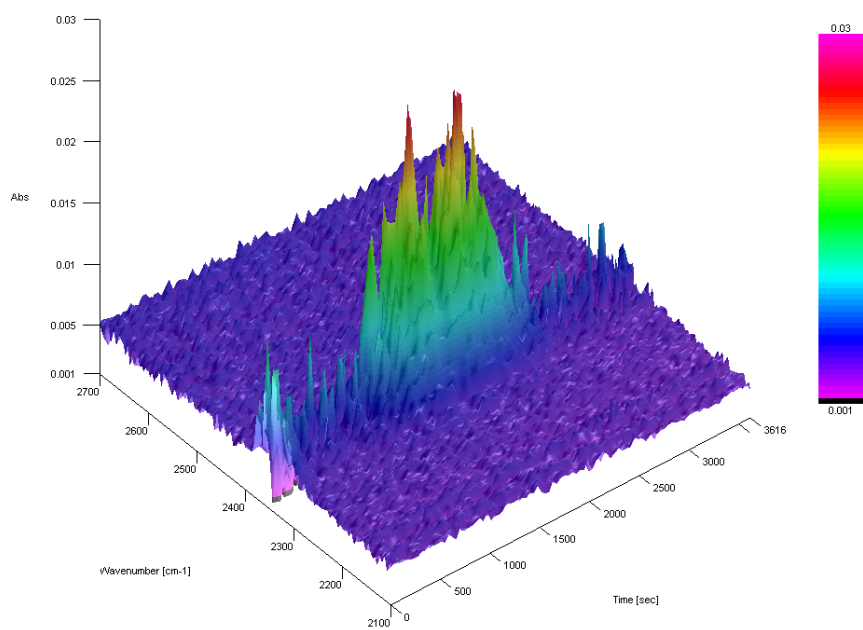


Figure 45: 3D FT-IR spectrum for analysis of TGA exhaust gasses from PEEK450PF processed in scCO₂, lag time = 60 min, (Processing conditions; P = 20.0 MPa, T = 413 K, t = 30 min)

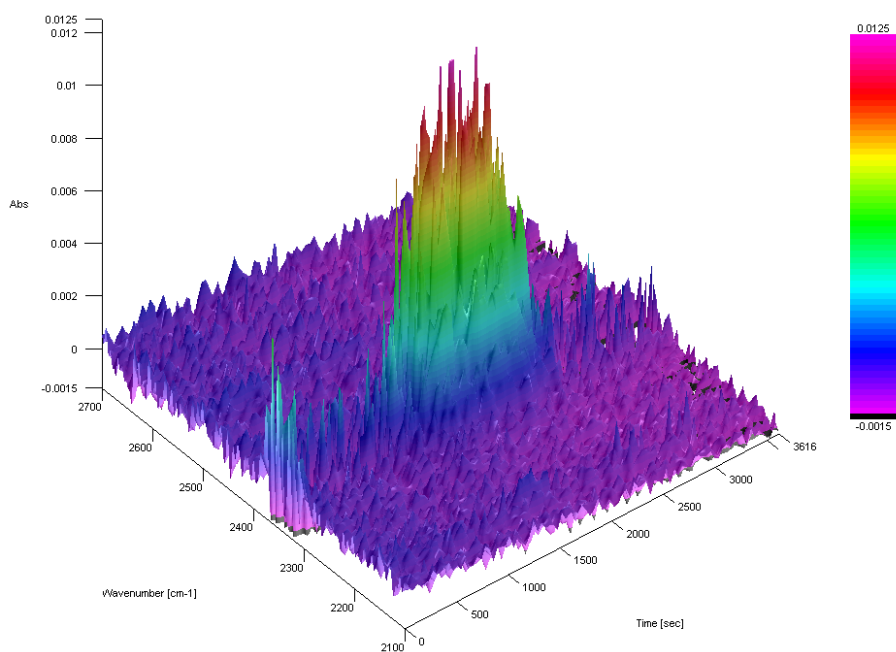


Figure 46: 3D FT-IR spectrum for analysis of TGA exhaust gasses from PEEK450PF processed in scCO₂, lag time = 180 min, (Processing conditions; P = 20.0 MPa, T = 413 K, t = 30 min)

Figure 45 and Figure 46 show absorbance at wavenumber of 2360 cm^{-1} , corresponding to unbound CO_2 . Inspection of Figure 45 shows that the absorbance volume consist of two individual peaks, the first peak occurring at approximately 1500 s (25 minutes) and the second at approximately 2100 s (35 minutes). By identifying the presence of CO_2 slightly later than the mass loss observed by TGA, in conjunction with the knowledge that the sample was exposed to scCO_2 exclusively, it is determined that the mass loss observed by TGA is directly attributable to CO_2 . Figure 46 is not resolved into two distinct peaks, possibly owing to the reduced mass of CO_2 release, leading to the appearance of a single peak. This method of identification is used qualitatively and as such no attempt to quantify the volume of CO_2 observed by FT-IR is made. Although it is acknowledged that doing so would not be impossible, doing so is extremely convoluted and does not necessarily provide any information unobtainable by TGA.

By conducting this study it is possible to demonstrate that CO_2 may be used to manipulate the glass transition temperature and induce crystallisation within the polymer matrix. Where the impact of scCO_2 processing upon the melting process of PEEK was previously unclear, it may now be seen that the CO_2 used to process the material escapes prior to reaching the melting temperature. It follows that the impact of scCO_2 processing upon the PEEK melt process is largely indirect and is a consequence of the production of dissimilar crystallites, principally those formed during the spontaneous thermodynamic crystallisation process and those induced due to the use of scCO_2 . *In-situ* measurements of the crystallisation process by HPDSC have shown that increasing the CO_2 pressure reduces the T_g and T_c but does not reduce the bulk melting temperature. The results suggest that the

crystallites produced by scCO_2 induction may have a melting point greater than that of the bulk material but further experimental work is required to confirm this. Having studied the impact of a supercritical fluid on the polymeric transitions of PEEK, attention is now focused on the decomposition and subsequent recycling of end-of-life PEEK by means of supercritical fluids.

4.2. DECOMPOSITION AND RECYCLING OF POLYETHERETHERKETONE COMPOSITE MATERIALS

The methodology for the decomposition and recycling of polyetheretherketone and its composite material is presented comprehensively in Chapter 3.3.2. As with the methodology, the results of this investigation are presented in three parts, owing to the differences in the reaction systems studied. However, in this chapter a combined explanation and comparison between the systems is given once the results of all three reaction systems have been presented. The format of these results follows that of the methodology, presenting the effects of the co-solvent concentration, followed by the effects of the catalyst and finally presenting the effects of reaction time.

4.2.1. Ethanol and Water Co-solvent System

Effects of Ethanol Concentration

The ethanol concentration was varied from 0 – 100 % by volume, maintaining a reactor solvent loading of 50%, with the PEEK and Cs_2CO_3 concentrations being maintained at 10 mg ml^{-1} . The reaction schedule is provided in Chapter 3.3.2. The aqueous fractions were

analysed by means of HPLC and GC-MS as detailed in Chapter 3.4.3, the concentration of phenol was used as an indicator for the decomposition as shown in Figure 47.

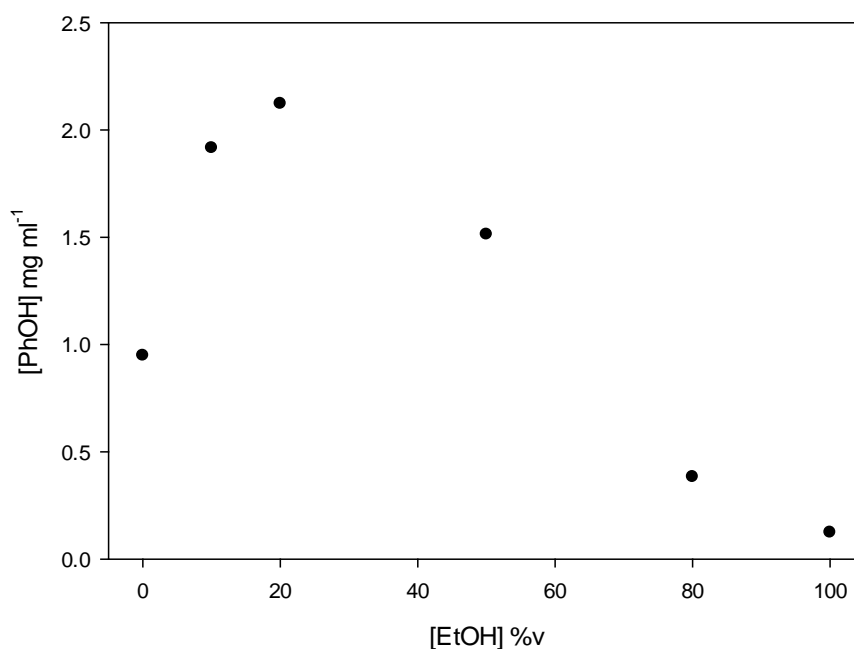


Figure 47: Phenol concentration [PhOH] with respect to ethanol concentration [EtOH], 623 K, 30 min, 10 mg ml⁻¹ Cs₂CO₃, P = 15.8 – 25.5 MPa. Determined by HPLC

By inspection of Figure 47 it is evident that ethanol functions effectively as a co-solvent with water but water is essential in the decomposition of PEEK. When the reaction medium contains more than approximately 65 %v ethanol the decomposition is less effective than a solution containing 0% ethanol. The optimum concentration is approximately 20%v ethanol, 80%v water. At the reaction temperature and pressure of 623 K and 17 MPa respectively and an ethanol concentration of 20 %v, the reaction medium was at the critical point for the mixture [314]. Supercritical fluids are able to swell polymers [10, 26, 86] and in preliminary work, supercritical water (scH₂O) has produced a macro-porous structure, Figure 48.

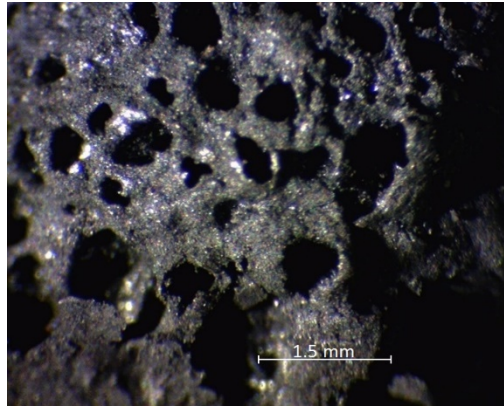


Figure 48: Optical Microscopy image of PEEK, Victrex 150CA30, post processing in scH_2O , 648 K, 25 min, 30 MPa, showing the macro-porous structure

The creation of a macro-porous structure may assist in the rate of decomposition owing to the significant increase in surface area, as well as decreasing the depth of material that the reaction medium has to penetrate. SEM has been used to qualitatively establish the relationship between ethanol concentration and the decomposition of PEEK, and subsequent release of the carbon fibres. Figure 49 'a' and 'b' show the effects of 20 %v and 100 %v ethanol, maintaining all other reaction conditions.

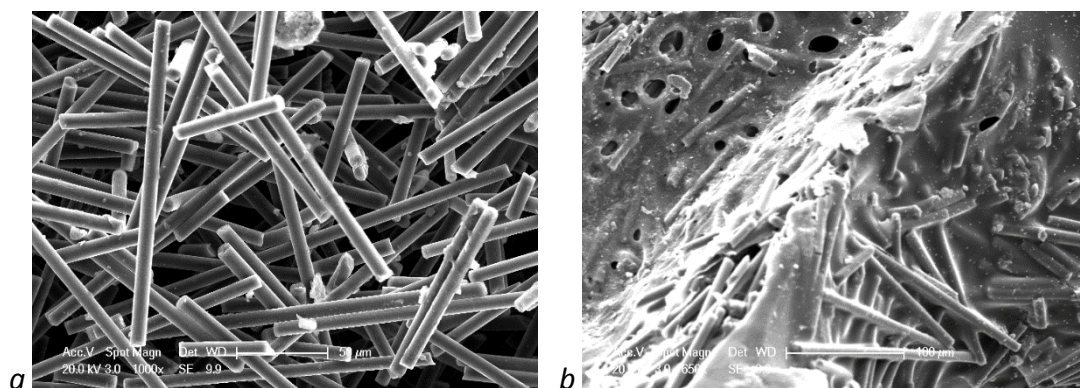


Figure 49: SEM Micrographs of post processed PEEK 150CA30, 30 min, 623 K, $10 \text{ mg ml}^{-1} \text{ Cs}_2\text{CO}_3$, a) $[\text{EtOH}] = 20 \text{ \%v}$, 16.7 MPa, b) $[\text{EtOH}] = 100 \text{ \%}$, 23.9 MPa

Figure 49 'b' shows that without the addition of water the decomposition of PEEK does not readily take place, the carbon fibres are visibly confined within the polymer matrix. A co-solvent system consisting of the 80 %v H₂O, 20 %v EtOH under the same conditions brings about complete decomposition of the polymer, allowing for separation of the fibres for subsequent testing and incorporation into new products. Having identified the ideal co-solvent composition with respect to ethanol concentration it was necessary to investigate the effects of the Cs₂CO₃ concentration.

Effects of Caesium Carbonate Concentration

By maintaining the concentration of ethanol at 20 %v (80 %v water), the reaction temperature at 623 K and a reaction time of 30 minutes the concentration of Cs₂CO₃ was varied from 0 – 10 mg ml⁻¹. The reaction conditions are presented in Chapter 3.3.2, the results are presented in Figure 50.

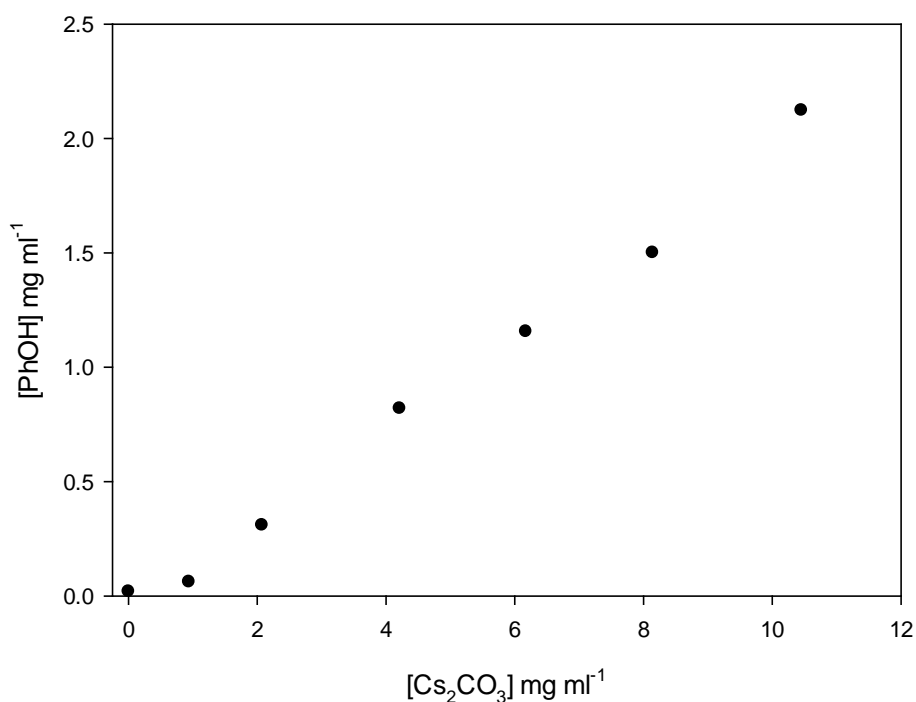


Figure 50: Effect of caesium carbonate concentration [Cs₂CO₃] on the production of phenol [PhOH] by the decomposition of PEEK. 20 %v ethanol, 80 %v water, 30 min, 623.15 K, 16.8 ± 0.2 MPa. Determined by HPLC

By inspection of Figure 50 it may be seen that the reaction is 1st order with respect to the caesium carbonate concentration. Without the addition of caesium carbonate the concentration of phenol was 0.02 mg ml⁻¹ indicating that the decomposition was minimal.

Fourier Transform Infra-Red Spectrometry Analysis

FT-IR may be used to analyse the functional groups of PEEK and by comparison of wavenumbers 1305 cm⁻¹ and 1280 cm⁻¹ it is possible to infer the percentage crystallinity [62, 310]. If the polymer has been decomposed it would not be expected to observe functional groups associated with PEEK, crystalline or amorphous. Figure 51 shows the FT-IR spectrum for a PEEK150CA30 sample processed for 30 minutes in a mixture containing 20 %v ethanol,

80 %v water without the addition of Cs_2CO_3 . It is evident that the polymeric functional groups associated with PEEK are still present, further indicating that the decomposition was minimal. By contrast, Figure 52 shows the FT-IR spectrum for a sample processed under identical conditions with the addition of $10 \text{ mg ml}^{-1} \text{ Cs}_2\text{CO}_3$.

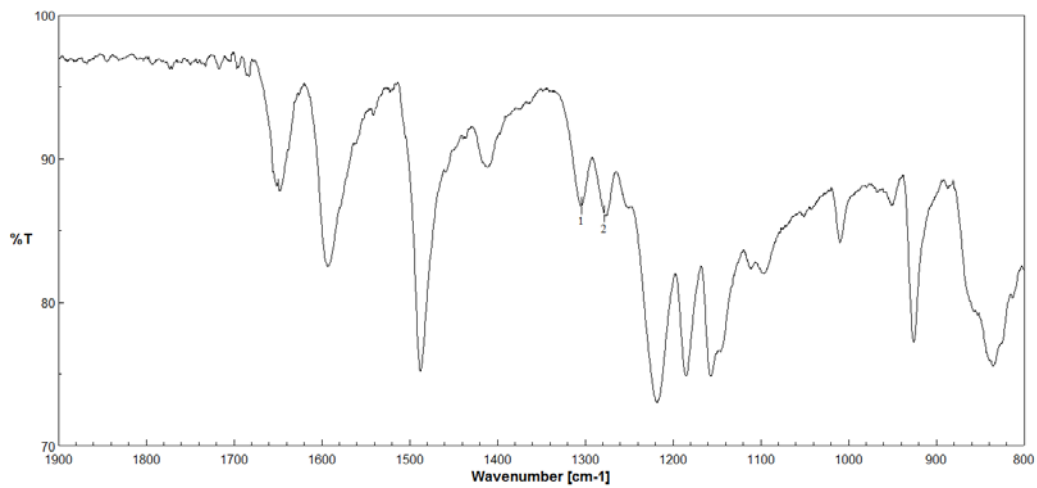


Figure 51: FT-IR of PEEK 150CA30 post processing, 30 min, 623.15 K, 20 %v ethanol, 80 %v water, $16.8 \pm 0.2 \text{ MPa}$, without Cs_2CO_3 ; Peak 1 = 1305 cm^{-1} , Peak 2 = 1280 cm^{-1}

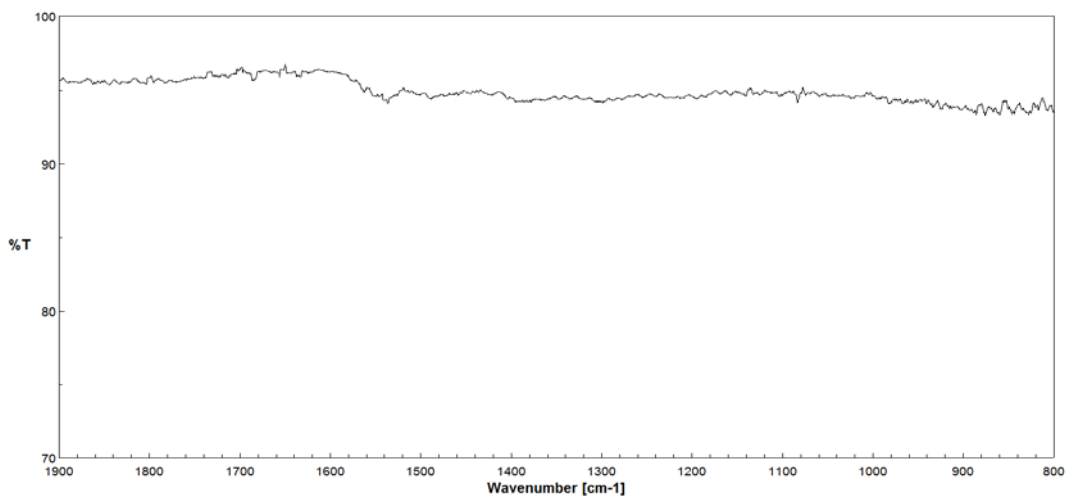


Figure 52: FT-IR of PEEK 150CA30 post processing, 30 min, 623.15 K, 20 %v ethanol, 80 % water, $16.8 \pm 0.2 \text{ MPa}$, $10 \text{ mg ml}^{-1} \text{ Cs}_2\text{CO}_3$

Comparison of Figure 51 and Figure 52 highlights the significant contribution that caesium carbonate makes in the decomposition of PEEK. The complete absence of functional groups is indicative of the FT-IR measuring only carbon fibres, a qualitative indication that the decomposition is substantial.

Differential Scanning Calorimetry Analysis

Additional information may be obtained from Differential Scanning Calorimetry (DSC). PEEK150CA30 is obtained in the semi-crystalline state, therefore crystallisation is not observed when analysing virgin samples. The crystallisation process of PEEK is rapid, taking place at approximately 450 K [85]. The reactor cooling process is sufficiently slow ($10 - 20 \text{ K min}^{-1}$) such that any PEEK in the melt phase would crystallise prior to being removed from the reactor. PEEK recovered from the reactor and analysed by DSC is expected to exhibit a T_g and T_m . Figure 53 shows the DSC thermogram for virgin PEEK 150CA30 and processed samples.

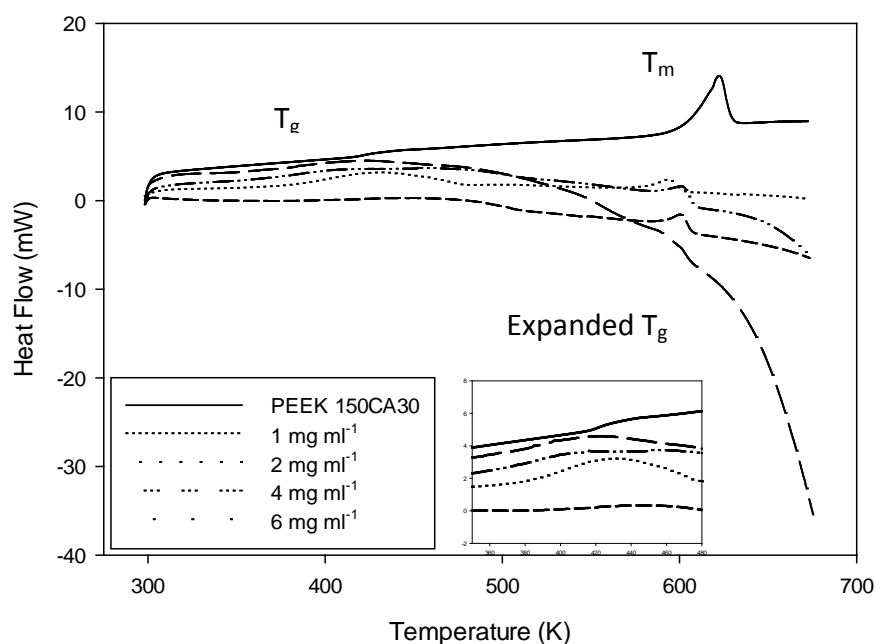


Figure 53: DSC thermogram for PEEK 150CA30 processed for 30 minutes using 20 %v ethanol, 80 %v water, 16.8 ± 0.2 MPa, $1 - 6 \text{ mg ml}^{-1} \text{ Cs}_2\text{CO}_3$

Figure 53 shows that when the caesium carbonate concentration is below 6 mg ml^{-1} PEEK partially maintains its polymeric structure, hence the melt transition is observed. HPLC analysis (see Figure 50) shows that even when the caesium carbonate concentration is 1 mg ml^{-1} small quantities of phenol are produced, indicating that the decomposition has begun. Once the caesium carbonate concentration exceeds 6 mg ml^{-1} the melt transition is no longer observed and the functional groups associated with PEEK are also not seen by FT-IR, implying that the decomposition is in the advanced stages. Samples processed with a Cs_2CO_3 concentration of 1 mg ml^{-1} exhibited a T_g at 432 K, whereas samples processed with a Cs_2CO_3 concentration of 2 mg ml^{-1} exhibited a T_g at an elevated temperature of 480 K.

Effects of Reaction Time

Using the production of phenol as an indicator as to the decomposition of PEEK, it is possible to investigate the effects of the reaction time. A reaction time of 0 minutes is considered to be heating and cooling of the reactor exclusively; once the reaction temperature is reached the furnace is removed and the reactor is cooled. This study was carried out at 623 K to ensure that the PEEK was in the melt phase, and therefore amorphous. Figure 54 shows the concentration of phenol with respect to the reaction time.

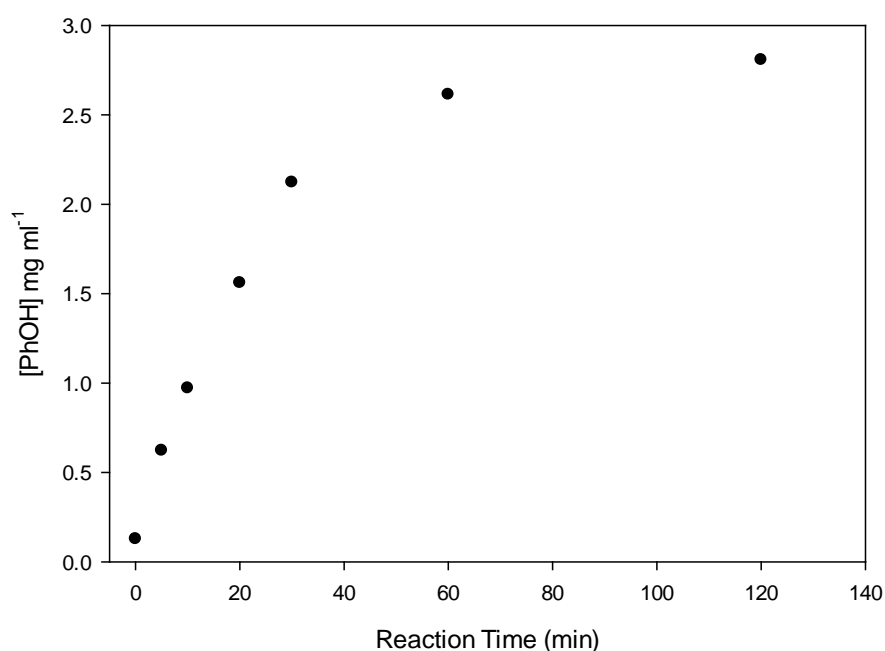


Figure 54: Phenol concentration [PhOH] with respect to reaction time, 623.15 K, [EtOH] = 20 %v, [H₂O] = 80 %v, 16.8 ± 0.2 MPa, 10 mg ml⁻¹ Cs₂CO₃, 10 mg ml⁻¹ PEEK. Determined by HPLC

Figure 54 shows that the production of phenol has taken place when the reaction time is 0 minutes (i.e. heating and cooling only). This implies that the decomposition of PEEK either takes place slightly below 623 K or that the reaction kinetics are sufficiently rapid such that the decomposition is immediate under the said conditions, leading to the production of

small quantities of phenol once the temperature (623.15 K) is attained. At the reaction time of 0 min the phenol concentration was 0.128 mg ml^{-1} and had increased to 0.623 mg ml^{-1} at 5 min. With a reaction time of 30 min the phenol concentration is 2.1 mg ml^{-1} , at which point doubling the reaction time to 60 min results in a phenol concentration of 2.6 mg ml^{-1} . No significant increase in phenol concentration was observed by subsequent doubling of the reaction time, indicating that the rate of degradation slowed.

Scanning Electron Microscopy and Energy Dispersive X-Ray Analysis

Scanning Electron Microscopy (SEM) has been used to analyse the fibres reclaimed from the polymer matrix. The fibres impregnated into PEEK150CA30 are short, typically several millimetres in length, and therefore have not been subjected to tensile testing due to physical constraints of the testing procedure. Examination of bulk fibres shows that after 0 min the vast majority of fibres appear to be confined within the polymer matrix, although some separated fibres are present. With increasing reaction time it is possible to separate the carbon fibres from the polymer matrix. It is also evident from the increased production of phenol (Figure 54) and the absence of polymeric functional groups (Figure 52) that the polymer has been decomposed and is no longer present. Figure 55, a – d, shows the effects of increasing reaction time on both decomposition of the polymer and release of the fibres.

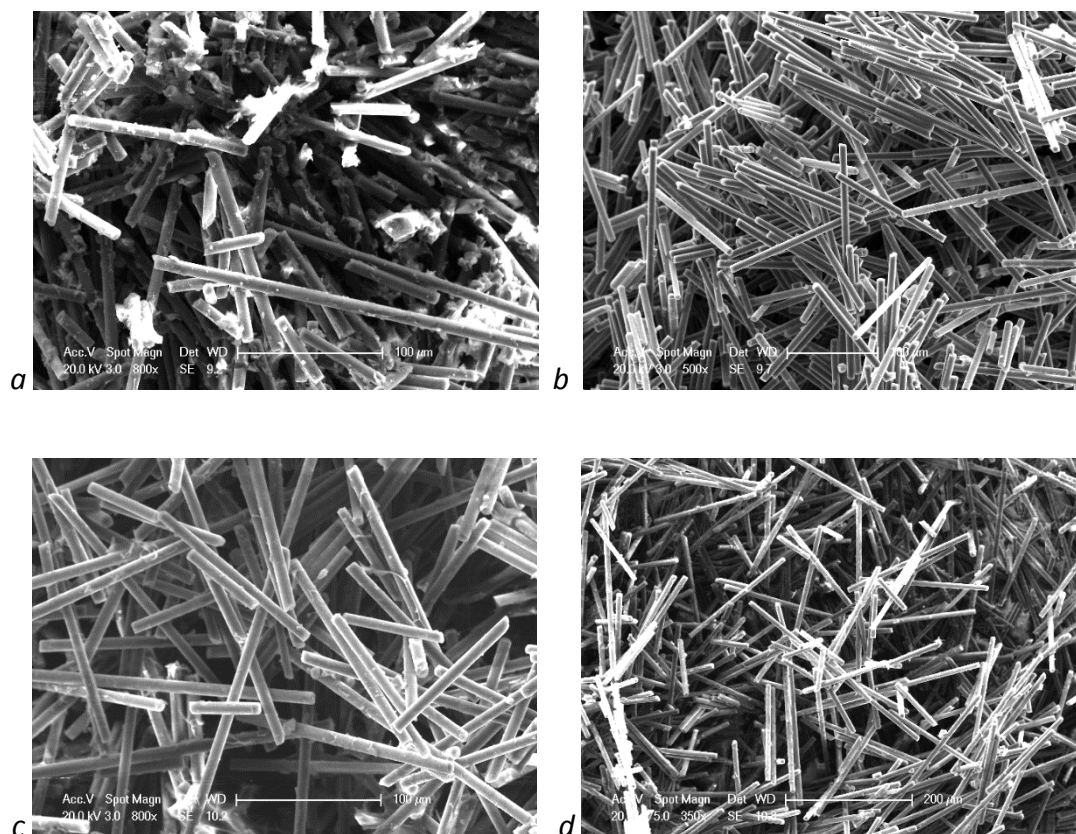


Figure 55: Decomposition of PEEK150CA30 and separation of the carbon fibres with increasing reaction time. 20 %v ethanol, 80 %v water, 16.8 ± 0.2 MPa, 623.15 K, 10 mg ml^{-1} , a) 0 min, b) 30 min, c) 60 min, d) 120 min

Inspection of the carbon fibres shows that the fibres reclaimed after a reaction time of 0 minutes contain some solid deposition. Qualitative analysis of the liquid fraction does not show significant deposition of carbon fibres, information which further implies that the polymer integrity is not heavily degraded. FT-IR analysis shows that for a reaction time of 0 minutes, the PEEK functional groups remain and analysis of the peaks at 1305 cm^{-1} and 1280 cm^{-1} show that the functional groups are not dissociated from the polymer backbone. By contrast, after 30 minutes the functional groups are not identified. Closer inspection of the carbon fibres by SEM shows that the fibres obtained after 0 minutes are partially coated, whereas those obtained from a 30 minute reaction are relatively clean and free of deposition (Figure 56).

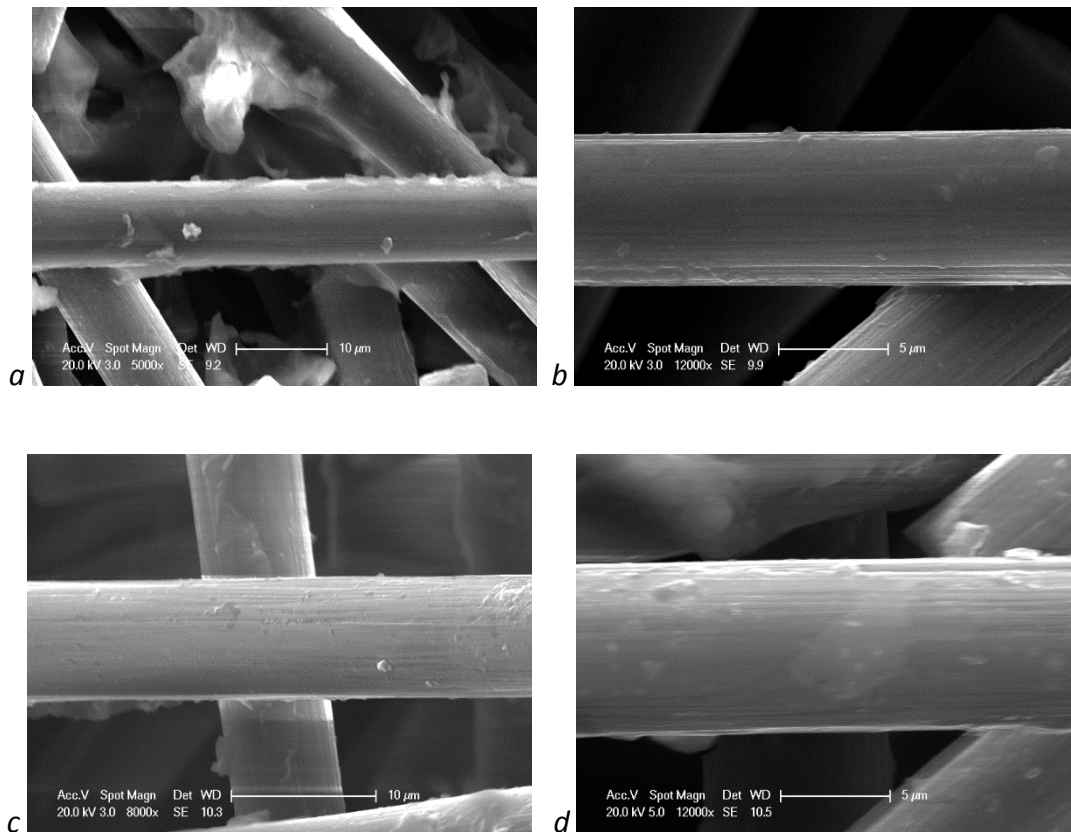


Figure 56: Fibres reclaimed from PEEK150CA30 using 20 %v ethanol, 80 %v water, 16.8 ± 0.2 MPa, 623.15 K, 10mg ml^{-1} , a) 0 min, b) 30 min, c) 60 min, d) 120 min

Fibres obtained from reaction times in excess of 30 minutes were not, in all cases, completely free of solid deposition. There are two primary suspected causes of this deposition, one being the solidification of the non-decomposed PEEK at ambient conditions and the other being the deposition of Cs_2CO_3 that has crystallised on the dried carbon fibres. Energy Dispersive X-Ray spectrometry (EDX) was used to identify the elemental composition of the deposits for reaction times of 0 and 60 min, Figure 57.

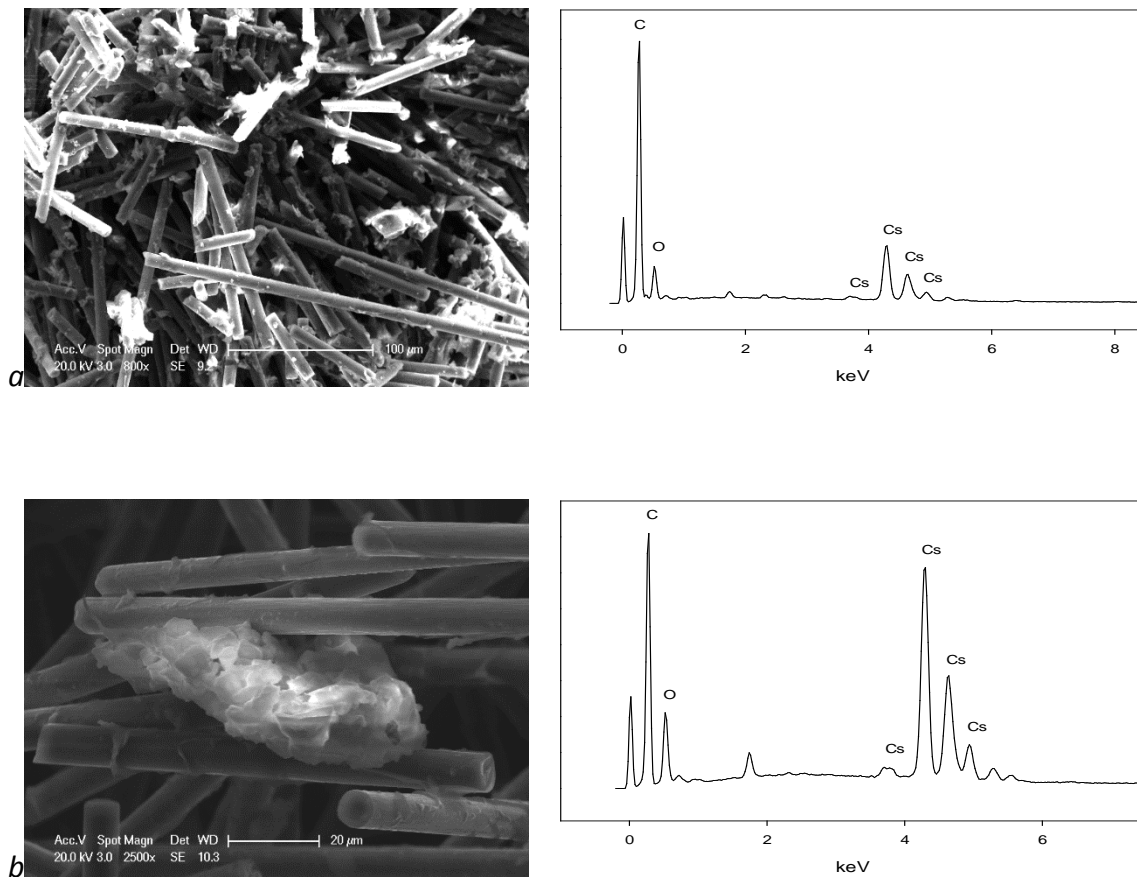


Figure 57: Energy Dispersive X-Ray Spectrometry of solids deposits using 20 %v ethanol, 80 %v water, 16.8 ± 0.2 MPa, 623.15 K, 10 mg ml^{-1} , a) 0 min, b) 60 min

The EDX analysis implies that the solid deposition observed on the carbon fibres for a reaction time of 60 minutes is Cs_2CO_3 , with Cs accounting for 8.96 % of the atoms identified compared with 3.17 % for a reaction time of 0 minutes. Considering that the Cs_2CO_3 concentration was the same in both reactions, and is not a product of the decomposition reactions, there is not sufficient evidence to suggest that there is any process leading to increased deposition of Cs_2CO_3 as a consequence of increased reaction times. In both cases, it is expected that the most abundant element in either sample would be carbon, which is indeed observed. However, in the case of the 0 min reaction there is also a significant amount of PEEK present, owing to the lack of decomposition. Almost 56 % of the PEEK

repeat unit is comprised of carbon atoms, and therefore should the decomposition be minimal, the relative abundance of caesium will be greatly reduced. The EDX data for the two conditions are tabulated in Table 23.

| Reaction Time (min) | C (%) | O (%) | Cs (%) |
|------------------------|----------|----------|-----------|
| 0 | 80.75 | 16.08 | 3.17 |
| 60 | 73.75 | 17.28 | 8.96 |

Table 23: EDX Analysis of solid deposits after 0 and 60 minute reactions (conditions as in figure 57)

The use of EDX in this context is not quantitative with respect to the entire sample, owing to its heterogeneity. EDX has been used to target deposits identified by means of SEM, allowing for the determination of their composition. Therefore, the quantitative analysis at any given point is not representative of the bulk sample.

Thermogravimetric Analysis

Thermogravimetric Analysis (TGA) was used to determine the percentage decomposition of PEEK. The thermal decomposition temperature is 848 K [105], at which point PEEK decomposes into a range of organic compounds. The quantity and composition of the remaining char is a function of the decomposition conditions, in an inert atmosphere N₂ approximately 70% of a carbon fibre reinforced PEEK sample remains as char[105]. It is therefore expected that should the polymer be decomposed and the organic compounds solubilised during the reaction, the percentage mass loss observed by TGA would be significantly reduced. The remaining mass would be attributed char and to the carbon fibres since they are not subject to significant thermal degradation in inert atmospheres until

temperatures in excess of 4273 K [315]. Figure 58 shows the TGA thermogram for PEEK 150CA30 samples processed for 0 – 120 minutes.

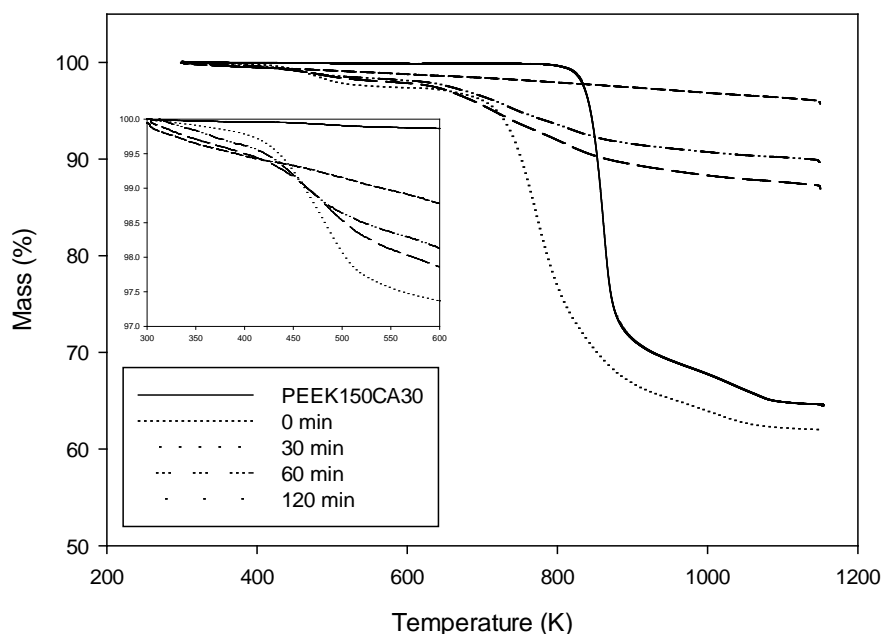


Figure 58: Effect of reaction time on observed mass loss by Thermogravimetric Analysis. 623 K, $10 \text{ mg ml}^{-1} \text{ Cs}_2\text{CO}_3$, $[\text{EtOH}] = 20 \text{ \%v}$, $[\text{H}_2\text{O}] = 80 \text{ \%v}$

Complete decomposition and subsequent removal of all organic compounds from the sample would leave only fibres. TGA analysis would then show approximately 4 % mass loss at temperatures up to 1150 K, attributable to the loss of functional groups associated with the sizing [316], by comparison the observed mass loss by TGA is 13 % or less for samples processed for 30 minutes or more. SEM analyses have shown that some solid deposition is present within the separated fibres, EDX has shown that some of the deposition is most likely to be Cs_2CO_3 , having a thermal decomposition temperature of 873 K. It is also possible that some decomposition products, such as phenol, may have crystallised within the fibre bundles upon drying. The mass loss onset associated with the processed samples is

significantly lower than that of PEEK, in some cases the mass loss appears linear below 600 K. It is therefore suggested that the TGA data for samples processed for longer than 30 minutes show the thermal degradation of the PEEK decomposition products, and not that of the polymer. The absence of a sharp increase in thermal degradation rate at 848 K further implies that the polymer decomposition is essentially complete for reaction times in excess of 30 minutes.

When the processing time is 0 minutes there is insufficient time for the decomposition to take place. However, prior to obtaining the reaction temperature of 623 K PEEK undergoes a transition to the melt phase at 616 K. Figure 47 and Figure 50 demonstrate that there is a synergistic effect between the ethanol and caesium carbonate concentrations. Experiments using 100 %v ethanol have shown that decomposition of the polymer did not take place, the solid samples were swollen but not degraded. It is known that Cs_2CO_3 is soluble in both water and ethanol, and also in mixtures of both solvents. It is suggested that ethanol / water mixture, being at its critical point, swells the PEEK allowing for an increased mass transport of the Cs_2CO_3 carried in the ethanol / water mixture into the PEEK structure. Similar material expansion and subsequent porosity has been identified with supercritical water (sch_2O). This similarity in the expansion of PEEK is thought to be accountable for the ability of Cs_2CO_3 in ethanol / water mixtures to decompose PEEK at 80 K below what is possible with water / Na_2CO_3 solutions.

When the reaction medium consists of ethanol and the reaction time is 0 minutes, an increase in the solid mass recovered from the reactor is observed. The SEM data have

shown that ethanol may be responsible for swelling PEEK and GC-MS has been used to identify phenol derivatives, such as 2-ethylphenol, which may indicate that ethanol may undergo some decomposition and subsequently react with the phenyl ring. Further work is required to confirm this inference, but should the substituted phenols remain within the polymer matrix post production, the mass of solids removed would be greater than the initial mass. In addition, the percentage mass loss upon decomposition would increase and the thermal decomposition temperature observed by TGA would be reduced due to the degradation of the polymer structure. These effects are both observed in Figure 58 where it may be seen that the percentage mass loss after a 0 minute reaction is greater than that of a virgin PEEK 150CA30 sample, the onset of decomposition being identified at approximately 700 K.

Differential Scanning Calorimetry Analysis

Since DSC is able to identify the polymeric transitions, T_g , T_c and T_m , associated with PEEK it is possible to identify the presence of PEEK. Consequently the absence of PEEK may be used to indicate that the decomposition of the polymer chains has taken place. PEEK 150CA30 is received in the semi-crystalline state, therefore in the virgin sample only the T_g and T_m should be observed. Figure 59 shows the DSC thermograms for samples processed for 0 – 120 minutes.

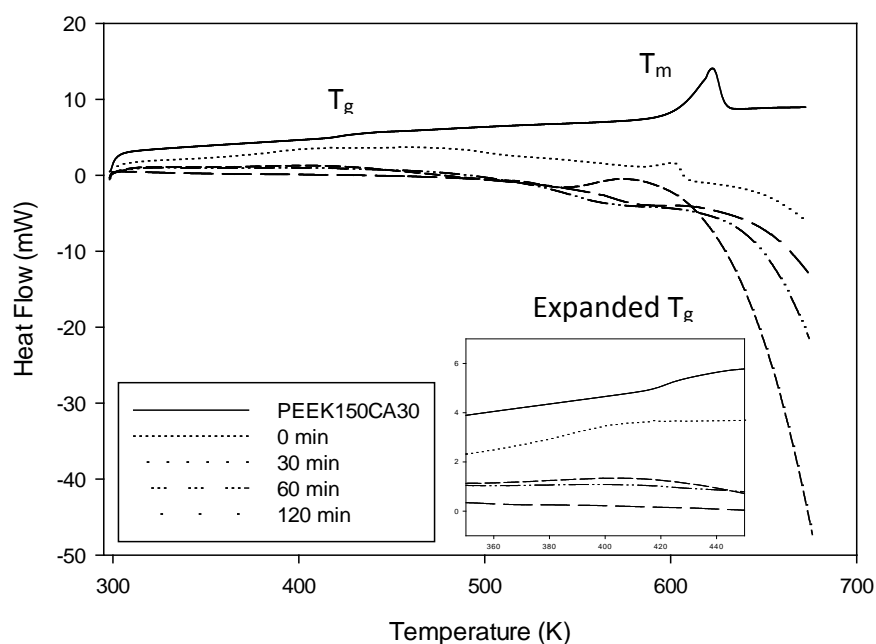


Figure 59: Differential Scanning Calorimetry of PEEK 150CA30 and processed samples, 0 - 120 min, 623 K, 10 mg ml⁻¹ Cs₂CO₃, [EtOH] = 20 %v, [H₂O] = 80 %v, 16.8 ± 0.2 MPa

Figure 59 shows that after a reaction time of 0 minutes (heating and cooling only) the sample retains some polymeric properties. The melt temperature has reduced slightly to 603 K and an exotherm indicative of the onset of decomposition is visible at 634 K. For reaction times of 30 minutes and greater the polymeric characteristics are completely lost and no PEEK transitions are observed. This is consistent with the TGA, FT-IR and SEM data that suggest that the polymer is decomposed into low molecular weight organic products.

Proposed Reaction Scheme

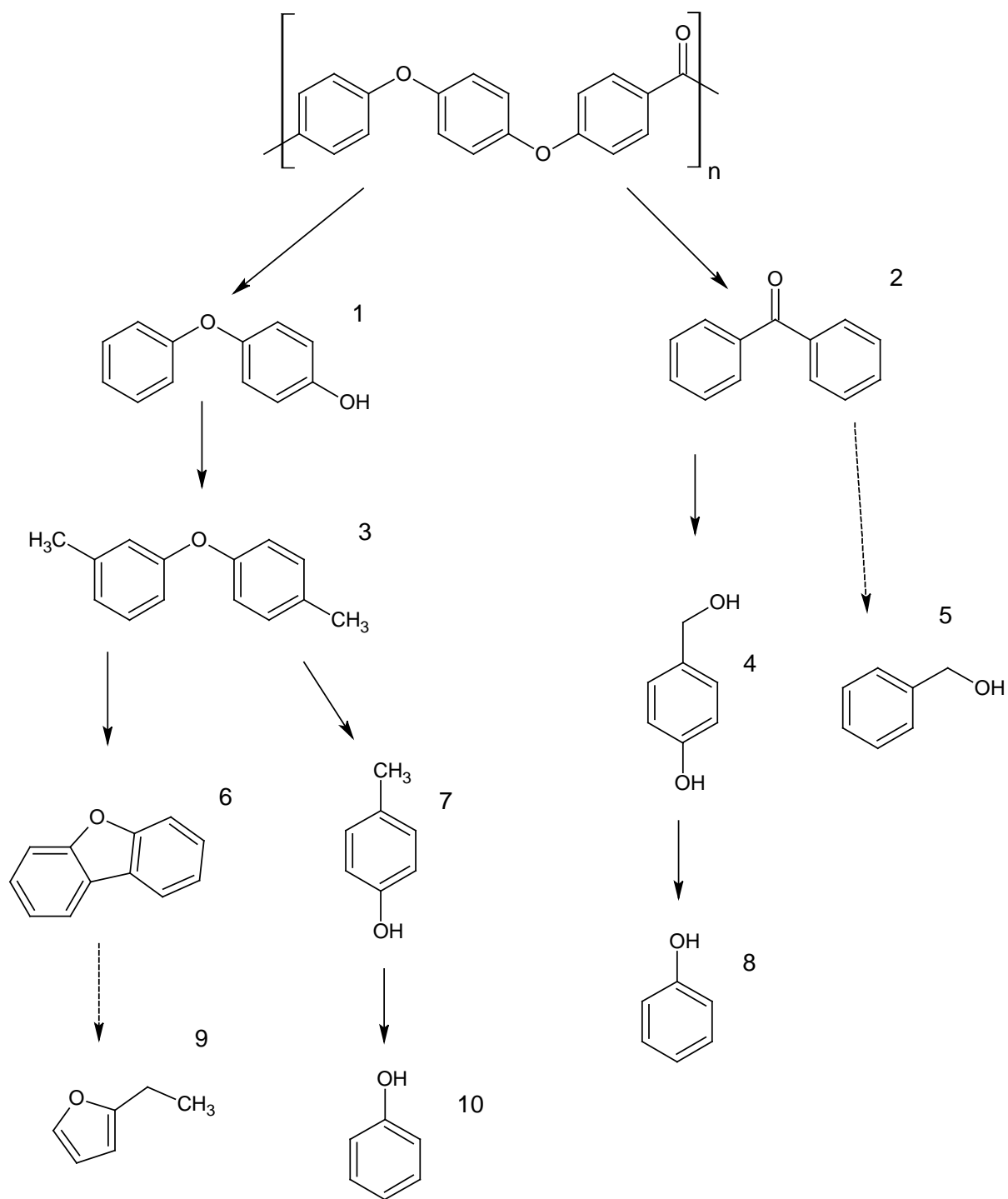


Figure 60: Main decomposition products from the decomposition of poly(oxy-1,4-phenyleneoxy-1,4-phenylecarbonyl-1,4-phenylene), solid arrows = major product formation, dashed arrows = minor product formation

All of the products shown in the proposed reaction scheme for the accelerated decomposition of PEEK, Figure 60, were observed by GC-MS with the exception of diphenylmethanone (2). Given that the ketone group is surrounded by 2 phenoxy groups, the absence of diphenylmethanone (2) suggest that the dissociation energy of the ketone group is less than that of the ether linkage. The absence of diphenylmethanone (2) has been observed and reported in the thermal decomposition of PEEK [105]. The production of either 4-phenoxyphenol (1) or diphenylmethanone (2) would ultimately lead to the production of phenol (8, 10), and consequently phenol is a major product of the reaction. 4-Phenoxyphenol (1) undergoes secondary reactions leading to the formation of 1-methyl-3-(4-methylphenoxy)benzene (3) which may undergo further reaction to form dibenzofuran (6) by radical addition [317]. The decomposition of dibenzofuran (6) to form 2-ethyl furan (9) is not thought to be dominant and is most often observed when the concentration of ethanol is 100 %.

A competing reaction for the decomposition of 1-methyl-3-(4-methylphenoxy)benzene (3) is the formation of 4-methylphenol (7), which may undergo subsequent decomposition into phenol (10). Phenol was identified in all samples where the ethanol concentration was less than 100 %. Moreover, when the ethanol concentration was 100 % the production of phenol was not identified by GC-MS irrespective of the Cs_2CO_3 concentration and the reaction time. It may be deduced therefore, that phenol is a major product of the decomposition of PEEK near its melting temperature and that, whilst ethanol works effectively as a co-solvent for the reaction system, the predominant reaction mechanism is one of hydrolysis.

4.2.2. Propanol and Water Co-solvent System

Effects of Propanol Concentration

The propanol concentration was varied from 0 – 100 % by volume, maintaining a reactor solvent loading of 50 %v, the PEEK and Cs_2CO_3 concentrations were 10 mg ml^{-1} . The reaction schedule is provided in Chapter 3.3.2, the reaction times of 30 minutes for all experiments in this investigation. The aqueous / organic fractions were analysed by means of HPLC and GC-MS as detailed in Chapter 3.4.3. The concentration of phenol was used as an indicator for the decomposition as shown in Figure 61.

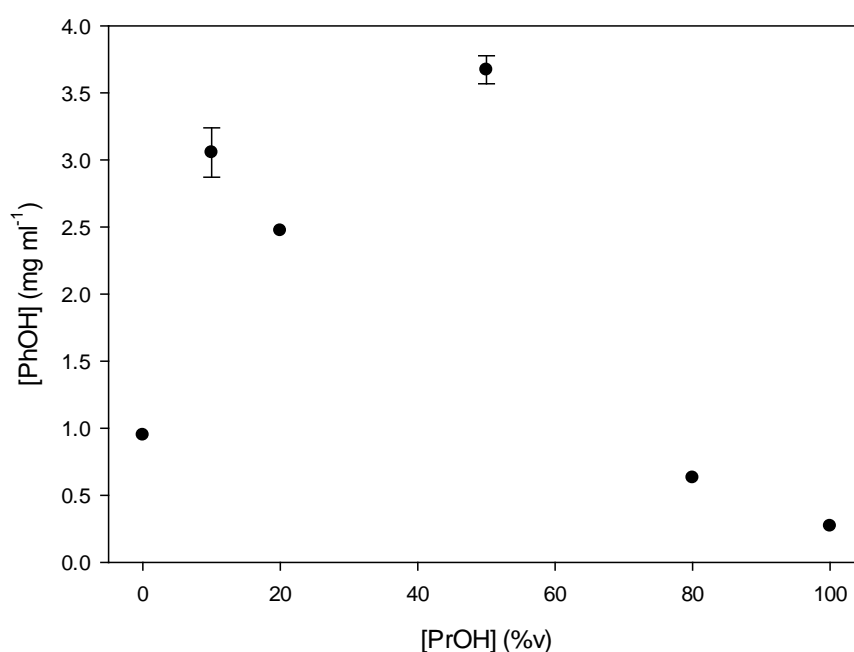


Figure 61: Phenol concentration [PhOH] with respect to propanol concentration [PrOH], 623 K, $t_r = 30 \text{ min}$, 10 mg ml^{-1} Cs_2CO_3 , $P = 15.8 - 20.5 \text{ MPa}$. Determined by HPLC

By analysis of Figure 61 it can be seen that the concentration profile of phenol produced as a consequence of the decomposition of PEEK is similar to the profile identified when ethanol is used as a co-solvent, with the exception of when the propanol concentration is 50 %v. The critical point of a 50 : 50 water / propanol mixture is 584 K and 10.23 MPa [314], whereas the critical point for a 20 : 80 water / propanol mixture, calculated by interpolation, is 620 K and 16.75 MPa. The reactor's internal pressure was measured as a function temperature for all reactions and is provided in Figure 62 for the two conditions in question.

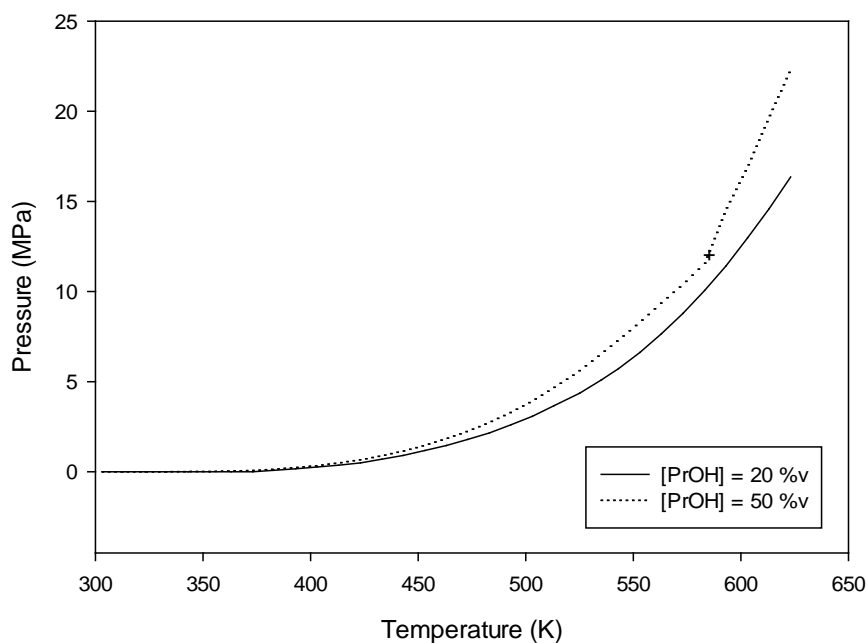


Figure 62: Pressure as a function of temperature for propanol and water co-solvent system, $T = 623 \text{ K}$, $[\text{Cs}_2\text{CO}_3] = 10 \text{ mg ml}^{-1}$, $t_r = 30 \text{ min}$, solvent loading = 50 %v, + = critical point

From Figure 62 it is evident that when the propanol concentration is 20 %v the reaction is subcritical. The reaction temperature was 623 K, 3 K above the critical temperature, but the reaction pressure was 16.35 MPa, 0.4 MPa below the critical pressure of the mixture.

Although these conditions are near-critical, the significant difference in the polymer decomposition and subsequent production of phenol shown in Figure 61, highlight the importance of the supercritical state. Without attaining such conditions, the diffusivity of the fluid through the polymer matrix is significantly lower and decomposition reactions are greatly inhibited.

As the critical point of propanol is lower than that of water, it follows that the critical point of the mixture reduces with increasing propanol concentration. If the diffusivity was solely responsible for the increased decomposition rate, and in turn the production of phenol, then the expectation would be to identify the highest phenol yields when the propanol concentration is 100 %. In similarity to the water / ethanol system, water is essential for the decomposition of PEEK to take place and therefore as the reaction conditions tend towards 100 % propanol there is insufficient water to support the reaction and the phenol yield is lower than when the propanol concentration is 0 %. The high phenol yield observed when the propanol concentration was 50 %v is therefore a result of achieving the supercritical state with a sufficient concentration of water, in conjunction with the caesium carbonate catalyst.

Effects of Caesium Carbonate Concentration

Whilst a propanol concentration of 50 %v appears more aggressive with respect to the decomposition of PEEK, a propanol concentration of 20 %v was used to allow for a fair and comparative study between the ethanol and propanol systems. The caesium carbonate concentration was varied between 0 and 10 mg ml⁻¹ according to the reaction schedule

provided in Chapter 3.3.2. with the phenol concentration being measured by HPLC as described in Chapter 3.4.3. The phenol concentration as a function of caesium carbonate concentration is given in Figure 63.

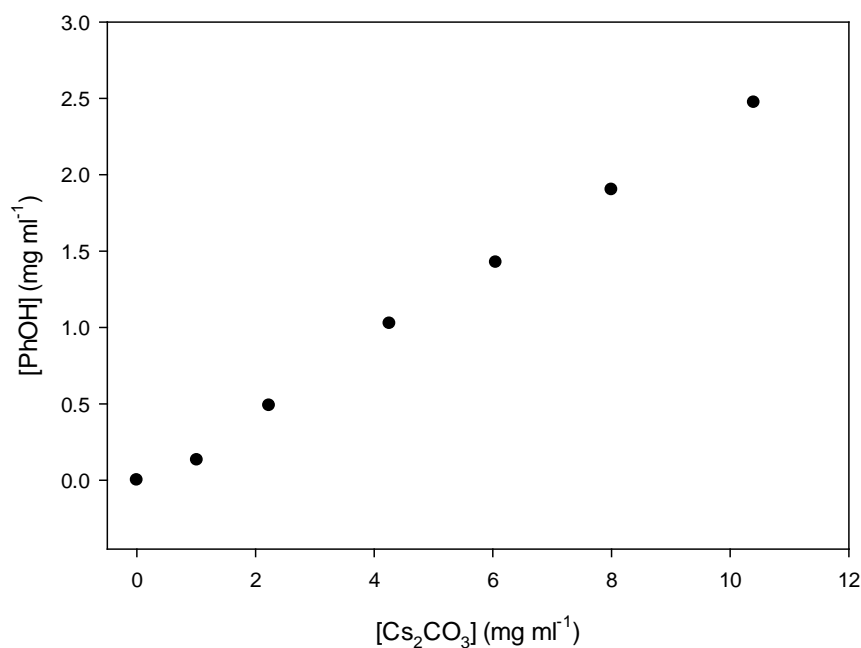


Figure 63: Effect of caesium carbonate concentration $[Cs_2CO_3]$ on the production of phenol $[PhOH]$ by the decomposition of PEEK. $[PrOH] = 20\%v$, $[H_2O] = 80\%v$, $t_r = 30$ min, 623.15 K, 16.4 ± 0.4 MPa. Determined by HPLC

The linear correlation shown in Figure 63 is similar to that of the ethanol / water system (Chapter 4.2.1), the reaction being first order with respect to $[Cs_2CO_3]$. The recovered solids were analysed by DSC as detailed in Chapter 3.4.3 and are shown in Figure 64.

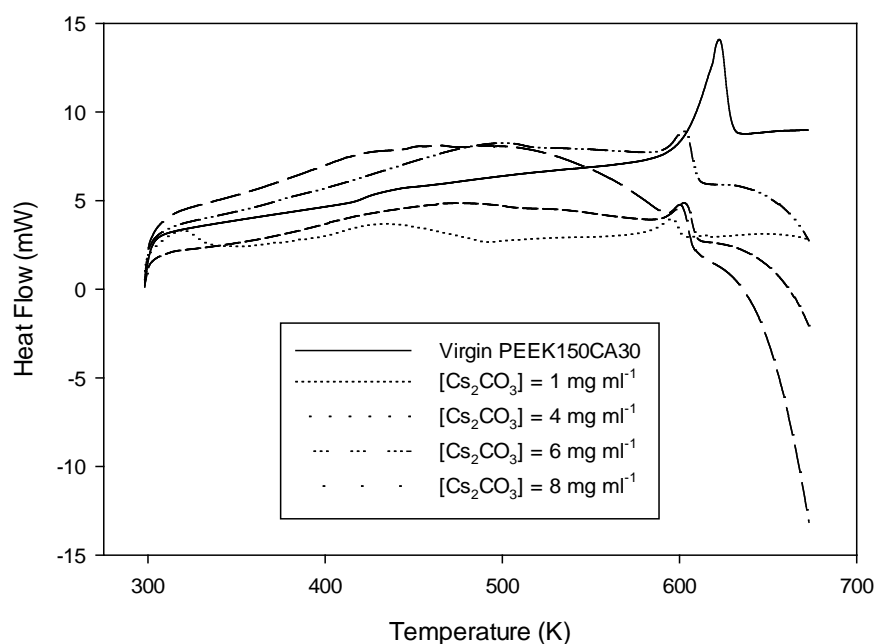


Figure 64: DSC thermograms for PEEK 150CA30 processed for 30 minutes using $[PrOH] = 20\%v$, $[H_2O] = 80\%v$, 16.4 ± 0.4 MPa, $1 - 8 \text{ mg ml}^{-1} \text{ Cs}_2\text{CO}_3$

Inspection of Figure 64 shows that the polymer transitions, in particular the melt temperature (T_m), are prominent when the caesium carbonate concentration is up to 8 mg ml^{-1} . There is a noticeable reduction in the T_m for all samples irrespective of the caesium carbonate concentration when compared to the virgin PEEK sample. The reduction in T_m for the processed samples may be due to the partial decomposition of a proportion of the polymer chains, leading to an increased polydispersity index (PDI) (not measure during this research). Should this occur, some decomposition products would exist and, having a different decomposition temperature to PEEK, could potentially decompose prematurely. This is consistent with empirical observation; inspection of Figure 64 shows that for samples processed with a $[\text{Cs}_2\text{CO}_3]$ of 4, 6 and 8 mg ml^{-1} , an exotherm is visible immediately after the T_m . It is also noted that when $[\text{Cs}_2\text{CO}_3]$ was 8 mg ml^{-1} the onset of the exotherm occurred prior to the T_m , with the sample becoming exothermic at approximately 510 K.

Effects of Reaction Time

The schedule for the investigation into the effects of the reaction time is given in Chapter 3.3.2. In summary, the reaction time was varied from 0 minutes, consisting of heating and cooling only, to 120 minutes. The concentration of phenol produced, measured by HPLC as described in detailed in Chapter 3.4.3, is presented in Figure 65.

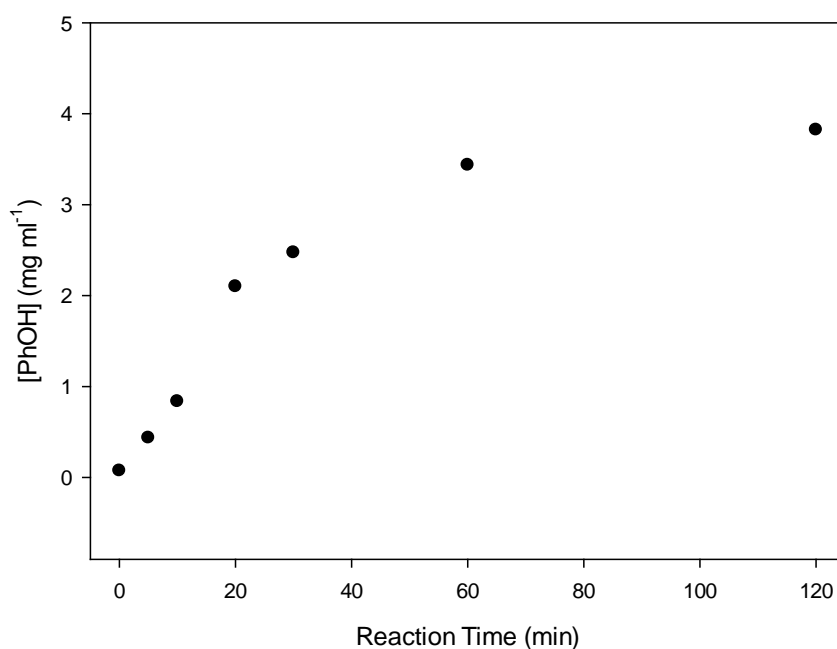


Figure 65: Phenol concentration [PhOH] with respect to reaction time, 623 K, [PrOH] = 20 %v, [H₂O] = 80 %v, 16.4 ± 0.2 MPa, 10 mg ml⁻¹ Cs₂CO₃, 10 mg ml⁻¹ PEEK. Determined by HPLC

Figure 65 shows that the water / propanol system responds in a similar way to the water / ethanol system when the concentration of alcohol [R-OH] is 20 %v. Rapid progression of the decomposition reaction takes place within the first 30 minutes, leading to a phenol concentration of 65 % of the maximum observed. Doubling the reaction time from 30 to 60 minutes leads to an increase of 25 % in the phenol concentration. Subsequent doubling of

the reaction time to 120 minutes leads to the complete decomposition of the polymer matrix, the absence of any observable polymer transitions by DSC and a complete departure from the polymer decomposition temperature when analysed by TGA as shown in Figure 66.

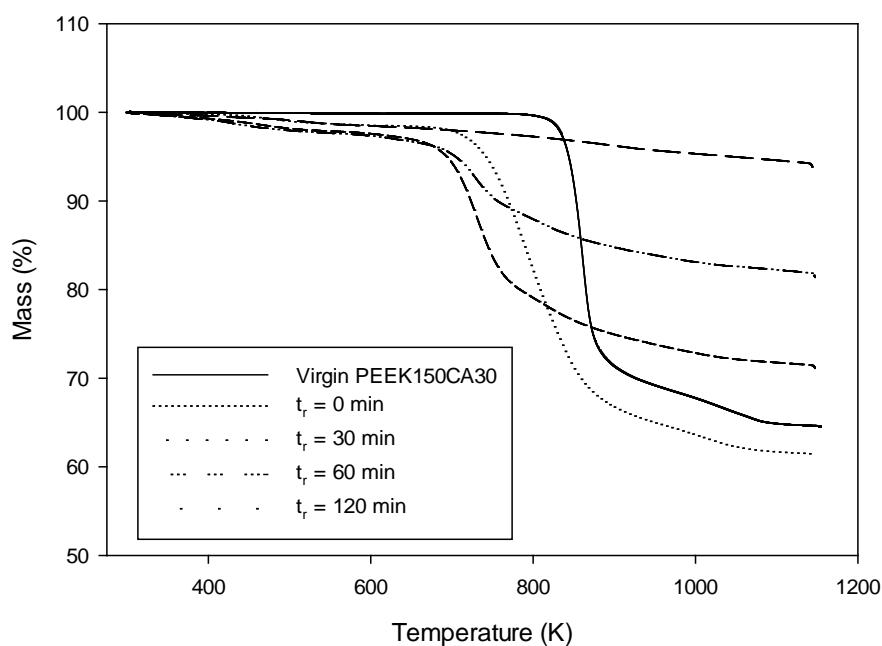


Figure 66: Thermogravimetric analysis of recovered solids according to reaction time, $t_r = 0 - 120$ min, $[\text{PrOH}] = 20\%v$, $[\text{H}_2\text{O}] = 80\%v$, $[\text{Cs}_2\text{CO}_3] = 10 \text{ mg ml}^{-1}$, $T = 623 \text{ K}$, $P = 16.4 \pm 0.2 \text{ MPa}$

Inspection of Figure 66 shows that the mass loss observed when the reaction time is 0 minutes is greater than the virgin PEEK150CA30 sample, and therefore the sample has acquired mass. This is consistent with the findings when a water / ethanol system is employed and is a result of the partial decomposition and subsequent reaction of the alcohol with the polymer matrix [318]. This effect is further evidenced by the reduction in the decomposition temperature of the remaining sample. That exception aside, it is observed that the mass loss by TGA is inversely proportional to the reaction time. Given that

PEEK150CA30 consists of 30 %v carbon fibre, and that the carbon fibre does not undergo significant decomposition below 1150 K, it follows that should all of the polymer matrix be decomposed the mass loss observed by TGA would be minimal. The empirical measurements are in accordance with this theory, and whilst the mass loss observed by TGA was never 0, the mass loss observed for extended reaction times is attributable to PEEK decomposition products and not the polymer matrix. This can be confirmed by analysing the rate of change of mass (DTG) as shown in Figure 67.

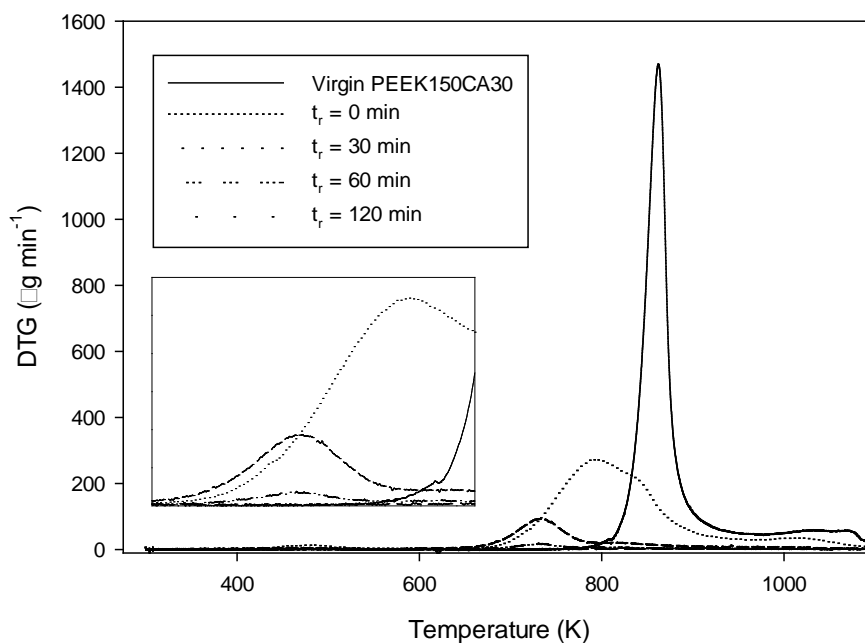


Figure 67: Thermogravimetric analysis of recovered solids according to reaction time, showing rate of mass change (DTG) as observed by TGA, $t_r = 0 - 120 \text{ min}$, $[\text{PrOH}] = 20 \text{ \%v}$, $[\text{H}_2\text{O}] = 80 \text{ \%v}$, $[\text{Cs}_2\text{CO}_3] = 10 \text{ mg ml}^{-1}$, $T = 623 \text{ K}$, $P = 16.4 \pm 0.2 \text{ MPa}$

The departure from the PEEK decomposition temperature is identified by inspection of Figure 67. It is shown that in addition to the reduction in the temperature at which the material undergoes decomposition, the maximum rate of mass loss is also reduced (DTG µg

min⁻¹). This is due to the reduced quantity of PEEK remaining within the sample, and is further evidence of the decomposition of the polymer matrix. Broadening of the DTG is indicative of an impure material or a mixture of products. The PEEK decomposition products have different decomposition temperatures to PEEK and, given that there are a range of different products, the decomposition of the sample observed by TGA takes place over a range of temperatures. This leads to a broad and, due to the number of different products, a shallow peak. As phenol is soluble in water it is not identified by TGA and does not influence these results.

4.2.3. Acetone and Water Co-solvent System

In attempting to use acetone (DMK) as a co-solvent a technical challenge was encountered. The intention was to vary the concentration of acetone from 0 to 100 % in discrete intervals, in-line with the work carried out using ethanol and propanol as co-solvents with water (see Chapter 3.3.2). In doing so, it was discovered that acetone and water mixtures containing 10 mg ml⁻¹ Cs₂CO₃ react with the reactor seal. Degradation of the reactor seal subsequently takes place, leading to rapid depressurisation and loss of containment. Acetone concentrations of up to 20 %v did not degrade the reactor seal within 30 minutes and therefore initial results are reported.

The reactor seal, supplied by Scientific and Medical Products Ltd (UK), is constructed from graphite. This is a requirement in order to withstand the temperatures that the reactor is routinely subjected. Although no loss of containment was observed when the acetone concentration was 20 %v, including 10 mg ml⁻¹ Cs₂CO₃, it was deemed inadvisable to

continue this area of research. Given that carbon fibres comprise, almost exclusively, of carbon it is thought that the conditions that degrade the graphite seal are likely to have a negative impact on the carbon fibre's physical properties. Therefore, such conditions were thought to be of little interest within the context of this research as they are unlikely to be employed industrially. The initial results are presented in Figure 68.

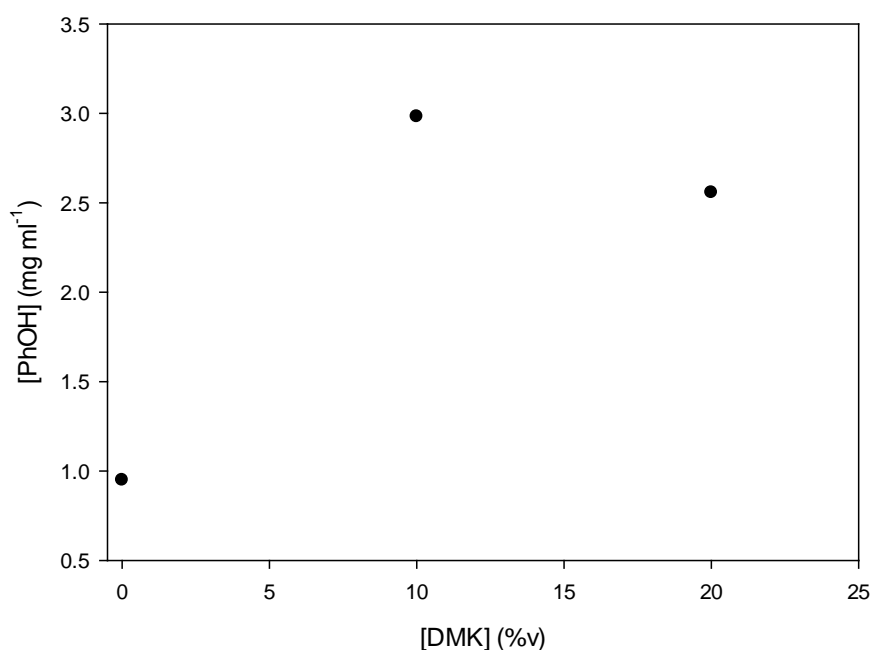


Figure 68: Phenol concentration $[PhOH]$ as a function of acetone concentration $[DMK]$, $t_r = 30$ min, $T = 623$ K, $[Cs_2CO_3] = 10$ mg ml⁻¹, $P = 15.7 - 16.2$ MPa. Determined by HPLC

The initial results shown in Figure 68 are similar to the observations made when propanol is used as a co-solvent. It appears that the concentration of phenol, which is used as a method of following the reaction, is likely to decrease with increasing acetone concentration. However, it is important to consider the state of the fluid within the reactor at each point. Figure 69 shows the pressure as a function of the reaction temperature for $[DMK] = 10 - 50$ %v.

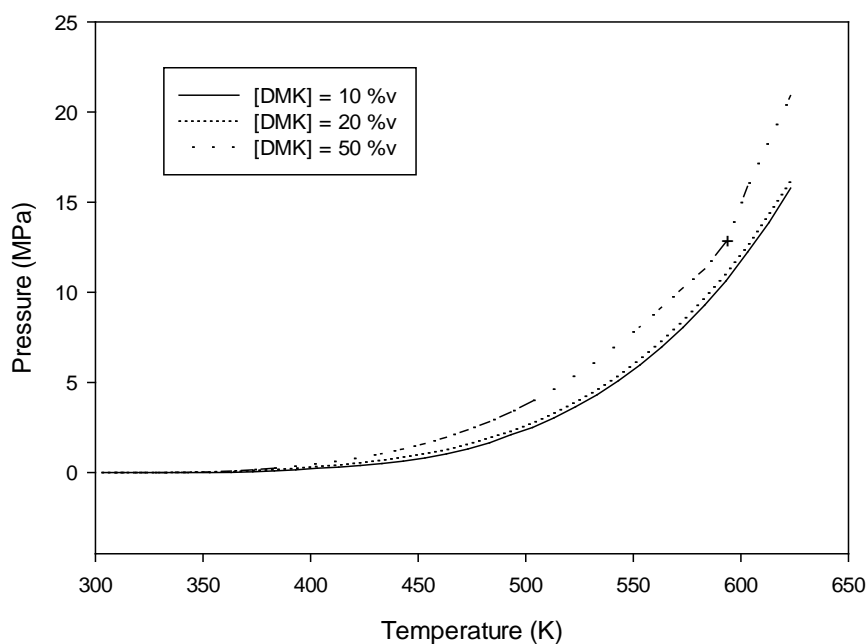


Figure 69: Pressure as a function of temperature for acetone (DMK) and water co-solvent system, $T = 623 \text{ K}$, $[\text{Cs}_2\text{CO}_3] = 10 \text{ mg ml}^{-1}$, $t_r = 30 \text{ min}$, $[\text{DMK}] = 10 - 50 \text{ \%v}$, $[\text{H}_2\text{O}] = 90 - 50 \text{ \%v}$, solvent loading = 50 %v, + = critical point

It is evident from inspection of Figure 69 that the critical point of the water / acetone mixtures was not attained when the concentration of acetone was 10 and 20 %v. When using propanol as a co-solvent it was observed that the presence of the supercritical state was responsible for greatly enhancing the decomposition of PEEK, producing greater yields of phenol than when the mixture was subcritical. It was also observed that water was essential for the decomposition of PEEK to take place, 100 % propanol was less effective than 100 % water. Whilst a complete data set are not available, there is reason to suspect that this system would behave in a similar way. The supercritical state of a 50 : 50 water : acetone mixture containing $10 \text{ mg ml}^{-1} \text{ Cs}_2\text{CO}_3$ was attained at 594 K and 12.95 MPa as shown in Figure 69. The diffusivity of a fluid in the supercritical state is much greater than

that of a liquid. This increased diffusivity, in conjunction with the Cs_2CO_3 catalyst, is most probably the cause of the reactor seal failure when the acetone concentration was 50 %v. Validation of this inference would require the quantitative analysis of the phenol concentration in the reactor fluid, carried out by HPLC as part of this research. However, in the case of an experiment terminated by a loss of containment quantitative analysis is not possible. This is due to an incomplete liquid sample being recovered. The recovered sample could potentially be enriched with phenol and therefore not representative of the bulk fluid.

4.2.4. Comparative Study of Ethanol, Propanol and Acetone Co-solvent Reaction Systems

A compilation of the concentration of the phenol produced as a consequence of the decomposition of PEEK is presented in Figure 70 for EtOH, PrOH and DMK reaction systems.

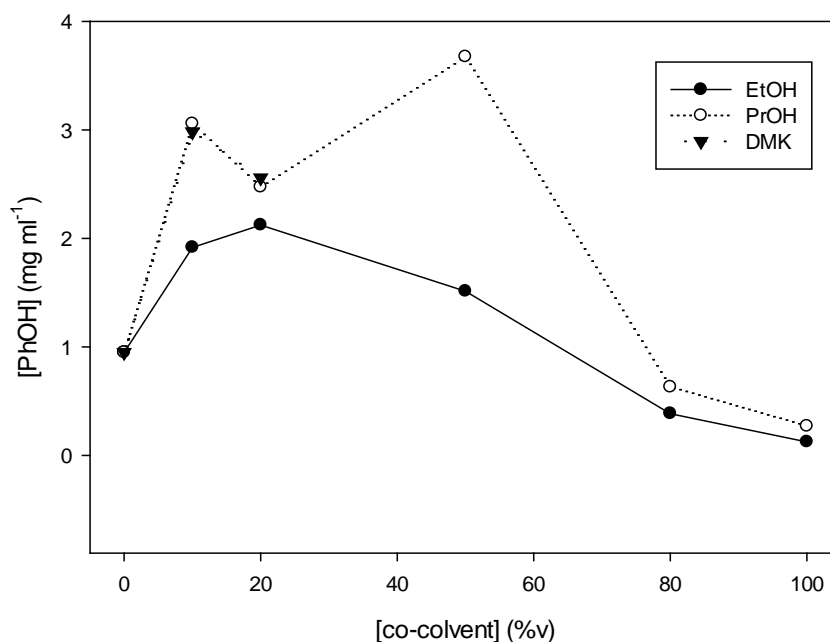


Figure 70: Comparative study of phenol concentration [PhOH] as a function of co-solvent concentration [co-solvent], $T = 623$ K, $t_r = 30$ min, solvent loading = 50 %v, $[Cs_2CO_3] = 10$ mg ml⁻¹, $[PEEK] = 10$ mg ml⁻¹, ethanol (EtOH), propanol (PrOH) and acetone (DMK)

It is exemplified in Figure 70 that the performance of the three co-solvents used, ethanol, propanol and acetone, is very similar with respect to the production of phenol when the co-solvent concentration is 20 %v. Both propanol and acetone outperform ethanol as co-solvents when the concentration is 10 %v, despite Cs_2CO_3 having a greater solubility in ethanol. The maximum phenol concentration was achieved by using a 50 : 50 water : propanol mixture, conditions under which it was not possible to recover any liquid fraction when acetone was used as a co-solvent. The increase in performance of propanol at 50 %v is thought to be a result of attaining the supercritical state and the carbon chain length. Under the same conditions, ethanol was also in the supercritical state and produced a phenol concentration of 1.5 mg ml⁻¹ in comparison to 3.7 mg ml⁻¹ when propanol was used. Similar

performance between ethanol and propanol systems is observed when the alcohol concentration is 100 %. Analysis of the performance of Cs_2CO_3 is presented in Figure 71.

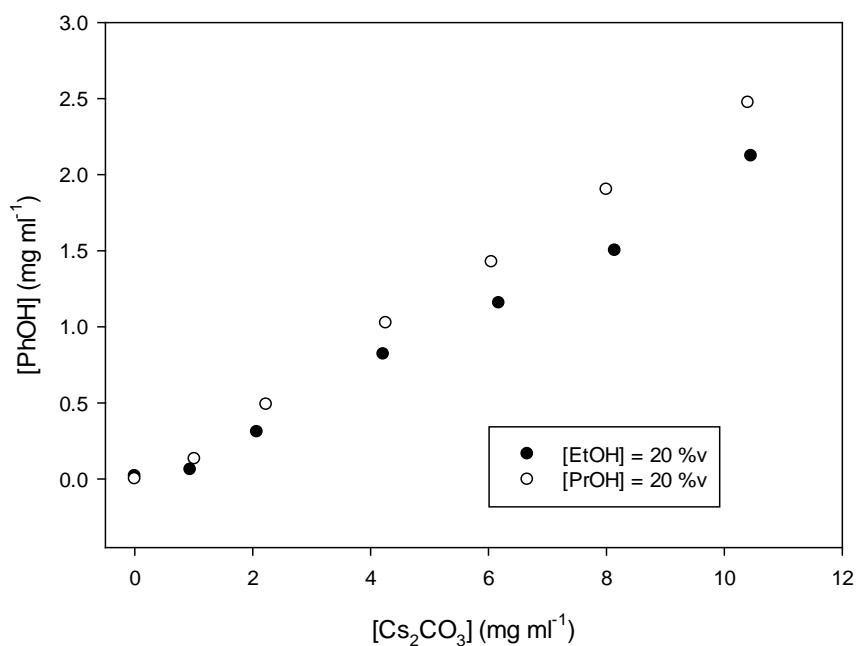


Figure 71: Comparative study of phenol concentration $[\text{PhOH}]$ as a function of caesium carbonate concentration $[\text{Cs}_2\text{CO}_3]$, $T = 623 \text{ K}$, $t_r = 30 \text{ min}$, $[\text{PEEK}] = 10 \text{ mg ml}^{-1}$, ethanol (EtOH), propanol (PrOH)

Performance of the Cs_2CO_3 catalyst was very similar irrespective of the co-solvent used as shown in Figure 71. In both cases the response, measured by the concentration of the phenol produced, was linear indicating that the primary decomposition reactions are 1st order with respect to $[\text{Cs}_2\text{CO}_3]$. The offset observed at all $[\text{Cs}_2\text{CO}_3]$ is a product of the increased performance of propanol, consistent with the observations made in Figure 70. A compilation of the performance of the ethanol and propanol co-solvent systems is provided in Figure 72.

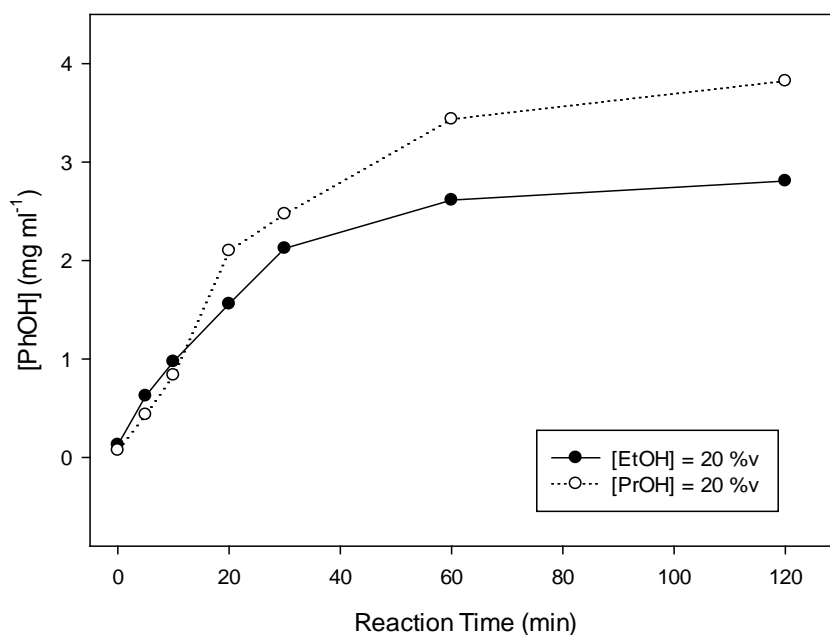


Figure 72: Phenol concentration [PhOH] as a function of reaction time for ethanol (EtOH) and propanol (PrOH) co-solvents, $T = 623\text{ K}$, $[Cs_2CO_3] = 10\text{ mg ml}^{-1}$

Consistent with Figure 70 and Figure 71, Figure 72 shows that the phenol concentration is greater when propanol is used as a co-solvent. Performance is similar when the reaction time is less than 30 minutes. Whilst it is known that phenol is a major product of the decomposition of PEEK, it is prudent to compare the mass loss observed by TGA. Expectation would place the mass loss observed by TGA for the propanol system to be lower than that of the ethanol system, indicating the increased decomposition of PEEK. These data are presented in Figure 73.

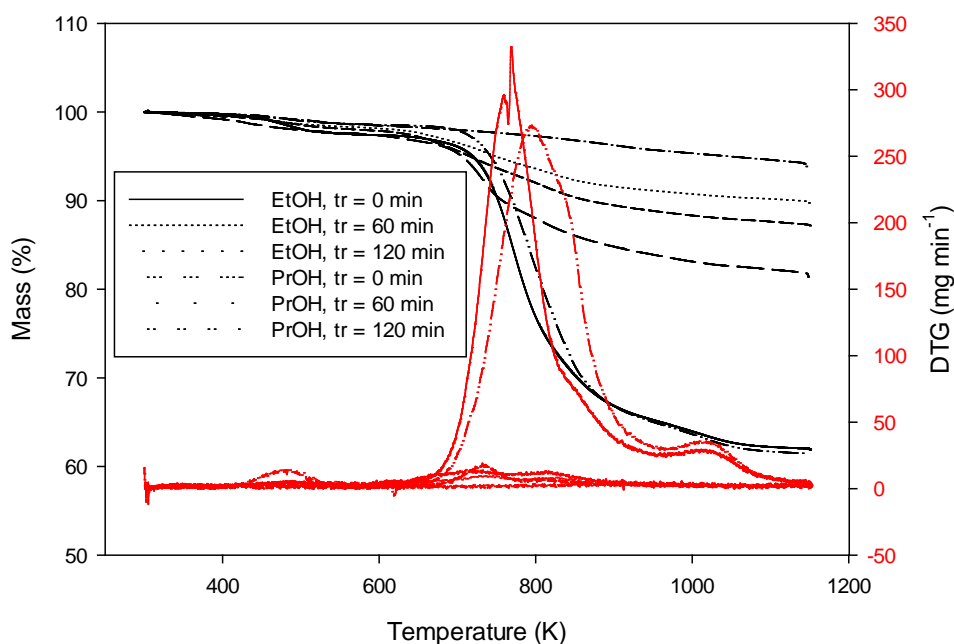


Figure 73: Thermogravimetric analysis compilation of recovered solids showing mass loss and rate of mass change (DTG) observed by TGA, $T = 623 \text{ K}$, $[\text{Cs}_2\text{CO}_3] = 10 \text{ mg ml}^{-1}$, $t_r = 0 - 120 \text{ min}$, ethanol concentration $[\text{EtOH}] = 20 \text{ \%v}$, propanol concentration $[\text{PrOH}] = 20 \text{ \%v}$, $[\text{H}_2\text{O}] = 80 \text{ \%v}$

Figure 73 shows that both ethanol and propanol perform similarly when the reaction time is 0 minutes, corresponding to heating and cooling only. In both cases, the final mass of the sample is greater than that of the initial and accordingly the mass loss observed by TGA is greater than that of the virgin sample. The increase in mass loss observed by TGA is the same for both solvents and is a result of the partial decomposition of the alcohol and subsequent reaction with the PEEK matrix. By conducting this comparative study it may be seen that propanol outperforms ethanol when used as a co-solvent with a concentration of 20 %v. It is also observed that increasing the propanol concentration to 50 % yields greater concentrations of phenol, indicating more extensive decomposition has taken place. However, sensitivity analysis is required to identify the rate of change of the percentage decomposition when the propanol concentration is close to 50 %, identifying whether

operation near to this point could potentially create instability. Conversely, ethanol presents consistent performance over all concentrations investigated. This attribute may be favourable when considering this research in an industrial context.

Having investigated the use of supercritical fluid mixtures to decompose and recycle a high-performance thermoplastic materials, typically used in aerospace and related industries, attention is now focused on the recycling of high-performance thermoset polymers. Although the materials are different in their nature, where thermoset resins are cross-linked and thermoplastics are not, they are often found in similar environments. For this reason, the findings from the research presented herein with respect to the decomposition and recycling of PEEK is of great value and importance to the research into the decomposition of thermoset resins and their associated composite materials.

CHAPTER 5. RESULTS PART B: DECOMPOSITION AND RECYCLING OF POLYEPOXIDE THERMOSET RESIN

5.1. SOLVOLYSIS OF EPOXY RESIN IN SUPERCRITICAL ALCOHOLS

A 2,2-Bis[4-(glycidylloxy)phenyl]propane (BAGDE) based polyepoxide thermoset resin was prepared as detailed in Chapter 3.3.3. and was subsequently used for the investigation into the decomposition of high-performance thermoset polymers using supercritical fluids. As was the case with the studies of PEEK, caesium carbonate was utilised as a catalyst in conjunction with ethanol and propanol as co-solvents with water. A limited study employing butanol (BuOH) as a co-solvent is also presented. The format of this results chapter follows that of the experimental methodology, starting with the control sample before investigating the effects of the co-solvent concentration, catalyst concentration and reaction time. Given their differences, each of the solvents is investigated separately prior to completing a comparative study and drawing conclusions.

Control sample

Control samples and samples required to undergo reaction were produced in an identical way as detailed in Chapter 3.3.3. an example of which is provided in Figure 74. The control samples, processed with water in the absence of a co-solvent or catalyst, show a mean mass loss of 7.7 % with a standard deviation (SD) of 0.92. The mean phenol concentration, determined quantitatively by HPLC, was 1.89 mg ml^{-1} with an SD of 0.24. It may therefore be inferred that whilst processing with water alone at 573 K does cause the samples to show

some mass loss, leading to the production phenol, significant decomposition of the resin does not take place.

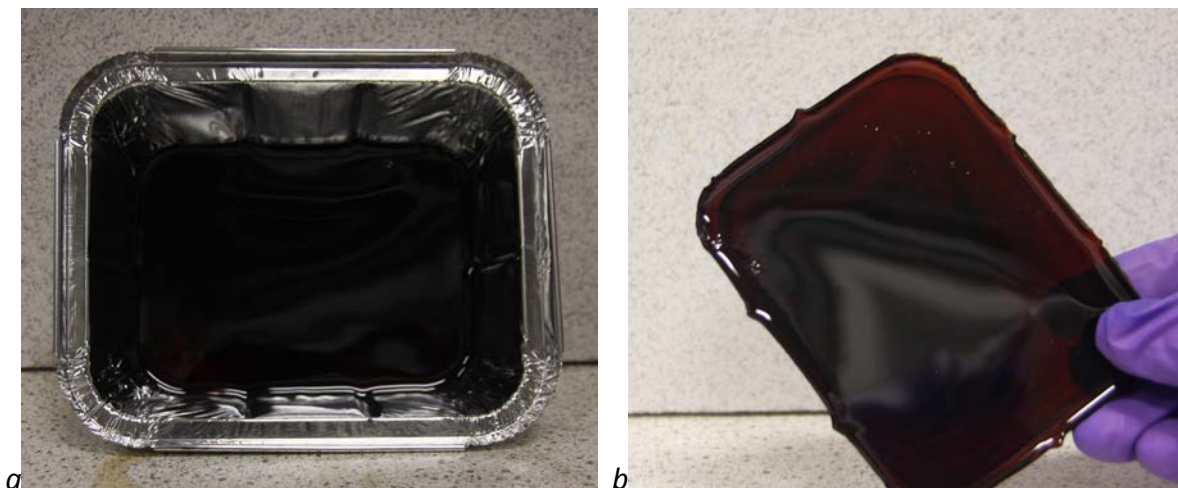


Figure 74: Virgin BADGE / DDS epoxy resin showing a) within mould, b) after de-moulding

5.1.1. Water and Ethanol Co-solvent Decomposition Reactions

Effect of Co-solvent Concentration

The effect of the co-solvent was investigated by varying the concentration of the ethanol from 0 – 100 %, in discrete intervals as given in Chapter 3.3.3. The percentage mass loss, determined by difference, and phenol concentration produced, as determined by HPLC, are presented in Figure 75 and Figure 76 respectively.

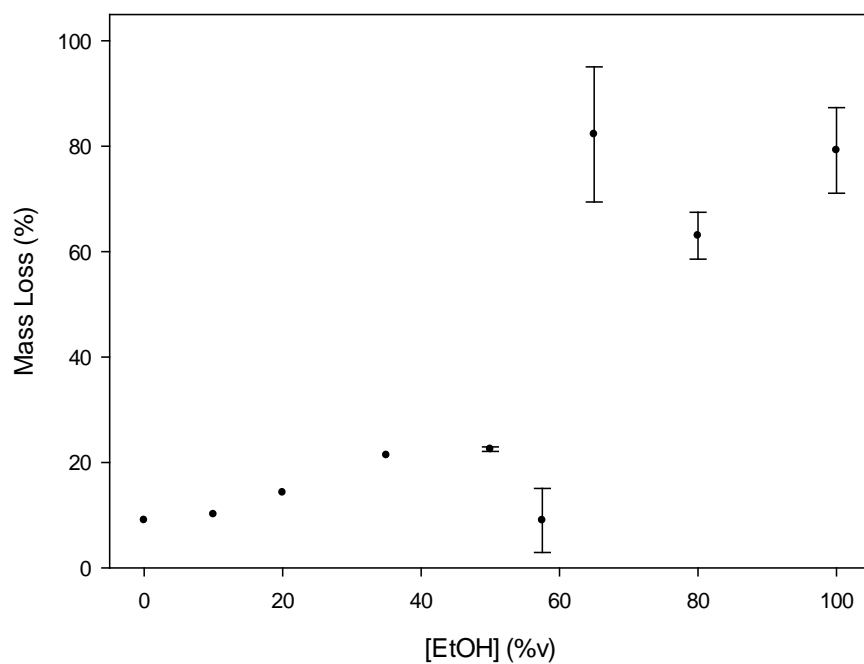


Figure 75: Effect of ethanol concentration [EtOH], $t = 30 \text{ min}$, $T = 573 \text{ K}$, $[\text{Cs}_2\text{CO}_3] = 10 \text{ mg ml}^{-1}$, $[\text{Resin}] = 33.3 \text{ mg} \pm \text{ml}^{-1}$

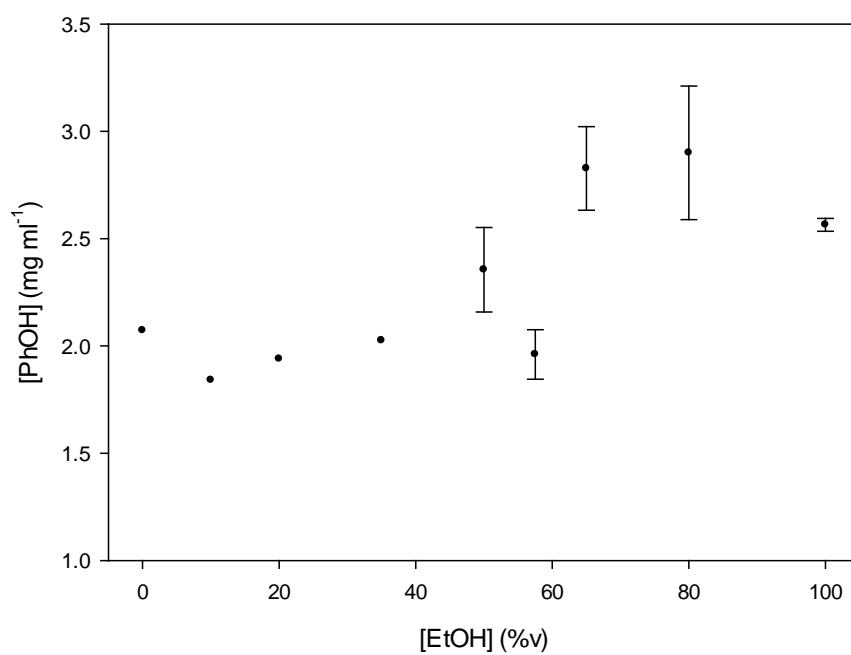


Figure 76: Production of phenol with respect to the ethanol concentration [EtOH], $t = 30 \text{ min}$, $T = 573 \text{ K}$, $10 \text{ mg ml}^{-1} \text{ Cs}_2\text{CO}_3$, $[\text{Resin}] 33.3 \text{ mg} \pm \text{ml}^{-1}$

From Figure 75 and Figure 76 it can be seen that in the absence of ethanol the percentage decomposition and the concentration of phenol produced are within close proximity to the results obtained with the control samples. It is inferred that the addition of 10 mg ml^{-1} Cs_2CO_3 to water alone does not significantly decompose the epoxy resin. The addition of ethanol up to 50 %v does not significantly increase the percentage mass loss and leads to a small increase in the concentration of phenol produced. Under such conditions at 573 K, the fluid is sub-critical (T_c 50 : 50, ethanol : water = 587 K) [314], and therefore has a liquid-like diffusivity. However, when the ethanol concentration is increased to 57.5 %v the system is operating at the critical point of the mixture and is extremely sensitive to small variations in temperature and pressure. When the ethanol concentration is greater than 65 %v the fluid is supercritical, as shown in Figure 77, and although stability in the pressure and temperature is increased the fluctuations in temperature and pressure are notable.

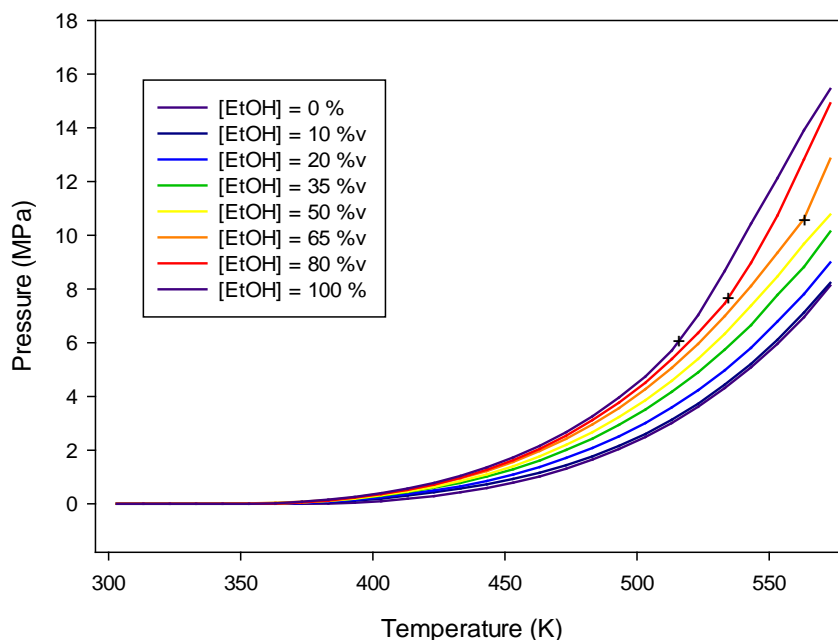


Figure 77: Reactor internal pressure as a function of temperature for ethanol concentrations [EtOH] = 0, 10, 20, 35, 50, 65, 80 and 100 %v; $[\text{Cs}_2\text{CO}_3] = 10 \text{ mg ml}^{-1}$, + =critical point

The percentage mass loss goes through a minima when the ethanol concentration is 57.5 %v and goes through a maxima at 65 %v. Whilst every effort was made to control the temperature, small perturbations of less than 1 K were sufficient to greatly impact the percentage decomposition, hence the increased standard deviation. Although the percentage decomposition is slightly lower at 100 % ethanol (79.2 %) compared to 65 %v ethanol (82.8 %) the increased stability of the system when 100 % ethanol was used is favoured, and was consequently selected as the solvent concentration for the investigation of the effects of the catalyst concentration.

Effect of Caesium Carbonate Concentration

Having pre-selected 100 % ethanol as the optimum concentration in which to carryout the decomposition, the Cs_2CO_3 concentration was varied from 0 – 10 mg ml⁻¹ to investigate its effects. The temperature was maintained at 573 K, and the reaction time of 30 minutes was also preserved. The reaction conditions used are given in Chapter 3.3.3. The percentage decomposition and the concentration of phenol produced are given in Figure 78 and Figure 79 respectively.

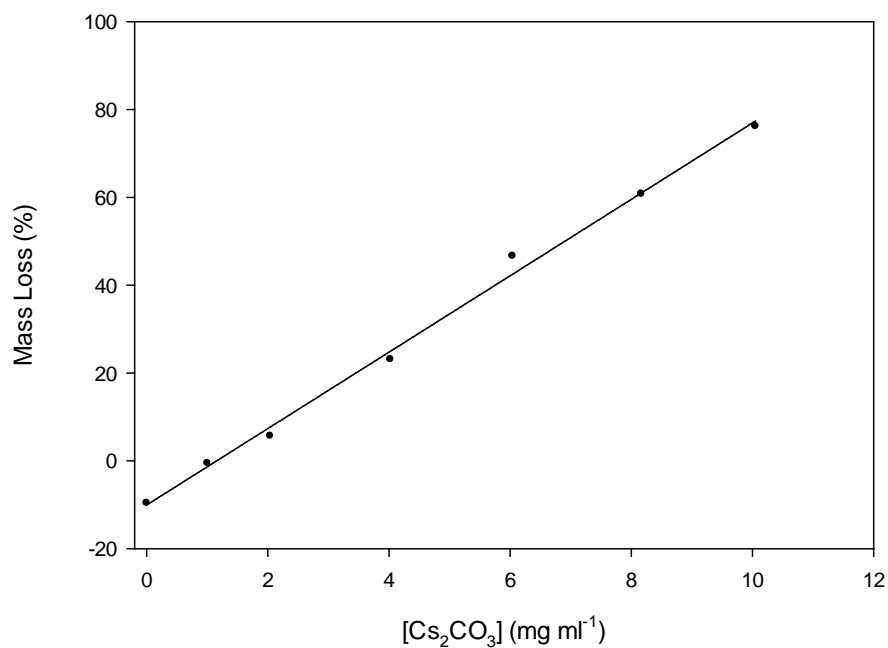


Figure 78: Percentage mass loss with respect to the caesium carbonate concentration [Cs₂CO₃], $T = 573\text{ K}$, $t = 30\text{ min}$, [Resin] = $32 \pm 3\text{ mg ml}^{-1}$, $P = 15.0 \pm 0.4\text{ MPa}$, $R^2 = 0.995$

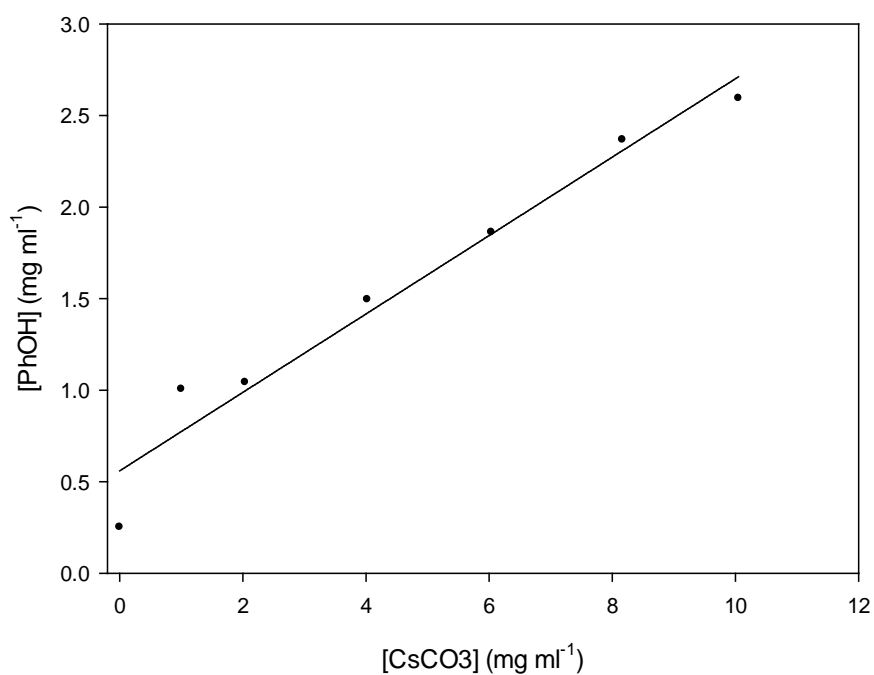


Figure 79: Phenol concentration [PhOH] with respect to caesium carbonate concentration [Cs₂CO₃], $T = 573\text{ K}$, $t = 30\text{ min}$, [Resin] = $32 \pm 3\text{ mg ml}^{-1}$, $P = 15.0 \pm 0.4\text{ MPa}$, $R^2 = 0.968$

Figure 78 and Figure 79 show the linear relationship between the caesium carbonate concentration, percentage mass loss and phenol concentration respectively. From inspection of Figure 78 it is evident that when the ethanol concentration is 100 %, without the addition of caesium carbonate the final mass of the polymer is greater than the initial mass. This is in stark contrast to the control samples, containing 100 % water without the addition of caesium carbonate, where the mass loss was 7.9 %, but is in accordance with what was observed during the investigation into the decomposition of PEEK (see Chapter 4.2). With Figure 78 and Figure 79 both showing linear relationships with respect to the caesium carbonate concentration, it follows that the decomposition of the polymer matrix ultimately leads to the production of phenol, indicating that these findings are in accordance with results presented in the literature [167, 305, 319].

Effect of Reaction Time

Having established the effect of the concentrations of the caesium carbonate and ethanol, the reaction time was varied from 0 to 60 minutes in discrete intervals. The optimal solvent and catalyst concentrations, established previously, were selected for this study. The percentage decomposition of the epoxy resin and the concentration of phenol in the resulting reactor liquor were measured and used as a means of characterising the reaction. Figure 80 and Figure 81 show the percentage mass loss and phenol concentration with respect to the reaction time.

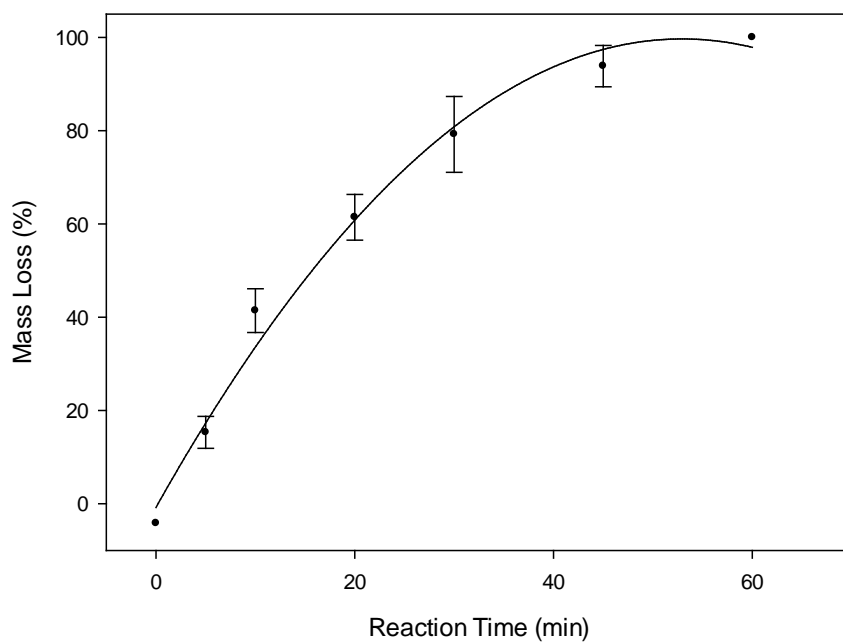


Figure 80: Percentage mass loss with respect to reaction time, $[\text{EtOH}] = 100\%$, $T = 573\text{ K}$, $[\text{Cs}_2\text{CO}_3] = 10\text{ mg ml}^{-1}$, $[\text{Resin}] = 35 \pm 5\text{ mg ml}^{-1}$, $P = 14.7 \pm 0.3\text{ MPa}$, $R^2 = 0.990$

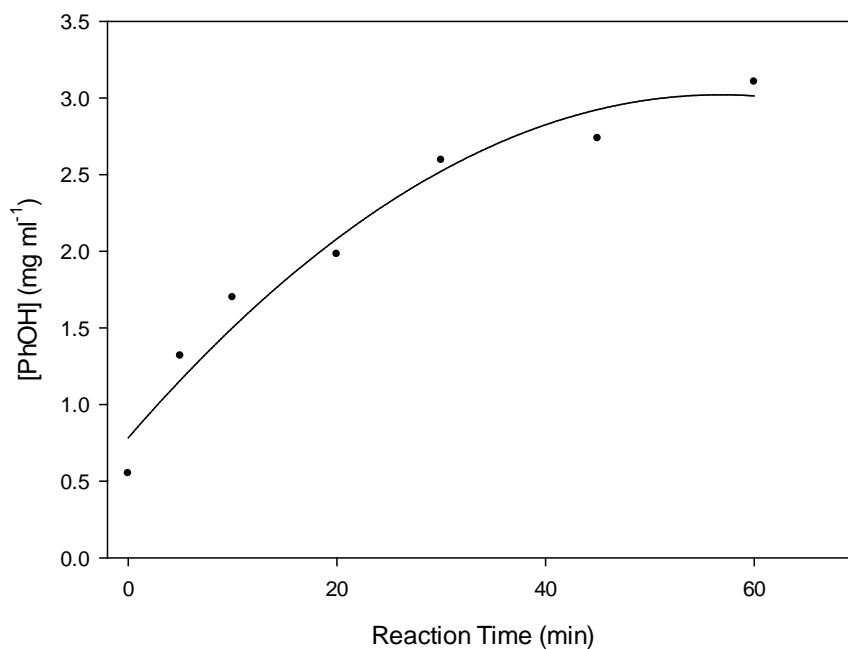


Figure 81: Phenol concentration $[\text{PhOH}]$ with respect to reaction time, $[\text{EtOH}] = 100\%$, $T = 576\text{ K}$, $[\text{Cs}_2\text{CO}_3] = 10\text{ mg ml}^{-1}$, $[\text{Resin}] = 35 \pm 5\text{ mg ml}^{-1}$, $P = 14.7 \pm 0.3\text{ MPa}$, $R^2 = 0.963$

Inspection of Figure 80 and Figure 81 shows that the reaction progresses rapidly between 5 and 45 minutes, at which point the percentage decomposition is in excess of 90 %, producing a phenol concentration of 2.7 mg ml^{-1} . Extending the reaction time to 60 minutes results in the complete decomposition of the polymer resin, with no recoverable solids, and a phenol concentration of 3.1 mg ml^{-1} . It is suggested that when the percentage decomposition of the polymer matrix of a CFRP is greater than 90 % it is likely that a significant proportion of the carbon fibres would have been released, as was observed with PEEK (see Chapter 4.2). It follows that extension of the reaction time beyond 45 minutes may not be economical, since a 33 % extension to the reaction time yields less than 10 % additional decomposition. It was noted that the residual pressure within the reactor at 313 K was proportional to the reaction time as is shown in Figure 82.

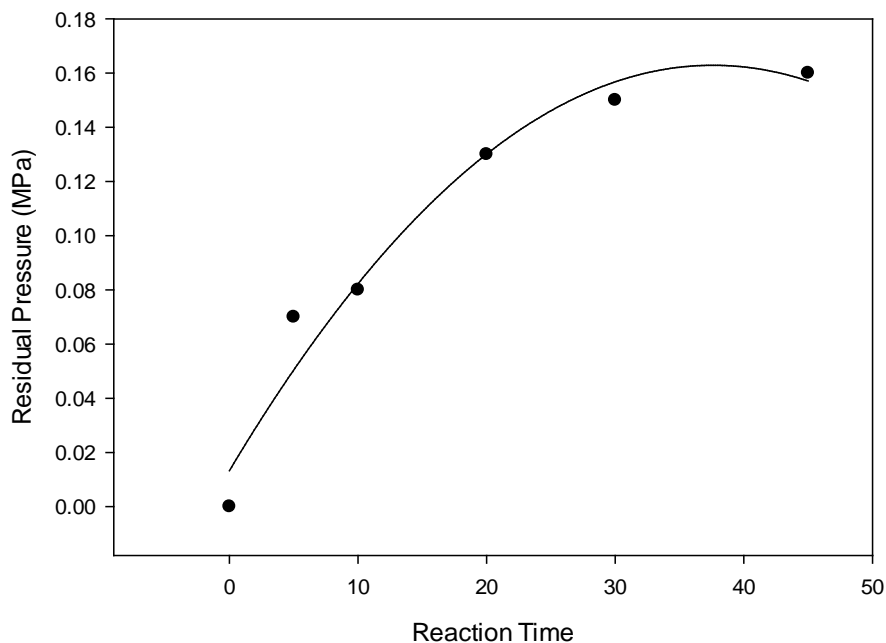


Figure 82: Reactor residual pressure at 313 K as a function of reaction time for $[\text{EtOH}] = 100 \%$, $T = 576 \text{ K}$, $[\text{Cs}_2\text{CO}_3] = 10 \text{ mg ml}^{-1}$, $[\text{Resin}] = 35 \pm 5 \text{ mg ml}^{-1}$, $P = 14.7 \pm 0.3 \text{ MPa}$, $R^2 = 0.9661$

The residual pressure after cooling the reactor to room temperature is thought to be attributable to the production of decomposition gasses under supercritical conditions. The crosslinking agent (DDS) contains sulfur which may be oxidised to SO_2 . Whilst SO_2 is soluble in ethanol [320], upon reaching saturation there additional SO_2 would exist in the gaseous phase and therefore would persist at the end of the reaction. The decomposition reactions have been shown to be time dependent and it is therefore expected that should the gasses be produced as part of the decomposition process, the residual reactor pressure should increase as a function of reaction time. This was the observation shown in Figure 82. A linear correlation between the percentage mass loss and the phenol concentration would further indicate a major decomposition product of the reaction is phenol, and that the production of phenol is directly proportional to the decomposition of the polymer matrix. This is presented in Figure 83.

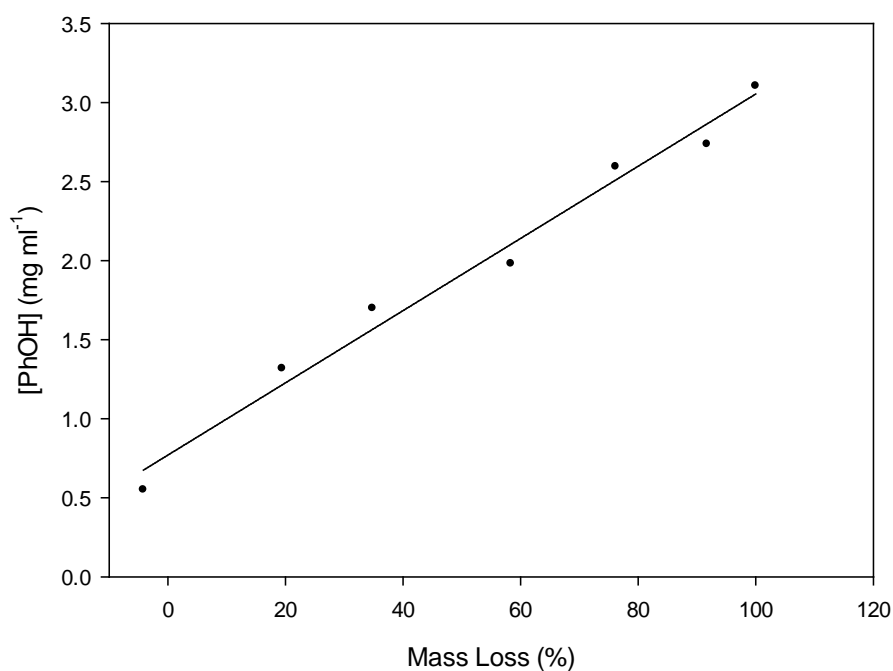


Figure 83: Production of phenol as a function of percentage mass loss of epoxy resin. $T = 573 \text{ K}$, $t = 0 - 60 \text{ min}$, $[\text{EtOH}] = 100 \%$, $[\text{Resin}] 32 \pm 3 \text{ mg ml}^{-1}$, $[\text{Cs}_2\text{CO}_3] = 10 \text{ mg ml}^{-1}$, $P = 15.1 \pm 0.4 \text{ MPa}$, $R^2 = 0.982$

Having ascertained the performance of the ethanol reaction system with respect the decomposition of the epoxy resin, the effect of changing the alcohol was also investigated. Propanol was chosen due to the similarity between its critical point and the critical point of ethanol and that it is also a solvent that is Generally Recognised as Safe (GRAS) and therefore has industrial significance.

5.1.2. Water and Propanol Co-solvent Decomposition Reactions

Effect of Co-solvent Concentration

The concentration of propanol was varied between 0 and 100 %v in order to establish, and compare, the effects of the concentration on the decomposition of the polymer resin. The reaction conditions used are given in Chapter 3.3.3. The percentage mass loss, determined by difference, and the concentration of phenol produced, as determined by HPLC, are presented in Figure 84 and Figure 85 respectively.

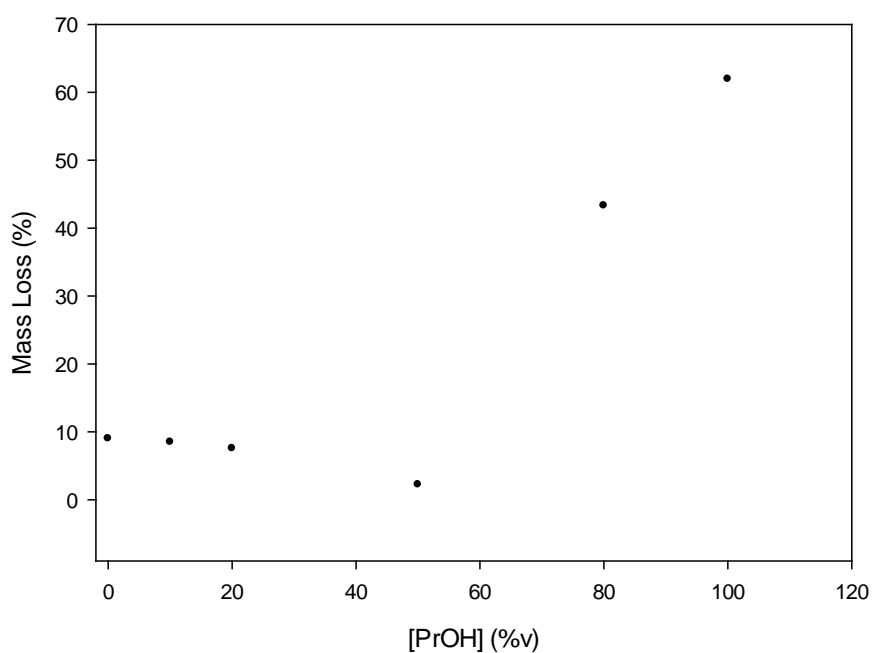


Figure 84: Percentage mass loss with respect to propanol concentration [PrOH], $T = 573 \text{ K}$, $t = 30 \text{ min}$, $[Cs_2CO_3] = 10 \text{ mg ml}^{-1}$, $[Resin] = 33.3 \text{ mg ml}^{-1}$, $R^2 = 0.975$

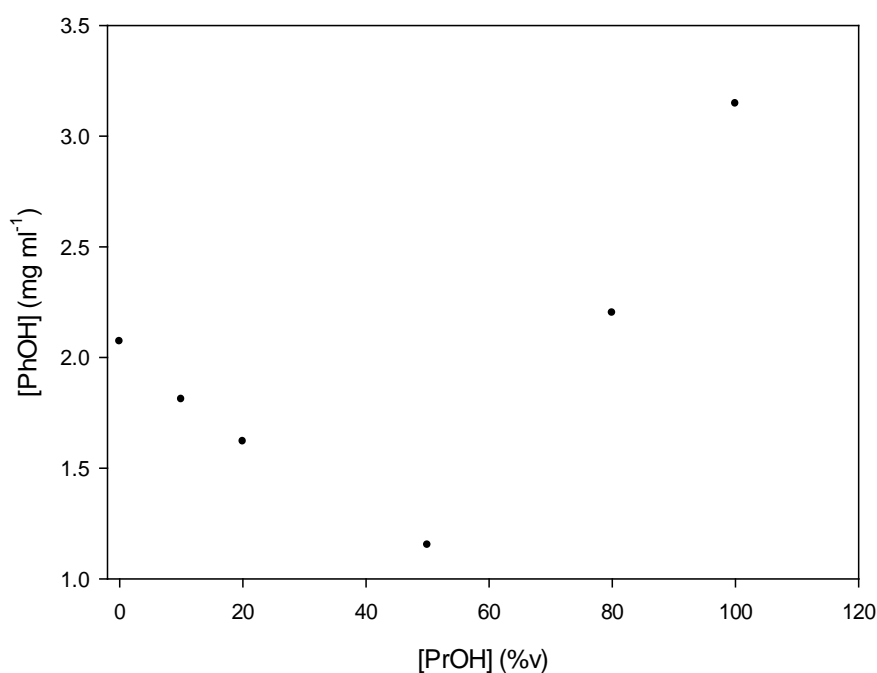


Figure 85: Phenol concentration [PhOH] with respect to propanol concentration [PrOH], $T = 573 \text{ K}$, $t = 30 \text{ min}$, $[Cs_2CO_3] = 10 \text{ mg ml}^{-1}$, $[Resin] = 33.3 \text{ mg} \pm \text{mg ml}^{-1}$, $R^2 = 0.970$

By inspection of Figure 84 and Figure 85 it may be seen that the decomposition of the epoxy resin relies heavily on the presence of the supercritical state, indicating that the process is diffusion limited. The percentage mass loss deviates slightly from the control sample observations when the propanol concentration is lower than 50 %v. The system, however, does differ from the ethanol water system in that when the co-solvent concentration (in this case propanol) is lower than 50 %v, the decomposition reaction is, in essence, inhibited. This can be seen by inspection of Figure 85 where there is a significant reduction in phenol concentration with increasing propanol concentration. The phenol concentration minima is located at [PrOH] = 50 %v and also corresponds to the minimal percentage mass loss, Figure 84. Increasing the propanol concentration beyond 50 %v leads to the fluid's critical temperature being below the reaction temperature, and therefore the reaction mixture is

supercritical. This may be observed by presenting the reactor's internal pressure as a function of temperature as shown in Figure 86.

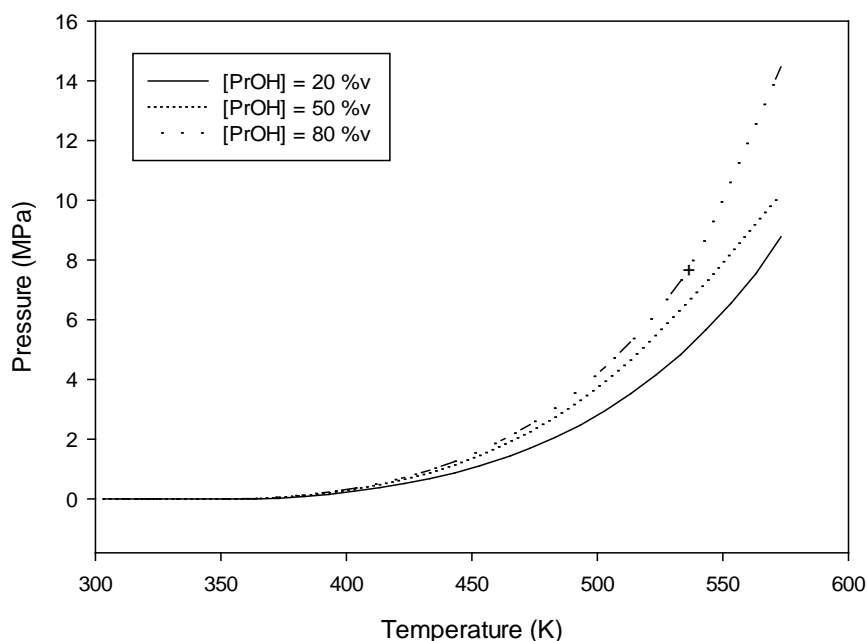


Figure 86: Reactor internal pressure as a function of temperature for varying propanol concentrations [PrOH], $[Cs_2CO_3] = 10 \text{ mg ml}^{-1}$, + = critical pressure

It is evident from observations, as presented in Figure 86, that for the reaction temperature used (573 K) the supercritical state was only achieved when the propanol concentration was 80 %v or greater. Attaining the supercritical state results in an increase of the fluids diffusivity, and decomposition of the epoxy resin is substantially increased (Figure 84). The linear increase in both the percentage mass loss and the phenol concentration in supercritical conditions indicate that the decomposition is by solvolysis, not requiring the presence of water. If the process was one of hydrolysis there would be a reduction in the percentage mass loss, and subsequent reduction in the phenol concentration observed, as the propanol concentration tends towards 100 %. Having identified 100 % propanol as the

optimum concentration for the decomposition, the effect of the caesium carbonate concentration was investigated.

Effect of Caesium Carbonate Concentration

The caesium carbonate concentration was varied from 0 – 10 mg ml⁻¹ in discrete intervals to compare its effects to those identified with the ethanol system. The percentage mass loss, determined by difference, and the phenol concentration, as determined by HPLC are presented in Figure 87 and Figure 88.

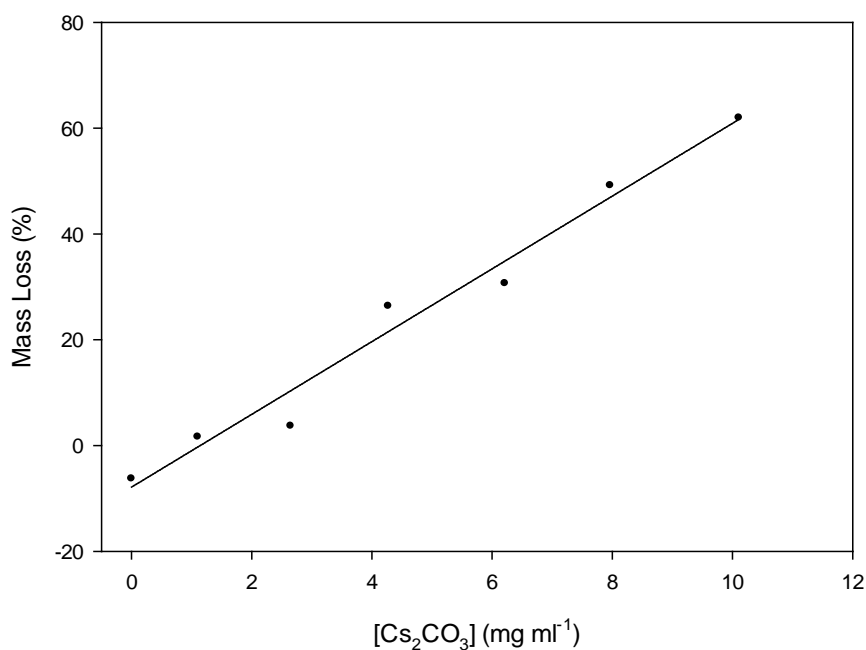


Figure 87: Percentage mass with respect to caesium carbonate concentration [Cs₂CO₃], T = 573 K, t = 30 min, [Resin] = 32 ± 3 mg ml⁻¹, P = 12.4 ± 0.4 MPa, R² = 0.985

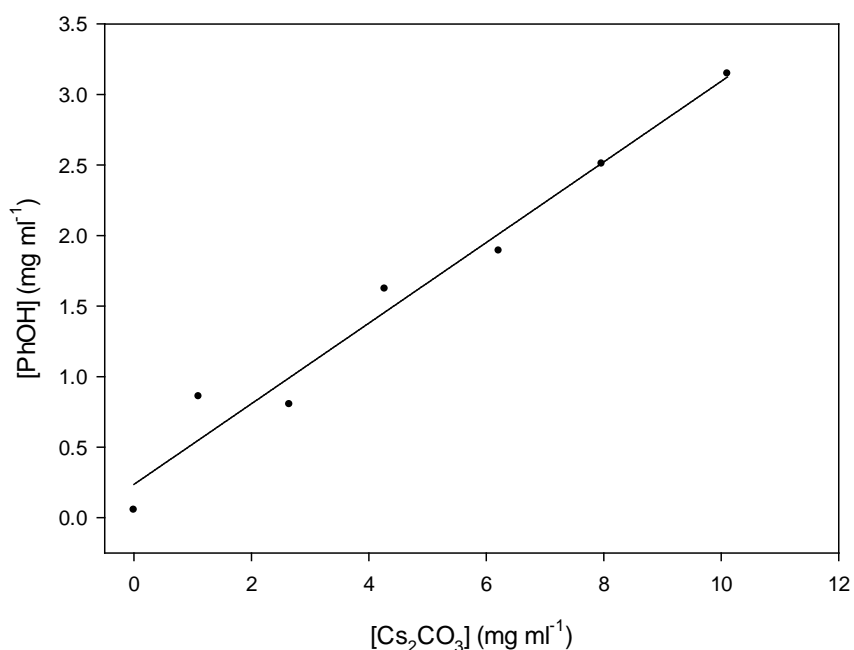


Figure 88: Phenol concentration [PhOH] with respect to caesium carbonate concentration [Cs₂CO₃], $T = 573\text{ K}$, $t = 30\text{ min}$, $[\text{Resin}] = 32 \pm 3\text{ mg ml}^{-1}$, $P = 12.4 \pm 0.4\text{ MPa}$, $R^2 = 0.974$

Observation of Figure 87 and Figure 88 shows that the system responds in a similar way as to when ethanol is used as the solvent. The addition of 1 mg ml^{-1} of caesium carbonate increases the percentage mass loss beyond that of propanol or water alone. The concentration of phenol produced is also increased above that identified with propanol or water alone, alluding to the catalytic effect of Cs₂CO₃. The linear relationships between caesium carbonate and the percentage mass loss and the concentration of phenol insinuates that phenol is a major product of the decomposition reaction, which is consistent with literature sources [305].

Effect of Reaction Time

With 10 mg ml^{-1} identified as the optimum caesium carbonate concentration of the range investigated, the reaction time was varied from 0 to 60 minutes to identify the optimum reaction conditions. The reaction conditions used are given in Chapter 3.3.3. The mass loss, determined by difference, and the phenol concentration, determined by HPLC, are presented in Figure 89 and Figure 90 respectively.

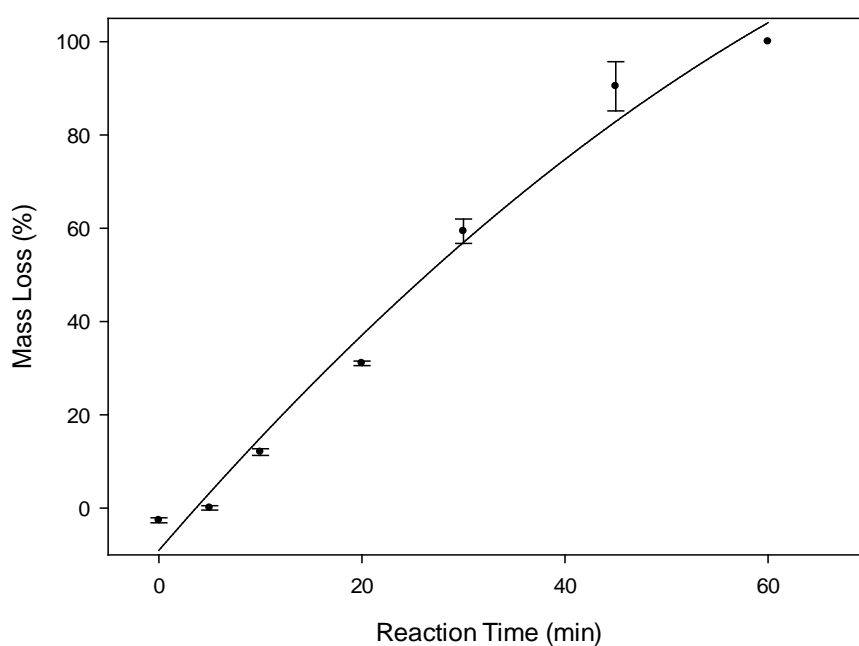


Figure 89: Percentage decomposition with respect to reaction time, $T = 573 \text{ K}$, $[\text{PrOH}] = 100 \%$, $[\text{Cs}_2\text{CO}_3] 10 \text{ mg ml}^{-1}$, $[\text{Resin}] = 35 \pm 5 \text{ mg ml}^{-1}$, $P = 12.2 \pm 0.5 \text{ MPa}$, $R^2 = 0.984$

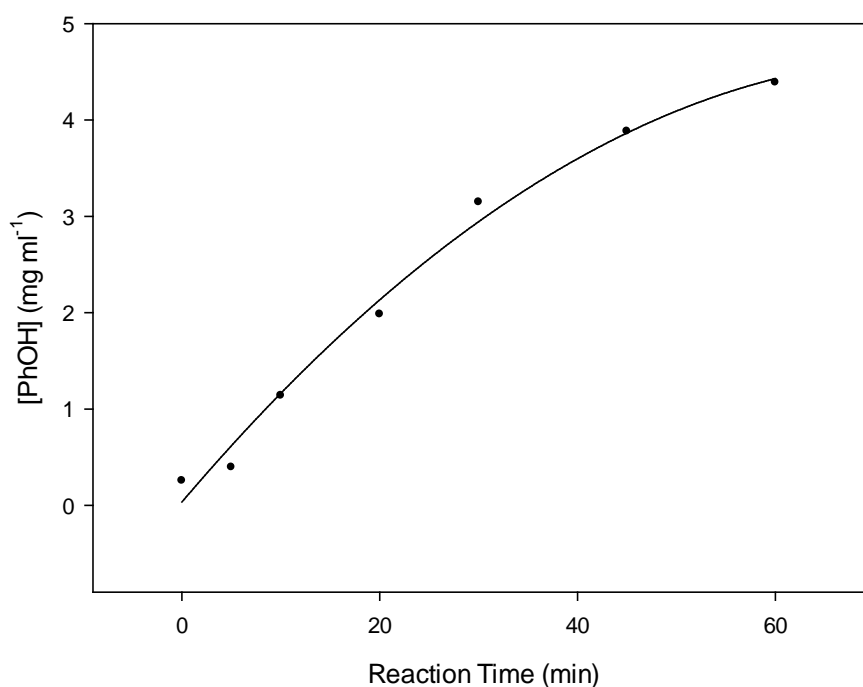


Figure 90: Phenol concentration [PhOH] with respect to reaction time, $T = 573 \text{ K}$, $[PrOH] = 100 \%$, $[Cs_2CO_3] = 10 \text{ mg ml}^{-1}$, $[Resin] = 35 \pm 5 \text{ mg ml}^{-1}$, $P = 12.2 \pm 0.5 \text{ MPa}$, $R^2 = 0.990$

Figure 89 and Figure 90 show that the reaction using 100 % propanol as a solvent, with the addition of $10 \text{ mg ml}^{-1} \text{ Cs}_2\text{CO}_3$, proceeds in a similar way to the 100 % ethanol system. In both cases, when the reaction time is 0 minutes (heating and cooling phases only) the presence of Cs_2CO_3 leads to a slight increase in mass of the recovered solids. The phenol concentration is significantly lower than the control sample observations, irrespective of the addition of Cs_2CO_3 . This is thought to be attributable to the reaction of the alcohol with the polymer, insufficient to create significant decomposition, and leading to entrapment of the partial decomposition products within the polymer matrix. In such cases the final mass recorded includes the mass of the partial decomposition products and would therefore be greater than that of the initial mass of polymer alone.

5.1.3. Water and Butanol Co-solvent Decomposition Reactions

Butanol was used to study the effects of the carbon chain-length on the decomposition of the polymer resin, as described in Chapter 3.3.3. The study focussed exclusively on the effects of the butanol concentration [BuOH]. The percentage decomposition with respect to [BuOH] is presented in Figure 91.

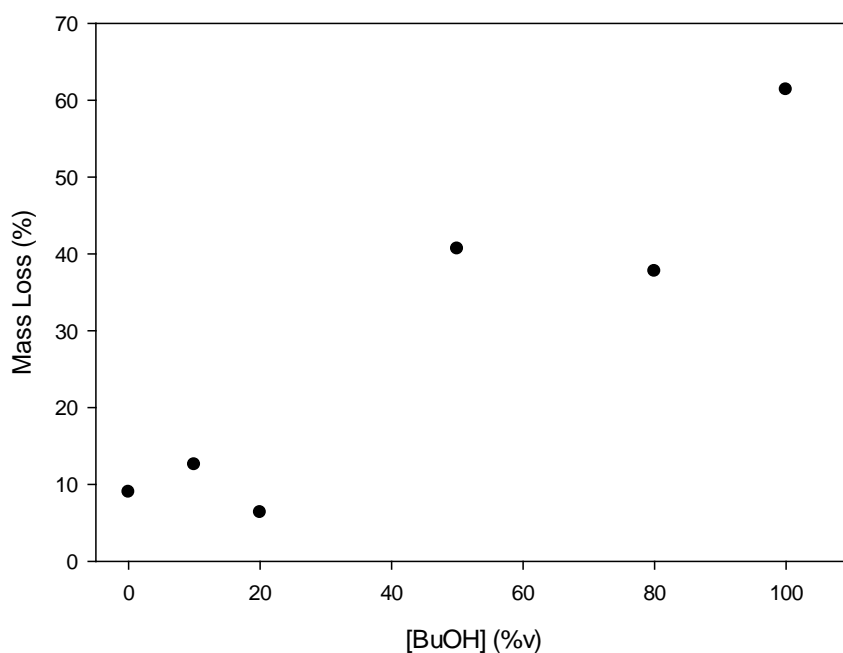


Figure 91: Mass loss as a function of butanol concentration [BuOH], $T = 573 \text{ K}$, $t_r = 30 \text{ min}$, $[Cs_2CO_3] = 10 \text{ mg ml}^{-1}$

Inspection of Figure 91 shows that the percentage decomposition of the resin is broadly linear with respect to the [BuOH]. The data from this initial investigation suggests that the decomposition is via solvolysis, as opposed to hydrolysis, and is therefore dependent upon the concentration of butanol and not that of water. The reaction system however was in part reliant upon the volume of water used, as the volume of water displaced air within the reactor and reduced the reaction volume. Since butanol and water are immiscible, displacement of the air and subsequent decrease in reaction leads to an increased reactor

loading by BuOH. Consequently the reaction pressure increased, enabling BuOH to attain the critical point and the subsequent increase in diffusivity. This can be observed in Figure 92.

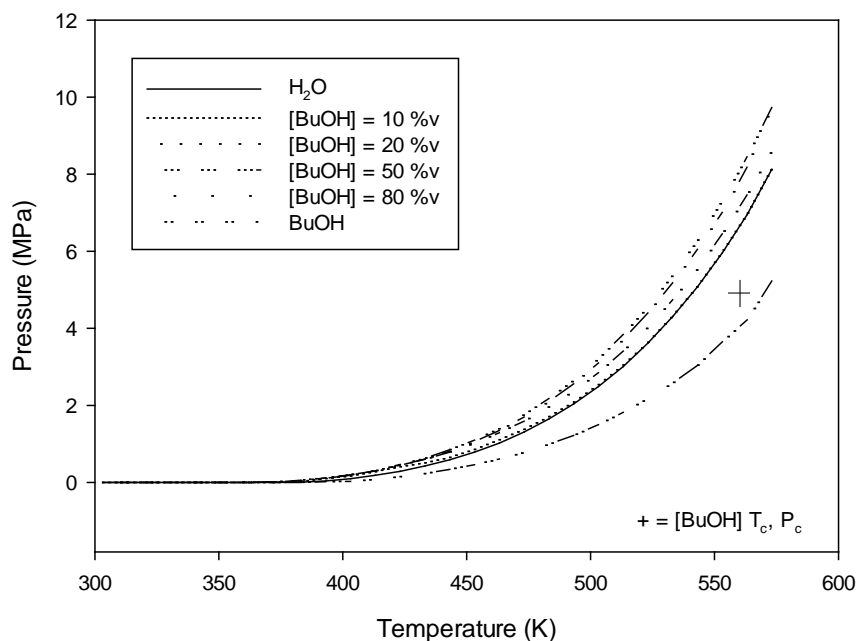


Figure 92: Reactor internal pressure as a function of temperature for $[BuOH] = 0 - 100\%v$, $t_r = 30\text{ min}$, $[Cs_2CO_3] = 10\text{ mg ml}^{-1}$, + = critical point

Examination of Figure 92 shows that only in the case of 100 % BuOH is the supercritical fluid phase transition observed. It should be noted that the pressure recorded is that of the reactor and is the sum of the partial pressures of the individual components. When miscible fluids are used, such as ethanol and water, there is a single transition to the supercritical phase. However, in the case of immiscible fluids it is possible for one fluid to attain the supercritical state whilst the second fluid remains subcritical. In such instances, deviation from the pressure / temperature correlation observed prior to the critical point is less pronounced and more difficult to identify. This is the case presented in Figure 92 where

identification of butanol in the supercritical phase is difficult. However, given that the critical point of butanol is 560 K, 4.9 MPa [7], it is evident that the supercritical conditions were achieved. Determination of the phenol concentration by HPLC for butanol and water mixtures is also more convoluted as detailed in Chapter 3.4.3. Essentially, the additional complexity arises from the differing solubility of phenol in water and butanol. In homogeneous fluid mixtures the phenol concentration is the same at all points, by definition, allowing for a sample taken at any point to be considered representative of the bulk. Consequently, when considering heterogeneous fluid mixtures the mean phenol concentration is reported, as presented in Figure 93.

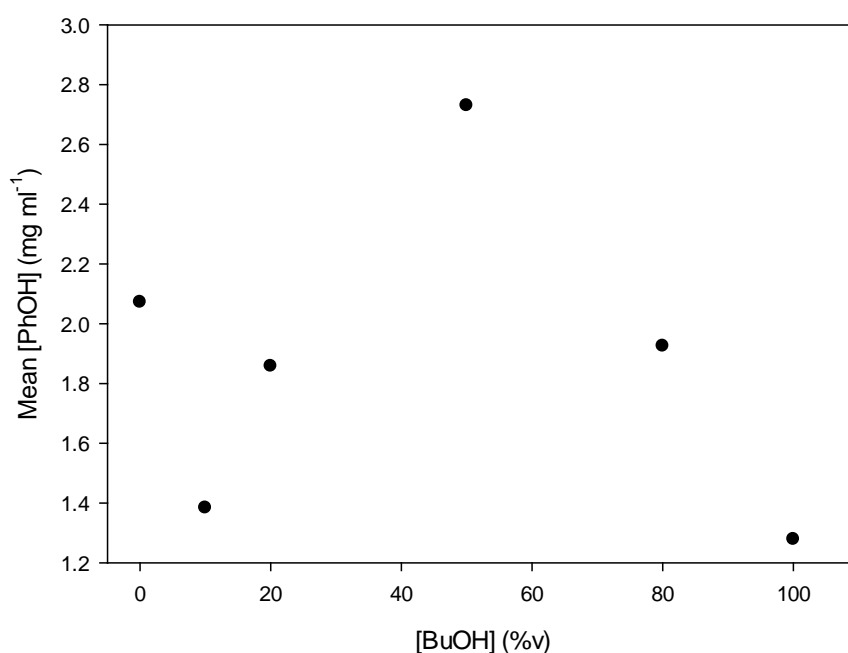


Figure 93: Average phenol concentration [PhOH] as a function of butanol concentration [BuOH], $T = 573 \text{ K}$, $t_r = 30 \text{ min}$, $[\text{Cs}_2\text{CO}_3] = 10 \text{ mg ml}^{-1}$

By examination of Figure 93 it is observed that the phenol concentration produced from the decomposition of the BADGE based epoxy resin, goes through a maximum when the butanol

concentration is 50 %v. It is known that one of the main decomposition products from the decomposition of BADGE based epoxy resins is phenol, and therefore it may initially appear that the greater the percentage decomposition the greater the phenol concentration observed. This conjecture implies that the phenol concentration should be greatest when [BuOH] = 100 %, since this condition gave the greatest percentage mass loss as presented in Figure 91. However, this does not consider the impact of the reaction pressure, which is an important factor when considering the state of the fluid. With a fluid composition of [BuOH] = 50 %v the reactor pressure is sufficient for the BuOH and H₂O to have a high density, with the BuOH being supercritical. Under such conditions it may be possible that the decomposition proceeds via simultaneous hydrolysis and solvolysis. To discuss this in more detail, the concentrations of phenol obtained in the aqueous and organic phases are presented in Table 24.

Table 24: Phenol concentration [PhOH] in organic and aqueous fractions, produced by the decomposition of epoxy resin. $T = 573 \text{ K}$, $t_r = 30 \text{ min}$, $[Cs_2CO_3] = 10 \text{ mg ml}^{-1}$

| [H ₂ O] (%v) | [BuOH] (%v) | P (MPa) | [PhOH] Aqueous Fraction (mg ml ⁻¹) | [PhOH] Organic Fraction (mg ml ⁻¹) |
|----------------------------|----------------|------------|--|--|
| 100 | 0 | 8.13 | 2.1 | 0.0 |
| 90 | 10 | 8.16 | 1.4 | 1.2 |
| 80 | 20 | 8.61 | 0.9 | 5.6 |
| 50 | 50 | 9.73 | 0.9 | 4.6 |
| 20 | 80 | 9.76 | 0.3 | 2.3 |
| 0 | 100 | 5.23 | 0.0 | 1.3 |

Examination of Table 24 shows that [PhOH] in the organic phase was typically much greater than in the aqueous phase. The exception to this is when [BuOH] = 10 %v and small amount of decomposition was observed, most probably predominantly via hydrolysis given the

composition of the fluid. With the data generated it is evident that the decomposition of the epoxy resin using butanol as a co-solvent proceeds in a manner distinctly different to that of the propanol and ethanol co-solvent systems. The difference is thought to be greater than what would be expected should the additional carbon chain-length be solely responsible. It is possible that the decomposition proceeds via hydrolysis and solvolysis simultaneously, with one process being dominant over the other. The implication is that the solvolysis process dominates, since the percentage decomposition is greatest when the [BuOH] tends to 100 %. It is also possible that the butanol extracts phenol from the aqueous phase, and consequently the concentration of phenol determined by HPLC of the aqueous fraction would not be representative of the decomposition by hydrolysis. This preliminary study has demonstrated that the butanol and water co-solvent system performs very differently to that of the other systems studied. The departure is thought to be attributable to more than a simple extension of the carbon chain-length, or the presence of a bi-phasic system alone. Within the timescale allocated it has not been possible to investigate this effect further and it is recommended as an area of study for future research. Having demonstrated that the butanol and water system represents a significant departure from the other systems studied, the following comparative study focuses on the use of water, ethanol and propanol co-solvent systems.

5.1.4. Comparative Study between Ethanol and Propanol Systems

It may be surmised that the decomposition of the BADGE based epoxy resin proceeds in a similar way in both ethanol and propanol when Cs_2CO_3 is used as a catalyst. The selection of alcohol may be undertaken by considering the attributes of each reaction system, paying

attention to the percentage mass loss and the concentration of phenol produced at a given reaction time.

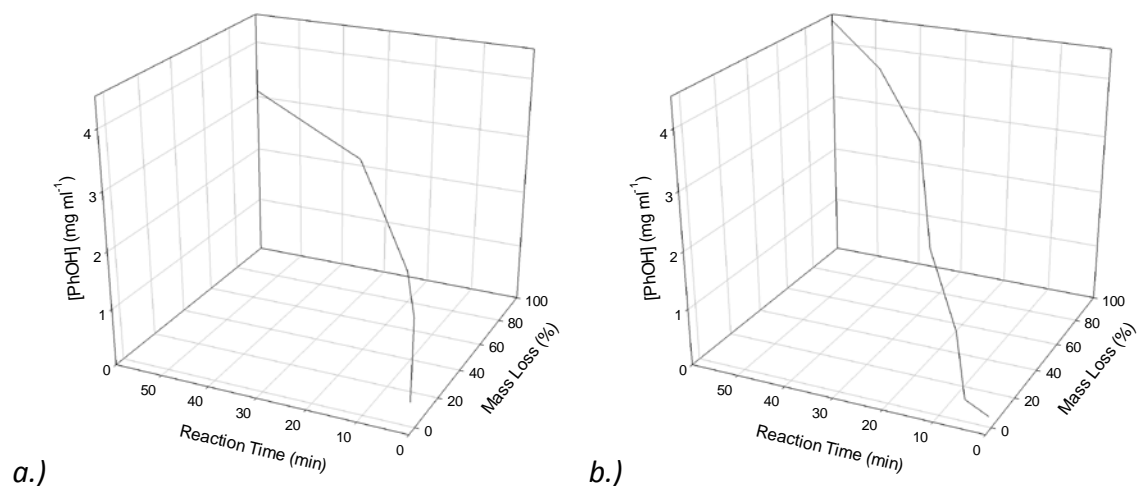


Figure 94: Evolution of phenol with respect to % mass loss as a function of reaction time, $[Resin] = 35 \text{ mg ml}^{-1}$, $[Cs_2CO_3] = 10 \text{ mg ml}^{-1}$, $T = 573 \text{ K}$; a.) $[EtOH] = 100 \%$, $P_{EtOH} = 15.1 \pm 0.7 \text{ MPa}$; b.) $[PrOH] = 100\%$, $P_{PrOH} = 12.1 \pm 1.0 \text{ MPa}$

Figure 94 'a' shows that the decomposition is more aggressive when ethanol is used as a solvent, leading to a greater percentage mass loss for a given reaction time. However, Figure 94 'b' shows that the concentration of phenol produced as a consequence of the decomposition is greater when propanol is used as a solvent. With the initial resin concentration being constant for both sets of data, these results indicate that the use of propanol as a solvent favours the production of phenol and produces less secondary products. A direct comparison between the percentage mass loss and the concentration of phenol produced is given in Figure 95.

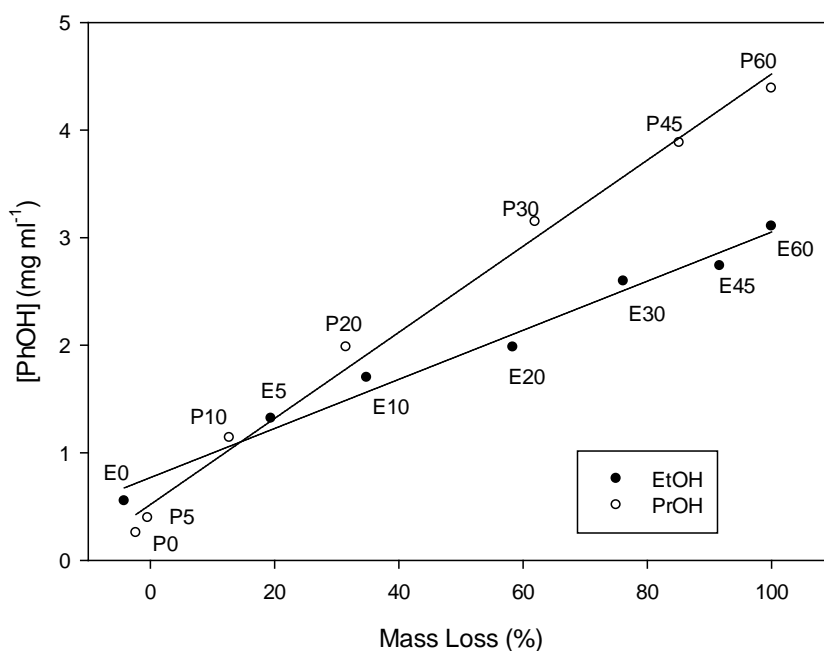


Figure 95: Comparison of phenol concentration [PhOH] with respect to percentage mass loss, [EtOH] = 100 %, [PrOH] = 100 %. $T = 573 \text{ K}$, $t = 0 - 60 \text{ min}$, $[\text{Cs}_2\text{CO}_3] = 0 - 10 \text{ mg ml}^{-1}$, $[\text{Resin}] = 35 \pm 5 \text{ mg ml}^{-1}$, $P_{\text{EtOH}} = 15.1 \pm 0.7 \text{ MPa}$, $P_{\text{PrOH}} = 12.1 \pm 1.0 \text{ MPa}$, $E_x = \text{time (min) in EtOH}$, $P_x = \text{time (min) in PrOH}$

By inspection of Figure 95 it may also be seen that for reaction times of 5 – 30 minutes the propanol system requires a reaction time approximately 50 % greater to achieve comparable results, with respect to the percentage mass loss. Figure 96 also shows that the use of ethanol results, on average, in a 17.9 % increase in the percentage decomposition for a specified reaction time between 5 and 45 minutes.

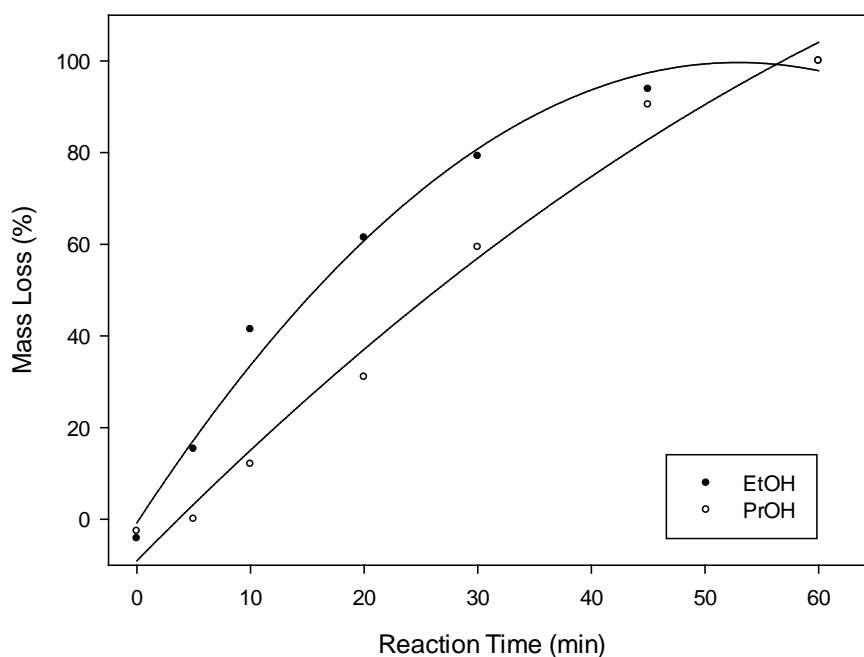


Figure 96: Comparison of percentage mass loss with respect to reaction time, $[EtOH] = 100\%$ and $[PrOH] = 100\%$. $T = 573\text{ K}$, $[Cs_2CO_3] = 10\text{ mg ml}^{-1}$, $[Resin] = 35 \pm 5\text{ mg ml}^{-1}$, $P_{EtOH} = 15.1 \pm 0.7\text{ MPa}$, $P_{PrOH} = 12.1 \pm 1.0\text{ MPa}$.

Identification of the decomposition products was performed by GC-MS as described in Chapter 3.4.3. Quantitative HPLC was used (as stated previously) to determine the phenol concentration. The expectation would be to identify additional decomposition products when ethanol is used as a solvent in comparison to those identified when propanol is the solvent, and further that these additional products may be phenolic derivatives produced by secondary reactions of the initial decomposition products. The GC-MS chromatograms providing this comparison are given in Figure 97.

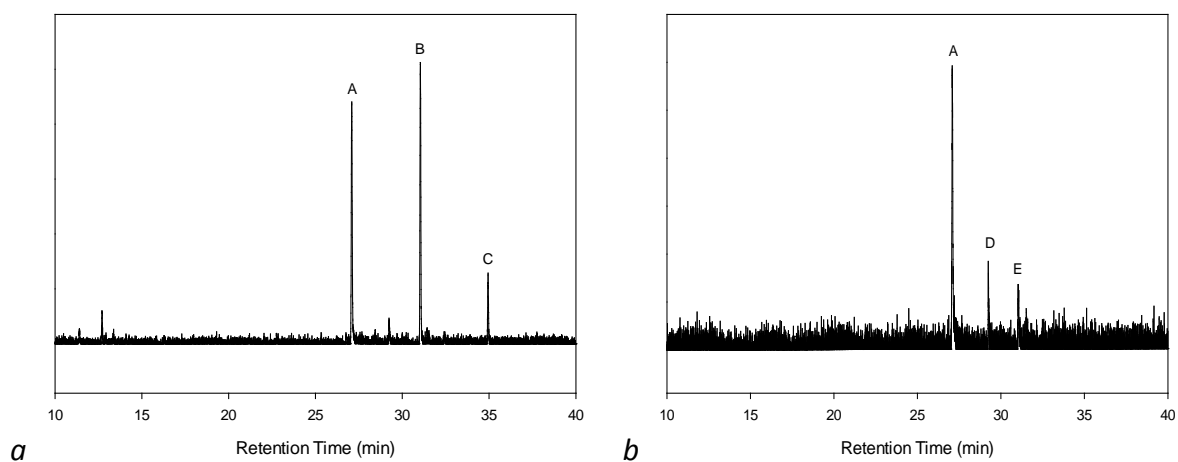


Figure 97: GC-MS Chromatogram comparison of decomposition products. $T = 573\text{ K}$, $t = 30\text{ min}$, $[Cs_2CO_3] = 10\text{ mg ml}^{-1}$; a.) $[EtOH] = 100\%$, b.) $[PrOH] = 100\%$. A = phenol, B = 4-(1-methylethyl)-phenol, C = *p*-isopropenylphenol, D = 2-(1-methylethyl)-phenol, E = 3-(1-methylethyl)-phenol.

Figure 97, 'a' and 'b', shows that for a 30 minute reaction time, ethanol produces substituted phenols that are not observed when propanol is used. This is in good agreement with the observation that although ethanol is more aggressive with respect to the percentage decomposition of the resin, propanol yields higher concentrations of phenol.

These data (Figure 94 – Figure 97) suggest that ultimately the choice of solvent system is dependent upon the objective and desired products. If the objective is to decompose a thermoset epoxy resin, resulting in the minimum residual resin for a given reaction time then ethanol is a more effective solvent than propanol. Conversely, if the objective is to recover higher purity decomposition products, to facilitate in the downstream processing, propanol is a more effective solvent than ethanol.

Given that the samples used were identical, having being produced in the same way, it was considered that the differences in the decomposition process may be of both chemical and physical phenomena. The data obtained suggest that should physical phenomena exist, it may be possible to identify them by means of Scanning Electron Microscopy (SEM) of the partially degraded resin samples. Attention is now focused on considering the physical state of the epoxy resin samples subjected to scEtOH and scPrOH processing.

5.2. SUPERCRITICAL FLUID INDUCED SWELLING OF EPOXY RESIN

The use of Scanning Electron Microscopy (SEM) offers the opportunity to image the samples processed by scEtOH and scPrOH, paying particular attention to the surface characteristics. By analysing samples processed for differing lengths of time it is possible to follow the decomposition process, given that it has been previously established that the reaction time is an important factor (see Chapter 5.1). It has also been established that the reaction process proceeds differently in ethanol and propanol, although the major product in both instances is phenol (Chapter 5.1.4.). Since this investigation analyses the samples utilised in Chapter 5.1. no separate reaction schedule exists. The reaction schedule used is presented in Chapter 3.3.3. Virgin samples of cured epoxy resin were used to compare and contrast the surface properties with those of processed samples. The SEM micrographs of the virgin samples are presented in Figure 98.

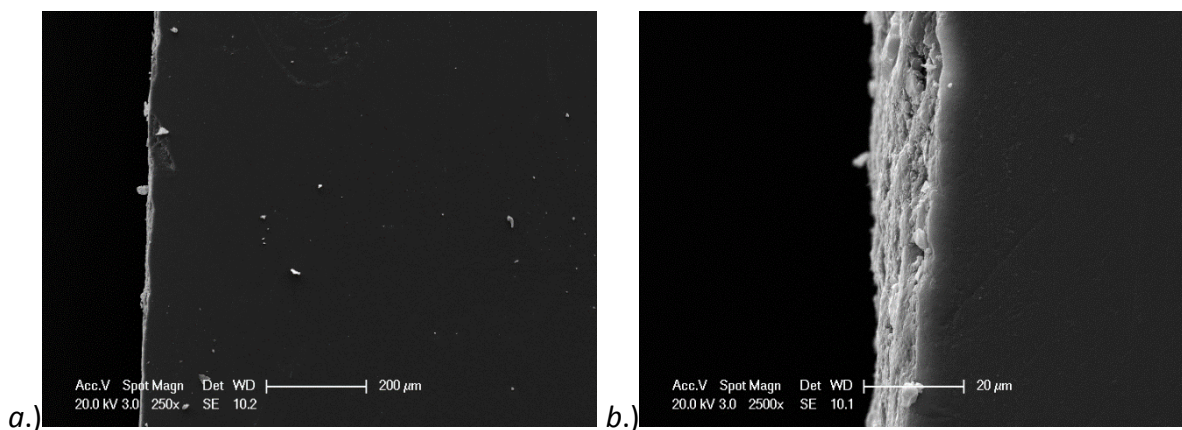


Figure 98: SEM Micrographs of virgin samples of cured epoxy resin showing; a.) top surface, Mag = 250x, WD = 10.2; b.) cross-section, Mag = 2500x, WD= 10.1

It can be seen from Figure 98, 'a' and 'b', that the surfaces of the virgin samples are smooth and free of voids, cavities and contours. Figure 98 'b' shows part of the cross section, in particular the face that was cut. As to be expected, the surface roughness is greater owing to the random fracturing of the material when cut. Using the virgin samples as a control, the processed samples are studied. Previous work has determined the percentage mass loss of the epoxy resin as a function of time (see Chapter 5.1), therefore, using SEM imaging it is possible to study the process of decomposition.

Supercritical Ethanol

Supercritical ethanol (scEtOH) was shown to be aggressive with respect to the decomposition of the epoxy resin. It was also observed that the mass of the processed sample was greater than that of the initial sample when the reaction time was 0 minutes (zero time corresponds to solely heating and cooling). This was observed both in the presence and absence of Cs_2CO_3 and therefore suggests that the ethanol reacts with the epoxy resin, producing organic molecules that become bound to, or entrapped within, the

polymer matrix and without the substantial decomposition of the resin, the final mass of the sample would be expected to be greater than that of the initial mass. SEM micrographs taken for a range of reaction time are presented in Figure 99.

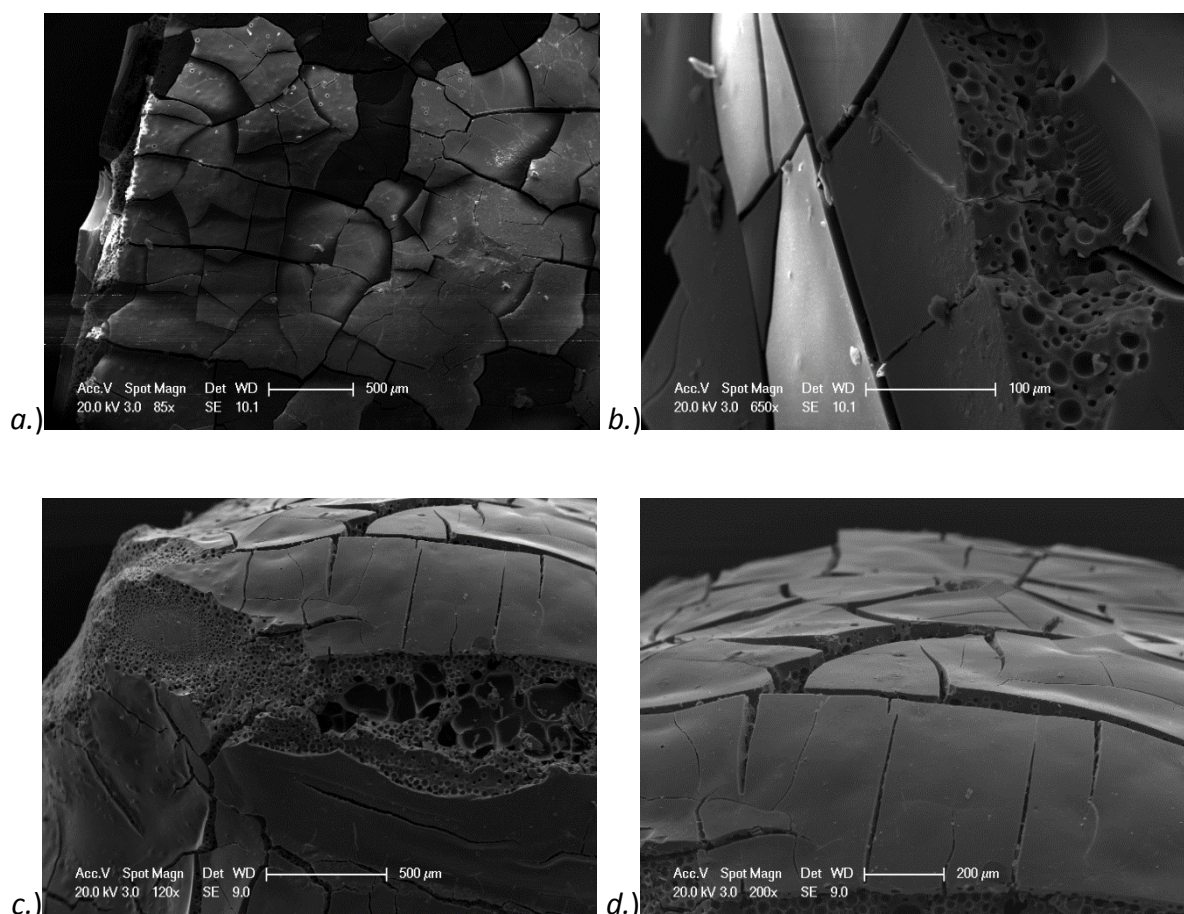


Figure 99: SEM micrographs for decomposition in scEtOH as a function of reaction time. $[EtOH] = 100\%$, $[Cs_2CO_3] = 10\text{ mg ml}^{-1}$, $T = 573\text{ K}$; a.) $t = 0\text{ min}$, $Mag = 85x$, $WD = 10.1$; b.) $t = 0\text{ min}$, $Mag = 650x$, $WD = 10.1$; c.) $t = 10\text{ min}$, $Mag = 120x$, $WD = 9.0$; d.) $t = 10\text{ min}$, $Mag = 200x$, $WD = 9.0$

It can be seen in Figure 99 'a' that there is extensive cracking along that surface of the polymer. Figure 99 'b' shows that, neglecting the cracks, the surface of the polymer appears smooth and free of voids, however beneath the surface the formation of pores has to taken place, indicating that the polymer swelling process is underway. After 10 minutes under the

reaction conditions the porosity becomes far more extensive, with sections of the polymer surface missing, and with some exposed areas being covered by pores, Figure 99 'c'. Where the polymer surface remains, it is free from pores, and the pores are confined to the inside of the cracks as can be seen in Figure 99 'd'. For reaction times of 10 minutes it was found that approximately 40 % of the polymer mass has been decomposed and increasing reaction times the polymer degradation was more extensive as shown in Figure 100.

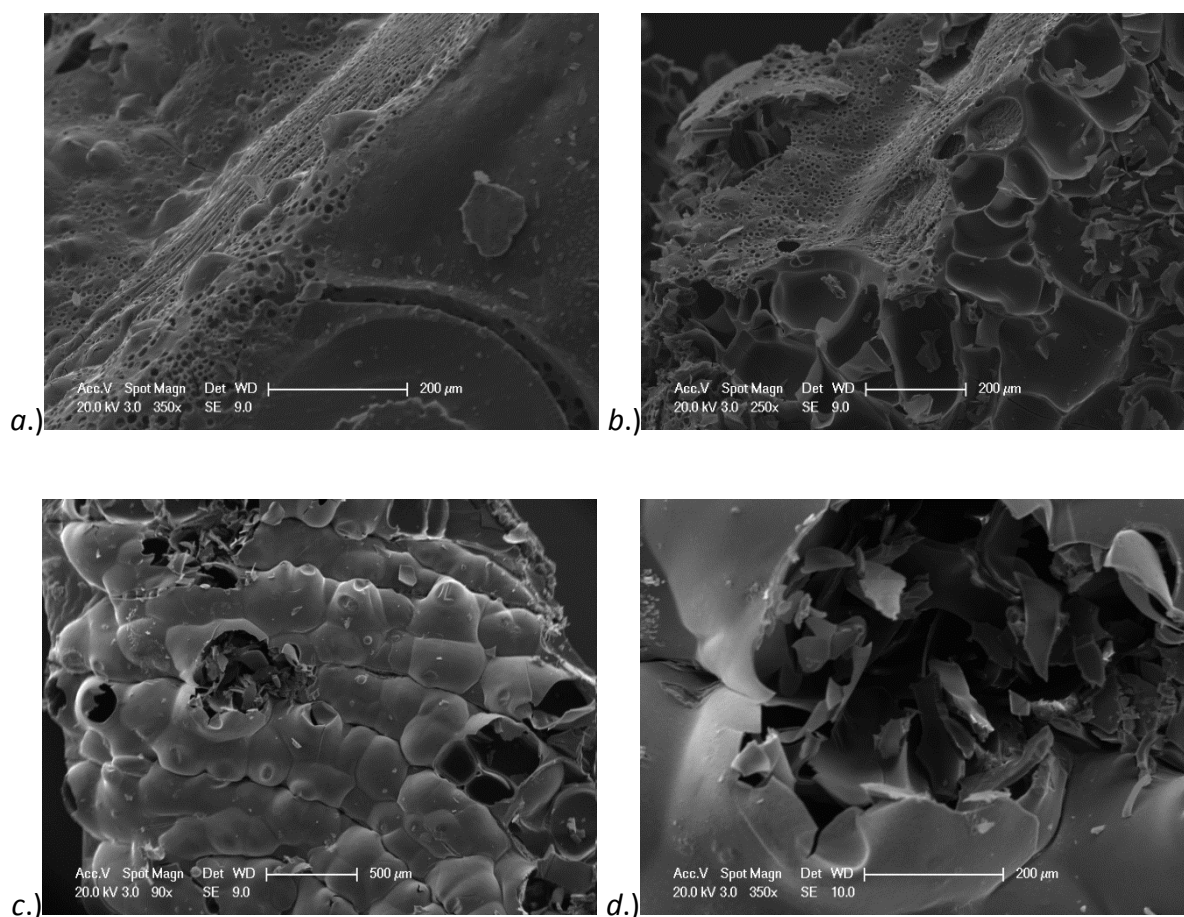


Figure 100: SEM micrographs for decomposition in scEtOH as a function of reaction time. $[\text{EtOH}] = 100\%$, $[\text{Cs}_2\text{CO}_3] = 10\text{ mg ml}^{-1}$, $T = 573\text{ K}$; a.) $t = 30\text{ min}$, $\text{Mag} = 350\text{x}$, $\text{WD} = 9.0$; b.) $t = 30\text{ min}$, $\text{Mag} = 250\text{x}$, $\text{WD} = 9.0$; c.) $t = 45\text{ min}$, $\text{Mag} = 90\text{x}$, $\text{WD} = 9.0$; d.) $t = 45\text{ min}$, $\text{Mag} = 350\text{x}$, $\text{WD} = 10$

Figure 100 'a' shows that for a reaction time of 30 minutes although some smooth surfaces remain, vast regions of the surface are covered with pores. Blistering is visible on the remaining smooth sections, indicating that the polymer swelling within the bulk material is advanced. This is further indicated by Figure 100 'b' where it is apparent that some fragmentation of the polymer surface has taken place. After 45 minutes under the reaction conditions the polymer swelling is extensive, with advanced blistering covering almost the entire surface of the sample, Figure 100 'c'. Several blisters have ruptured forming fragments and exposing the voids beneath as seen in Figure 100 'd'. The shutdown sequence of the reactor was the same in all experiments and is not thought to contribute to the results obtained.

By evaluation of Figure 99 and Figure 100 it may be inferred that the decomposition process, when scEtOH is used as a solvent in the presence of Cs_2CO_3 , begins with the swelling of the polymer. Upon reaching the reaction conditions the polymer swelling is confined to the bulk sample and is manifested only in the cracking of the polymer surface, with porosity only observed along leading edges of the polymer post cutting. Within the first 10 minutes under the reaction conditions the polymer swelling process becomes extensive and the cracked sections are able to separate to accommodate the increased bulk volume. As this process takes place it is likely that some of the polymer surface swell and move relative to the bulk material, leading to the loss of the polymer surface and consequently the sub surface pores become visible as can be seen in Figure 100 'c'. The degradation products, of which phenol is one [321], are likely to diffuse from the bulk polymer into the bulk solvent and may be involved in the swelling process. As localised swelling takes place

blisters are formed, having a much greater diameter than the pores formed within the bulk of the sample. The evolution of these large blisters occurs more slowly than the rapid formation of the pores, and they become visible after 30 minutes under reaction conditions and still remain visible after 45 minutes. Conversely, the pores, although few are visible when the reaction time is 0 minutes, are wide spread and likely to be found throughout the bulk sample within 10 minutes. This is consistent with the observation that 79.2 % of the polymer is decomposed within the first 30 minutes and, an additional 50 % reaction time is required to decompose a further 14 %. A doubling of the reaction time from 30 to 60 minutes is required to decompose the entire sample.

It was observed that the decomposition of the polymer resin in supercritical propanol scPrOH progressed in a slightly different manner to when scEtOH was used, both reaction conditions incorporating the use of Cs_2CO_3 as a catalyst. Ethanol was found to be more aggressive with respect to the percentage mass loss, whereas scPrOH appeared more selective with respect to the formation of decomposition products. In light of these differences, the decomposition under scPrOH was also investigated by SEM.

Supercritical Propanol

Supercritical propanol was proven to be less aggressive with respect to the percentage decomposition of the polymer resin. It would therefore be expected that the decomposition process proceeds in a slightly different manner. The same reaction times (t_r) that were used for the ethanol investigation, $t_r = 0, 10, 30$ and 45 minutes, were selected for the propanol

investigation to produce a fair comparison. The SEM micrographs for $t = 0$ and 10 minutes are shown in Figure 101.

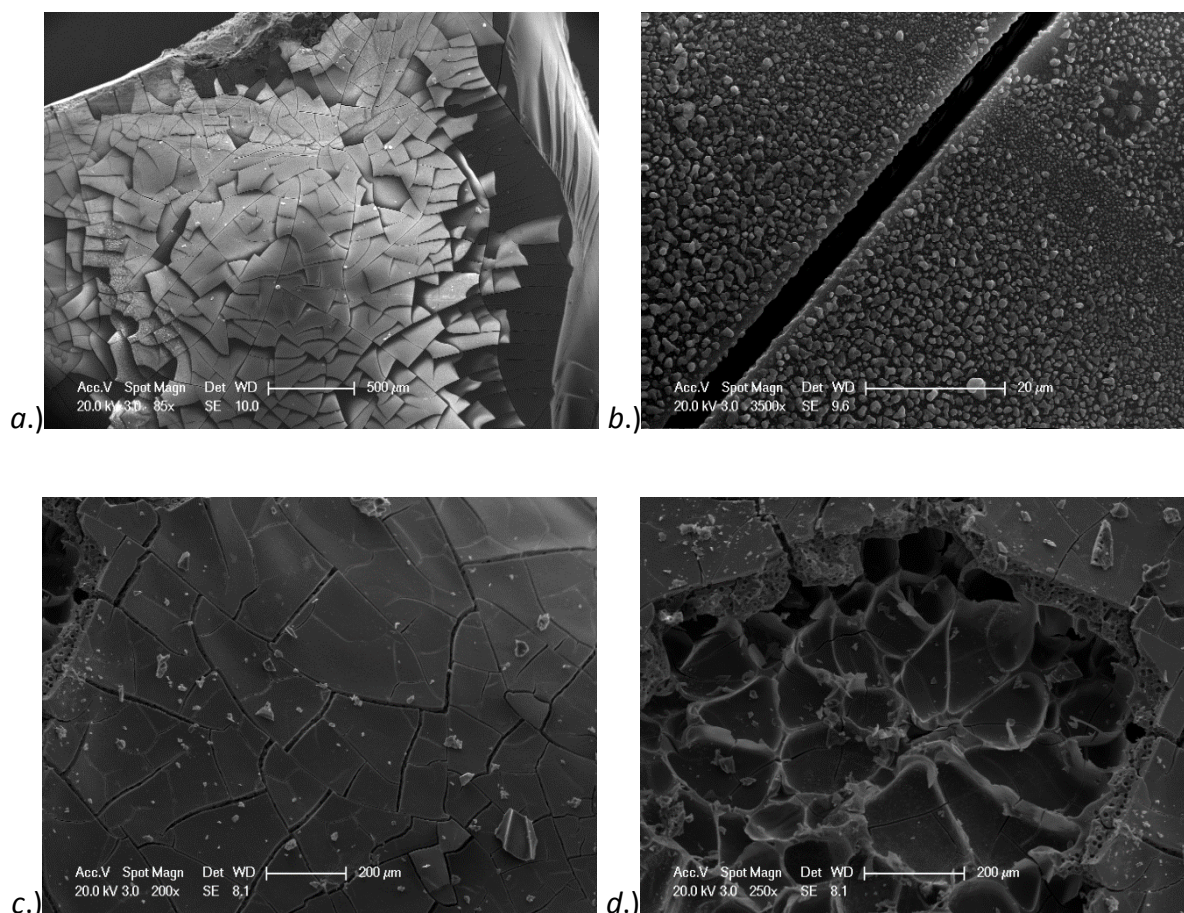


Figure 101: SEM micrographs for decomposition in scPrOH as a function of reaction time. $[PrOH] = 100\%$, $[Cs_2CO_3] = 10\text{ mg ml}^{-1}$, $T = 573\text{ K}$; a.) $t = 0\text{ min}$, $Mag = 80x$, $WD = 10.0$; b.) $t = 0\text{ min}$, $Mag = 3500x$, $WD = 9.6$; c.) $t = 10\text{ min}$, $Mag = 200x$, $WD = 8.1$; d.) $t = 10\text{ min}$, $Mag = 250x$, $WD = 8.1$

By inspection of Figure 101 'a' it can be seen that when the reaction time is 0 minutes the results are much the same as the ethanol system, there is widespread surface cracking with the absence of blistering and surface ruptures. The solubility of Cs_2CO_3 in propanol is lower than in ethanol and consequently deposition of the catalyst on the polymer surface is observed upon attaining ambient conditions (Figure 101 'b'), determined by EDX as shown

in Figure 102. The detection of gold is a result of the sputter coating of the sample, necessary due to epoxy resin being an electrical insulator.

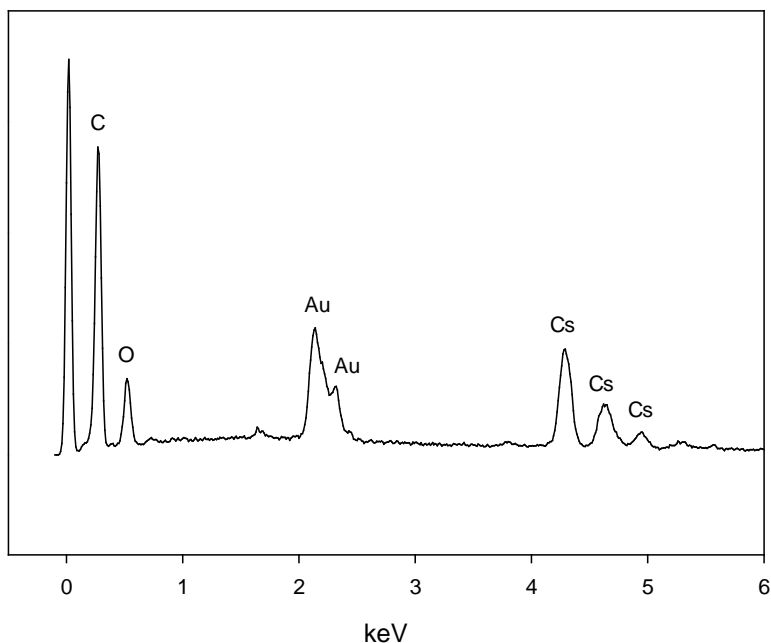


Figure 102: EDX Analysis of solid deposits on the surface of epoxy resin post-processing

Having a lower solubility, and subsequent reduction in Cs_2CO_3 concentration compared to the ethanol system, the catalyst concentration within the bulk polymer will be lower. This in turn leads to a reduction in the percentage decomposition for a given reaction time. Figure 101 'c' shows that after a reaction time of 10 minutes some fragmentation is visible; Figure 101 'd' shows an area of surface removal exposing a secondary layer. The surface layer is highly porous with the exposed area showing a macro-porous cell structure. The progression of the reaction on polymer degradation is shown in Figure 103.

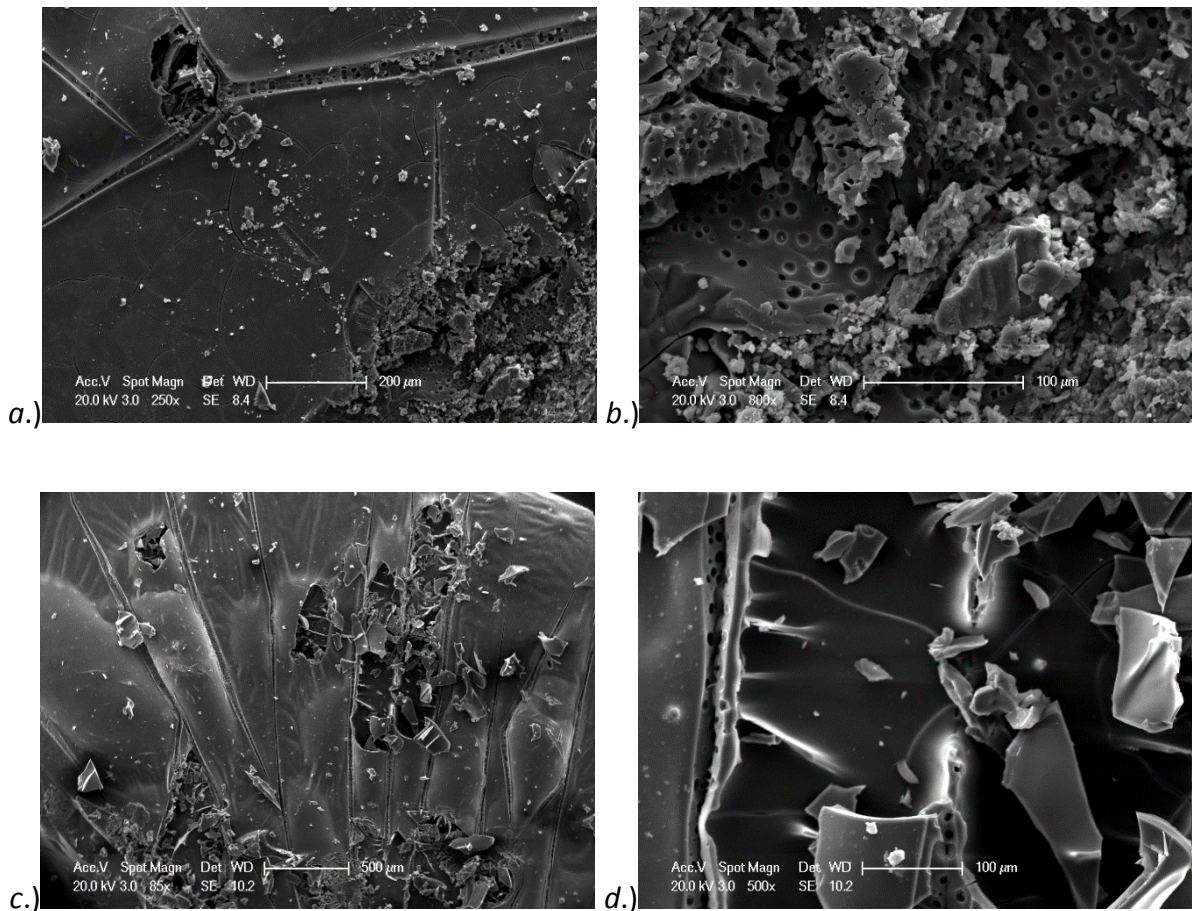


Figure 103: SEM micrographs for decomposition in *scPrOH* as a function of reaction time. $[PrOH] = 100\%$, $[Cs_2CO_3] = 10\text{ mg ml}^{-1}$, $T = 573\text{ K}$; a.) $t = 30\text{ min}$, $Mag = 250\times$, $WD = 8.4$; b.) $t = 30\text{ min}$, $Mag = 800\times$, $WD = 8.4$; c.) $t = 45\text{ min}$, $Mag = 85\times$, $WD = 10.2$; d.) $t = 45\text{ min}$, $Mag = 500\times$, $WD = 10.2$

Figure 103 'a' shows that after 30 minutes under reaction conditions areas of the polymer have undergone swelling. The initial surface fractures are still visible in many regions but the dominant process is now the swelling of the bulk polymer, a process that out-paces the expansion capabilities of the surface and leads to peeling. Unlike the surface fractures identified at the start of the reaction, these peeling fissures are on the macro-scale and may span the entire surface of the polymer. As these fissures open they expose the sub-surface pores, which may in turn increase the mass transfer of material into and out of the polymer, thereby accelerating the process further. Where these fissures connect, rupture points are observed, possibly due to stress concentration. Ruptures of this type produce significant

quantities of small fragments (Figure 103 'b'), therefore increasing the surface area of the polymer available for reaction and further enhancing the decomposition rate.

When the polymer has been under reaction conditions for 45 minutes the remaining polymer is heavily swollen, having blisters that are in the millimetre size range (Figure 103 'c'). The fissures divide the polymer into individual segments, confining the growing blisters until the stretching action overcomes the physical properties of the polymer. These blisters then rupture in what appears to be a violent eruption, producing significant quantities of debris, leaving cavities in the millimetre size range. In doing so the effect would accelerate the decomposition in two ways; firstly, with the production of smaller fragments (Figure 103 'd') the surface area available has increased which in turn would increase the rate of reaction. Secondly, the surface area of the entire cavity is now directly accessible to the fluid and may provide a channel of reduced tortuosity to the bulk polymer.

The auto-accelerating nature of the decomposition outlined above would explain the observation that whilst the ethanol system is more aggressive with respect to the percentage decomposition, increasing the mass loss by 18 %, when the reaction time is between 5 and 45 minutes, after 45 minutes under reaction conditions the percentage decomposition obtained with the propanol system is within 3 % of that observed with the ethanol system.

Development of Fissures

The evolution of surface cracks into fissures, points where the polymer is peeling apart, has been investigated for the propanol system. This phenomenon was not observed when ethanol was used as a solvent and is thought to be the consequence of swelling of the bulk polymer as opposed to a surface effect. In the latter stages of decomposition in an ethanol system severe surface blistering was identified (see Figure 101), leading to ruptures and the formation of fragments. The evolution of cracks into fissures for a propanol system is shown in Figure 104.

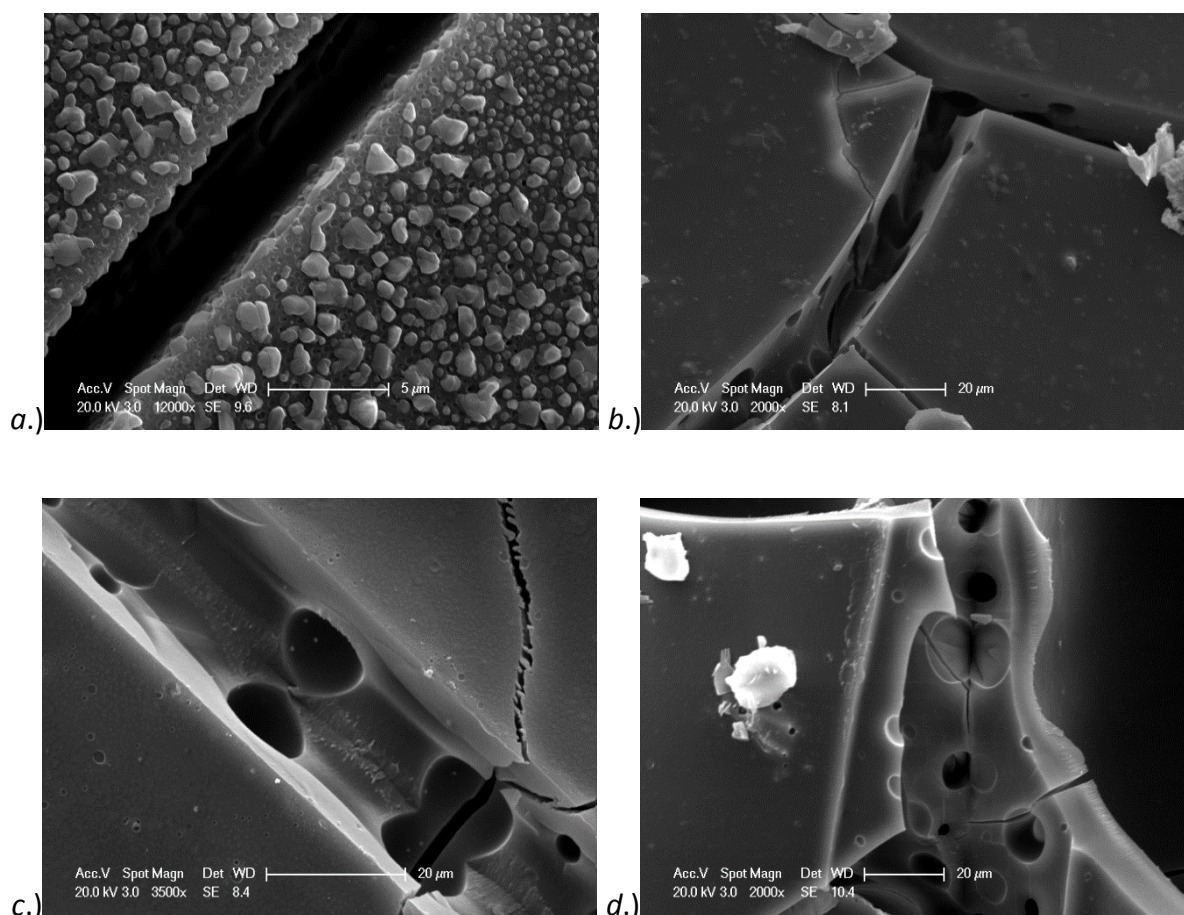


Figure 104: SEM micrographs of swelling derived fissure evolution. $[\text{PrOH}] = 100\%$, $[\text{Cs}_2\text{CO}_3] = 10 \text{ mg ml}^{-1}$, $T = 573 \text{ K}$; a.) $t = 0$ min, Mag = 12,000x, WD = 9.6; b.) $t = 10$ min, Mag 2,000x, WD = 8.1; c.) $t = 30$ min, Mag = 3,500x, WD 8.4; d.) $t = 45$ min, Mag 2,000x, WD = 10.4

It can be seen from Figure 104 'a' that the initial fractures result in distinct surfaces after $t_r = 0$ minutes under reaction conditions, which are beginning to separate after a reaction time of 10 minutes, Figure 104 'b'. After 30 minutes under reaction conditions it can be seen that the surfaces, whilst aligned, are peeling away from each other exposing the interconnecting pores in the process, Figure 104 'c'. Figure 104 'd' shows that after a reaction time of 45 minutes the surfaces, now undergoing surface swelling and rupturing in addition to the sub-surface swelling, are moving further apart. The alignment of the pores is still visible and is used to identify that the polymer is peeling at the surface.

The significance of this process is that it demonstrates that whilst deposition of the Cs_2CO_3 catalyst on the surface does take place, as can be seen in Figure 104 'a' and Figure 101 'b', it does not inhibit the polymer swelling process. It does, however, play an important role in determining the way in which the polymer is decomposed. It is apparent that when propanol is used as a solvent the polymer swelling is primary to the decomposition, the decomposition auto-accelerating as the pores, potentially being used as routes for the catalyst to the bulk polymer, become available at the surface of the material.

Having investigated the decomposition process of a model thermoset polyepoxide resin, and followed the decomposition by SEM analysis, it should be noted that the presence of fibres in a CFRP may influence the swelling process although the decomposition reactions are likely to remain unchanged. It has been demonstrated that the reaction conditions presented are capable of decomposing the BADGE based epoxy resin into small organic molecules, with phenol being the predominant product. By understanding the impact of

these reactions conditions on the physical properties of carbon fibres it is possible to understand, with detail, the potential impact on Carbon Fibre Reinforced Polymers (CFRP's). Therefore, attention is now directed towards the impact of the reaction conditions used on the tensile strength of carbon fibres.

CHAPTER 6. RESULTS PART C: CHARACTERISATION AND RECYCLING OF CARBON FIBRE

6.1. TENSILE PROPERTIES OF RECYCLED CARBON FIBRES

Carbon fibres were subjected to reaction conditions that had demonstrated a capability to decompose either thermoplastic or thermoset resins. By subjecting the fibres to these conditions, the objective was to identify the effects of the reaction conditions on the fibres in a direct manner, without the added complication of the effects of polymer degradation products. Having developed a method for counting [245], with precision, the number of carbon fibres within a bundle this research aims to extend the tensile testing of carbon fibres to bundles (as opposed to single fibres). This approach allows for the testing of several hundred fibres within a very small number of experiments, something that is fundamentally not possible with single fibre testing. The reaction conditions used are presented in Chapter 3.3.4. and the analytical equipment setup is provided in Chapter 3.4.4.

When testing carbon fibre bundles, aside from accurately determining the number of fibres, other factors may influence the results. The tensile strength calculated is the mean tensile strength of a single fibre within the bundle and it is acknowledged that the strength of any given fibre may deviate from this value. However, since individual fibres are not used alone, the strength of a single fibre is of little consequence and thought to be less valuable than an understanding of the entire bundle. A complication exists in the fibre alignment. To date, there has not been a suitable method for the re-alignment of recycled fibres. Recycled fibres are currently being considered for the manufacture of random chopped mats, which by

definition do not require alignment, and where alignment has been carried out it is by manual processes. By using manual alignment, as was done in this research, it is not possible to prevent physical interaction between the fibres within a bundle or to ensure that all fibres are parallel. Consequently, not all of the fibres within a bundle sustain the applied load simultaneously. A comparison between the tensile strength of single fibres and fibre bundles processed under identical conditions is given in Figure 105.

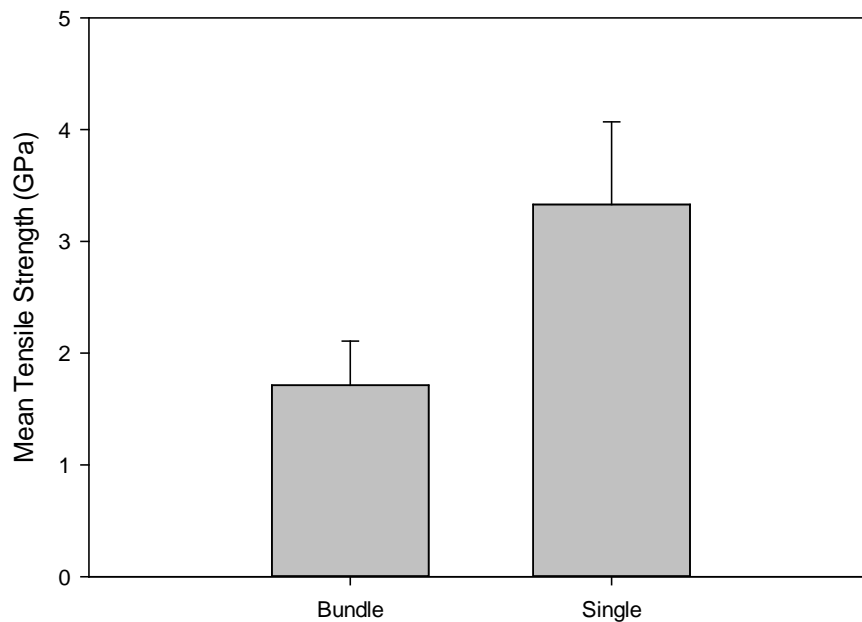


Figure 105: Comparison between tensile strength of single fibres and the mean fibre within a bundle; $T = 623\text{ K}$, $t_r = 30\text{ min}$, $[\text{EtOH}] = 80\%$, # Single fibre test = 40, # Fibre bundle test = 5 x 300

Inspection of Figure 105 shows that the average tensile strength of a fibre within a bundle of 300 fibres is approximately 50 % of that of a single fibre processed under identical conditions. This effect has been reported previously in the literature [322, 323] and is likely to be combination of fibre interactions within the bundle, as well as the bundle having a

load distribution with respect to cross-head separation. Consequently, it is possible for some fibres to break prior to the bundle achieving the maximum force, whilst other fibres may break after reaching the maximum force of the bundle. To alleviate this effect, consideration was given to integrating the curve produced by the tensile test, thus yielding the work done by the Universal Testing Machine (UTM) to break the bundle of fibres. This, in conjunction with the number of fibres, allows for calculation of the mean work done per fibre. Whilst initially appearing as an attractive option, this method introduces a secondary error in that it assumes that no fibre interactions exist immediately after reaching the force maxima. Clearly this assumption is invalid and consequently the initial approach, taking the quotient of the maximum force and the number of fibres, was maintained. It is noted that no relationship between the number of fibres within a given bundle and the average tensile strength of a fibre in the said bundle is identified, the two parameters are mutually exclusive.

The effect of co-solvents was investigated, using the reaction schedule presented in Chapter 3.3.4. The effects on the tensile strength with respect to the concentrations of ethanol [EtOH], 2-propanol [PrOH] and acetone [DMK] are presented in Figure 106, Figure 107 and Figure 108 respectively.

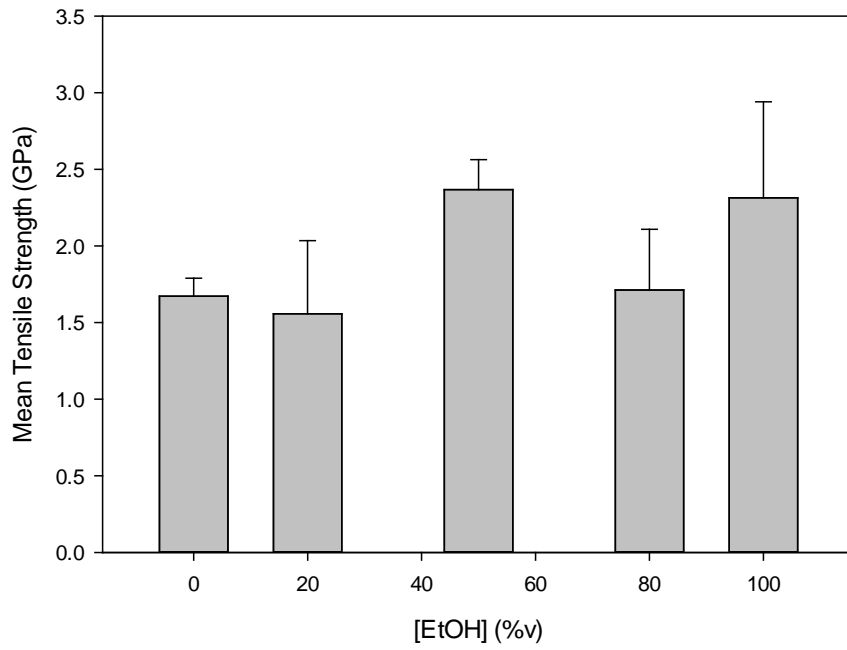


Figure 106: Effect of ethanol concentration [EtOH] on the mean tensile strength of carbon fibre (Toray T700S 50E); $T = 623$ K, $t_r = 30$ min

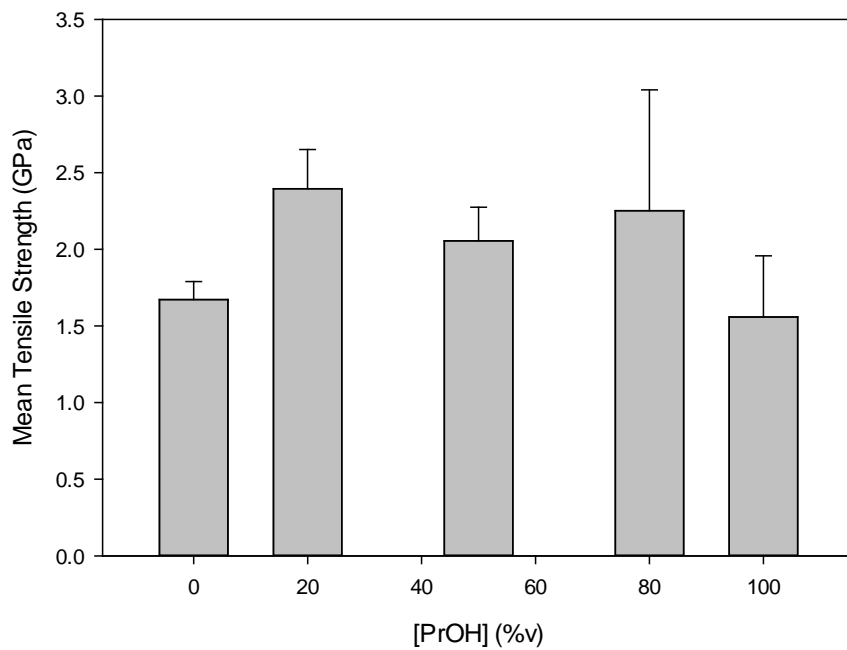


Figure 107: Effect of propanol concentration [PrOH] on the mean tensile strength of carbon fibre (Toray T700S 50E); $T = 623$ K, $t_r = 30$ min

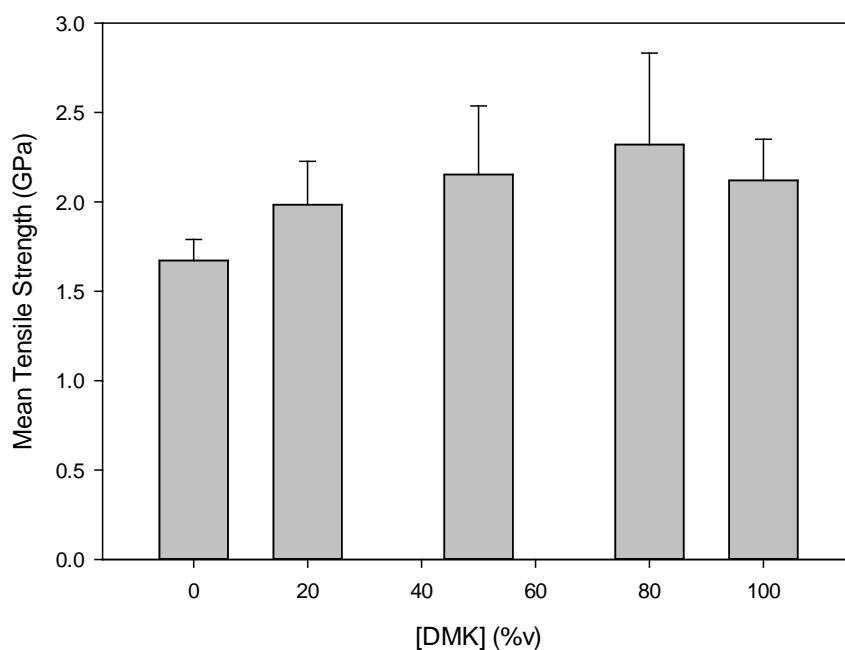


Figure 108: Effect of acetone concentration [DMK] on the mean tensile strength of carbon fibre (Toray T700S 50E); $T = 623$ K, $t_r = 30$ min

Carbon fibres processed in water ([co-solvent] = 0 %) at 623 K for 30 minutes are used as control samples shown in Figure 106 – Figure 108. Although data for virgin fibres were obtained, by definition, virgin fibres have not been exposed to the same temperature as the processed samples and therefore may respond differently to tensile testing. Using samples processed in water alone for the same period of time mitigates this potential source of error and presents only the effects of the co-solvents. By observation of Figure 106 – Figure 108, it is determined that the use of ethanol, propanol and acetone as co-solvents does not significantly degrade the tensile strength of carbon fibres. It is further identified that for the majority of cases where a co-solvent is used, the tensile strength of the fibres appears to be greater than when water is used alone. In some instances, the tensile strength of processed fibres exceed that observed when virgin fibres were tested, an effect that is not without precedent and is reported in the literature [304]. The tensile strength of virgin carbon fibres

is compared to that of the control samples, as well as fibres processed using a Cs_2CO_3 catalyst as shown in Figure 109.

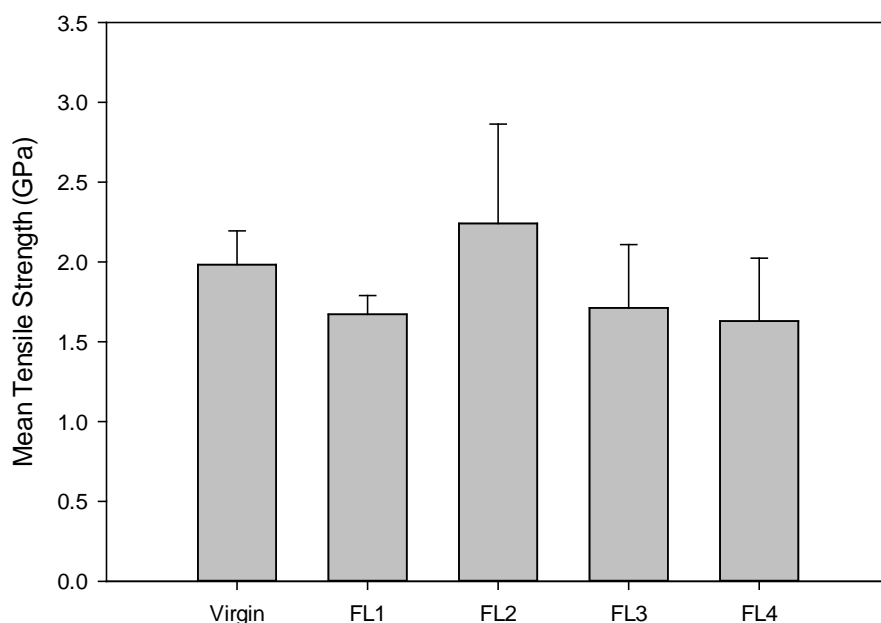


Figure 109: Effect of Cs_2CO_3 catalyst on the tensile strength of carbon fibres. $T = 623 \text{ K}$, $t_r = 30 \text{ min}$; FL1: H_2O ; FL2 H_2O , $[\text{Cs}_2\text{CO}_3] = 10 \text{ mg ml}^{-1}$; FL3: $[\text{EtOH}] = 80 \text{ \%v}$; FL4: $[\text{EtOH}] = 80 \text{ \%v}$, $[\text{Cs}_2\text{CO}_3] = 10 \text{ mg ml}^{-1}$

By inspection of Figure 109 it is possible to identify a slight reduction in the tensile strength of carbon fibres a result of exposure to water alone at 623 K (FL1). Contrary to expectation, the tensile strength appears to increase in the presence of Cs_2CO_3 when water is used without a co-solvent (FL2). By comparison, the use of 80 %v ethanol in the presence (FL3), or absence (FL4), of Cs_2CO_3 has a negligible impact on the tensile strength of the fibres. It was previously established that there is a strong synergistic relation between the co-solvent concentration and caesium carbonate concentration when considering the decomposition of both thermoplastic (Chapter 4.2) and thermoset resins (Chapter 5.1). It is thought that a

similar synergistic effect is responsible for the reduced tensile strength of fibres processed with both a co-solvent and catalyst (FL4), or co-solvent alone (FL3), in comparison to fibres processed with water and the catalyst (FL2). Insight into this synergy may begin with the understanding that FL3 and FL4 were conducted in supercritical fluid mixtures, whereas FL2 is in sub-critical water. Further investigation of this effect is recommended in order to confirm the inference stated.

6.2. EFFECTS OF RECYCLING ON CARBON FIBRE SIZING

During the manufacturing process of carbon fibres, a polymer sizing is applied to the surface of the fibres to facilitate good adhesion between the carbon fibres and the polymer matrix of a CFRP. A description of the manufacturing process of carbon fibres is provided in Chapter 2.4. The composition of the sizing is held in commercial confidence and is therefore not available in the public domain. It is likely that the composition of the sizing varies between manufacturers, although the fundamental principle is constant. Using X-Ray Photoelectron Spectroscopy (XPS) it is possible to analyse the surface of carbon fibres, with the intention of identifying functional groups. The purpose of this preliminary investigation is to identify changes, or lack thereof, to the functional groups on the surface of carbon fibres as a consequence of processing conditions, as opposed to the elucidation of the precise chemical structure of the sizing. The high-resolution spectra of carbon, oxygen, nitrogen and silicon obtained from virgin carbon fibres are presented in Figure 110, Figure 111, Figure 112 and Figure 113 respectively.

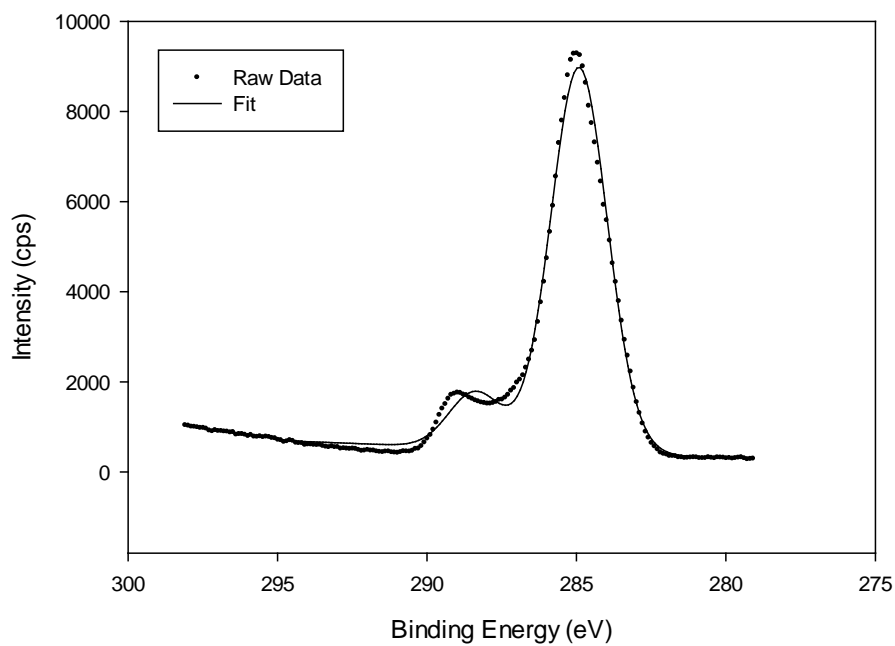


Figure 110: High-resolution XPS carbon spectrum of virgin carbon fibre, Toray T700S

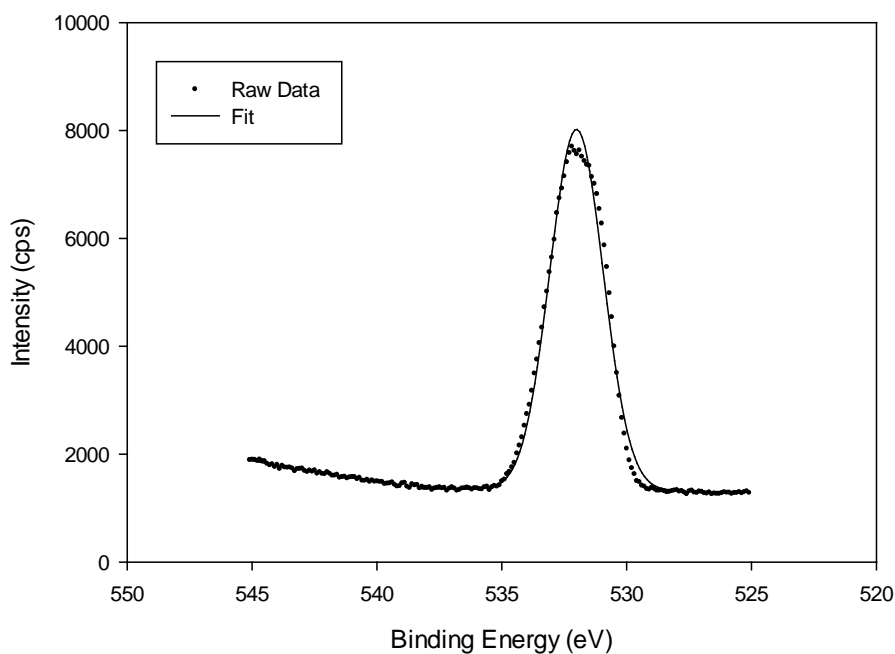


Figure 111: High-resolution XPS oxygen spectrum of virgin carbon fibre, Toray T700S

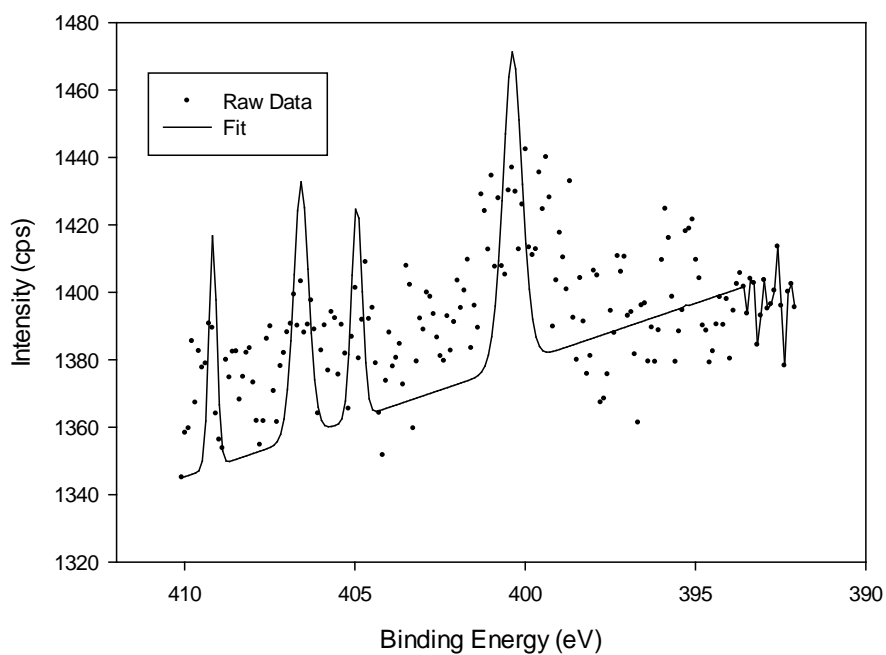


Figure 112: High-resolution XPS nitrogen spectrum of virgin carbon fibre, Toray T700S

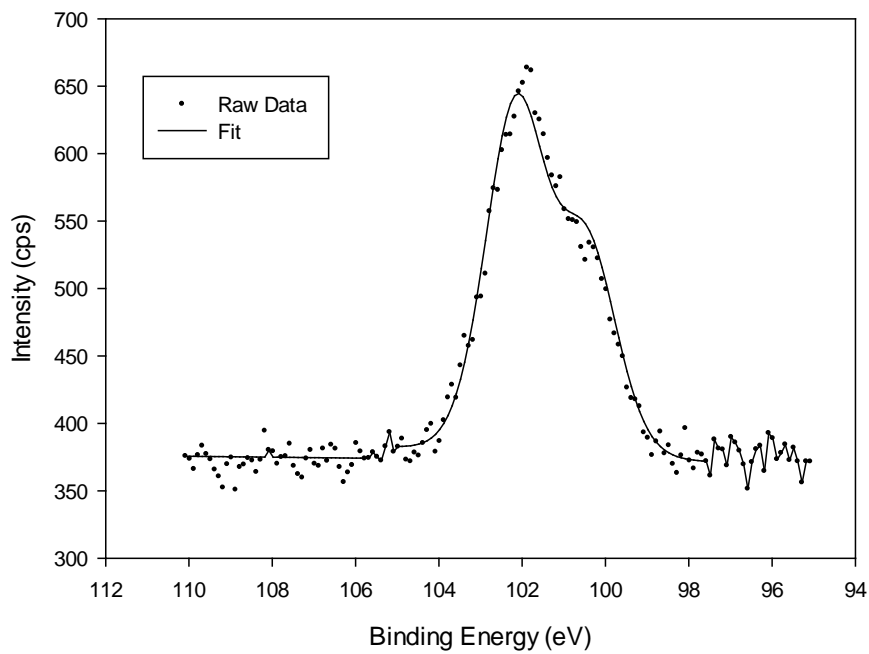


Figure 113: High-resolution XPS silicon spectrum of virgin carbon fibre, Toray T700S

By inspection of Figure 110 – Figure 113 it can be seen that on the surface of virgin carbon fibres there are 2 carbon species (Figure 110), a single oxygen species (Figure 111), essentially no nitrogen (indicated by the poor fit result, Figure 112) and 2 silicon species (Figure 113). The binding energy (BE) is specific to a chemical functional group or bond type. A selection of binding energies corresponding to specific functional groups is provided in Table 25.

Table 25: XPS binding energy of specific functional groups

| Element | Binding Energy (eV) | Functional Group |
|----------|---------------------|------------------------------|
| Carbon | 285 | C-C |
| | 288 | -C=O |
| Oxygen | 531.5 - 532 | -C-O |
| | 532.9 | SiO ₂ |
| Nitrogen | 400 | C-NH ₂ |
| | >405 | NO ₃ ⁻ |
| Silicon | 102 | Organic Si |
| | 99 | Elemental Si |

By comparison of Table 25 and Figure 110 it may be shown that the vast majority of the surface carbon atoms are bonded to other carbon atoms (BE = 285 eV), as to be expected for carbon fibres. The second peak (BE = 288 eV) corresponds to a carbonyl group thought to be part of the sizing. Figure 111 in conjunction with Table 25 shows that the single peak (BE = 532 eV) is attributable to the carbonyl functional group (-C-O). This is in support of the inference that the sizing contains the carbonyl functional group, potentially in 2 distinct species. Organic silicon is observed on the surface of virgin carbon fibres, Figure 113 and Table 25, whilst ethylamine and nitrates are not observed. The distribution of functional groups observed by XPS on the surface of virgin carbon fibres is given in Figure 114.

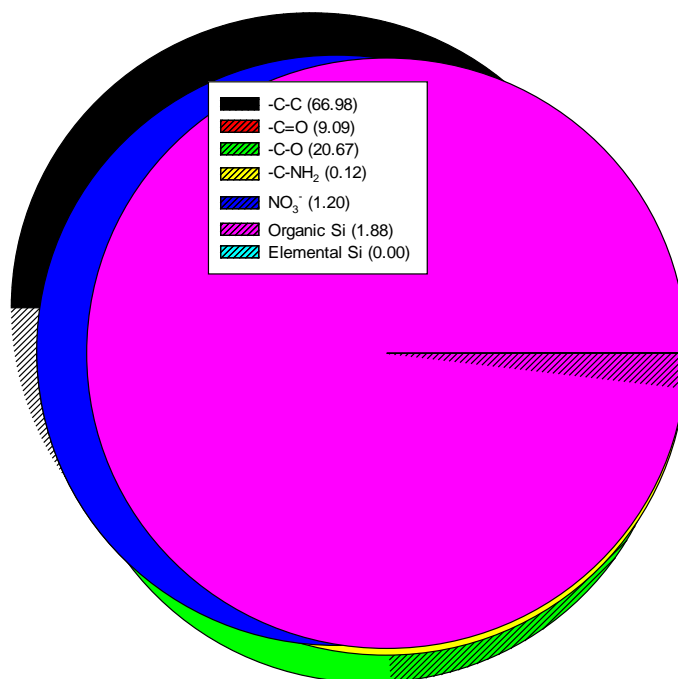


Figure 114: Functional group distribution on the surface of virgin carbon fibre, determined by XPS

By inspection of Figure 114 it is observed that 29.76 % of the surface is attributed to carbonyl functional groups with a small amount of nitrated functional groups also being identified. It is therefore suggested that the carbonyl functional group is a major component of the carbon fibre sizing. Using this postulation the surfaces of carbon fibres processed under differing conditions may be compared to that of virgin fibres to determine the impact on the sizing. The distribution of functional groups identified on the surface of carbon fibres processed for 30 minutes at 523 K in 80 %v ethanol, 20 %v water, is given in Figure 115.

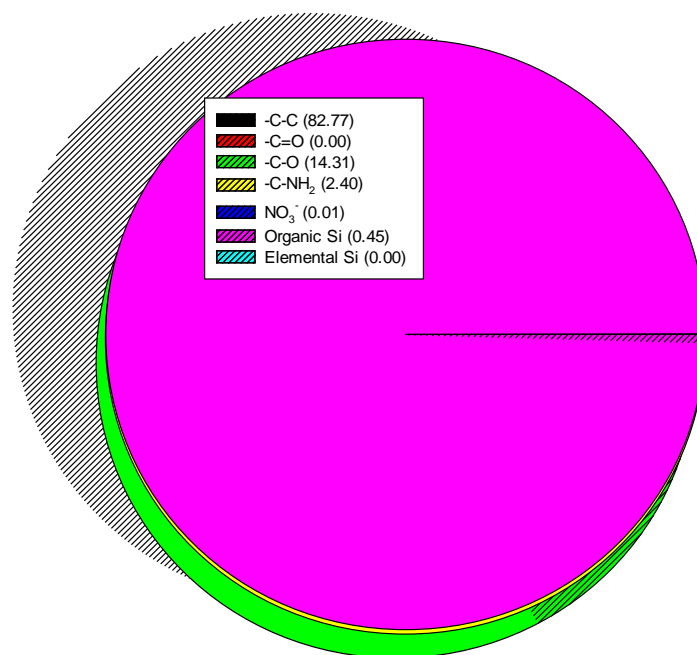


Figure 115: Functional group distribution on the surface of processed carbon fibres; $T = 523\text{ K}$, $t_r = 30\text{ min}$, $[\text{EtOH}] = 80\%v$, determined by XPS

By comparison of Figure 114 and Figure 115 it can be seen that the processing method has removed the $-\text{C}=\text{O}$ moiety and simultaneously reduced the concentration of $-\text{C}-\text{O}$ functional groups. It is further noticed that the relative concentration of amine groups has significantly increased from 0.12 % to 2.40 %. This effect is not specific to these conditions and is the observation for all samples analysed post-processing, as shown in Figure 116.

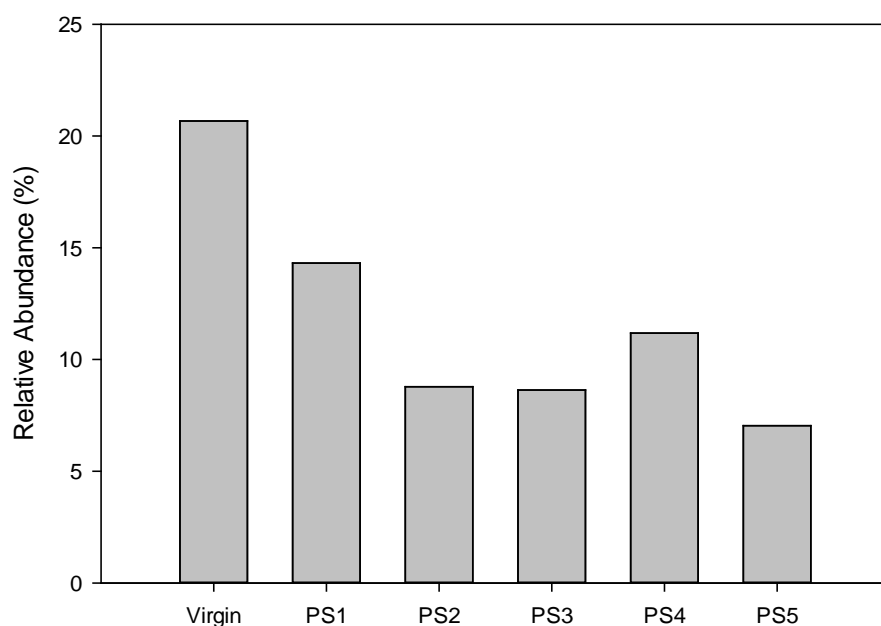


Figure 116: Relative abundance of carbonyl functional groups post-processing, determined by XPS; PS1, $T = 523\text{ K}$; PS2, PS3, PS4, $T = 573\text{ K}$; PS5, $T = 623\text{ K}$

By inspection of Figure 116, for which the reaction schedule is provided in Table 15, Chapter 3.3.4, it can be seen that the supercritical fluid processing conditions result in substantial removal of the sizing, which was determined to consist of carbonyl functional groups. It is notable that although PS5 (Figure 116) shows the greatest removal of the sizing this is not reflected in a reduced tensile strength (see Figure 106, [EtOH] = 50 %v). It is noteworthy that the greatest tensile strength recorded for the range of ethanol concentrations investigated (Figure 106). Without further experimental investigation it is not possible to determine whether there is significance, leading to the understanding of cause and effect, in the observation. The complete XPS functional group identification data are provided in Appendix 3.

Having established, to some extent, the effect of the thermochemical processing on the tensile strength of carbon fibres, as well as an investigation into the removal of sizing, the recycling of CFRP's was directly investigated.

CHAPTER 7. RESULTS PART D: RECYCLING OF CARBON FIBRE REINFORCED COMPOSITE MATERIALS

Owing to the limitation of time, a limited set of experiments were used to transfer the knowledge gained by investigating thermoset polymer degradation, and the effects the conditions have on carbon fibres, to the recycling of CFRP's. These preliminary data are intended to provide insight into the potential of this technique, and to lead the future direction of this research. The limited set of experiments is detailed in Table 17, Chapter 3.3.5.

A challenge arises in assessing the effectiveness of the reaction conditions when using commercially available CFRP's. Manufacturers often retain specific information about the composition of the resin and the mass fraction of carbon fibre used in the construction of CFRP's. Nonetheless, many modern composite materials take advantage of the mechanical properties exhibited by polyepoxide thermoset resins, in particular BADGE-based resins as detailed in Chapter 2.3. The decomposition of BADGE-based resins invariably leads to the production of phenol and consequently this was the target molecule for the analysis of this initial study, the results of which are presented in Table 26.

Table 26: Initial findings for the recycling of commercially available CFRP's

| Sample | T (K) | P (MPa) | t _r (min) | Solvent | [Cs ₂ CO ₃] (mg ml ⁻¹) | [comp] (mg ml ⁻¹) | [PhOH] (mg ml ⁻¹) |
|--------|----------|------------|-------------------------|---------|--|----------------------------------|----------------------------------|
| CS1 | 573 | 15.0 ± 0.2 | 60 | EtOH | 10 | 30.6 | 1.010 |
| CS2 | | | | | | 31.7 | 0.000 |
| CS3 | | | | | | 67.5 | 0.042 |

Table 26 shows that the phenol concentrations in the reactor extract were lower than what was observed with epoxy resin alone. For a resin concentration of approximately 30 mg ml⁻¹ the typical phenol concentration, recovered from the reactor, is approximately 2.5 mg ml⁻¹. With a composite concentration ([comp]) of 30 mg ml⁻¹ the concentration of recovered phenol was not expected to be 2.5 mg ml⁻¹, owing to the composite having a mass fraction of carbon fibres. Carbon fibre mass fractions in excess of 50 % are not uncommon [324], reducing the mass of resin and subsequently lower concentrations of phenol are to be expected. However, without obtaining such information it is not possible to speculate further as to the magnitude of reduction to be expected.

This fibre mass fraction does not account for the phenol concentration observed for CS3 (Table 26). The composite concentration is twice that of the epoxy resin loading used, despite this the phenol concentration is extremely low (0.042 mg ml⁻¹). It is possible that the resins used for CS2 and CS3 are not predominantly phenol based. To investigate this hypothesis TGA of the processed samples was conducted and is given in Figure 117.

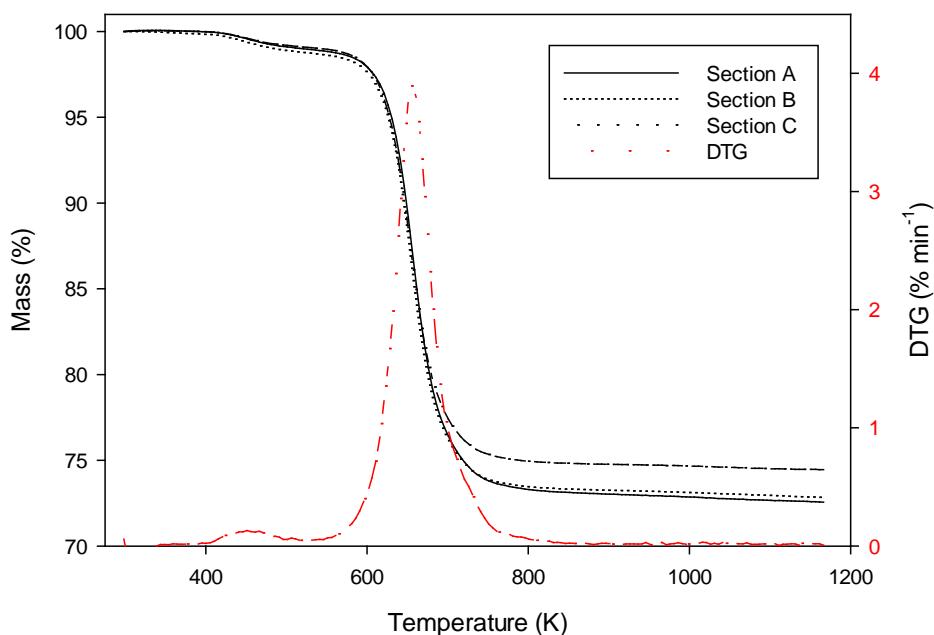


Figure 117: TGA thermograph of Hexcel CFRP's used in the manufacture of wing spas, post processing (Sample CS3); $T = 573$ K, $P = 15 \pm 0.2$ MPa, $t_r = 60$ min, $[EtOH] = 100\%$, $[Cs_2CO_3] = 10$ mg ml⁻¹, $[comp] = 67.5$ mg ml⁻¹

Figure 117 suggests that the fibre mass fraction is high, possibly greater than 70 %. It is also shown that significant quantities of resin remained within the CFRP after a reaction time of 60 minutes. This indicates that the resin used in the manufacture of this CFRP demonstrates greater resistance to the thermochemical processing than the BADGE based analogue. Due to the cross-sectional thickness of the sample it was necessary to separate the sample into three sections (A, B and C) for analysis by TGA. This constraint is due to the physical dimensions of the TGA pans. Separation into distinct sections is not possible pre-processing and impedes the use of TGA to directly determine the fibre mass fraction. SEM was used to analyse the surface of the CFRP (CS3) and is presented in Figure 118.

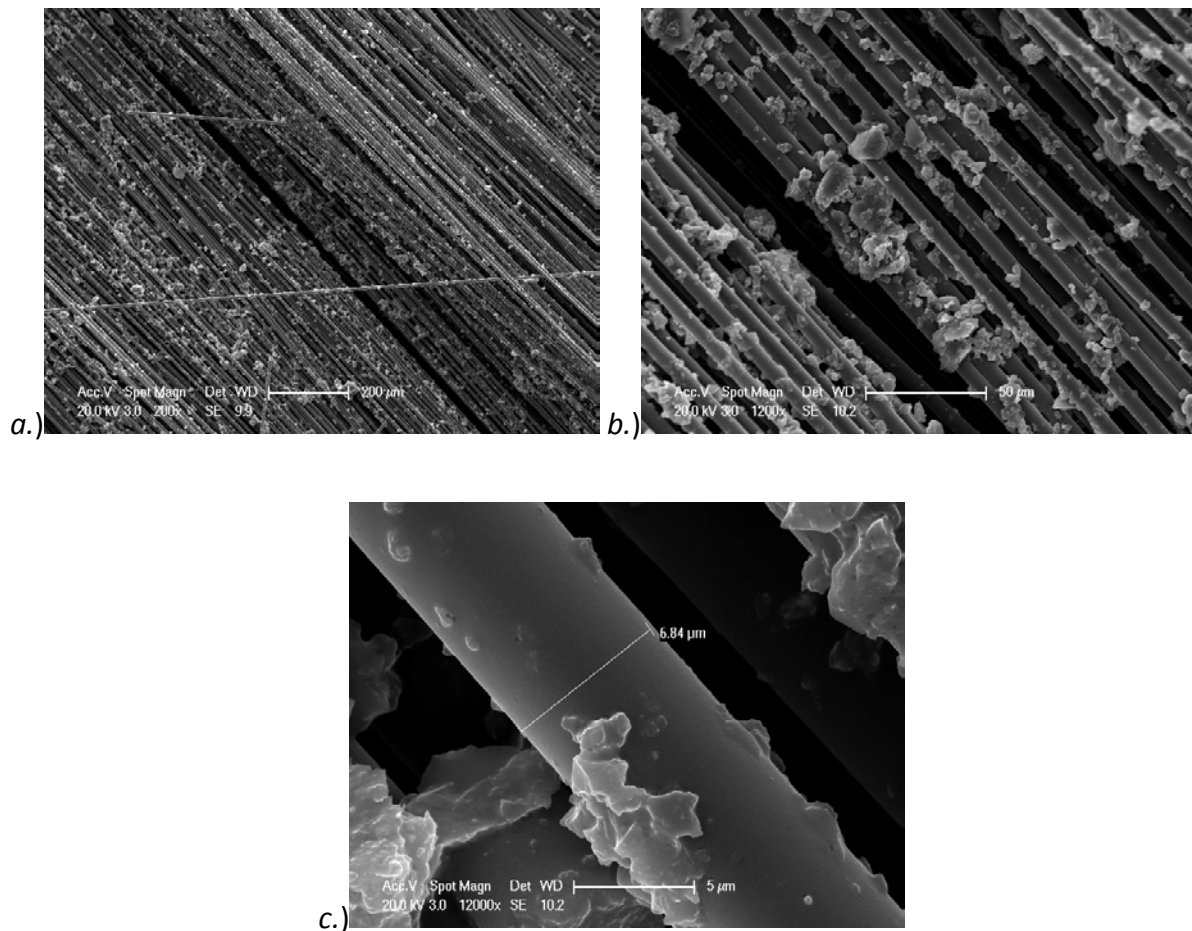


Figure 118: SEM micrographs of CFRP post processing (CS3); $T = 573 \text{ K}$, $t_r = 60 \text{ min}$, $P = 15.0 \pm 0.2 \text{ MPa}$, $[\text{EtOH}] = 100 \%$, $[\text{Cs}_2\text{CO}_3] = 10 \text{ mg ml}^{-1}$, $[\text{comp}] = 67.5 \text{ mg ml}^{-1}$

Inspection of Figure 118 shows that the resin was partially degraded from the composite, exposing relatively free fibres. The diameter of the carbon fibres within the sample were determined to be $6.84 \mu\text{m}$, typical of many commercially available fibres. There is an abundance of deposits visible on the fibres, believed to be polymeric in nature, although confirmation would be required in future experiments. It is thought likely that some of the partially degraded resin remained within the sample post-processing and gives rise to the initial mass loss identified on the DTG of the TGA thermograph (Figure 117). It has been demonstrated that the conditions necessary to decompose high-performance polymers differs according to their composition (cf. PEEK and BADGE epoxy resins). Further

experimentation with the solvent and catalyst concentrations is recommended in order to derive conditions conducive to the decomposition of CFRP's. It is further recommended that the principle parameter to vary is the reaction temperature, given that the evidence suggests that some decomposition of the resin has in fact taken place. There is also a requirement to devise a method for accurately determining the carbon fibre mass fraction as this is a requisite for calculating the resin loading of the reactor.

CHAPTER 8. CONCLUSIONS – THE PROCESSING AND RECYCLING OF HIGH PERFORMANCE MATERIALS FOR USE IN AEROSPACE AND RELATED INDUSTRIES

It has been demonstrated that supercritical fluids may be used to influence the polymer transition temperatures of high-performance thermoplastic polymers and their composite materials. An initial investigation, using supercritical carbon dioxide (scCO₂), revealed that as well as manipulating the polymer transitions, it is possible to confine gaseous CO₂ within the polymer matrix. The release of CO₂ from the polymer matrix was found to be temperature dependent, typically occurring at the glass transition and crystallisation temperatures. This was manifest as a mass loss observed by TGA, with FT-IR simultaneously performing analysis of carrier gas and thereby confirming the CO₂ confinement theory. This insight is particularly useful when considering recycling by thermochemical means as it demonstrates the possibility of entrapment of small organic molecules, such as decomposition products, within partially degraded resins. By processing with scCO₂ it is possible to induce crystallisation below the thermodynamic crystallisation temperature of PEEK, however, the induced crystallites are dissimilar to those spontaneously formed at the crystallisation temperature. High-Pressure Differential Scanning Calorimetry (HPDSC) was used to investigate the potential of supercritical fluids to reduce the melting temperature of PEEK. At present there is no evidence to substantiate this application, although there is a complex relationship between the use of CO₂ and the melting temperature due to induced crystallisation.

Upon exposure to temperatures beyond its continuous use temperature for extended periods of time, PEEK undergoes radical formation and subsequent cross-linking, leading to the degradation in physical properties. Cross-links are not destroyed during melt processing and consequently impeded the polymer's ability to be quenched into the amorphous state. The incorporation of reinforcing fibres, forming a composite material, inhibits melt processing due to concerns over the lack of fibre alignment control. Moreover, melt processing does not remove contaminants from the polymer matrix. It has been shown that the application of supercritical fluid mixtures, either ethanol or propanol and water, may be used to decompose PEEK at 623 K within 30 minutes when used with a caesium carbonate (Cs_2CO_3) catalyst. Effects of the co-solvent concentration, catalyst concentration and reaction time are presented. The decomposition reaction is found to be 1st order with respect to the Cs_2CO_3 concentration, the optimum reaction time being 30 minutes. The optimum co-solvent concentration is dependent upon the solvent and was found to be 20 %v for ethanol and water mixtures. Analysis of the decomposition products was carried out by High-Performance Liquid Chromatography (HPLC), Gas Chromatography Mass Spectrometry (GC-MS), Fourier Transform Infra-Red Spectroscopy (FT-IR), Differential Scanning Calorimetry (DSC), Scanning Electron Microscopy Energy Dispersive X-Ray Spectroscopy (SEM-EDX) and Thermogravimetric Analysis (TGA).

Variation of the co-solvent concentration allows for the decomposition of a 2,2-Bis[4-(glycidyoxy)phenyl]propane (BADGE) based high-performance thermoset resin, cross-linked with 4,4'-diaminodiphenyl sulfone (DDS). This particular resin is analogous to resins used to produce carbon fibre reinforced polymers (CFRP's) and was synthesised as part of this

research for this reason. Degradation of approximately 90 % of the polymer mass is possible within 45 minutes at 573 K, using either 100 %v ethanol or propanol, in conjunction with 10 mg ml⁻¹ of Cs₂CO₃. Similarly to PEEK, the decomposition reaction was found to be 1st order with respect to the catalyst concentration. The decomposition products were analysed by HPLC, GC-MS, SEM-EDX, TGA, DSC and FT-IR. By investigating the decomposition of the BADGE-based resin as a function of time, using SEM-EDX, it has been possible to describe the physical decomposition process. The process consists of 4 principle stages, adsorption, swelling / blistering and fragmentation. Whilst it has been shown that 90 % of the polymeric mass is decomposed within 45 minutes under reaction conditions using either 100 %v ethanol or 100 %v propanol, the decomposition process is solvent specific and governs the size and geometry of the solid decomposition products produced. The Cs₂CO₃ used is also identifiable by SEM-EDX, providing confirmation that it is not consumed as part of the reaction process and does in fact act as a catalyst. With additional analysis by TGA it has been demonstrated that short reaction times may lead to an increase in the sample mass, a process that was subsequently determined to be a consequence of a reaction between the alcohol and the polymer matrix. Analysis by HPLC and GC-MS showed that phenol is the major product of the decomposition of the BADGE-based resin, consistent with literature sources.

The effects of supercritical fluid processing on the physical properties of carbon fibres was investigated using a Universal Testing Machine (UTM). Using a method for determining the number of carbon fibres within a bundle, developed as part of this research, it was possible to perform tensile testing of carbon fibre bundles as opposed to single fibres. Development

of a fibre alignment process is required to further advance this work. The initial results indicate that the thermochemical processing has little impact on the tensile strength. Surface analysis using X-Ray Photoelectron Spectrometry (XPS) showed that exposure to supercritical fluids removes a substantial proportion of the carbon fibre sizing, which may prove decisive when considering the reuse of recycled carbon fibres. Although the impact on the physical properties of the fibres is minimal, it is thought that the removal of the carbon fibres sizing may have a significant impact on the adhesion of the polymer matrix. Reduced fibre / matrix bonding leads to the production of composite materials with reduced physical properties and is therefore an undesired side-effect. An initial data set for the recycling of commercially available CFRP's is presented, essentially demonstrating that the conditions developed are effective in decomposing CFRP's obtained from sports equipment, with further development work required to process aerospace components.

Future Work

It is recommended that the future direction of this work should consider;

1. The development of an effective carbon fibre alignment process or technology
 2. Further optimisation of the reaction temperature to recycle aerospace grade CFRP's
 3. A combined process to recycle high-performance thermoplastic and thermoset composite materials
 4. Life Cycle Analysis (LCA) of the thermochemical processes developed
-
1. The alignment of carbon fibres is trivial for single fibres and is an important consideration when performing tensile tests to ensure that forces are applied evenly

across the cross-sectional area of the fibre. The alignment of bundles of carbon fibres has not been achieved to date and is likely to remain a challenge to the testing of carbon fibre bundles whilst the recycling industry is in its infancy. Fibre alignment may also be important when considering the manufacturing of composite materials from recycled carbon fibres, given that the composite material's strength is dependent on the fibre orientation.

2. The reaction conditions developed through this research are demonstrated to be effective in the decomposition of a high-performance thermoplastic and high-performance thermoset resin. The decomposition of a commercially available CFRP has also been performed. However, in the case of the aerospace grade CFRP tested, it was found that the decomposition was less substantial. It is possible that an increase in temperature would significantly increase the rate and extent of the decomposition.
3. Both PEEK and polyepoxide resins are routinely reinforced with carbon fibres, enhancing the physical properties. The major decomposition product of both resins is phenol and the decomposition of both resins was found to be 1st order with respect to the caesium carbonate concentration. The decomposition of PEEK proceeds most efficiently in mixtures of alcohol and water, whereas the decomposition of the BADGE-based resin required 100 % alcohol. It is conceivable that a system comprising of 100 % R-OH, 10 mg ml⁻¹ Cs₂CO₃ at 573 K could be used to initially decompose a BADGE-based thermoset resin, before injecting water

(containing $10 \text{ mg ml}^{-1} \text{ Cs}_2\text{CO}_3$) to achieve a mixture of 20 %v R-OH, 80 %v H₂O and increasing the temperature to 623 K to decompose PEEK. In doing so, the comprehensive decomposition of a mixed waste stream of both thermoplastic and thermoset polymers may be processed.

4. A comprehensive LCA of the thermochemical process developed in the research is highly recommended. This would allow the environmental impacts to be assessed in context and may influence process parameters and operating conditions. Whilst this research has been carried out on a laboratory scale, a comprehensive LCA may highlight potential challenges or opportunities that may not be realised until pilot scale.

By addressing the development proposal outlined it is thought to be possible to satisfy the conditions necessary to consider the scale-up of this process, providing a pilot plant design for the investigation of industrial considerations. It is hoped that this fundamental research goes some way to addressing the present and future concerns over the use and disposal of high-performance carbon fibre reinforced composite materials.

LIST OF REFERENCES

1. Nielsen, R.P., *Chapter 5 - Near- and Supercritical Water*, in *Chemistry of Advanced Environmental Purification Processes of Water*, E.G. Sørensen, Editor. 2014, Elsevier: Amsterdam. p. 171-197.
2. Postorino, P., et al., *The interatomic structure of water at supercritical temperatures*. *Nature*, 1993. **366**(6456): p. 668-670.
3. Wagner, W. and A. Prüss, *The IAPWS formulation 1995 for the thermodynamic properties of ordinary water substance for general and scientific use*. *Journal of Physical and Chemical Reference Data*, 2002. **31**(2): p. 387-535.
4. Kirkham, M.B., *Chapter 3 - Structure and Properties of Water*, in *Principles of Soil and Plant Water Relations (Second Edition)*, M.B. Kirkham, Editor. 2014, Academic Press: Boston. p. 27-40.
5. Zhao, L.-C., et al., *A catalyst-free novel synthesis of diethyl carbonate from ethyl carbamate in supercritical ethanol*. *Chinese Chemical Letters*, 2014. **25**(10): p. 1395-1398.
6. Kamitanaka, T., T. Matsuda, and T. Harada, *Mechanism for the reduction of ketones to the corresponding alcohols using supercritical 2-propanol*. *Tetrahedron*, 2007. **63**(6): p. 1429-1434.
7. Sun, Y., et al., *Optimization of high-energy density biodiesel production from camelina sativa oil under supercritical 1-butanol conditions*. *Fuel*, 2014. **135**(0): p. 522-529.
8. Jin, J., et al., *Determination and calculation of solubility of bisphenol A in supercritical carbon dioxide*. *Chemical Engineering Research and Design*, 2013. **91**(1): p. 158-164.
9. Kendall, J.L., et al., *Polymerizations in supercritical carbon dioxide*. *Chemical Reviews*, 1999. **99**(2): p. 543-564.
10. Fleming, O.S. and S.G. Kazarian, *Polymer Processing with Supercritical Fluids*, in *Supercritical Carbon Dioxide*. 2006, Wiley-VCH Verlag GmbH & Co. KGaA. p. 205-238.
11. Iwai, Y., T. Nakashima, and S. Yonezawa, *Preparation of dye sensitized solar cell by using supercritical carbon dioxide drying*. *The Journal of Supercritical Fluids*, 2013. **77**(0): p. 153-157.
12. Brown, Z.K., et al., *Drying of agar gels using supercritical carbon dioxide*. *The Journal of Supercritical Fluids*, 2010. **54**(1): p. 89-95.
13. Almeida-Rivera, C., et al., *Mathematical description of mass transfer in supercritical-carbon-dioxide-drying processes*, in *Computer Aided Chemical Engineering*, M.C.G. E.N. Pistikopoulos and A.C. Kokossis, Editors. 2011, Elsevier. p. 36-40.
14. Brown, Z.K., et al., *Drying of foods using supercritical carbon dioxide — Investigations with carrot*. *Innovative Food Science & Emerging Technologies*, 2008. **9**(3): p. 280-289.
15. Lee, M.Y., et al., *Surfactant-aided supercritical carbon dioxide drying for photoresists to prevent pattern collapse*. *The Journal of Supercritical Fluids*, 2007. **42**(1): p. 150-156.
16. Shao, Q., et al., *Essential oils extraction from *Anoectochilus roxburghii* using supercritical carbon dioxide and their antioxidant activity*. *Industrial Crops and Products*, 2014. **60**(0): p. 104-112.
17. Ni, H., et al., *Supercritical carbon dioxide extraction of petroleum on kieselguhr*. *Fuel*, 2015. **141**(0): p. 74-81.

18. Taher, H., et al., *Supercritical carbon dioxide extraction of microalgae lipid: Process optimization and laboratory scale-up*. The Journal of Supercritical Fluids, 2014. **86**(0): p. 57-66.
19. De Zordi, N., et al., *The supercritical carbon dioxide extraction of polyphenols from Propolis: A central composite design approach*. The Journal of Supercritical Fluids, 2014. **95**(0): p. 491-498.
20. İçen, H. and M. Gürü, *Effect of ethanol content on supercritical carbon dioxide extraction of caffeine from tea stalk and fiber wastes*. The Journal of Supercritical Fluids, 2010. **55**(1): p. 156-160.
21. Wood, C.D., et al., *Chapter 21 - Supercritical Carbon Dioxide as a Green Solvent for Polymer Synthesis*, in *Thermodynamics, Solubility and Environmental Issues*, T.M. Letcher, Editor. 2007, Elsevier: Amsterdam. p. 383-396.
22. Tan, B. and A.I. Cooper, *Functional Oligo(vinyl acetate) CO₂-philes for Solubilization and Emulsification*. Journal of the American Chemical Society, 2005. **127**(25): p. 8938-8939.
23. Wang, D., et al., *Effect of supercritical carbon dioxide on the crystallization behavior of poly(ether ether ketone)*. Journal of Polymer Science Part B: Polymer Physics, 2007. **45**(21): p. 2927-2936.
24. Liu, T., et al., *Manipulation of polymer foam structure based on CO₂-induced changes in polymer fundamental properties*. Particuology, 2010. **8**(6): p. 607-612.
25. Forest, C., et al., *Polymer nano-foams for insulating applications prepared from CO₂ foaming*. Progress in Polymer Science, (0).
26. Wang, D., et al., *Diffusion and swelling of carbon dioxide in amorphous poly(ether ether ketone)s*. Journal of Membrane Science, 2006. **281**(1-2): p. 203-210.
27. Bologna, S., D.R. G, and G. Spagnoli, *Sorption / Desorption Of Carbon Dioxide Into Amorphous And Semicrystalline Peek Films*. p. 1-6.
28. Scholz, M.S., et al., *The use of composite materials in modern orthopaedic medicine and prosthetic devices: A review*. Composites Science and Technology, 2011. **71**(16): p. 1791-1803.
29. Bijwe, J., et al., *Exploration of potential of solid lubricants and short fibers in Polyetherketone (PEK) composites*. Wear, 2013. **301**(1-2): p. 810-819.
30. Kewekordes, T., S. Wille, and M. Kern, *Wear of polyetherketoneketone (PEKK) caused by different antagonists*. Dental Materials, 2014. **30**, **Supplement 1**(0): p. e77.
31. Liu, T., et al., *Isothermal melt and cold crystallization kinetics of poly(aryl ether ether ketone ketone) (PEEKK)*. European Polymer Journal, 1997. **33**(9): p. 1405-1414.
32. Ramani, K., W.J. Weidner, and G. Kumar, *Silicon sputtering as a surface treatment to titanium alloy for bonding with PEKEKK*. International Journal of Adhesion and Adhesives, 1998. **18**(6): p. 401-412.
33. Toth, J.M., et al., *Polyetheretherketone as a biomaterial for spinal applications*. Biomaterials, 2006. **27**(3): p. 324-334.
34. Katzer, A., et al., *Polyetheretherketone—cytotoxicity and mutagenicity in vitro*. Biomaterials, 2002. **23**(8): p. 1749-1759.
35. Sagomonyants, K.B., et al., *The in vitro response of human osteoblasts to polyetheretherketone (PEEK) substrates compared to commercially pure titanium*. Biomaterials, 2008. **29**(11): p. 1563-1572.

36. Morrison, C., et al., *In vitro biocompatibility testing of polymers for orthopaedic implants using cultured fibroblasts and osteoblasts*. *Biomaterials*, 1995. **16**(13): p. 987-992.
37. Han, C.-M., et al., *The electron beam deposition of titanium on polyetheretherketone (PEEK) and the resulting enhanced biological properties*. *Biomaterials*, 2010. **31**(13): p. 3465-3470.
38. Scotchford, C.A., et al., *Use of a novel carbon fibre composite material for the femoral stem component of a THR system: in vitro biological assessment*. *Biomaterials*, 2003. **24**(26): p. 4871-4879.
39. Godara, A., D. Raabe, and S. Green, *The influence of sterilization processes on the micromechanical properties of carbon fiber-reinforced PEEK composites for bone implant applications*. *Acta Biomater*, 2007. **3**(2): p. 209-20.
40. Ma, R. and T. Tang, *Current Strategies to Improve the Bioactivity of PEEK*. *International Journal of Molecular Sciences*, 2014. **15**(4): p. 5426-5445.
41. Moskalewicz, T., S. Seuss, and A.R. Boccaccini, *Microstructure and properties of composite polyetheretherketone/Bioglass® coatings deposited on Ti-6Al-7Nb alloy for medical applications*. *Applied Surface Science*, 2013. **273**: p. 62-67.
42. Ramakrishna, S., et al., *Biomedical applications of polymer-composite materials: a review*. *Composites Science and Technology*, 2001. **61**(9): p. 1189-1224.
43. Kurtz, S.M. and J.N. Devine, *PEEK biomaterials in trauma, orthopedic, and spinal implants*. *Biomaterials*, 2007. **28**(32): p. 4845-69.
44. Parsons, A.J., et al., *Mimicking Bone Structure and Function with Structural Composite Materials*. *Journal of Bionic Engineering*, 2010. **7**, **Supplement**(0): p. S1-S10.
45. Li, J., H. Liao, and C. Coddet, *Friction and wear behavior of flame-sprayed PEEK coatings*. *Wear*, 2002. **252**(9-10): p. 824-831.
46. Zhang, G., et al., *Investigation of friction and wear behaviour of SiC-filled PEEK coating using artificial neural network*. *Surface and Coatings Technology*, 2006. **200**(8): p. 2610-2617.
47. Zhang, G., et al., *On dry sliding friction and wear behaviour of PEEK and PEEK/SiC-composite coatings*. *Wear*, 2006. **260**(6): p. 594-600.
48. Jones, D.P., D.C. Leach, and D.R. Moore, *Mechanical properties of poly(ether-etherketone) for engineering applications*. *Polymer*, 1985. **26**(9): p. 1385-1393.
49. Small, G., *Outstanding physical properties make PEEK ideal for sealing applications*. *Sealing Technology*, 2014. **2014**(4): p. 9-12.
50. Lai, Y.H., et al., *On the PEEK composites reinforced by surface-modified nano-silica*. *Materials Science and Engineering: A*, 2007. **458**(1-2): p. 158-169.
51. Mohiuddin, M. and S.V. Hoa, *Estimation of contact resistance and its effect on electrical conductivity of CNT/PEEK composites*. *Composites Science and Technology*, 2013. **79**(0): p. 42-48.
52. Chen, J., et al., *Structures and Mechanical Properties of PEEK/PEI/PES Plastics Alloys Blent by Extrusion Molding Used for Cable Insulating Jacketing*. *Procedia Engineering*, 2012. **36**(0): p. 96-104.
53. Chen, J., et al., *Research on Friction and Wear Behaviors of PEEK/PEI/PES Plastics Alloys under Sliding Contact Condition*. *Procedia Engineering*, 2012. **36**(0): p. 285-291.

54. Díez-Pascual, A.M., et al., *Influence of carbon nanotubes on the thermal, electrical and mechanical properties of poly(ether ether ketone)/glass fiber laminates*. Carbon, 2011. **49**(8): p. 2817-2833.
55. Mohiuddin, M. and S.V. Hoa, *Temperature dependent electrical conductivity of CNT-PEEK composites*. Composites Science and Technology, 2011. **72**(1): p. 21-27.
56. Shirakawa, H., et al., *Synthesis of electrically conducting organic polymers: halogen derivatives of polyacetylene, (CH)_x*. Journal of the Chemical Society, Chemical Communications, 1977(16): p. 578-578.
57. Li, C. and G. Shi, *Synthesis and electrochemical applications of the composites of conducting polymers and chemically converted graphene*. Electrochimica Acta, 2011. **56**(28): p. 10737-10743.
58. Riaz, U., C. Nwaoha, and S.M. Ashraf, *Recent advances in corrosion protective composite coatings based on conducting polymers and natural resource derived polymers*. Progress in Organic Coatings, 2014. **77**(4): p. 743-756.
59. Barra, G.M.O., S.L. Mireski, and A.T.N. Pires, *Preparation and Characterization of Poly(Ether Ether Ketone) Derivatives*. 2008. **19**(1): p. 111-116.
60. Henneuse-Boxus, C., et al., *Surface amination of PEEK film by selective wet-chemistry*. Polymer, 1998. **39**(22): p. 5359-5369.
61. Henneuse-Boxus, C., et al., *Covalent attachment of fluorescence probes on the PEEK-OH film surface*. Polymer, 2000. **41**(7): p. 2339-2348.
62. Díez-Pascual, A.M., G. Martínez, and M.A. Gómez, *Synthesis and Characterization of Poly(ether ether ketone) Derivatives Obtained by Carbonyl Reduction*. Macromolecules, 2009. **42**(18): p. 6885-6892.
63. Shibata, M., J. Cao, and R. Yosomiya, *Synthesis and properties of the block copolymers of poly(ether ether ketone) and the poly(aryl ether sulfone) containing biphenylene moiety*. Polymer, 1997. **38**(12): p. 3103-3108.
64. Cao, J., et al., *Crystallization behaviour of poly(ether ether ketone)/poly(ether sulfone) block copolymer*. Polymer, 1996. **37**(20): p. 4579-4584.
65. Gao, C., et al., *Synthesis of poly(ether ether ketone)-block-polyimide copolymer and its compatibilization for poly(ether ether ketone)/thermoplastic polyimide blends*. Polymer, 2014. **55**(1): p. 119-125.
66. Shan, J., et al., *Sulfonated polyether ether ketone (PEEK-WC)/phosphotungstic acid composite: Preparation and characterization of the fuel cell membranes*, in *Pure and Applied Chemistry*. 2006. p. 1781.
67. Chae, K.-J., et al., *Sulfonated polyether ether ketone (SPEEK)-based composite proton exchange membrane reinforced with nanofibers for microbial electrolysis cells*. Chemical Engineering Journal, 2014. **254**(0): p. 393-398.
68. Ismail, A.F., N.H. Othman, and A. Mustafa, *Sulfonated polyether ether ketone composite membrane using tungstosilicic acid supported on silica-aluminium oxide for direct methanol fuel cell (DMFC)*. Journal of Membrane Science, 2009. **329**(1-2): p. 18-29.
69. Colicchio, I., et al., *Sulfonated poly(ether ether ketone)-silica membranes doped with phosphotungstic acid. Morphology and proton conductivity*. Journal of Membrane Science, 2009. **326**(1): p. 45-57.
70. Wu, T., et al., *Novel copoly(ether ether ketone)s with pendant phenyl groups: synthesis and characterization*. Polymer International, 2011: p. n/a-n/a.

71. Zhang, Z. and H. Zeng, *The branching characteristic of the spherulites of poly(ether ether ketone)*. *Polymer*, 1993. **34**(7): p. 1551-1553.
72. Jonas, A. and R. Legras, *Thermal stability and crystallization of poly(aryl ether ether ketone)*. *Polymer*, 1991. **32**(15): p. 2691-2706.
73. Chen, H.-L. and R.S. Porter, *Observation of two-stage crystallization of poly(ether ether ketone) by thermal mechanical analysis*. *Polymer*, 1993. **34**(21): p. 4576-4578.
74. McLauchlin, A.R., O.R. Ghita, and L. Savage, *Studies on the reprocessability of poly(ether ether ketone) (PEEK)*. *Journal of Materials Processing Technology*, 2014. **214**(1): p. 75-80.
75. Bassett, D.C., R.H. Olley, and I.A.M. Al Raheil, *On crystallization phenomena in PEEK*. *Polymer*, 1988. **29**(10): p. 1745-1754.
76. Yuan, M., et al., *Influence of molecular weight on rheological, thermal, and mechanical properties of PEEK*. *Polymer Engineering & Science*, 2011. **51**(1): p. 94-102.
77. Kariduraganavar, M.Y., A.A. Kittur, and R.R. Kamble, *Chapter 1 - Polymer Synthesis and Processing*, in *Natural and Synthetic Biomedical Polymers*, S.G.K.T.L. Deng, Editor. 2014, Elsevier: Oxford. p. 1-31.
78. Leeke, G.A., J. Cai, and M. Jenkins, *Solubility of Supercritical Carbon Dioxide in Polycaprolactone (CAPA 6800) at 313 and 333 K*. *Journal of Chemical & Engineering Data*, 2006. **51**(5): p. 1877-1879.
79. Yang, J., et al., *Probing structure–heterogeneous nucleation efficiency relationship of mesoporous particles in polylactic acid microcellular foaming by supercritical carbon dioxide*. *The Journal of Supercritical Fluids*, 2014. **95**(0): p. 228-235.
80. Nofar, M. and C.B. Park, *Poly (lactic acid) foaming*. *Progress in Polymer Science*, 2014. **39**(10): p. 1721-1741.
81. Corre, Y.-M., et al., *Batch foaming of chain extended PLA with supercritical CO₂: Influence of the rheological properties and the process parameters on the cellular structure*. *The Journal of Supercritical Fluids*, 2011. **58**(1): p. 177-188.
82. Salerno, A., et al., *Solid-state supercritical CO₂ foaming of PCL and PCL-HA nano-composite: Effect of composition, thermal history and foaming process on foam pore structure*. *The Journal of Supercritical Fluids*, 2011. **58**(1): p. 158-167.
83. Salerno, A., et al., *Novel 3D porous multi-phase composite scaffolds based on PCL, thermoplastic zein and ha prepared via supercritical CO₂ foaming for bone regeneration*. *Composites Science and Technology*, 2010. **70**(13): p. 1838-1846.
84. Gao, S.-L. and J.-K. Kim, *Cooling rate influences in carbon fibre/PEEK composites. Part 1. Crystallinity and interface adhesion*. *Composites Part A: Applied Science and Manufacturing*, 2000. **31**(6): p. 517-530.
85. Blundell, D.J. and B.N. Osborn, *The morphology of poly(aryl-ether-ether-ketone)*. *Polymer*, 1983. **24**(8): p. 953-958.
86. Handa, Y.P., S. Capowski, and M. O'Neill, *Compressed-gas-induced plasticization of polymers*. *Thermochimica Acta*, 1993. **226**(0): p. 177-185.
87. Handa, Y.P., J. Roovers, and F. Wang, *Effect of Thermal Annealing and Supercritical Fluids on the Crystallization Behavior of Methyl-Substituted Poly(aryl ether ether ketone)*. *Macromolecules*, 1994. **27**(19): p. 5511-5516.
88. Handa, Y.P., Z. Zhang, and J. Roovers, *Compressed-gas-induced crystallization in tert-butyl poly(ether ether ketone)*. *Journal of Polymer Science Part B: Polymer Physics*, 2001. **39**(13): p. 1505-1512.

89. Nemoto, T., J. Takagi, and M. Ohshima, *Nanocellular foams—cell structure difference between immiscible and miscible PEEK/PEI polymer blends*. *Polymer Engineering & Science*, 2010. **50**(12): p. 2408-2416.
90. Normand, B., et al., *Electrochemical impedance spectroscopy and dielectric properties of polymer: application to PEEK thermally sprayed coating*. *Electrochimica Acta*, 2004. **49**(17-18): p. 2981-2986.
91. Kang, P.H., C. Lee, and K.Y. Kim, *Radiation and thermal effects on the dielectric relaxation properties of PEEK*. *Journal of Industrial and Engineering Chemistry - Seoul*, 2007. **13**(2): p. 250.
92. Boinard, E., R.A. Pethrick, and C.J. MacFarlane, *The influence of thermal history on the dynamic mechanical and dielectric studies of polyetheretherketone exposed to water and brine*. *Polymer*, 2000. **41**(3): p. 1063-1076.
93. Middleton, J., et al., *Aging of a polymer core composite conductor: Mechanical properties and residual stresses*. *Composites Part A: Applied Science and Manufacturing*, 2015. **69**(0): p. 159-167.
94. Minaev, V.S., et al., *The polymer–polymorphoid nature of glass aging*. *Journal of Non-Crystalline Solids*, 2014. **404**(0): p. 174-181.
95. Mahomed, A., *Ageing processes of biomedical polymers in the body*, in *Durability and Reliability of Medical Polymers*, M. Jenkins and A. Stamboulis, Editors. 2012, Woodhead Publishing. p. 164-182.
96. Aref-Azar, A., et al., *The effect of physical ageing on the properties of poly(ethylene terephthalate)*. *Polymer*, 1983. **24**(10): p. 1245-1251.
97. Sınmazçelik, T. and T. Yılmaz, *Thermal aging effects on mechanical and tribological performance of PEEK and short fiber reinforced PEEK composites*. *Materials & Design*, 2007. **28**(2): p. 641-648.
98. Hou, T. and H. Chen, *Isothermal physical aging of PEEK and PPS investigated by fractional Maxwell model*. *Polymer*, 2012. **53**(12): p. 2509-2518.
99. Kern, M. and F. Lehmann, *Influence of surface conditioning on bonding to polyetheretherketone (PEEK)*. *Dental Materials*, 2012. **28**(12): p. 1280-1283.
100. D'Aniello, C., et al., *Influence of time and temperature on deformed films of poly ether-ether-ketone (PEEK)*. *European Polymer Journal*, 2000. **36**(8): p. 1571-1577.
101. Brennan, W.J., et al., *Investigation of the ageing of plasma oxidized PEEK*. *Polymer*, 1991. **32**(8): p. 1527-1530.
102. Schambron, T., A. Lowe, and H.V. McGregor, *Effects of environmental ageing on the static and cyclic bending properties of braided carbon fibre/PEEK bone plates*. *Composites Part B: Engineering*, 2008. **39**(7–8): p. 1216-1220.
103. D'Amore, A. and L. Nicolais, *The effect of fibre and crystallinity content on the structural relaxation of polyetheretherketone (peek)*. *Composites Manufacturing*, 1992. **3**(1): p. 25-31.
104. D'Amore, A., A. Pompo, and L. Nicolais, *Viscoelastic effects in poly(ether ether ketone) (PEEK) and PEEK-based composites*. *Composites Science and Technology*, 1991. **41**(3): p. 303-325.
105. Patel, P., et al., *Mechanism of thermal decomposition of poly(ether ether ketone) (PEEK) from a review of decomposition studies*. *Polymer Degradation and Stability*, 2010. **95**(5): p. 709-718.

106. Crosky, A., et al., *Thermoset matrix natural fibre-reinforced composites*, in *Natural Fibre Composites*, A. Hodzic and R. Shanks, Editors. 2014, Woodhead Publishing. p. 233-270.
107. Shelke, N.B., R.K. Nagarale, and S.G. Kumbar, *Polyurethanes*, in *Natural and Synthetic Biomedical Polymers*, S.G.K.T.L. Deng, Editor. 2014, Elsevier: Oxford. p. 123-144.
108. Min, B.G., et al., *Quantitative analysis of the cure reaction of DGEBA/DDS epoxy resins without and with thermoplastic polysulfone modifier using near infra-red spectroscopy*. *Polymer*, 1993. **34**(17): p. 3620-3627.
109. Omrani, A., et al., *Study on curing mechanism of DGEBA/nickel–imidazole system*. *Thermochimica Acta*, 2008. **468**(1–2): p. 39-48.
110. Zhou, T., et al., *Studying on the curing kinetics of a DGEBA/EMI-2,4/nano-sized carborundum system with two curing kinetic methods*. *Polymer*, 2005. **46**(16): p. 6174-6181.
111. Calabrese, L. and A. Valenza, *Effect of CTBN rubber inclusions on the curing kinetic of DGEBA–DGEBF epoxy resin*. *European Polymer Journal*, 2003. **39**(7): p. 1355-1363.
112. Santiago, D., et al., *Comparative curing kinetics and thermal–mechanical properties of DGEBA thermosets cured with a hyperbranched poly(ethyleneimine) and an aliphatic triamine*. *Thermochimica Acta*, 2011. **526**(1–2): p. 9-21.
113. Li, Q., X. Li, and Y. Meng, *Curing of DGEBA epoxy using a phenol-terminated hyperbranched curing agent: Cure kinetics, gelation, and the TTT cure diagram*. *Thermochimica Acta*, 2012. **549**(0): p. 69-80.
114. Min, B.G., Z.H. Stachurski, and J.H. Hodgkin, *Cure kinetics of elementary reactions of a DGEBA/DDS epoxy resin: 1. Glass transition temperature versus conversion*. *Polymer*, 1993. **34**(23): p. 4908-4912.
115. Stevens, G.C. and M.J. Richardson, *Factors influencing the glass transition of DGEBA-anhydride epoxy resins*. *Polymer*, 1983. **24**(7): p. 851-858.
116. Mustata, F. and I. Bicu, *Rheological and thermal behaviour of DGEBA/EA and DGEHQ/EA epoxy systems crosslinked with TETA*. *Polymer Testing*, 2001. **20**(5): p. 533-538.
117. González, L., et al., *Characterization of new reworkable thermosetting coatings obtained by cationic and anionic curing of DGEBA and some Meldrum acid derivatives*. *Progress in Organic Coatings*, 2009. **65**(2): p. 175-181.
118. Foix, D., et al., *Impact resistance enhancement by adding epoxy ended hyperbranched polyester to DGEBA photocured thermosets*. *Polymer*, 2012. **53**(15): p. 3084-3088.
119. Morell, M., et al., *New improved thermosets obtained from DGEBA and a hyperbranched poly(ester-amide)*. *Polymer*, 2009. **50**(23): p. 5374-5383.
120. Atta, A.M., N.O. Shaker, and N.E. Maysour, *Influence of the molecular structure on the chemical resistivity and thermal stability of cured Schiff base epoxy resins*. *Progress in Organic Coatings*, 2006. **56**(2–3): p. 100-110.
121. Kagathara, V.M. and P.H. Parsania, *Preparation and evaluation of mechano-electrical properties and chemical resistance of epoxy laminates of halogenated bisphenol-C resins*. *Polymer Testing*, 2001. **20**(6): p. 713-716.
122. Niu, Y., et al., *Bisphenol A and nonylphenol in foodstuffs: Chinese dietary exposure from the 2007 total diet study and infant health risk from formulas*. *Food Chemistry*, 2015. **167**(0): p. 320-325.

123. Rochester, J.R., *Bisphenol A and human health: A review of the literature*. Reproductive Toxicology, 2013. **42**(0): p. 132-155.
124. vom Saal, F.S. and W.V. Welshons, *Evidence that bisphenol A (BPA) can be accurately measured without contamination in human serum and urine, and that BPA causes numerous hazards from multiple routes of exposure*. Molecular and Cellular Endocrinology, 2014. **398**(1–2): p. 101-113.
125. Míguez, J., et al., *A LC–MS/MS method for the determination of BADGE-related and BFDGE-related compounds in canned fish food samples based on the formation of [M + NH4]+ adducts*. Food Chemistry, 2012. **135**(3): p. 1310-1315.
126. Cabado, A.G., et al., *Migration of BADGE (bisphenol A diglycidyl-ether) and BFDGE (bisphenol F diglycidyl-ether) in canned seafood*. Food and Chemical Toxicology, 2008. **46**(5): p. 1674-1680.
127. Satoh, K., et al., *Study on anti-androgenic effects of bisphenol a diglycidyl ether (BADGE), bisphenol F diglycidyl ether (BFDGE) and their derivatives using cells stably transfected with human androgen receptor, AR-EcoScreen*. Food and Chemical Toxicology, 2004. **42**(6): p. 983-993.
128. Sueiro, R.A., et al., *Study on mutagenic effects of bisphenol A diglycidyl ether (BADGE) and its derivatives in the Escherichia coli tryptophan reverse mutation assay*. Mutation Research/Genetic Toxicology and Environmental Mutagenesis, 2006. **609**(1): p. 11-16.
129. Chang, Y., et al., *Analysis of bisphenol A diglycidyl ether (BADGE) and its hydrolytic metabolites in biological specimens by high-performance liquid chromatography and tandem mass spectrometry*. Journal of Chromatography B, 2014. **965**(0): p. 33-38.
130. Suárez, S., R.A. Sueiro, and J.n. Garrido, *Genotoxicity of the coating lacquer on food cans, bisphenol A diglycidyl ether (BADGE), its hydrolysis products and a chlorohydrin of BADGE*. Mutation Research/Genetic Toxicology and Environmental Mutagenesis, 2000. **470**(2): p. 221-228.
131. Sun, C., et al., *Single laboratory validation of a method for the determination of Bisphenol A, Bisphenol A diglycidyl ether and its derivatives in canned foods by reversed-phase liquid chromatography*. Journal of Chromatography A, 2006. **1129**(1): p. 145-148.
132. Biles, J.E., et al., *Determination of the Diglycidyl Ether of Bisphenol A and Its Derivatives in Canned Foods*. Journal of Agricultural and Food Chemistry, 1999. **47**(5): p. 1965-1969.
133. Pouokam, G.B., et al., *Use of Bisphenol A-containing baby bottles in Cameroon and Nigeria and possible risk management and mitigation measures: community as milestone for prevention*. Science of The Total Environment, 2014. **481**(0): p. 296-302.
134. Nam, S.-H., Y.-M. Seo, and M.-G. Kim, *Bisphenol A migration from polycarbonate baby bottle with repeated use*. Chemosphere, 2010. **79**(9): p. 949-952.
135. Li, X., et al., *Simultaneous determination and assessment of 4-nonylphenol, bisphenol A and triclosan in tap water, bottled water and baby bottles*. Environment International, 2010. **36**(6): p. 557-562.
136. Fan, Y.-Y., et al., *Effects of storage temperature and duration on release of antimony and bisphenol A from polyethylene terephthalate drinking water bottles of China*. Environmental Pollution, 2014. **192**(0): p. 113-120.

137. Maia, J., et al., *Effect of amines in the release of bisphenol A from polycarbonate baby bottles*. Food Research International, 2010. **43**(5): p. 1283-1288.
138. Maia, J., et al., *Effect of detergents in the release of bisphenol A from polycarbonate baby bottles*. Food Research International, 2009. **42**(10): p. 1410-1414.
139. Chang, H.C., et al., *Facile preparation of a phosphinated bisphenol and its low water-absorption epoxy resins for halogen-free copper clad laminates*. Polymer Degradation and Stability, 2013. **98**(1): p. 102-108.
140. Braun, J., et al., *Non-destructive, three-dimensional monitoring of water absorption in polyurethane foams using magnetic resonance imaging*. Polymer Testing, 2003. **22**(7): p. 761-767.
141. Biron, M., *Thermoset Processing*, in *Thermosets and Composites (Second Edition)*, M. Biron, Editor. 2014, William Andrew Publishing: Oxford. p. 269-297.
142. Sun, M., et al., *A study on water absorption in freestanding polyurethane films filled with nano-TiO₂ pigments by capacitance measurements*. Acta Metallurgica Sinica (English Letters), 2009. **22**(1): p. 27-34.
143. Tcharkhtchi, A., P.Y. Bronnec, and J. Verdu, *Water absorption characteristics of diglycidylether of butane diol-3,5-diethyl-2,4-diaminotoluene networks*. Polymer, 2000. **41**(15): p. 5777-5785.
144. Pitarresi, G., et al., *Absorption kinetics and swelling stresses in hydrothermally aged epoxies investigated by photoelastic image analysis*. Polymer Degradation and Stability, 2015. **111**(0): p. 55-63.
145. Delor-Jestin, F., et al., *Thermal and photochemical ageing of epoxy resin – Influence of curing agents*. Polymer Degradation and Stability, 2006. **91**(6): p. 1247-1255.
146. El Yagoubi, J., et al., *Thermomechanical and hygroelastic properties of an epoxy system under humid and cold-warm cycling conditions*. Polymer Degradation and Stability, 2014. **99**(0): p. 146-155.
147. Colombini, D., J.J. Martinez-Vega, and G. Merle, *Dynamic mechanical investigations of the effects of water sorption and physical ageing on an epoxy resin system*. Polymer, 2002. **43**(16): p. 4479-4485.
148. Quino, G., J. El Yagoubi, and G. Lubineau, *Characterizing the toughness of an epoxy resin after wet aging using compact tension specimens with non-uniform moisture content*. Polymer Degradation and Stability, 2014. **109**(0): p. 319-326.
149. Alessi, S., et al., *Accelerated ageing due to moisture absorption of thermally cured epoxy resin/polyethersulphone blends. Thermal, mechanical and morphological behaviour*. Polymer Degradation and Stability, 2011. **96**(4): p. 642-648.
150. El Yagoubi, J., et al., *Monitoring and simulations of hydrolysis in epoxy matrix composites during hygrothermal aging*. Composites Part A: Applied Science and Manufacturing, 2015. **68**(0): p. 184-192.
151. Zahra, Y., et al., *Thermo-oxidative aging of epoxy coating systems*. Progress in Organic Coatings, 2014. **77**(2): p. 380-387.
152. Queiroz, D.P.R., et al., *Radiochemical ageing of epoxy coating for nuclear plants*. Radiation Physics and Chemistry, 2010. **79**(3): p. 362-364.
153. Damian, C., E. Espuche, and M. Escoubes, *Influence of three ageing types (thermal oxidation, radiochemical and hydrolytic ageing) on the structure and gas transport properties of epoxy-amine networks*. Polymer Degradation and Stability, 2001. **72**(3): p. 447-458.

154. Devanne, T., et al., *Radiochemical ageing of an amine cured epoxy network. Part I: change of physical properties*. Polymer, 2005. **46**(1): p. 229-236.
155. Devanne, T., et al., *Radiochemical ageing of an amine cured epoxy network. Part II: kinetic modelling*. Polymer, 2005. **46**(1): p. 237-241.
156. Longi eras, N., et al., *Degradation of epoxy resins under high energy electron beam irradiation: Radio-oxidation*. Polymer Degradation and Stability, 2007. **92**(12): p. 2190-2197.
157. Longi eras, N., et al., *Multiscale approach to investigate the radiochemical degradation of epoxy resins under high-energy electron-beam irradiation*. Journal of Polymer Science Part A: Polymer Chemistry, 2006. **44**(2): p. 865-887.
158. Nguyen Dang, D., et al., *Effect of mechanical stresses on epoxy coating ageing approached by Electrochemical Impedance Spectroscopy measurements*. Electrochimica Acta, 2014. **124**(0): p. 80-89.
159. Fromonteil, C., P. Bardelle, and F. Cansell, *Hydrolysis and Oxidation of an Epoxy Resin in Sub- and Supercritical Water*. Industrial & Engineering Chemistry Research, 2000. **39**(4): p. 922-925.
160. Liu, Y.Y., et al., *Kinetic Study of Epoxy Resin Decomposition in Near-Critical Water*. Chemical Engineering & Technology, 2012. **35**(4): p. 713-719.
161. Luda, M.P., A.I. Balabanovich, and G. Camino, *Thermal decomposition of fire retardant brominated epoxy resins*. Journal of Analytical and Applied Pyrolysis, 2002. **65**(1): p. 25-40.
162. Wang, Q. and W. Shi, *Kinetics study of thermal decomposition of epoxy resins containing flame retardant components*. Polymer Degradation and Stability, 2006. **91**(8): p. 1747-1754.
163. Liu, W., R.J. Varley, and G.P. Simon, *Understanding the decomposition and fire performance processes in phosphorus and nanomodified high performance epoxy resins and composites*. Polymer, 2007. **48**(8): p. 2345-2354.
164. Braun, U., et al., *Influence of the oxidation state of phosphorus on the decomposition and fire behaviour of flame-retarded epoxy resin composites*. Polymer, 2006. **47**(26): p. 8495-8508.
165. Luda, M.P., et al., *Thermal decomposition of fire retardant brominated epoxy resins cured with different nitrogen containing hardeners*. Polymer Degradation and Stability, 2007. **92**(6): p. 1088-1100.
166. Grittner, N., W. Kaminsky, and G. Obst, *Fluid bed pyrolysis of anhydride-hardened epoxy resins and polyether-polyurethane by the Hamburg process*. Journal of Analytical and Applied Pyrolysis, 1993. **25**(0): p. 293-299.
167. Yin, J., et al., *Hydrothermal decomposition of brominated epoxy resin in waste printed circuit boards*. Journal of Analytical and Applied Pyrolysis, 2011. **92**(1): p. 131-136.
168. Li, J. and X. Zeng, *Recycling printed circuit boards*, in *Waste Electrical and Electronic Equipment (WEEE) Handbook*, V. Goodship and A. Stevels, Editors. 2012, Woodhead Publishing. p. 287-311.
169. Matsumoto, Y. and Y. Oshima, *Au and Cu recovery from printed boards by decomposition of epoxy resin in supercritical water*. The Journal of Supercritical Fluids, 2014. **95**(0): p. 462-467.

170. Xing, M. and F.-S. Zhang, *Degradation of brominated epoxy resin and metal recovery from waste printed circuit boards through batch sub/supercritical water treatments*. Chemical Engineering Journal, 2013. **219**(0): p. 131-136.
171. Tagaya, H., et al., *Decomposition reactions of epoxy resin and polyetheretherketone resin in sub- and supercritical water*. Journal of Material Cycles and Waste Management, 2004. **6**(1): p. 1-5.
172. Shih, G.C. and L.J. Ebert, *The effect of the fiber/matrix interface on the flexural fatigue performance of unidirectional fiberglass composites*. Composites Science and Technology, 1987. **28**(2): p. 137-161.
173. Giampieretti, R., et al., *CYCLIC BENDING TESTS ON FIBREGLASS, HIGH STRENGTH, STRUCTURAL COMPOSITES FOR ELECTRICAL TRANSMISSION LINES*, in *FRC 2000–Composites for the Millennium*, A.G. Gibson, Editor. 2000, Woodhead Publishing. p. 295-302.
174. Zhong, Y. and S.C. Joshi, *Impact behavior and damage characteristics of hygrothermally conditioned carbon epoxy composite laminates*. Materials & Design, 2015. **65**(0): p. 254-264.
175. Herszberg, I. and T. Weller, *Impact damage resistance of buckled carbon/epoxy panels*. Composite Structures, 2006. **73**(2): p. 130-137.
176. Petrucci, R., et al., *Impact and post-impact damage characterisation of hybrid composite laminates based on basalt fibres in combination with flax, hemp and glass fibres manufactured by vacuum infusion*. Composites Part B: Engineering, 2015. **69**(0): p. 507-515.
177. Scarponi, C. and M. Messano, *Comparative evaluation between E-Glass and hemp fiber composites application in rotorcraft interiors*. Composites Part B: Engineering, 2015. **69**(0): p. 542-549.
178. sunny, T., J. Babu, and J. Philip, *Experimental Studies on Effect of Process Parameters on Delamination in Drilling GFRP Composites Using Taguchi Method*. Procedia Materials Science, 2014. **6**(0): p. 1131-1142.
179. Thomason, J.L., L. Yang, and R. Meier, *The properties of glass fibres after conditioning at composite recycling temperatures*. Composites Part A: Applied Science and Manufacturing, 2014. **61**(0): p. 201-208.
180. Vassilopoulos, A.P., M. Shahverdi, and T. Keller, *Mode I fatigue and fracture behavior of adhesively-bonded pultruded glass fiber-reinforced polymer (GFRP) composite joints*, in *Fatigue and Fracture of Adhesively-Bonded Composite Joints*, A.P. Vassilopoulos, Editor. 2015, Woodhead Publishing. p. 149-186.
181. Wei, B., H. Cao, and S. Song, *Tensile behavior contrast of basalt and glass fibers after chemical treatment*. Materials & Design, 2010. **31**(9): p. 4244-4250.
182. Liu, J., et al., *Tensile behaviors of ECR-glass and high strength glass fibers after NaOH treatment*. Ceramics International, 2013. **39**(8): p. 9173-9178.
183. Lezzi, P.J., J.H. Seaman, and M. Tomozawa, *Strengthening of E-glass fibers by surface stress relaxation*. Journal of Non-Crystalline Solids, 2014. **402**(0): p. 116-127.
184. Vautard, F., et al., *Influence of surface defects on the tensile strength of carbon fibers*. Applied Surface Science, 2014. **322**(0): p. 185-193.
185. Lefevre, A., et al., *Tensile properties of elementary fibres of flax and glass: Analysis of reproducibility and scattering*. Materials Letters, 2014. **130**(0): p. 289-291.

186. Markov, A., B. Fiedler, and K. Schulte, *Electrical conductivity of carbon black/fibres filled glass-fibre-reinforced thermoplastic composites*. Composites Part A: Applied Science and Manufacturing, 2006. **37**(9): p. 1390-1395.
187. Jacob, A., *Composite aircraft and repair*. Reinforced Plastics, 2011. **55**(6): p. 3.
188. *GKN manufactures A350 XWB wing spars using Umeco tooling*. Reinforced Plastics, 2012. **56**(3): p. 20.
189. Horan, P., P.R. Underhill, and T.W. Krause, *Pulsed eddy current detection of cracks in F/A-18 inner wing spar without wing skin removal using Modified Principal Component Analysis*. NDT & E International, 2013. **55**(0): p. 21-27.
190. Dilger, R., H. Hickethier, and M.D. Greenhalgh, *Eurofighter a safe life aircraft in the age of damage tolerance*. International Journal of Fatigue, 2009. **31**(6): p. 1017-1023.
191. Ju, A.Q., S.Y. Guang, and H.Y. Xu, *A novel poly[acrylonitrile-co-(3-ammoniumcarboxylate-butenoic acid-methylester)]copolymer for carbon fiber precursor*. Chinese Chemical Letters, 2012. **23**(11): p. 1307-1310.
192. Hanna, T.A., *The role of bismuth in the SOHIO process*. Coordination Chemistry Reviews, 2004. **248**(5-6): p. 429-440.
193. El-Newehy, M.H., A. Alamri, and S.S. Al-Deyab, *Optimization of amine-terminated polyacrylonitrile synthesis and characterization*. Arabian Journal of Chemistry, 2014. **7**(2): p. 235-241.
194. Qin, X.-H., et al., *Effect of LiCl on the stability length of electrospinning jet by PAN polymer solution*. Materials Letters, 2005. **59**(24-25): p. 3102-3105.
195. Zhang, X., et al., *The Morphology of the Hollow PAN Fibers through Electrospinning*. AASRI Procedia, 2012. **3**(0): p. 236-241.
196. Tan, L., A. Wan, and D. Pan, *Pregelged gel spinning of polyacrylonitrile precursor fiber*. Materials Letters, 2011. **65**(5): p. 887-890.
197. Kim, S., et al., *Preparation and characterization of polyacrylonitrile-based carbon fiber papers*. Journal of Industrial and Engineering Chemistry, 2014. **20**(5): p. 3440-3445.
198. Rahaman, M.S.A., A.F. Ismail, and A. Mustafa, *A review of heat treatment on polyacrylonitrile fiber*. Polymer Degradation and Stability, 2007. **92**(8): p. 1421-1432.
199. Li, Z., et al., *Anodic Oxidation on Structural Evolution and Tensile Properties of Polyacrylonitrile Based Carbon Fibers with Different Surface Morphology*. Journal of Materials Science & Technology, 2012. **28**(12): p. 1123-1129.
200. Barnet, F.R. and M.K. Norr, *Carbon fiber etching in an oxygen plasma*. Carbon, 1973. **11**(4): p. 281-288.
201. Yuan, L.Y., et al., *Plasma surface treatment on carbon fibers. Part 1: Morphology and surface analysis of plasma etched fibers*. Composites Science and Technology, 1992. **45**(1): p. 1-7.
202. Ozkan, C., et al., *Short carbon fiber reinforced polycarbonate composites: Effects of different sizing materials*. Composites Part B: Engineering, 2014. **62**(0): p. 230-235.
203. Dai, Z., et al., *Effect of sizing on carbon fiber surface properties and fibers/epoxy interfacial adhesion*. Applied Surface Science, 2011. **257**(15): p. 6980-6985.
204. Yao, L., et al., *Comparison of sizing effect of T700 grade carbon fiber on interfacial properties of fiber/BMI and fiber/epoxy*. Applied Surface Science, 2012. **263**(0): p. 326-333.

205. Giraud, I., et al., *Preparation of aqueous dispersion of thermoplastic sizing agent for carbon fiber by emulsion/solvent evaporation*. Applied Surface Science, 2013. **266**(0): p. 94-99.
206. Yuan, H., S. Zhang, and C. Lu, *Surface modification of carbon fibers by a polyether sulfone emulsion sizing for increased interfacial adhesion with polyether sulfone*. Applied Surface Science, 2014. **317**(0): p. 737-744.
207. Song, Y.S., J.R. Youn, and T.G. Gutowski, *Life cycle energy analysis of fiber-reinforced composites*. Composites Part A: Applied Science and Manufacturing, 2009. **40**(8): p. 1257-1265.
208. Howarth, J., S.S.R. Mareddy, and P.T. Mativenga, *Energy intensity and environmental analysis of mechanical recycling of carbon fibre composite*. Journal of Cleaner Production, 2014. **81**(0): p. 46-50.
209. Stringer, L.G., *Optimization of the wet lay-up/vacuum bag process for the fabrication of carbon fibre epoxy composites with high fibre fraction and low void content*. Composites, 1989. **20**(5): p. 441-452.
210. Jiang, G., et al., *Characterisation of carbon fibres recycled from carbon fibre/epoxy resin composites using supercritical n-propanol*. Composites Science and Technology, 2009. **69**(2): p. 192-198.
211. Pimenta, S. and S.T. Pinho, *The effect of recycling on the mechanical response of carbon fibres and their composites*. Composite Structures, 2012. **94**(12): p. 3669-3684.
212. Wulfsberg, J., et al., *Combination of Carbon Fibre Sheet Moulding Compound and Prepreg Compression Moulding in Aerospace Industry*. Procedia Engineering, 2014. **81**(0): p. 1601-1607.
213. Sozer, E.M., P. Simacek, and S.G. Advani, *Resin transfer molding (RTM) in polymer matrix composites*, in *Manufacturing Techniques for Polymer Matrix Composites (PMCs)*, S.G. Advani and K.-T. Hsiao, Editors. 2012, Woodhead Publishing. p. 245-309.
214. Zhang, K., et al., *Effect of rapid curing process on the properties of carbon fiber/epoxy composite fabricated using vacuum assisted resin infusion molding*. Materials & Design, 2014. **54**(0): p. 624-631.
215. Hsiao, K.T. and D. Heider, *Vacuum assisted resin transfer molding (VARTM) in polymer matrix composites*, in *Manufacturing Techniques for Polymer Matrix Composites (PMCs)*, S.G. Advani and K.-T. Hsiao, Editors. 2012, Woodhead Publishing. p. 310-347.
216. Joshi, S.C., *The pultrusion process for polymer matrix composites*, in *Manufacturing Techniques for Polymer Matrix Composites (PMCs)*, S.G. Advani and K.-T. Hsiao, Editors. 2012, Woodhead Publishing. p. 381-413.
217. Khennane, A., *Filament winding processes in the manufacture of advanced fibre-reinforced polymer (FRP) composites*, in *Advanced Fibre-Reinforced Polymer (FRP) Composites for Structural Applications*, J. Bai, Editor. 2013, Woodhead Publishing. p. 187-206.
218. Hörmann, P., et al., *On the numerical prediction of radiative heat transfer for thermoset automated fiber placement*. Composites Part A: Applied Science and Manufacturing, 2014. **67**(0): p. 282-288.
219. Achim, V. and E. Ruiz, *Guiding selection for reduced process development time in RTM*. International Journal of Material Forming, 2010. **3**(2): p. 1277-1286.

220. Poodts, E., et al., *Fabrication, process simulation and testing of a thick CFRP component using the RTM process*. Composites Part B: Engineering, 2014. **56**(0): p. 673-680.
221. Grujicic, M., K.M. Chittajallu, and S. Walsh, *Non-isothermal preform infiltration during the vacuum-assisted resin transfer molding (VARTM) process*. Applied Surface Science, 2005. **245**(1-4): p. 51-64.
222. Bickerton, S., Q. Govignon, and P. Kelly, *Resin infusion/liquid composite moulding (LCM) of advanced fibre-reinforced polymer (FRP)*, in *Advanced Fibre-Reinforced Polymer (FRP) Composites for Structural Applications*, J. Bai, Editor. 2013, Woodhead Publishing. p. 155-186.
223. Atas, C., et al., *An experimental investigation on the low velocity impact response of composite plates repaired by VARIM and hand lay-up processes*. Composite Structures, 2011. **93**(3): p. 1178-1186.
224. Jia, X., et al., *Effect of geometric factor, winding angle and pre-crack angle on quasi-static crushing behavior of filament wound CFRP cylinder*. Composites Part B: Engineering, 2013. **45**(1): p. 1336-1343.
225. Mack, J. and R. Schledjewski, *Filament winding process in thermoplastics*, in *Manufacturing Techniques for Polymer Matrix Composites (PMCs)*, S.G. Advani and K.-T. Hsiao, Editors. 2012, Woodhead Publishing. p. 182-208.
226. Sayem Uddin, M., E.V. Morozov, and K. Shankar, *The effect of filament winding mosaic pattern on the stress state of filament wound composite flywheel disk*. Composite Structures, 2014. **107**(0): p. 260-275.
227. Vargas Rojas, E., et al., *Unified approach of filament winding applied to complex shape mandrels*. Composite Structures, 2014. **116**(0): p. 805-813.
228. Wang, R., et al., *Slippage coefficient measurement for non-geodesic filament-winding process*. Composites Part A: Applied Science and Manufacturing, 2011. **42**(3): p. 303-309.
229. Crossley, R.J., P.J. Schubel, and D.S.A. De Focatiis, *Time-temperature equivalence in the tack and dynamic stiffness of polymer prepreg and its application to automated composites manufacturing*. Composites Part A: Applied Science and Manufacturing, 2013. **52**(0): p. 126-133.
230. Lin, L., et al., *PMAC-based Tracking Control System for 8-axis Automated Tape-laying Machine*. Chinese Journal of Aeronautics, 2009. **22**(5): p. 558-563.
231. Hardesty, E.E., *Design and construction of a large, fully automated tape placement machine for aircraft structures*. Composites, 1972. **3**(6): p. 248-253.
232. Lukaszewicz, D.H.J.A., C. Ward, and K.D. Potter, *The engineering aspects of automated prepreg layup: History, present and future*. Composites Part B: Engineering, 2012. **43**(3): p. 997-1009.
233. Croft, K., et al., *Experimental study of the effect of automated fiber placement induced defects on performance of composite laminates*. Composites Part A: Applied Science and Manufacturing, 2011. **42**(5): p. 484-491.
234. Marsh, G., *Automating aerospace composites production with fibre placement*. Reinforced Plastics, 2011. **55**(3): p. 32-37.
235. Tserpes, K.I., et al., *Strain and damage monitoring in CFRP fuselage panels using fiber Bragg grating sensors. Part I: Design, manufacturing and impact testing*. Composite Structures, 2014. **107**(0): p. 726-736.

236. Lu, S., et al., *Low velocity impact localization system of CFRP using fiber Bragg grating sensors*. Optical Fiber Technology, 2015. **21**(0): p. 13-19.
237. Yamada, M., et al., *Three-dimensional measurement of CFRP deformation during high-speed impact loading*. Nuclear Instruments and Methods in Physics Research Section A: Accelerators, Spectrometers, Detectors and Associated Equipment, 2011. **646**(1): p. 219-226.
238. Wicklein, M., et al., *Hypervelocity impact on CFRP: Testing, material modelling, and numerical simulation*. International Journal of Impact Engineering, 2008. **35**(12): p. 1861-1869.
239. Appleby-Thomas, G.J., P.J. Hazell, and G. Dahini, *On the response of two commercially-important CFRP structures to multiple ice impacts*. Composite Structures, 2011. **93**(10): p. 2619-2627.
240. Hazell, P.J. and G. Appleby-Thomas, *A study on the energy dissipation of several different CFRP-based targets completely penetrated by a high velocity projectile*. Composite Structures, 2009. **91**(1): p. 103-109.
241. Hazell, P.J., et al., *Penetration of a woven CFRP laminate by a high velocity steel sphere impacting at velocities of up to 1875 m/s*. International Journal of Impact Engineering, 2009. **36**(9): p. 1136-1142.
242. Hazell, P.J., et al., *Normal and oblique penetration of woven CFRP laminates by a high velocity steel sphere*. Composites Part A: Applied Science and Manufacturing, 2008. **39**(5): p. 866-874.
243. Hazell, P.J., C. Stennett, and G. Cooper, *The effect of specimen thickness on the shock propagation along the in-fibre direction of an aerospace-grade CFRP laminate*. Composites Part A: Applied Science and Manufacturing, 2009. **40**(2): p. 204-209.
244. Sato, N., M. Hojo, and M. Nishikawa, *Novel test method for accurate characterization of intralaminar fracture toughness in CFRP laminates*. Composites Part B: Engineering, 2014. **65**(0): p. 89-98.
245. Dandy, L.O., et al., *Counting carbon fibres by electrical resistance measurement*. Composites Part A: Applied Science and Manufacturing, 2015. **68**(0): p. 276-281.
246. Zantout, A.E. and O.I. Zhupanska, *On the electrical resistance of carbon fiber polymer matrix composites*. Composites Part A: Applied Science and Manufacturing, 2010. **41**(11): p. 1719-1727.
247. Todoroki, A., M. Tanaka, and Y. Shimamura, *Measurement of orthotropic electric conductance of CFRP laminates and analysis of the effect on delamination monitoring with an electric resistance change method*. Composites Science and Technology, 2002. **62**(5): p. 619-628.
248. Shen, L., et al., *Modeling and analysis of the electrical resistance measurement of carbon fiber polymer-matrix composites*. Composites Science and Technology, 2007. **67**(11-12): p. 2513-2520.
249. Wen, J., Z. Xia, and F. Choy, *Damage detection of carbon fiber reinforced polymer composites via electrical resistance measurement*. Composites Part B: Engineering, 2011. **42**(1): p. 77-86.
250. Irving, P.E. and C. Thiagarajan, *Fatigue damage characterization in carbon fibre composite materials using an electrical potential technique*. Smart Materials and Structures, 1998. **7**(4): p. 456-466.

251. Wang, X., S. Wang, and D.D.L. Chung, *Sensing damage in carbon fiber and its polymer-matrix and carbon-matrix composites by electrical resistance measurement*. Journal of Materials Science, 1999. **34**(11): p. 2703-2713.
252. Suzuki, Y., et al., *Impact-damage visualization in CFRP by resistive heating: Development of a new detection method for indentations caused by impact loads*. Composites Part A: Applied Science and Manufacturing, 2012. **43**(1): p. 53-64.
253. He, Y., et al., *Non-destructive testing of low-energy impact in CFRP laminates and interior defects in honeycomb sandwich using scanning pulsed eddy current*. Composites Part B: Engineering, 2014. **59**(0): p. 196-203.
254. He, Y., et al., *Impact evaluation in carbon fiber reinforced plastic (CFRP) laminates using eddy current pulsed thermography*. Composite Structures, 2014. **109**(0): p. 1-7.
255. Minakuchi, S., et al., *Life cycle monitoring of large-scale CFRP VARTM structure by fiber-optic-based distributed sensing*. Composites Part A: Applied Science and Manufacturing, 2011. **42**(6): p. 669-676.
256. Lu, C., P. Ding, and Z. Chen, *Time-frequency Analysis of Acoustic Emission Signals Generated by Tension Damage in CFRP*. Procedia Engineering, 2011. **23**(0): p. 210-215.
257. Tsuda, H., *Ultrasound and damage detection in CFRP using fiber Bragg grating sensors*. Composites Science and Technology, 2006. **66**(5): p. 676-683.
258. Guzmán, E., J. Cugnoni, and T. Gmür, *Multi-factorial models of a carbon fibre/epoxy composite subjected to accelerated environmental ageing*. Composite Structures, 2014. **111**(0): p. 179-192.
259. Aldajah, S., A. Al-omari, and A. Biddah, *Accelerated weathering effects on the mechanical and surface properties of CFRP composites*. Materials & Design, 2009. **30**(3): p. 833-837.
260. Byon, O.I. and A. Kudo, *Weatherability flexural properties of CFRP subjected to accelerated and outdoor exposures*. Composites Science and Technology, 2001. **61**(13): p. 1913-1921.
261. Pickering, S.J., *Recycling technologies for thermoset composite materials—current status*. Composites Part A: Applied Science and Manufacturing, 2006. **37**(8): p. 1206-1215.
262. *Europe gets tough on end-of-life composites*. Reinforced Plastics, 2003. **47**(8): p. 34-39.
263. McConnell, V.P., *Launching the carbon fibre recycling industry*. Reinforced Plastics, 2010. **54**(2): p. 33-37.
264. Biron, M., *The Plastics Industry: Economic Overview*, in *Thermosets and Composites (Second Edition)*, M. Biron, Editor. 2014, William Andrew Publishing: Oxford. p. 25-104.
265. Palmer, J., et al., *Sheet moulding compound (SMC) from carbon fibre recycle*. Composites Part A: Applied Science and Manufacturing, 2010. **41**(9): p. 1232-1237.
266. Boylan, S. and J.M. Castro, *Effect of reinforcement type and length on physical properties, surface quality, and cycle time for sheet molding compound (SMC) compression molded parts*. Journal of Applied Polymer Science, 2003. **90**(9): p. 2557-2571.
267. *Body panel containing recycled SMC gains approval*. Reinforced Plastics, 1995. **39**(4): p. 8.

268. *Carbon fibre SMC halves weight of automotive parts*. Reinforced Plastics, 2003. **47**(7): p. 16.
269. Palmer, J., et al., *Successful closed-loop recycling of thermoset composites*. Composites Part A: Applied Science and Manufacturing, 2009. **40**(4): p. 490-498.
270. Thomas, C., et al., *Epoxy composites containing CFRP powder wastes*. Composites Part B: Engineering, 2014. **59**(0): p. 260-268.
271. Schinner, G., J. Brandt, and H. Richter, *Recycling Carbon-Fiber-Reinforced Thermoplastic Composites*. Journal of Thermoplastic Composite Materials, 1996. **9**(3): p. 239-245.
272. Schmidt, J., et al., *Production of polymer particles below 5 μ m by wet grinding*. Powder Technology, 2012. **228**(0): p. 84-90.
273. Wang, E., F. Shi, and E. Manlapig, *Experimental and numerical studies of selective fragmentation of mineral ores in electrical comminution*. International Journal of Mineral Processing, 2012. **112–113**(0): p. 30-36.
274. Wang, E., F. Shi, and E. Manlapig, *Mineral liberation by high voltage pulses and conventional comminution with same specific energy levels*. Minerals Engineering, 2012. **27–28**(0): p. 28-36.
275. Wang, E., F. Shi, and E. Manlapig, *Factors affecting electrical comminution performance*. Minerals Engineering, 2012. **34**(0): p. 48-54.
276. Zhao, Y., et al., *Material port fractal of fragmentation of waste printed circuit boards (WPCBs) by high-voltage pulse*. Powder Technology, 2015. **269**(0): p. 219-226.
277. Duan, C.L., et al., *Liberation of valuable materials in waste printed circuit boards by high-voltage electrical pulses*. Minerals Engineering, 2015. **70**(0): p. 170-177.
278. Roux, M.D., C; Eguemann, N; Giger, L, *Processing and Recycling of a Thermoplastic Composite Carbon Fibre / PEEK Aerospace Part*. European Conference on Composite Materials (ECCM16), 2014. **25.1.4-R13**.
279. DalmasNeto, C.J., et al., *Production of Biofuels from Algal Biomass by Fast Pyrolysis*, in *Biofuels from Algae*, A.P.-J.L.C.R. Soccol, Editor. 2014, Elsevier: Amsterdam. p. 143-153.
280. Peters, J.F., D. Iribarren, and J. Dufour, *Simulation and life cycle assessment of biofuel production via fast pyrolysis and hydrougrading*. Fuel, 2015. **139**(0): p. 441-456.
281. Fréty, R., et al., *Flash pyrolysis of model compounds adsorbed on catalyst surface: A method for screening catalysts for cracking of fatty molecules*. Journal of Analytical and Applied Pyrolysis, 2014. **109**(0): p. 56-64.
282. Antonakou, E.V., et al., *Catalytic and thermal pyrolysis of polycarbonate in a fixed-bed reactor: The effect of catalysts on products yields and composition*. Polymer Degradation and Stability, 2014. **110**(0): p. 482-491.
283. Seitz, M., et al., *Influence of catalysts on the pyrolysis of lignites*. Fuel, 2014. **134**(0): p. 669-676.
284. Liu, S., et al., *Modeling and analysis of the pyrolysis of bio-oil aqueous fraction in a fixed-bed reactor*. Fuel, 2014. **133**(0): p. 1-6.
285. Liu, S., et al., *Hydrogen production via catalytic pyrolysis of biomass in a two-stage fixed bed reactor system*. International Journal of Hydrogen Energy, 2014. **39**(25): p. 13128-13135.
286. Butler, E., et al., *Fluidised bed pyrolysis of lignocellulosic biomasses and comparison of bio-oil and micropyrolyser pyrolysate by GC/MS-FID*. Journal of Analytical and Applied Pyrolysis, 2013. **103**(0): p. 96-101.

287. Pattiya, A., *Bio-oil production via fast pyrolysis of biomass residues from cassava plants in a fluidised-bed reactor*. Bioresource Technology, 2011. **102**(2): p. 1959-1967.
288. Yun, Y.M., et al., *Pyrolysis characteristics of GFRP (Glass Fiber Reinforced Plastic) under non-isothermal conditions*. Fuel, 2014. **137**(0): p. 321-327.
289. Meyer, L.O., K. Schulte, and E. Grove-Nielsen, *CFRP-Recycling Following a Pyrolysis Route: Process Optimization and Potentials*. Journal of Composite Materials, 2009. **43**(9): p. 1121-1132.
290. Yin, C., *Microwave-assisted pyrolysis of biomass for liquid biofuels production*. Bioresource Technology, 2012. **120**(0): p. 273-284.
291. Lei, H., et al., *Microwave pyrolysis of distillers dried grain with solubles (DDGS) for biofuel production*. Bioresource Technology, 2011. **102**(10): p. 6208-6213.
292. Menéndez, J.A., et al., *Microwave heating processes involving carbon materials*. Fuel Processing Technology, 2010. **91**(1): p. 1-8.
293. Lester, E., et al., *Microwave heating as a means for carbon fibre recovery from polymer composites: a technical feasibility study*. Materials Research Bulletin, 2004. **39**(10): p. 1549-1556.
294. Kundu, A., et al., *Taguchi optimization approach for production of activated carbon from phosphoric acid impregnated palm kernel shell by microwave heating*. Journal of Cleaner Production, (0).
295. Xin-hui, D., et al., *Preparation of activated carbon from Jatropha hull with microwave heating: Optimization using response surface methodology*. Fuel Processing Technology, 2011. **92**(3): p. 394-400.
296. Huang, L., et al., *Comparative study on characterization of activated carbons prepared by microwave and conventional heating methods and application in removal of oxytetracycline (OTC)*. Chemical Engineering Journal, 2011. **171**(3): p. 1446-1453.
297. Nie, W., et al., *Decomposition of waste carbon fiber reinforced epoxy resin composites in molten potassium hydroxide*. Polymer Degradation and Stability, 2015. **111**(0): p. 247-256.
298. Dang, W., et al., *An approach to chemical recycling of epoxy resin cured with amine using nitric acid*. Polymer, 2002. **43**(10): p. 2953-2958.
299. Dang, W., et al., *Chemical recycling of glass fiber reinforced epoxy resin cured with amine using nitric acid*. Polymer, 2005. **46**(6): p. 1905-1912.
300. Severini, F., et al., *Chemical modification of carbon fiber surfaces*. Carbon, 2002. **40**(5): p. 735-741.
301. Wu, Z., C.U. Pittman Jr, and S.D. Gardner, *Nitric acid oxidation of carbon fibers and the effects of subsequent treatment in refluxing aqueous NaOH*. Carbon, 1995. **33**(5): p. 597-605.
302. Liu, Y., et al., *Chemical recycling of carbon fibre reinforced epoxy resin composites in subcritical water: Synergistic effect of phenol and KOH on the decomposition efficiency*. Polymer Degradation and Stability, 2012. **97**(3): p. 214-220.
303. Piñero-Hernanz, R., et al., *Chemical recycling of carbon fibre reinforced composites in nearcritical and supercritical water*. Composites Part A: Applied Science and Manufacturing, 2008. **39**(3): p. 454-461.

304. Bai, Y., Z. Wang, and L. Feng, *Chemical recycling of carbon fibers reinforced epoxy resin composites in oxygen in supercritical water*. *Materials & Design*, 2010. **31**(2): p. 999-1002.
305. Li, J., et al., *A promising strategy for chemical recycling of carbon fiber/thermoset composites: self-accelerating decomposition in a mild oxidative system*. *Green Chemistry*, 2012. **14**(12): p. 3260.
306. Okajima, I., et al., *Chemical recycling of carbon fiber reinforced plastic using supercritical methanol*. *The Journal of Supercritical Fluids*, 2014. **91**(0): p. 68-76.
307. Yan, H., et al., *Chemical degradation of TGDDM/DDS epoxy resin in supercritical 1-propanol: Promotion effect of hydrogenation on thermolysis*. *Polymer Degradation and Stability*, 2013. **98**(12): p. 2571-2582.
308. Piñero-Hernanz, R., et al., *Chemical recycling of carbon fibre composites using alcohols under subcritical and supercritical conditions*. *The Journal of Supercritical Fluids*, 2008. **46**(1): p. 83-92.
309. Patel, P., et al., *Flammability properties of PEEK and carbon nanotube composites*. *Polymer Degradation and Stability*, 2012. **97**(12): p. 2492-2502.
310. Jaekel, D.B., Henk, *Validation of Crystallinity Measurements of Medical Grade PEEK Using Specular Reflectance FTIR-microscopy*.
311. Schieber, A., P. Keller, and R. Carle, *Determination of phenolic acids and flavonoids of apple and pear by high-performance liquid chromatography*. *Journal of Chromatography A*, 2001. **910**(2): p. 265-273.
312. Irving, P.E. and C. Thiagarajan, *Fatigue damage characterization in carbon fibre composite materials using an electrical potential technique*. *Smart Materials and Structures*, 1998. **7**(4): p. 456.
313. Sauceau, M., et al., *New challenges in polymer foaming: A review of extrusion processes assisted by supercritical carbon dioxide*. *Progress in Polymer Science*, 2011. **36**(6): p. 749-766.
314. Yuan, X.Z., et al., *Sub- and supercritical liquefaction of rice straw in the presence of ethanol–water and 2-propanol–water mixture*. *Energy*, 2007. **32**(11): p. 2081-2088.
315. Troitzsch, J., *Plastics Flammability Handbook - Principles, Regulations, Testing, and Approval (3rd Edition)*. Hanser Publishers.
316. Sha, J.J., et al., *Influence of thermal treatment on thermo-mechanical stability and surface composition of carbon fiber*. *Applied Surface Science*, 2013. **274**(0): p. 89-94.
317. Hay, J.N. and D.J. Kemmish, *Thermal decomposition of poly(aryl ether ketones)*. *Polymer*, 1987. **28**(12): p. 2047-2051.
318. Dandy, L.O., et al., *Accelerated degradation of Polyetheretherketone (PEEK) composite materials for recycling applications*. *Polymer Degradation and Stability*, 2015. **112**(0): p. 52-62.
319. Shibasaki, Y., et al., *Decomposition reactions of epoxy resin and polyetheretherketone resin in sub- and supercritical water*. *Journal of Material Cycles and Waste Management*, 2004. **6**(1): p. 1-5.
320. Tokunaga, J., *Solubilities of sulfur dioxide in aqueous alcohol solutions*. *Journal of Chemical & Engineering Data*, 1974. **19**(2): p. 162-165.
321. Dandy, L.O., et al., *Catalytic Decomposition of Thermoset Polymers for Recycling Applications*. *Polymer Degradation and Stability (Under Review)*, 2015.

322. Manders, P.W. and T.-W. Chou, *Variability of Carbon and Glass Fibers, and the Strength of Aligned Composites*. Journal of Reinforced Plastics and Composites, 1983. **2**(1): p. 43-59.
323. Coleman, B.D., *On the strength of classical fibres and fibre bundles*. Journal of the Mechanics and Physics of Solids, 1958. **7**(1): p. 60-70.
324. H., A.F., et al., *Determination of volume fraction values of filament wound glass and carbon fiber reinforced composites*. Journal of Engineering and Applied Sciences, 2008.

APPENDICES

APPENDIX 1. HIGH-PRESSURE REACTOR VOLUME CALCULATION (CO₂)

The high-pressure reactor vessel has a nominal volume of 100 cm³, this does not include the associated pipework, valves and fittings nor does it account for the reduction in volume attributed to the agitator, thermal well and dip-tube. The reaction volume may be calculated from the initial loading rate, which is elucidated from the pressure/temperature relationship. The pressure and temperature were recorded during the experiment, the data are presented in Table A1. The volume of CO₂ within the reactor was determined to be 0.0426 m³ by measurement using a Zeal DM3A volumetric flowmeter during the depressurisation stage. Under isochoric conditions the density of the fluid at the critical point is equal to the initial loading rate of the reactor. This is explained by the fluid having a single phase and filling the reactor volume. Isochoric properties for CO₂ were obtained from the National Institute for Standards and Technology (NIST), covering a range of 0.10-0.85 g l⁻¹. These data are shown in Figure A1. The data obtained from the CO₂ experiment have been overlaid onto the NIST data in Figure A1.

Table A1: Reactor pressure as a function of temperature

| Temperature (K) | Pressure (MPa) |
|-----------------|----------------|
| 313.15 | 10.0 |
| 318.15 | 11.9 |
| 323.15 | 13.5 |
| 328.15 <td 15.2 | |
| 333.15 | 16.6 |
| 338.15 | 18.2 |

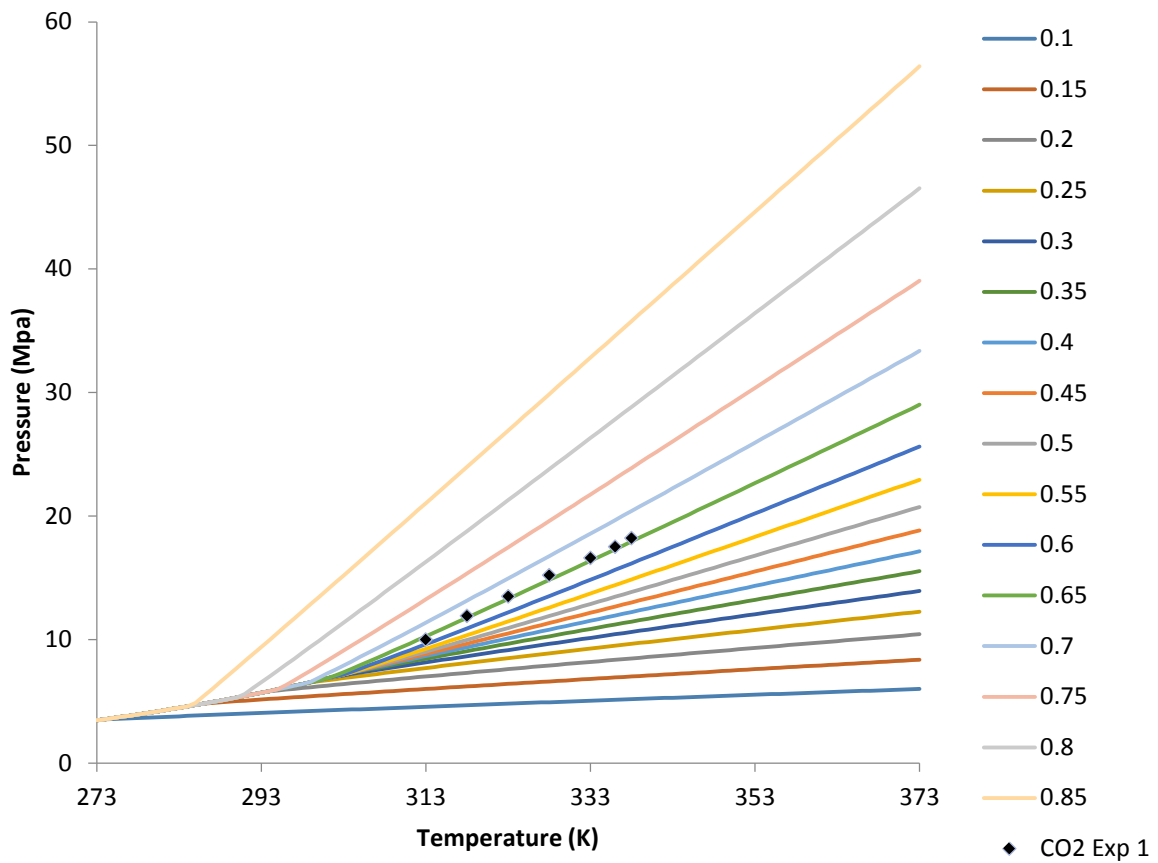


Figure A1: Pressure-Temperature relationship for CO₂ (NIST)

The data obtained are within reasonable proximity to the line corresponding to an initial loading rate of 0.65, therefore the density of the supercritical phase is determined to be

0.65 g cm⁻³ (650 kg m⁻³). This density may then be used to calculate the reaction volume as shown in Calculation A1.

Calculation A1

Volume of CO₂ = 0.0426 m³ = 42.6 l

Since 1mol of any gas occupies 22.465 l at 25 °C, 1 atm;

$$n = \frac{42.6}{22.465} = 1.8963 \text{ mol}$$

M_r of CO₂ = 44 g mol⁻¹

Therefore, mass of CO₂;

$$m_{\text{CO}_2} = 1.8963 \times 44.01 = 83.455 \text{ g}$$

Fluid density (ρ_{sc}) = 0.65 g cm⁻³ = 650 kg m⁻³

$$V_{sc} = \frac{m}{\rho_{sc}} = \frac{83.455}{0.65} = 128.39 \text{ cm}^3$$

The reaction volume is 128.39cm³, an increase of 28.4% above the vessel's nominal volume.

The reaction volume calculated is specific to CO₂, calculations for different fluids must be carried out individually due to variations in fluids properties.

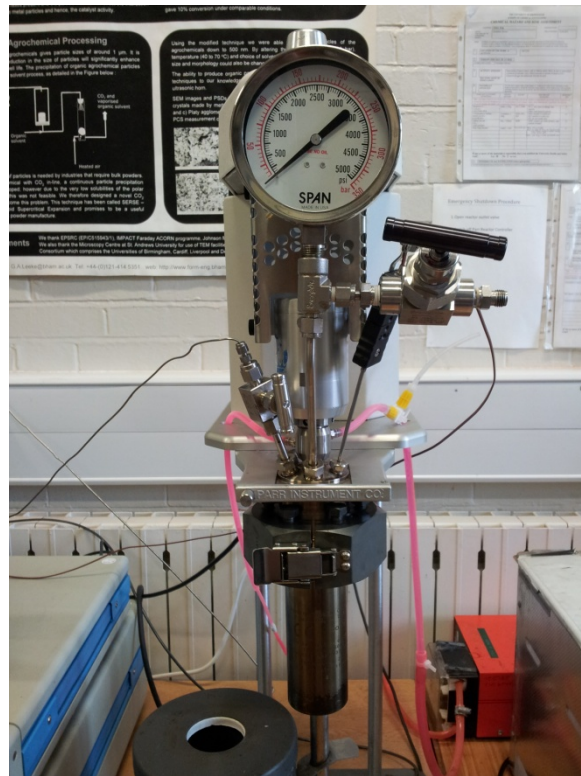


Figure A2: High-Pressure Reactor setup

As shown in Figure A2, the length of tubing outside of the reactor is significant and not negligible. The length of tubing is necessary to ensure that the valves and pressure gauge are not exposed to temperatures exceeding their maximum working conditions. Consequently, the tubing outside of the reactor is at a much lower temperature than the reactor, and therefore the fluid contained within this tubing will behave in a very different manner. In the case of water the difference in conditions is such that the fluid within the reactor may be supercritical whereas that fluid within the tubing is subcritical.

APPENDIX 2. FIBRE DIAMETER VARIABILITY WITH RESPECT TO LENGTH

Table A2: Fibre diameter variability with respect to length

| Fibre Number | Position Number | Diameter (μm) | Mean (μm) | Standard Deviation (Fibre) (μm) |
|--------------------|-----------------|----------------------------|------------------------|--|
| 1 | 1 | 6.90 | 6.91 | 0.01 |
| | 2 | 6.90 | | |
| | 3 | 6.90 | | |
| | 4 | 6.92 | | |
| | 5 | 6.92 | | |
| 2 | 1 | 6.94 | 6.90 | 0.03 |
| | 2 | 6.88 | | |
| | 3 | 6.88 | | |
| | 4 | 6.92 | | |
| | 5 | 6.86 | | |
| 3 | 1 | 7.17 | 7.16 | 0.01 |
| | 2 | 7.17 | | |
| | 3 | 7.15 | | |
| | 4 | 7.15 | | |
| | 5 | 7.15 | | |
| 4 | 1 | 6.88 | 6.85 | 0.04 |
| | 2 | 6.81 | | |
| | 3 | 6.81 | | |
| | 4 | 6.86 | | |
| | 5 | 6.90 | | |
| 5 | 1 | 7.13 | 7.11 | 0.02 |
| | 2 | 7.12 | | |
| | 3 | 7.12 | | |
| | 4 | 7.08 | | |
| | 5 | 7.08 | | |
| Minimum | | 6.81 | | |
| Maximum | | 7.17 | | |
| Mean | | 6.98 | | |
| Standard Deviation | | 0.13 | | |

APPENDIX 3. X-RAY PHOTOELECTRON SPECTROSCOPY DATA

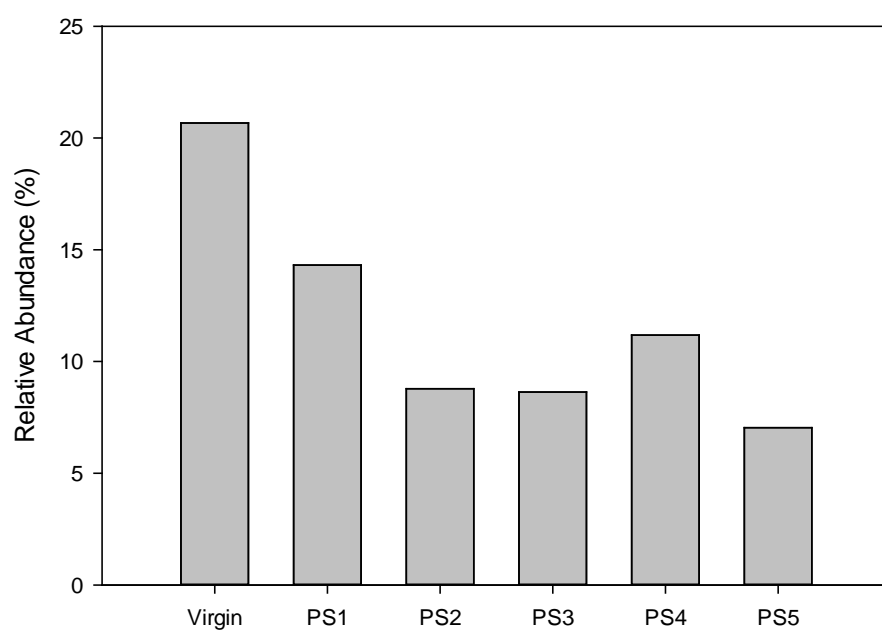


Figure A3: Functional group; -C-O

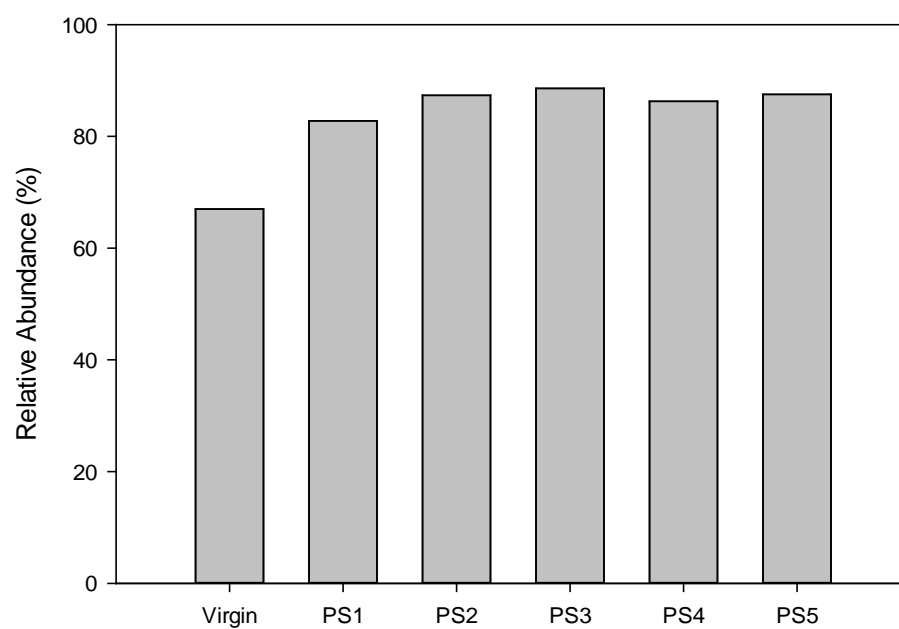


Figure A4: Functional group; -C-C

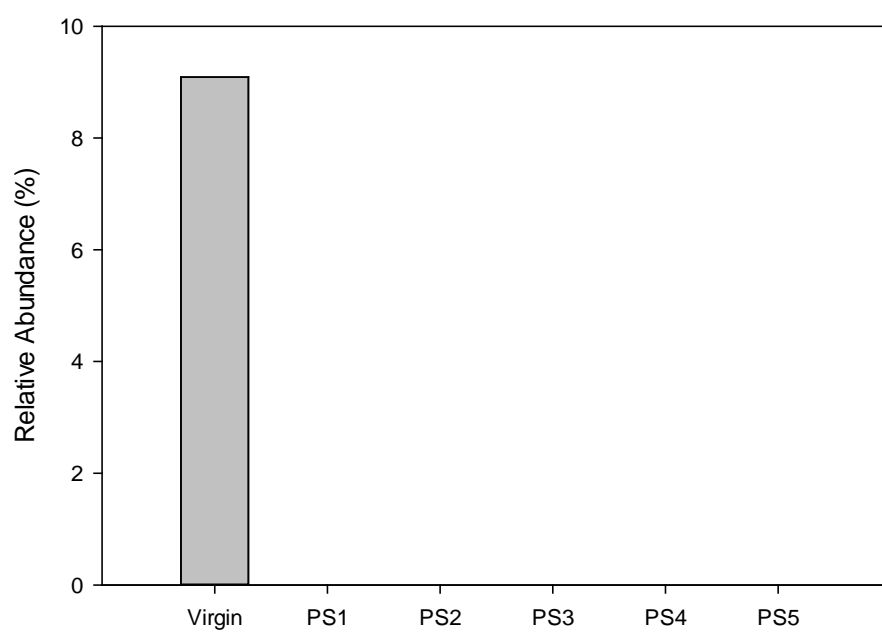


Figure A5: Functional group; -C=O

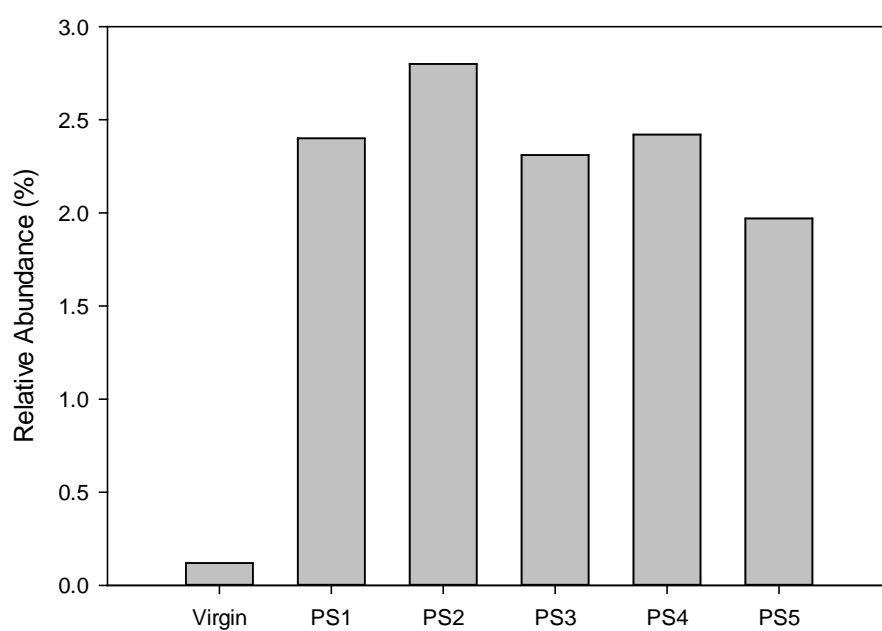


Figure A6: Functional group; -C-NH₂

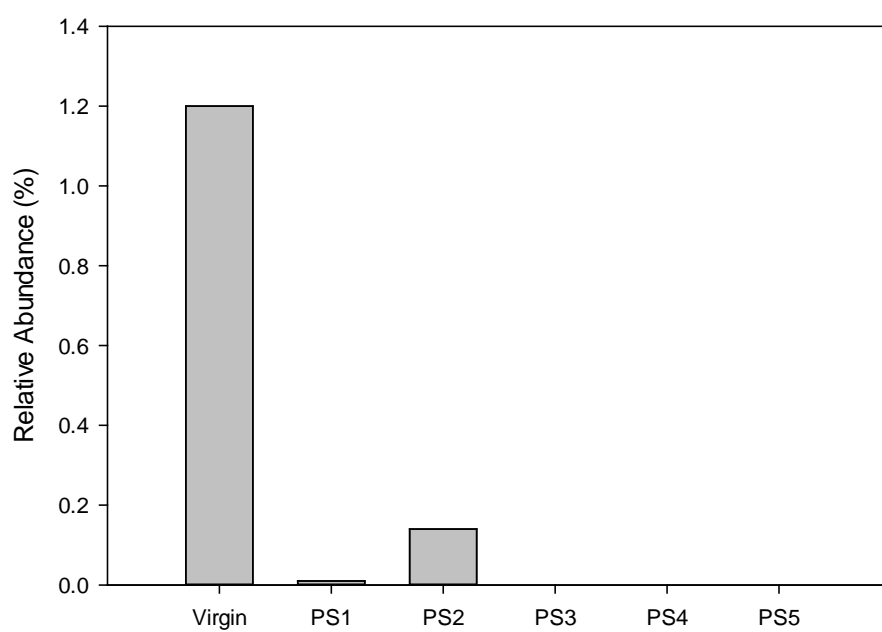


Figure A7: Functional group; NO_3^-

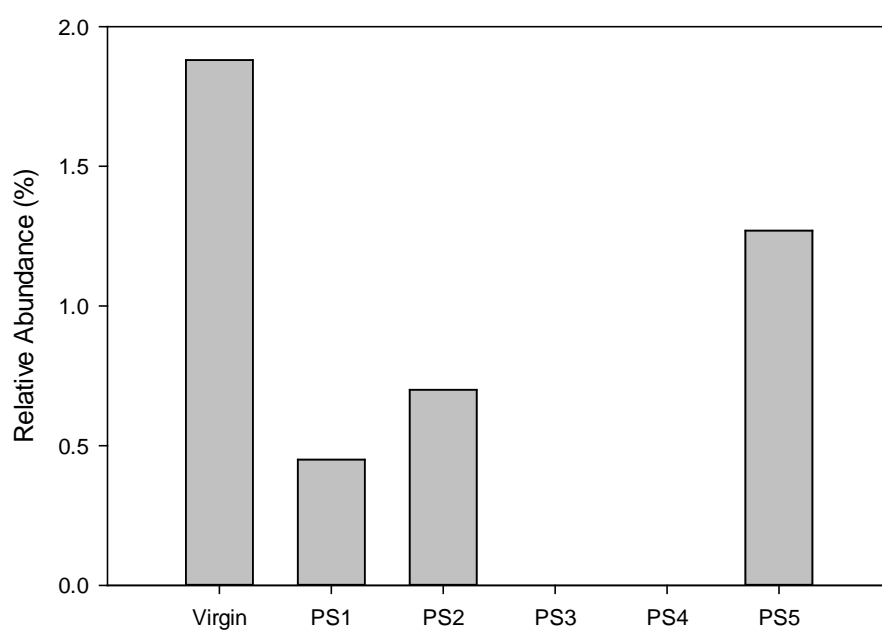


Figure A8: Functional group; Organic Si

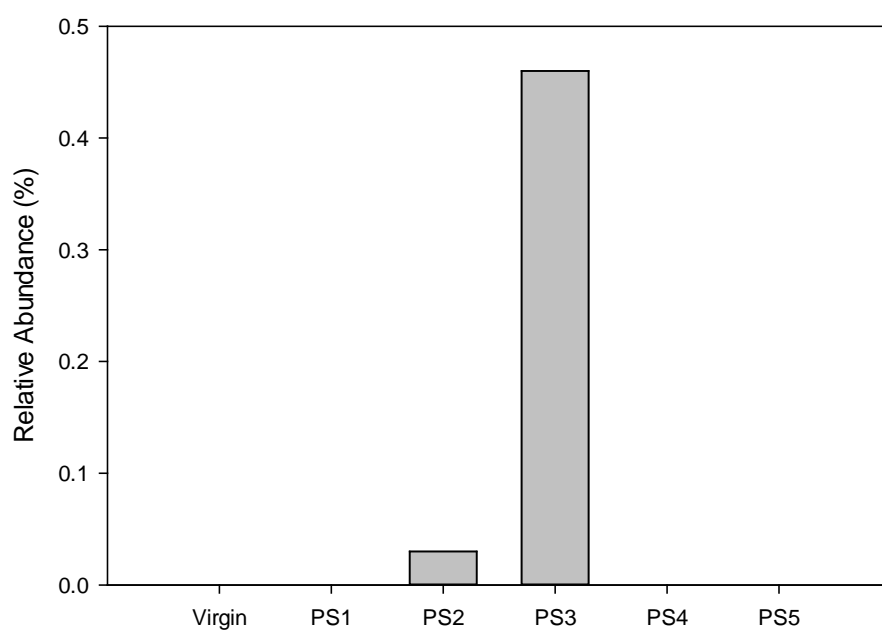


Figure A9: Functional group; Elemental Si

Table A3: Relative abundance of functional groups according to sample, XPS

| Sample | C-C | -C=O | C-O | C-NH ₂ | NO ₃ ⁻ | Organic Si | Elemental Si |
|--------|-------|------|-------|-------------------|------------------------------|------------|--------------|
| Virgin | 66.98 | 9.09 | 20.67 | 0.12 | 1.20 | 1.88 | 0.00 |
| PS1 | 82.77 | 0.00 | 14.31 | 2.40 | 0.01 | 0.45 | 0.00 |
| PS2 | 87.33 | 0.00 | 8.78 | 2.80 | 0.14 | 0.70 | 0.03 |
| PS3 | 88.58 | 0.00 | 8.63 | 2.31 | 0.00 | 0.00 | 0.46 |
| PS4 | 86.26 | 0.00 | 11.18 | 2.42 | 0.00 | 0.00 | 0.00 |
| PS5 | 87.51 | 0.00 | 7.04 | 1.97 | 0.00 | 1.27 | 0.00 |

APPENDIX 4. IMPEDANCE OF FIBRE BUNDLES

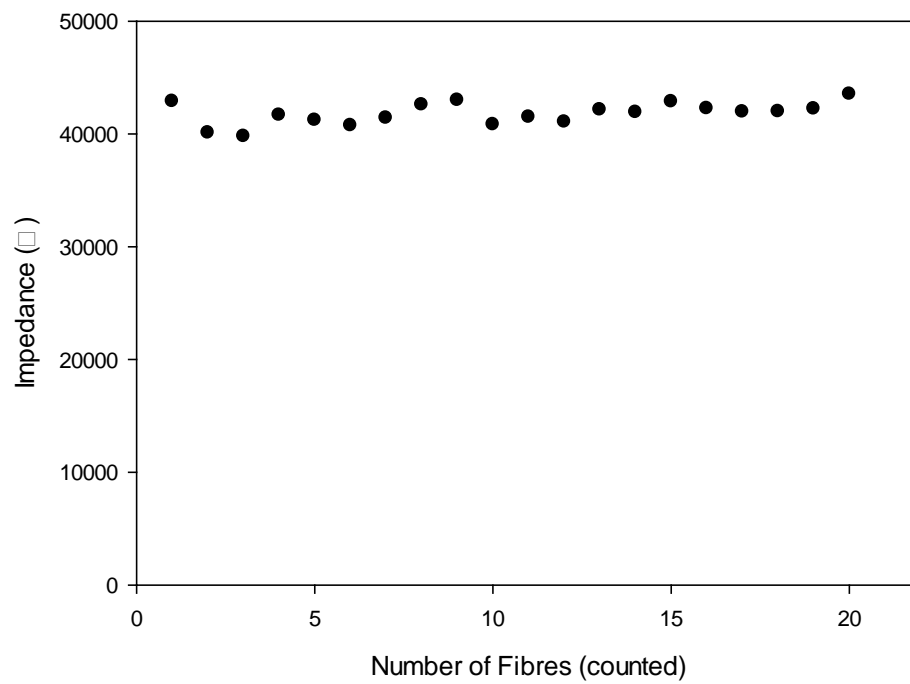


Figure A10: Average impedance of a single fibre as a function of bundle size

APPENDIX 5. REACTOR SCHEMATIC DIAGRAMS

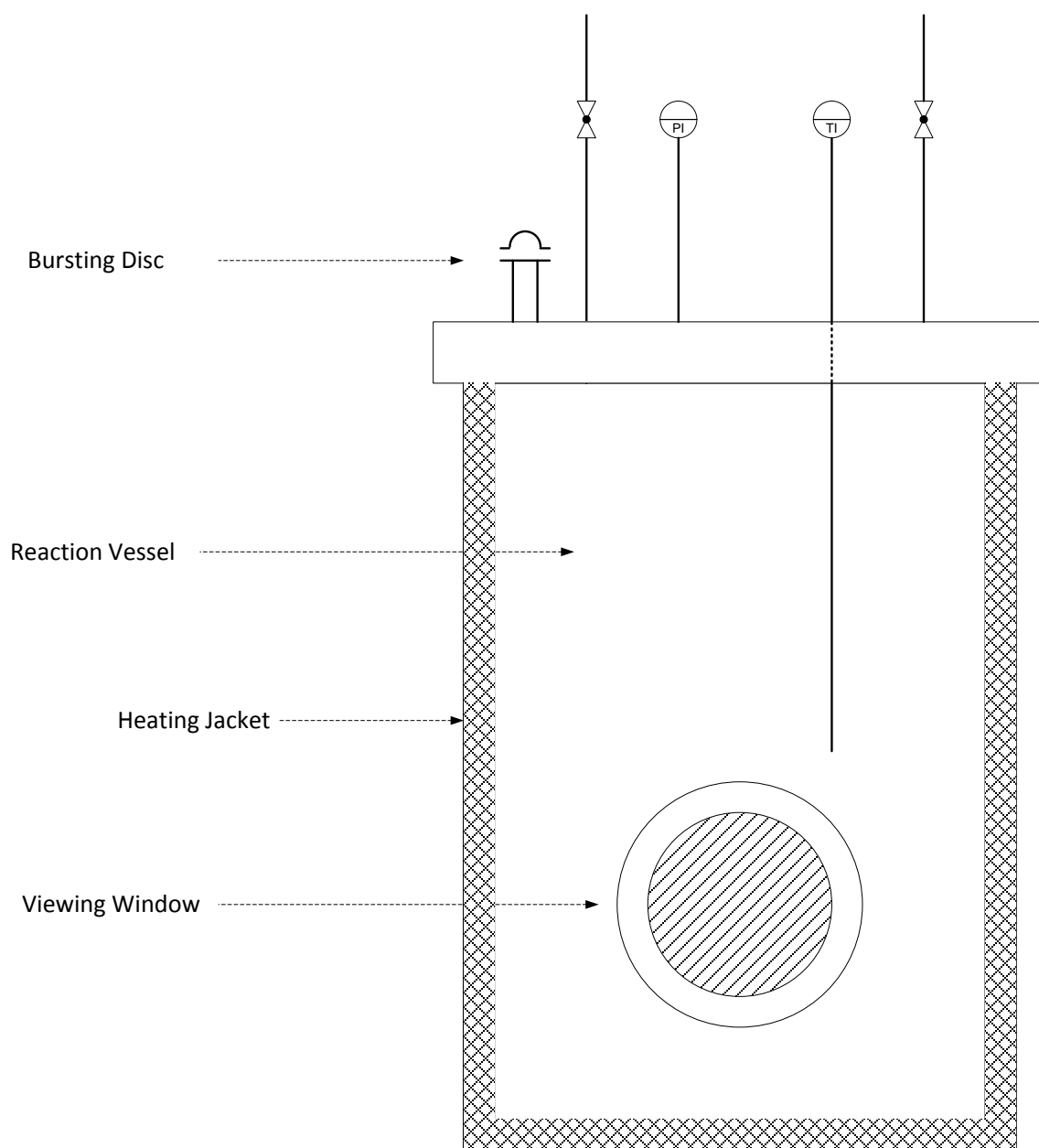


Figure A11: LTR Schematic diagram

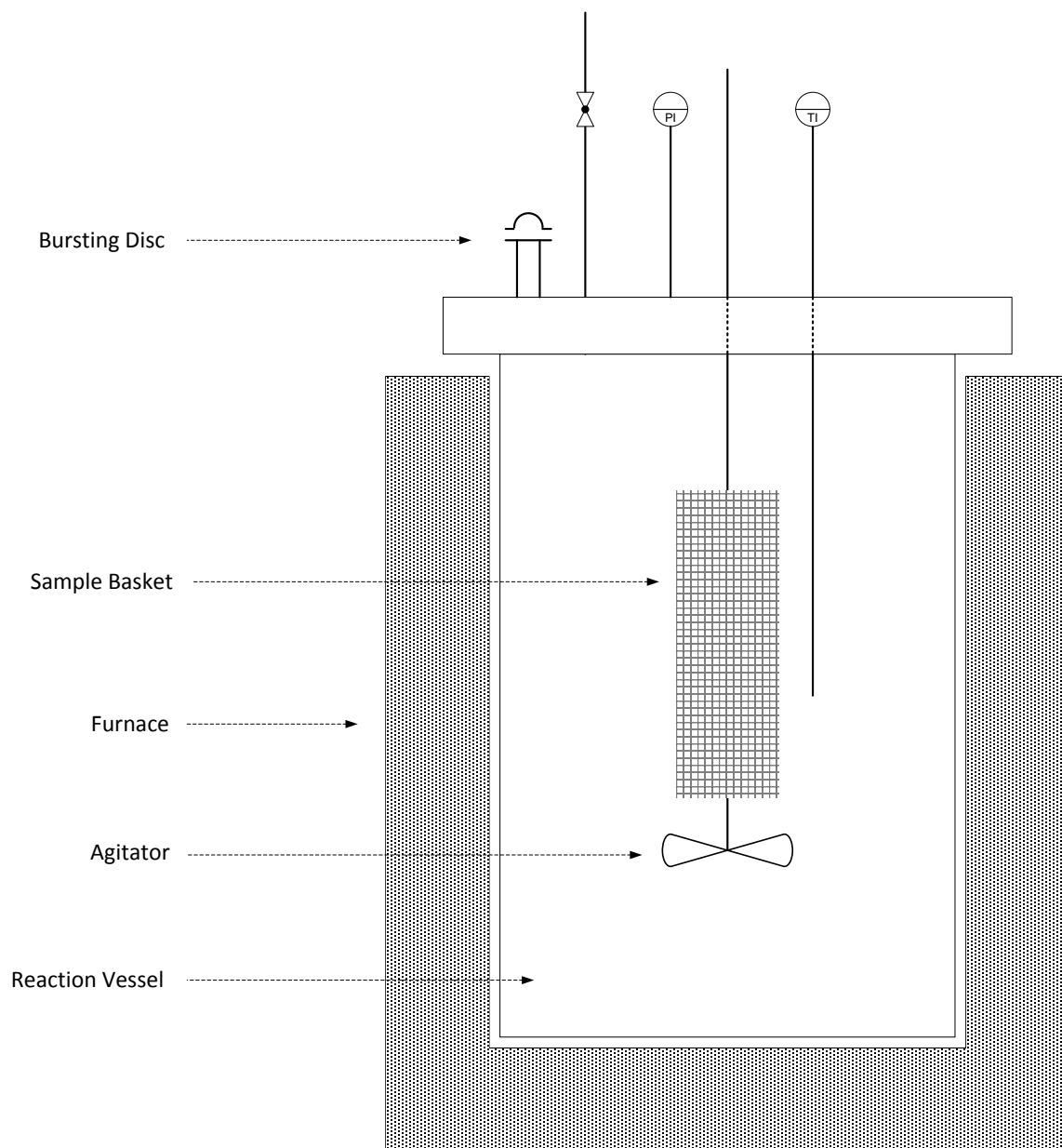


Figure A12: HTR Schematic diagram